Bayesian calibration and imaging in radio interferometry

INAUGURAL-DISSERTATION

zur
Erlangung des Doktorgrades
der Mathematisch-Naturwissenschaftlichen Fakultät
der Universität zu Köln

vorgelegt von

Jong-Seo Kim
aus Incheon, South Korea

angenommen in Köln, 2025

Abstract

Radio interferometry enables to investigate cosmic objects at an exceptional emission sensitivity and a record high angular resolution. Reaching these high standards sets stringent requirements on accuracy of instrumental calibration and reliability of image reconstruction from interferometric data.

In order to obtain a high-fidelity image, instrumental and atmospheric effects in the data should be identified and removed in calibration. After calibration, image reconstruction requires additional assumptions, namely prior knowledge, to obtain a reliable image from sparse and noisy radio interferometric data. A majority of existing software, such as `AIPS`, `CASA`, `DIFMAP` performs calibration and imaging separately, even though our prior in the calibration and imaging is the same knowledge about the source and instrument.

This thesis introduces a joint inference of calibration and image from radio interferometric data using Bayesian imaging software `resolve`. Thus far, Bayesian calibration and imaging has not been investigated extensively due to the high computational cost. In this work, we overcome this limitation with the help of novel variational inference methods. Bayesian approach provides a robust framework to solve degenerate ill-posed inverse problems by exploring correlation between calibration and imaging parameters, instead of point estimates employed by the conventional `CLEAN` algorithm and regularized maximum likelihood (RML) methods. In the Bayesian approach, calibration uncertainties are taken into account naturally in the final reconstruction and we can reconstruct a robust image with improved resolution, also known as super resolution compared to conventional `CLEAN` method. Moreover, the reliability of calibration solutions can be quantified using uncertainty estimation. These advantages of the Bayesian approach are fully incorporated in this dissertation into the imaging and calibration framework which is subsequently applied to imaging emission from compact extragalactic radio sources residing in active galactic nuclei.

Active galactic nuclei (AGNs) are one of the primary targets for radio interferometric observations in order to study the supermassive black hole at the center of AGNs and their jet launching mechanism, which requires imaging at extremely high angular resolutions reaching down to just a few dozens of microarcseconds. To date, very long baseline interferometry (VLBI) technique is able to achieve the highest angular resolution ($\sim 20\mu$as) to investigate the innermost region of AGN at scales of a few gravitational radii for the black hole at the center of our own Galaxy and in several nearby AGN, including the one in the galaxy M87. In the energy extraction mechanism and jet formation, magnetic fields in the AGN play a key role. Therefore, providing robust polarimetric results from the interferometric data becomes a crucial task for understanding the AGN phenomenon. However, polarimetry in radio interferometry has been demanding so far, owing to the low signal to noise ratio (S/N) of polarized signal and antenna leakages. The Bayesian approach for radio interferometric imaging is further extended in this dissertation to include the instrumental polarization calibration and to provide imaging results for the full set of polarimetric products.

In this work, we validate our Bayesian calibration and imaging methods using radio interferometric observations of AGNs. First, Bayesian self-calibration and imaging method was utilized to reconstruct reliable total intensity images of galaxy M87 using VLBI observations at 43 and 86 GHz. Especially, we revisit the global millimeter VLBI array (GMVA)+Atacama Large Millimeter/Submillimeter Array (ALMA) M87 observation at 86 GHz in 2018 and confirm the simultaneous observation of the black hole shadow and extended jet with improved angular resolution. Furthermore, the posterior distribution of ring parameters of M87 at 86 GHz is explored to provide more precise measurements with uncertainty estimation. Our results indicate that the black hole shadow of M87 at 3 mm predominantly originates from accretion flows due to the opacity effect. Second, our Bayesian polarization calibration and imaging method is able to reconstruct robust polarimetric images from Very Long Baseline Array (VLBA) observation of the quasar 3C273 at 15 GHz and GMVA+ALMA observation of the blazar OJ287 at 86 GHz with improved resolution and reliable calibration solutions (gains and Dterms) simultaneously. Third, we performed Bayesian calibration and imaging, including the flux density calibration and gain calibration and self-calibration, for Very Large Array (VLA) Hydra A observation at 2.5 GHz.

Altogether, this dissertation demonstrates that Bayesian calibration and imaging approach for full polarimetric radio interferometric data can reconstruct reliable calibration solutions and images with high resolution and provide better observational constraints with uncertainties to understand the inner structure of AGNs and their jet formation.

Zusammenfassung

Radiointerferometrie ermöglicht die Untersuchung kosmischer Objekte mit einer hervorragenden Emissionsempfindlichkeit und einer unübertroffenen Winkelauflösung. Das Erreichen dieser hohen Genauigkeit stellt strenge Anforderungen an die Instrumentenkalibrierung und die Zuverlässigkeit der Bildrekonstruktion aus interferometrischen Daten.

Um ein hochauflösendes Bild zu erhalten, müssen instrumentelle und atmosphärische Effekte in den Daten identifiziert und bei der Kalibrierung entfernt werden. Nach der Kalibrierung erfordert die Bildrekonstruktion zusätzliche Annahmen, nämlich Vorwissen, um aus dünn besetzte und verrauschten Radiointerferometriedaten ein zuverlässiges Bild zu erhalten. Die meisten vorhandenen Softwareprogramme, wie `AIPS`, `CASA` und `DIFMAP`, führen die Kalibrierung und die Bildgebung separat durch, obwohl unsere Vorinformationen für die Kalibrierung und die Bildgebung das gleiche Wissen über die Quelle und das Instrument teilen.

Diese Arbeit stellt eine gleichzeitige Rekonstruktion der Kalibrierung des Bilds aus Radiointerferometriedaten unter Verwendung der Bayes'schen Bildgebungssoftware `resolve` vor. Bislang wurde die Bayes'sche Kalibrierung und Bildgebung aufgrund des hohen Rechenaufwands noch nicht umfassend untersucht. In dieser Arbeit überwinden wir diese Einschränkung mit Hilfe neuartiger variationaler Inferenzmethoden. Der Bayes'sche Ansatz bietet einen robusten Rahmen zur Lösung degenerierter, nicht eindeutiger inverser Probleme, indem er die Korrelation zwischen Kalibrierungs- und Bildgebungsparametern untersucht, anstatt Punktschätzungen zu verwenden, wie sie beim herkömmlichen `CLEAN`-Algorithmus und bei regulierten Maximum-Likelihood-Methoden (RML) verwendet werden. Beim Bayes'schen Ansatz werden Kalibrierungsunsicherheiten bei der endgültigen Rekonstruktion automatisch berücksichtigt. Dadurch ist eine robustere Rekonstruktion des Bildes möglich, wodurch eine verbesserter Auflösung erreicht werden kann. Dieses wird im Vergleich zur herkömmlichen `CLEAN`-Methode auch als Superauflösung bezeichnet. Darüber hinaus kann die Zuverlässigkeit von Kalibrierungslösungen mithilfe einer Unsicherheitsschätzung quantifiziert werden. Diese Vorteile des Bayes'schen Ansatzes werden in dieser Dissertation vollständig in den Bildgebungs- und Kalibrierungsrahmen integriert, der anschließend auf die Bildgebung von Emissionen aus kompakten extragalaktischen Radioquellen in aktiven Galaxienkernen angewendet wird.

Aktive Galaxienkerne (Active galactic nuclei, AGNs) sind eines der Hauptziele für radiointerferometrische Beobachtungen, um supermassive Schwarze Locher im Zentrum von AGNs und ihren Jet-Ausstoßmechanismus zu untersuchen. Für

solche Untersuchungen ist eine Abbildung mit extrem hoher Winkelauflösung von nur wenigen Dutzend Mikrosekunden erforderlich. Bislang kann mit der Very Long Baseline Interferometry (VLBI)-Technik die höchste Winkelauflösung ($\sim 20\mu$as) erreicht werden, um den innersten Bereich von AGNs in Größenordnungen von wenigen Gravitationsradien für das Schwarze Loch im Zentrum unserer eigenen Galaxie und in mehreren nahe gelegenen AGNs, darunter das in der Galaxie M87, zu untersuchen. Beim Energiegewinnungsmechanismus und der Jet-Bildung spielen Magnetfelder im AGN eine wichtige Rolle. Daher ist die Extraktion robuster polarimetrischer Informationen aus den interferometrischen Daten eine entscheidende Aufgabe für das Verständnis des AGN-Phänomens. Bislang war die Polarimetrie in der Radiointerferometrie jedoch aufgrund des niedrigen Signal-Rausch-Verhältnisses (S/R) des polarisierten Signals und dem Leck-Effekt zwischen den Polarisationsrichtungen sehr anspruchsvoll.

Der Bayesianische Ansatz für die radiointerferometrische Bildgebung wird in dieser Dissertation weiter ausgebaut, um die instrumentelle Polarisationskalibrierung einzubeziehen und Bildgebungsergebnisse für den alle polarizationen zu liefern. In dieser Arbeit validieren wir unsere Bayes'schen Kalibrierungs- und Bildgebungsverfahren anhand von radiointerferometrischen Beobachtungen von AGNs. Zunächst wurde das bayessche Selbstkalibrierung und Bildgebungsverfahren verwendet, um anhand von VLBI-Beobachtungen bei 43 und 86 GHz zuverlässige Gesamtintensitätsbilder der Galaxie M87 zu rekonstruieren. Insbesondere analysieren wir die Beobachtung von M87 mit dem Global Millimeter VLBI Array (GMVA) und dem Atacama Large Millimeter/Submillimeter Array (ALMA) bei 86 GHz aus dem Jahr 2018 erneut und bestätigen die gleichzeitige Beobachtung des Schatten des Schwarzen Lochs und des ausgedehnten Jets mit verbesserter Winkelauflösung. Darüber hinaus wird die a Posteriori Verteilung der Ringparameter von M87 bei 86 GHz untersucht, um genauere Messungen mit Unsicherheitsschätzung zu erhalten. Unsere Ergebnisse deuten darauf hin, dass der Schatten des Schwarzen Lochs von M87 bei 3 mm vorwiegend aus Akkretionsströmen aufgrund des Opazitätseffekts stammt. Zweitens ist unsere bayessche Polarisationskalibrierung und Bildgebungsmethode in der Lage, robuste polarimetrische Bilder aus VLBA-Beobachtungen (Very Long Baseline Array) des Quasars 3C273 bei 15 GHz und GMVA+ALMA-Beobachtungen des Blazars OJ287 bei 86 GHz mit verbesserter Auflösung und zuverlässigen Kalibrierungslösungen (Gains und Dterms) gleichzeitig zu rekonstruieren. Drittens haben wir eine Bayes'sche Kalibrierung und Bildgebung durchgeführt, einschließlich der Flussdichtekalibrierung und Antennen Sensitivitätskalibrierung sowie Selbstkalibrierung, für Very Large Array (VLA)-Hydra A-Beobachtungen bei 2,5 GHz.

Insgesamt zeigt diese Dissertation, dass die Bayes'sche Kalibrierung und Bildgebung für polarimetrische Radiointerferometriedaten zuverlässige Kalibrierungslösungen liefern und eine Rekonstruktion von Bildern mit hoher Auflösung ermöglichen. Dadurch können bessere Beobachtungsergebnisse mit Unsicherheiten bereitstellt werden, um die innere Struktur von AGNs und ihre Jetbildung zu verstehen.

Contents

List of Figures

List of Tables

Chapter 1

Introduction

Humankind have been trying to understand the universe beyond our planet Earth. Historically, our eyes have been a great instrument to observe and image objects in the sky. In 1933, Karl Jansky reported the radio emission originated from the outside of our solar system, which means a new window to observe and understand our Universe was open (Jansky 1933).

To date, we have massive amount of data from radio telescopes all over the world since we can observe radio waves on Earth due to the low atmospheric opacity (see Figure 3.1) and radio telescopes are affordable compared to optical or space-based telescopes. How much information is in the radio data we observed so far? And did we extract all relevant information to understand the universe? At this point, it is already challenging to process all the radio data by our hands due to the large volume of the data. In the near future, the enormous data from next generation radio telescopes will hinder us to process data manually. Fortunately, there is still some room for improvement from the algorithmic side in order to extract information from radio data optimally and automatically. This thesis discusses how to process the radio interferometric data and obtain more robust signal using Bayesian calibration and imaging in a less supervised fashion.

In physics and philosophy, we often prefer the simplest model and theory to explain the nature. This principle is called Occam's Razor and here is the famous quote about the Occam's Razor:

> *"Entities must not be multiplied beyond necessity."*

In other words, *"everything should be made as simple as possible, but not simpler."* Indeed, this philosophy is familiar to physicists. In Physics, we try to understand natural phenomena in the Universe with simplest equations. In fact, Occam's razor is closely related to the Bayesian evidence: the model, which achieves the greatest Bayesian evidence, is determined by a trade-off between favoring the simplicity of the model and minimizing the misfit of data (Mackay 2003).

In this work, the same philosophy is used for the Bayesian calibration and imaging: find the most concise calibration and imaging model to fit the data. Radio interferometer measurement equation (RIME, Hamaker et al. (1996); Smirnov (2011); Thompson et al. (2017)) provides a neat mathematical framework to solve calibration and imaging problems in radio interferometry. According to the Occam's Razor, we should avoid using additional terms tailored to specific data. Inserting additional terms in the model might be able to fit the data we are dealing with but such terms for specific data set is not always suitable for other data. Therefore, we aim to employ a generic calibration and imaging method, which can be applicable for different types of interferometric data.

Indeed, most of the problems in astronomy and astrophysics can be interpreted as an inference problem. We infer parameters in the model from the data and our models based on physics and our knowledge. In this work, we mainly focus on inference problems in radio interferometry. Precise calibration and imaging in radio interferometry can provide more in-depth understanding of the Universe.

As an example, we are able to understand the supermassive black holes at the center of the active galactic nuclei (AGN) and their relativistic jet and magnetic fields using super-resolved polarimetric images from radio interferometric data. Recently, extremely high resolution ($\sim 20\mu$as) in millimeter very long baseline interferometry (VLBI) enabled the central engine (supermassive black hole) to be observed down to a few gravitational radii (Event Horizon Telescope Collaboration et al. 2019a, 2022; Lu et al. 2023).

1.1 Overview of the thesis

This dissertation is structured as follows, In chapter 2, we discuss theory about the active galactic nucleus (AGN), chapter 3 is a brief introduction of the radio interferometry. In chapter 4, we introduce Bayesian calibration and imaging method. In chapter 5, we present Bayesian self-calibration and imaging method with M87 Very long baseline array (VLBA) observation at 43GHz. In chapter 6, the global millimeter VLBI array (GMVA)+Atacama Large Millimeter/Submillimeter Array (ALMA) observation of the galaxy M87 in 2018 at 86GHz is revisited using Bayesian self-calibration and imaging method. chapter 7 discusses Bayesian polarization calibration and imaging method with 3C273 VLBA observation at 15GHz and OJ287 GMVA+ALMA observation at 86GHz. chapter 8 presents Bayesian calibration and imaging with Very Large Array (VLA) Hydra A observation at 2.5GHz. In chapter 9, we summarize our results.

Chapter 2

Active Galactic Nuclei

This chapter explains a brief overview about the Active Galactic Nucleus (AGN) and their physical mechanism. For an extensive introduction, we refer the reader to Carroll (2004) for general relativity and Rybicki & Lightman (1979); Ghisellini (2013) the radiative processes.

2.1 The central region of the active galaxy

In 1963, a star-like object with large redshift ($z = 0.158$) was observed by Maarten Schmidt (Schmidt 1963). He discussed the possibility that the bright emission is from the core region of a galaxy. This was the quasar 3C273, one of the first discovered AGN. The central region of the galaxy releases vast amount of energy across the electromagnetic spectrum and it cannot be explained by the thermonuclear reactions, which is the process that powers the stars.

A plausible explanation is that an AGN is powered by a supermassive black hole, at the center of the galaxy, with a mass in the range $10^6 M_\odot \lesssim M \lesssim 10^{10} M_\odot$, where $M_\odot$ is the solar mass. At the center of the active galaxy, strong gravity accretes matter around the supermassive black hole and the matter is compressed, heated, and accelerated. The observed radiation from accelerated particles indicates that there is a mechanism to extract energy from the black hole (see section 2.4). It contradicts the popular belief that nothing can escape from the gravity of the black hole. The galaxy can emit electromagnetic waves from radio waves to gamma-rays. Especially, in radio frequency, relativistic jets from the active central engine are observed up to $\sim 7\,\mathrm{Mpc}$ scales (Oei et al. 2024). Furthermore, recent studies suggests that there is strong correlation between neutrino emission and blazars with high relativistic beaming (Plavin et al. 2020). However, the physical mechanism to process high energy neutrinos up to $\sim 100\mathrm{PeV}$ is unknown (KM3NeT Collaboration et al. 2025).

There are also other types of black holes (stellar mass and intermediate mass black holes). The periodic radial velocity measurements of X-ray binary system Cygnus X-1 (a period of 5.6 days) from spectrogram were the first empirical evidence of the existence of the stellar mass black holes (Webster & Murdin 1972; Bolton 1972). Among stellar mass black holes, the heaviest black hole ever found is the Gaia BH3, which has the mass of 33 $M_\odot$ (Gaia Collaboration et al. 2024). Intermediate mass black holes was discovered by the LIGO-Virgo collaboration in 2020, named GW190521, a merger of two black holes and formed a black hole of about the mass of 142 $M_\odot$ (Abbott et al. 2020).

There are many subgroups in AGN, such as quasars, Seyfert galaxies, radio galaxies, and blazars. Notably, AGN's are classified into two distinct classes: radio-quiet AGN and radio-loud AGN [1]. The radio-quiet AGN have the spectral energy distribution (SED) primarily dominated by thermal emission from accretion disks, it therefore is faint in the radio regime. On the other hand, the radio-loud AGN are characterized by relativistically beamed jets composed of highly magnetized plasma (Hada et al. 2024). In fact, the majority of AGNs is radio-quiet AGN and the radio-loud AGN are only $10-15\%$ of all AGN. In this thesis, we mostly focus on radio-loud AGNs, such as M87 galaxy and Sgr A* at the center of our Milky way, that can be studied by radio interferometric observations.

2.2 Einstein's theory of gravity

In 1915, Albert Einstein presented the general theory of relativity (Einstein 1915a, 1916). Einstein came up with his theory of gravity using a thought experiment. He argued that, in small enough regions of spacetime, we are not able to distinguish the difference between gravity and acceleration, they therefore are equivalent. It is called the equivalence principle. According to the equivalence principle, the light should bend from the Earth gravity same as the bending light from the the flashlight in a accelerating spacecraft. According to his theory, the gravity is described by the curvature of spacetime instead of a force. If the gravity attracts not only matter but also light, it is natural to imagine a massive dark object that even light cannot escape.

In Newtonian gravity theory, let us imagine a particle that can barely escape from the gravitational force of an object. Since the kinetic energy of the particle and gravitational potential energy is equal, the total energy is $\frac{1}{2}mv^2 - \frac{GMm}{r} = 0$, where m is the particle mass, v is the velocity, G is the gravitational constant, M is the mass of the object, r is the radius between the object and the particle.

---

[1] AGN is defined as a radio-loud AGN if the ratio of radio-to-optical luminosity between the radio flux density at 5GHz and optical flux density at 4400Å(6.8×10^{14}Hz) is higher than 10 (Kellermann et al. 1989).

As a result, the particle has a velocity $v = \sqrt{2GM/r}$, called the escape velocity. If the radius is smaller than $2GM/c^2$, even the particle moving with the speed of light c cannot escape from the object. This radius in general relativity is called the event horizon, a coordinate singularity from a spherically symmetric, static, and vacuum solution (Equation 2.12) of the Einstein field equations, that the boundary around a black hole beyond which event cannot affect an observer outside.

In 1919, Frank Dyson and Arthur Eddington performed observations of deflection of starlight during a total solar eclipse to test Einstein's theory. They measured the deflection of lights by the Sun's gravitational field and the results support Einstein's theory rather than Newton's gravity theory (Dyson et al. 1920). The general relativity is supported by numerous experimental results, such as the precession of Mercury (Einstein 1915b), gravitational lensing (Walsh et al. 1979), gravitational redshift (Pound & Rebka 1960), and the detection of gravitational waves (Abbott et al. 2016).

According to the general relativity, the spacetime is described as a pseudo-Riemannian manifold with indefinite metric signature, e.g., $(-,+,+,+)$. The manifold is a mathematical space, that locally looks like Euclidean space $\mathbb{R}^n$, where n is the dimension. The metric $g_{\mu\nu}$ is a mathematical object describing the geometry of the space, we therefore can calculate the distance, volume, and time intervals using the metric. The spacetime interval in general relativity is $ds^2 = g_{\mu\nu}dx^\mu dx^\nu$. However, the metric is not enough to describe curved space time, we need Affine connection, known as Christoffel symbol:

$$\Gamma^\sigma_{\mu\nu} = \frac{1}{2}g^{\sigma\rho}(\partial_\mu g_{\nu\rho} + \partial_\nu g_{\rho\mu} - \partial_\rho g_{\mu\nu}), \tag{2.1}$$

where $g^{\sigma\rho}$ is the inverse metric ($g^{\mu\nu}g_{\nu\sigma} = \delta^\mu_\sigma$, where δ^μ_σ is the Kronecker delta, if $\mu = \sigma$, $\delta^\mu_\mu = 1$, if $\mu \neq \sigma$, $\delta^\mu_\sigma = 0$).

As it can be seen, we can calculate the Christoffel connection from the metric. We use the Christoffel connection to make the covariant derivative ∇_μ of a vector V^ν be a tensor: $\nabla_\mu V^\nu = \partial_\mu V^\nu + \Gamma^\nu_{\mu\lambda}V^\lambda$, where ∂_μ is the partial derivative. As a result, we can describe geometrical and physical quantities, such as the energy-momentum $T^{\mu\nu}$ as tensors, which are covariant.

The Christoffel connection appears in the definition of geodesic, which is the curved-space generalized version of a straight line in Euclidean space. The geodesic is the trajectory along which a vector is parallel transported to itself. A parameterized curve $x^\mu(\lambda)$ is a geodesic if it follows

$$\frac{D}{d\lambda}\frac{dx^\mu}{d\lambda} = \frac{d^2x^\mu}{d\lambda^2} + \Gamma^\mu_{\rho\sigma}\frac{dx^\rho}{d\lambda}\frac{dx^\sigma}{d\lambda} = 0, \tag{2.2}$$

where $\frac{D}{d\lambda}$ is the parallel transport operator.

For example, massless particles, such as photons, follow null geodesics and the trajectory of the massive particles is described by time-like geodesics. The parallel transport is an important concept to define the curvature of the spacetime since the critical difference between flat and curved space is that, the parallel transported vector from one point to another will depend on the path taken between the points. The curvature tensor (Riemann tensor) $R^\rho_{\sigma\mu\nu}$ is defined by the commutator of two covariant derivaties:

$$[\nabla_\mu, \nabla_\nu]V^\rho = \nabla_\mu\nabla_\nu V^\rho - \nabla_\nu\nabla_\mu V^\rho = R^\rho_{\sigma\mu\nu}V^\sigma - 2\Gamma^\lambda_{[\mu\nu]}\nabla_\lambda V^\rho, \tag{2.3}$$

where $2\Gamma^\lambda_{[\mu\nu]} = \Gamma^\lambda_{\mu\nu} - \Gamma^\lambda_{\nu\mu}$ is the torsion tensor, which is zero in Einstein's general relativity.

Consequently, the Riemann tensor is

$$R^\rho_{\sigma\mu\nu} = \partial_\mu\Gamma^\rho_{\nu\sigma} - \partial_\nu\Gamma^\rho_{\mu\sigma} + \Gamma^\rho_{\mu\lambda}\Gamma^\lambda_{\nu\sigma} - \Gamma^\rho_{\nu\lambda}\Gamma^\lambda_{\mu\sigma}\,. \tag{2.4}$$

Now we have mathematical tools to describe the curved spacetime. There is a famous quote about the general relativity by John Wheeler: *"Spacetime tells matter how to move, matter tells spacetime how to curve"*. We can describe how the matter and energy determine the curved spacetime by the Einstein field equations (Einstein 1915a, 1916):

$$R_{\mu\nu} - \frac{1}{2}Rg_{\mu\nu} = \frac{8\pi G}{c^4}T_{\mu\nu}, \tag{2.5}$$

where $R_{\mu\nu} = R^\lambda_{\mu\lambda\nu}$ is a contraction of the Riemann tensor called the Ricci tensor, $R = R^\mu_\mu = g^{\mu\nu}R_{\mu\nu}$ is another contraction known as the Ricci scalar, $T_{\mu\nu}$ is the energy-momentum tensor.

One can introduce the Einstein tensor $G_{\mu\nu} = R_{\mu\nu} - \frac{1}{2}Rg_{\mu\nu}$, which is the Riemann curvature plus an additional term. We need the additional term in the Einstein field equation (Equation 2.5) for the local conservation of energy and momentum $\nabla^\mu T_{\mu\nu} = 0$. $\nabla^\mu G_{\mu\nu} = 0$ can be derived by the twice-contracted Bianchi identity ($g^{\nu\sigma}g^{\mu\lambda}(\nabla_\lambda R_{\rho\sigma\mu\nu} + \nabla_\rho R_{\sigma\lambda\mu\nu} + \nabla_\sigma R_{\lambda\rho\mu\nu}) = 0$). Note that the Einstein field equations can be interpreted as coupled non-linear partial differential equation for the metric tensor $g_{\mu\nu}$.

The Einstein's gravity theory can be derived by the principle of least action.

The Einstein-Hilbert action S_H is

$$S_H = \int d^4x \mathcal{L}_H = \int d^4x \sqrt{-g} R, \tag{2.6}$$

where $\mathcal{L}_H$ is the Lagrangian density and $g = \det(g_{\mu\nu})$ is the determinant of the metric tensor.

The Einstein field equations in vacuum can be obtained using the least action principle, which means the trajectory of the system between two points follows the one that minimizes the action ($\delta S = 0$). To derive the full Einstein field equations with the energy-momentum tensor, we need to add the action for matter S_M to the action S:

$$S = \frac{c^4}{8\pi G} S_H + S_M, \tag{2.7}$$

where S_M is the action for matter, which can be used for the definition of the energy-momentum tensor:

$$T_{\mu\nu} = -\frac{1}{\sqrt{-g}} \frac{\delta S_M}{\delta g^{\mu\nu}}. \tag{2.8}$$

Note that in flat (Minkowski) spacetime, the conservation of the energy-momentum tensor results from the symmetry of the Lagrangian under spacetime translations by the Noether's theorem. Noether's theorem connects the symmetry and the conservation laws in physics, which is the foundation of the modern physics. In general relativity, the symmetry of the spacetime geometry can be described by the Killing vector field K^μ. If the vector fields satisfy $\nabla_\mu K^\nu + \nabla_\nu K^\mu = 0$, we can find a conserved scalar $K_\nu p^\nu$ along the geodesic ($p^\mu \nabla_\mu (K_\nu p^\nu) = 0$).

We note that it is possible to add additional term to the Einstein-Hilbert action:

$$S = \int d^n x \sqrt{-g} (R - 2\Lambda), \tag{2.9}$$

where Λ is the cosmological constant (Einstein 1917).

The resulting field equations are

$$R_{\mu\nu} - \frac{1}{2} R g_{\mu\nu} + \Lambda g_{\mu\nu} = 0. \tag{2.10}$$

We can have the energy momentum tensor in the Einstein field equations by adding an action for matter S_M:

$$R_{\mu\nu} - \frac{1}{2}Rg_{\mu\nu} + \Lambda g_{\mu\nu} = \frac{8\pi G}{c^4}T_{\mu\nu}. \tag{2.11}$$

The Einstein field equations with the cosmological constant Λ can describe the expansion of the universe. Note that the cosmological constant Λ can be ignored, if the length scale of the object is much smaller than the cosmological scale, such as studying supermassive black holes.

In the weak gravitational field (Newtonian) limit, the Poisson equation for the Newtonian gravitational potential ($\nabla^2\Phi = 4\pi G\rho$, where Φ is the gravitational potential, ρ is the the density of the object) is derived from the Einstein field equations (Equation 2.5) using $g_{00} = -(1 + 2\Phi)$.

2.2.1 Schwarzschild black hole

Henceforce, we use a system of natural units ($c = 1$) for simplicity. There exists the most famous exact solution (static and spherically symmetric vacumn solution) for Einstein field equations, namely the Schwarzschild metric (Schwarzschild 1916):

$$ds^2 = -\left(1 - \frac{2GM}{r}\right)dt^2 + \left(1 - \frac{2GM}{r}\right)^{-1}dr^2 + r^2(d\theta^2 + \sin^2\theta d\phi^2), \tag{2.12}$$

where G is Newton's constant and (t, r, θ, ϕ) are spherical spacetime coordinates.

This metric can be derived from a spherically symmetrical field assumption and the Newtonian limit ($g_{00} = -(1 + 2\Phi)$). There is a characteristic length scale in the Schwarzschild metric $r_g = GM/c^2$ restoring explicit factors of the speed of light c, called gravitational radius. Note that the Schwarzschild metric becomes the Minkowski metric as $r \to \infty$, namely asymptotic flatness.

In the Schwarzschild solution, the metric coefficients become infinite at $r = 0$ and $r = 2GM$. $r = 0$ is a real singularity. We can show that the quadratic scalar invariant, also known as Kretschmann scalar, from the curvature becomes infinite at r=0:

$$R^{\mu\nu\rho\sigma}R_{\mu\nu\rho\sigma} = \frac{48G^2M^2}{r^6}. \tag{2.13}$$

On the other hand, none of the curvature becomes infinite at $r_s = 2GM$, also known as the Schwarzschild radius. It is not a true singularity, just an artifact of the coordinate system (coordinate singularity) and can be removed by changing coordinates. In fact, this radius is called event horizon, the surface beyond nothing can escape from the gravity of the black hole. The event horizon is a null hypersurface, surface where the normal vector is null (lightlike). For spherically symmetric or axisymmetric stationary metric, the event horizon $r = r_H$ is the hypersurface at which g^{rr} switches from being positive to negative: $g^{rr}(r_H) = 0$. In other words, the null hypersurface r = const has a normal vector $n_\mu = \partial_\mu r = (0,1,0,0)$ and the norm of the normal is $n^\mu n_\mu = g^{rr} = 0$. For the Schwarzschild metric, $g^{rr} = 1 - 2GM/r$, the event horizon therefore is $r_H = r_s = 2GM$.

The Scwarzschild metric can describe a non-rotating and uncharged spherically symmetric black hole, that is Schwarzschild black hole. For convenience, we can normalize λ along null geodesics such that the four-velocity is equal to the four-momentum, $p^\mu = dx^\mu/d\lambda$. The geodesic equation has the constant quantity along the path: $-g_{\mu\nu}U^\mu U^\nu = -U_\nu U^\nu = \epsilon$, if it is null geodesic for massless particles, ϵ=0, if it is time-like geodesic for massive particles, ϵ= 1, where $U^\mu = \frac{dx^\mu}{d\lambda} = (\dot{t}, \dot{r}, \dot{\theta}, \dot{\phi})$ is the null tangent vector, λ is the affine parameter. Due to spherical symmetry, we can choose the equatorial plane ($\theta = \frac{\pi}{2}$) without loss of generality.

We can solve $-U_\nu U^\nu = \epsilon$ in Schwarzschild geometry:

$$-\left(1 - \frac{2GM}{r}\right)\left(\frac{dt}{d\lambda}\right)^2 + \left(1 - \frac{2GM}{r}\right)^{-1}\left(\frac{dr}{d\lambda}\right)^2 + r^2\left(\frac{d\phi}{d\lambda}\right)^2 = -\epsilon. \tag{2.14}$$

We can simplify this equation using two Killing vectors in Schwarzschild metric: $K^\mu = (\partial_t)^\mu = (1,0,0,0)$ and $R^\mu = (\partial_\phi)^\mu = (0,0,0,1)$. According to the Killing's equation, there are conserved quantities corresponding to each Killing vector, the energy $E = -K_\mu \frac{dx^\mu}{d\lambda}$, the angular momentum $L = R_\mu \frac{dx^\mu}{d\lambda}$:

$$E = \left(1 - \frac{2GM}{r}\right)\frac{dt}{d\lambda},\ L = r^2\frac{d\phi}{d\lambda}. \tag{2.15}$$

As a result, we can obtain a second-order differential equation for radial behavior of a classical particle of unit mass and energy $\mathcal{E}$ moving in a effective potential energy $V_{\text{eff}}(r)$ in order to understand the orbits of particles near the Schwarzschild black hole:

$$\frac{1}{2}\left(\frac{dr}{d\lambda}\right)^2 + V_{\text{eff}}(r) = \mathcal{E}, \tag{2.16}$$

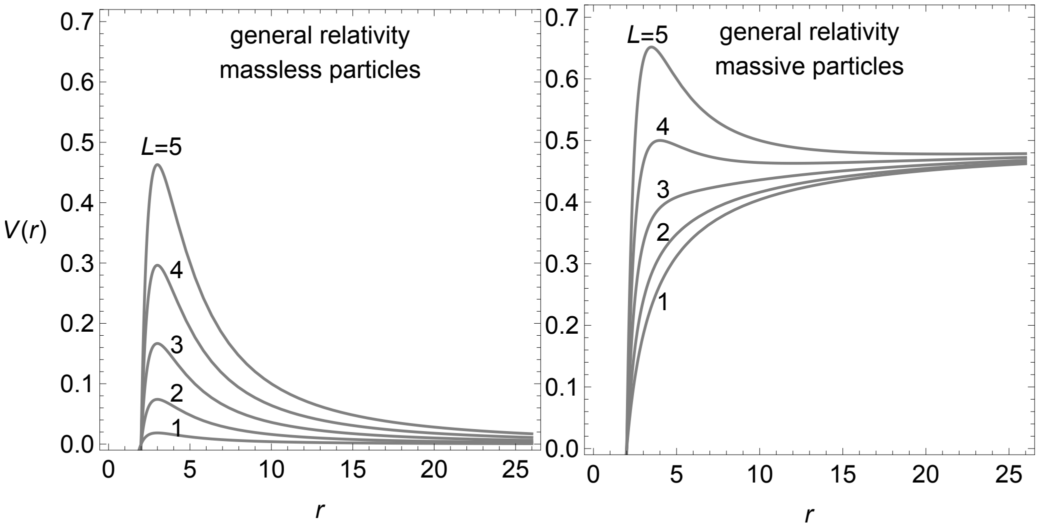

Figure 2.1: Effective potentials in Schwarzschild geometry. There are five curves corresponding to the listed values of the angular momentum L with $GM = 1$. Credit: Arman Tursunov.

where the effective potential energy:

$$V_{\text{eff}}(r) = \frac{1}{2}\epsilon - \epsilon\frac{GM}{r} + \frac{L^2}{2r^2} - \frac{GML^2}{r^3}, \tag{2.17}$$

and the energy $\mathcal{E} = \frac{1}{2}E^2$.

We note that the second term in the effective potential energy is the Newtonian gravitational potential, the third term is the a contribution from angular momentum, and the last term is purely general relativistic contribution.

For photon (massless particle, $\epsilon = 0$) orbit, the particle moves in a circular orbit at radius r_c, if the effective potential is flat:

$$\frac{dV_{\text{eff}}}{dr} = -\frac{L^2}{r^3} + \frac{3GML^2}{r^4} = 0. \tag{2.18}$$

Therefore, the photon has a circular orbit $r_c = 3GM/c^2 = 3r_g$ (see Figure 2.1) restoring explicit factors of the speed of light, which is 1.5 times larger than the Schwarzschild radius r_s. The circular orbit of the photon r_c is unstable because it corresponds to a maximum of the effective potential. In other words, any perturbation will make the photon either go away to $r = 0$ or $r = \infty$.

When the effective potential at $3r_g$ is equal to the energy $\mathcal{E}$, photons are captured on the unstable circular orbit:

$$\frac{L^2}{54G^2M^2} = \frac{1}{2}E^2 \tag{2.19}$$

$$b^2 = \frac{L^2}{E^2} = 27G^2M^2, \tag{2.20}$$

where the impact parameter $b = L/E$ is the ratio of angular momentum to energy.

In other words, photons with a specific impact parameter $b = 3\sqrt{3}GM$ are trapped in the unstable circular photon orbit $r = 3r_g$. This orbit characterizes the emission from the innermost region of the black hole, also known as the black hole shadow (see section 2.3).

For massive particle ($\epsilon = 1$), the circular orbits are at r_c defined by a quadratic function:

$$\frac{dV_{\rm eff}}{dr}r^4 = GMr^2 - L^2r - 3GML^2 = 0. \tag{2.21}$$

As a result, the circular orbits is

$$r_c = \frac{L^2 \pm \sqrt{L^4 - 12G^2M^2L^2}}{2GM}. \tag{2.22}$$

For large L, there are one stable (larger r_c) and one unstable (smaller r_c) circular orbit. When $L \to \infty$, $r_c = (3GM, L^2/GM)$. In this limit, the stable circular orbit (L^2/GM) becomes farther away, while the unstable circular orbit approaches $3GM$, the same as the orbit of massless particle. If $L = \sqrt{12}GM$ ($r_c = 6GM$), the two circular orbits coincide and they disappear entirely for smaller L. Therefore, $6GM/c^2$ ($= 6r_g$) with explicit factors of the speed of light, is the smallest possible radius of a stable circular orbit, namely innermost stable circular orbit (ISCO) for the Schwarzschild black hole.

2.2.2 Kerr black hole

In 1963, Roy Kerr reported the solution for an uncharged stationary rotating black hole (Kerr 1963). His result, the Kerr metric, in Boyer-Lindquist coordinates (t, r, ϕ, θ) is:

$$ds^2 = -\left(1 - \frac{2GMr}{\rho^2}\right)dt^2 - \frac{2GMar\sin^2\theta}{\rho^2}(dtd\phi + d\phi dt) \tag{2.23}$$

$$+\frac{\rho^2}{\Delta}dr^2 + \rho^2 d\theta^2 + \frac{\sin^2\theta}{\rho^2}\left[(r^2 + a^2)^2 - a^2\Delta\sin^2\theta\right]d\phi^2, \tag{2.24}$$

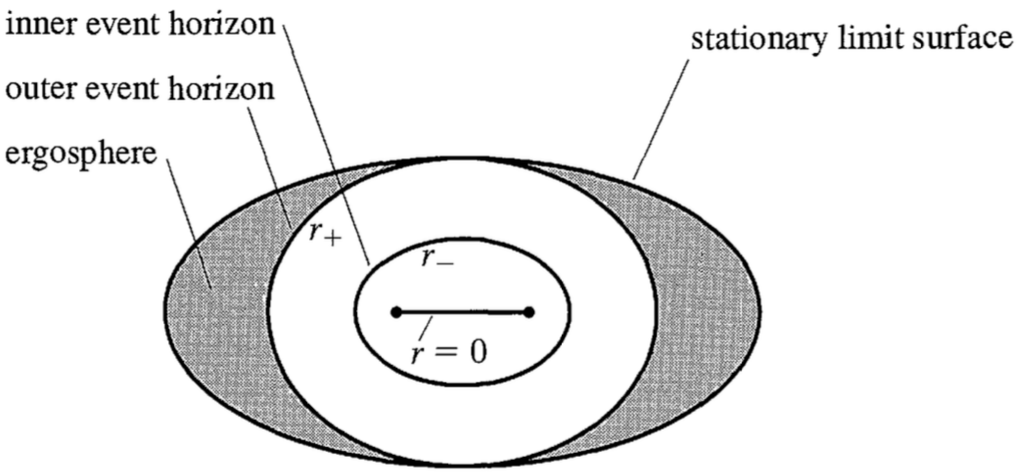

Figure 2.2: Schematic illustration of Kerr metric. Figure taken from Carroll (2004).

where $\Delta = r^2 - 2GMr + a^2$, $\rho^2 = r^2 + a^2\cos^2\theta$, and $a = J/M$ is the angular momentum per unit mass.

We note that the Boyer-Lindquist coordinates are not the same as the spherical spacetime coordinates in the Schwarzschild metric (Equation 2.12). The coordinate transform from Boyer-Lindquist coordinates to Cartesian coordinates is given by:

$$x = \sqrt{r^2 + a^2}\,\sin\theta\,\cos\phi,\ \ y = \sqrt{r^2 + a^2}\,\sin\theta\,\sin\phi,\ \ z = r\cos\theta. \tag{2.25}$$

If $a = 0$ (non-spinning case), The Kerr metric reduces to the Schwarzschild metric in Equation 2.12. Using the same argument for the Schwarzschild black hole ($g^{rr}(r_H) = 0$), the event horizons (null hypersurface) of the Kerr black hole occur when:

$$g^{rr} = \frac{\Delta}{\rho^2} = \frac{r^2 - 2GMr + a^2}{r^2 + a^2\cos^2\theta} = 0. \tag{2.26}$$

If $GM < a$, it is a naked singularity, there is no event horizon. If $GM = a$, this extreme case is unstable. Therefore, we focus on more physically interesting case: $GM > a$. Since $\rho^2 \geq 0$, there are two event horizons (see Figure 2.2):

$$r_\pm = GM \pm \sqrt{G^2M^2 - a^2}, \tag{2.27}$$

where r_+ is the outer event horizon and r_- is the inner event horizon.

We are interested in the outer event horizon r_+, which is physically possi-

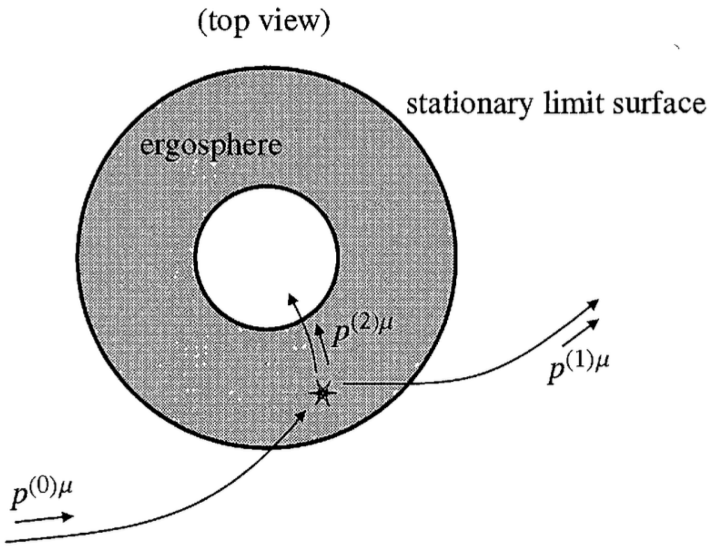

Figure 2.3: Schematic illustration of the Penrose process. Figure taken from Carroll (2004).

ble to observe. In the Kerr metric, there exists another type of horizon, namely Killing horizon, a null hypersurface where a Killing vector becomes null. In the Schwarzschild metric, the Killing horizon for time Killing vector $K = \partial_t$ is the event horizon. However, the Killing horizon for time Killing vector in the Kerr metric is not the event horizon. This results in a region in Kerr solution, known as the ergosphere.

The norm of K^μ is:

$$K^\mu K_\mu = g_{tt} = -\left(1 - \frac{2GMr}{\rho^2}\right). \tag{2.28}$$

The Killing horizons occur when the norm $K^\mu K_\mu = 0$:

$$r_{erg,\pm} = GM \pm \sqrt{G^2M^2 - a^2\cos^2\theta}, \tag{2.29}$$

where r_{erg} is the radius of ergosurface, also known as stationary limit surface.

The inner ergosurface $r_{erg,-}$ is inside the event horizon, the outer ergosurface $r_{erg,+}$ therefore is physically relavent. The ergosphere is defined as a region between the outer event horizon r_+ and the outer ergosurface (stationary limit surface). The object in the ergosphere cannot be stationary, you must move in the direction of the rotation of the black hole (the ϕ direction).

Penrose (1969) suggested a mechanism to extract the energy from the ergosphere, known as the Penrose process. Inside the ergosphere, K^μ becomes spacelike, we can therefore imagine particles with negative energy $E = -K_\mu p^\mu < 0$. Figure 2.3 visualizes the Penrose process that an object with the momentum $p^{(0)\mu}$

falls toward a Kerr black hole and split in two, with one piece with the momentum $p^{(2)\mu}$ entering through the horizon and the other escapes to infinity with a large energy $p^{(1)\mu}$ than the original energy of the object. According to the momentum conservation,

$$p^{(0)\mu} = p^{(1)\mu} + p^{2\mu}. \tag{2.30}$$

By contracting with the Killing vector K_μ,

$$E^{(0)} = E^{(1)} + E^{(2)}. \tag{2.31}$$

The energy $E^{(2)}$ in the ergosphere can be negative, the object can obtain energy from the rotating black hole: $E^{(0)} < E^{(1)}$.

In fact, astrophysical processes that extract rotation energy from black holes are more efficiently driven by electromagnetic mechanisms, e.g. Blandford-Znajek process (Blandford & Znajek 1977). However, the Penrose process remains a fundamental concept. The exact mechanisms responsible for black hole energy extraction have not yet been observationally proven.

2.3 Imaging supermassive black holes Sgr A* and M87*

At the center of our galaxy Milky Way, the existence of a supermassive compact object ($\sim 4.3 \times 10^6 M_\odot$) was confirmed by mapping the orbits of bright stars around the center of Milky Way (Ghez et al. 2008; Gillessen et al. 2009). To accomplish this, two research groups led by Reinhard Genzel and Andrea Ghez utilized the adaptive optics technique to correct for the atmospheric turbulence using a bright reference object next to the science target. They traced individual star orbits and estimated the mass of the compact object at the center of Milky Way. Figure 2.4 shows the orbit of the S2 star around the supermassive compact object at the Galactic Center. Reinhard Genzel and Andrea Ghez were awarded the Nobel Prize in Physics in 2020 for the discovery of a supermassive compact object at the center of our galaxy.

Among many theories to explain this compact object, supermassive black hole (SMBH) is one of the most convincing explanations. To date, we expect that all active galaxies host a SMBH at the center and AGNs are powered by accretion of gas falling towards central BH because of the strong gravitational potential. The observational evidence for the presence of accretion flows is thermal continuum emission in the optical and ultraviolet wavelengths, namely Big Blue

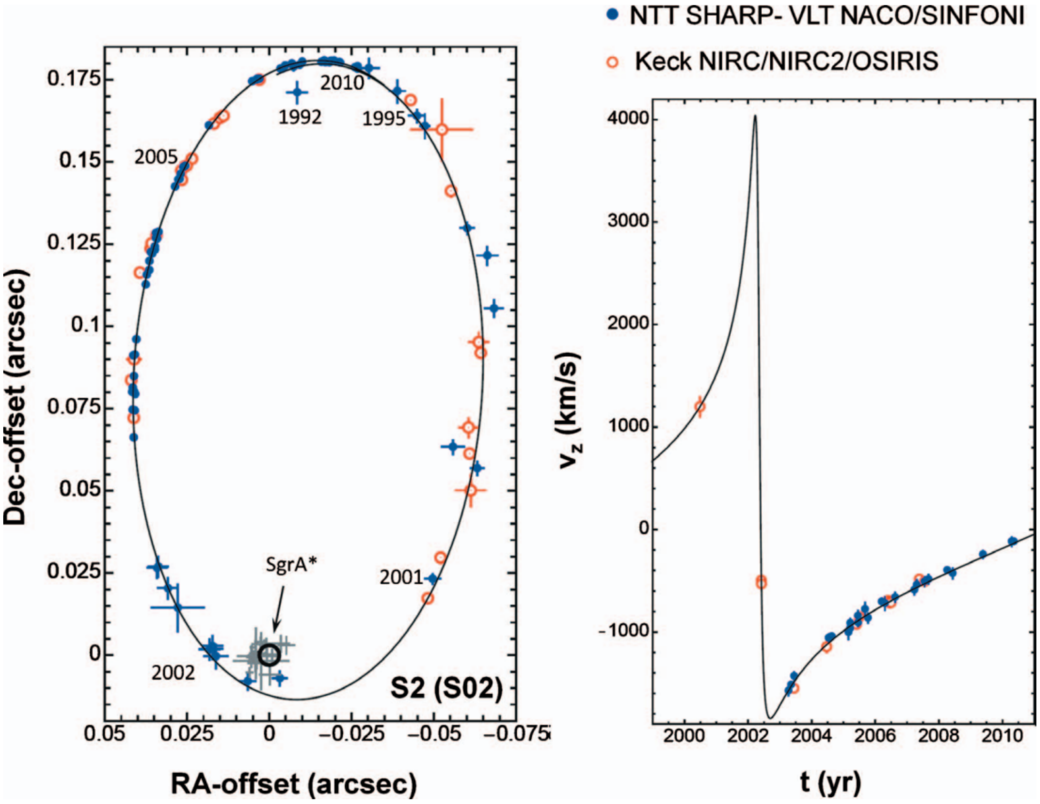

Figure 2.4: Orbit of the star S2 on the sky (left panel) and radial velocity of the star S2 (right panel) from the NTT/VLT and Keck telescopes. Figure taken from Genzel et al. (2010).

Bump (Shields 1978).

On horizon scales, general relativity predicts the black hole shadow due to the strong bending of light in an optically thin region surrounding the black hole (Falcke et al. 2000). In order to image those SMBHs on horizon scales, extremely high angular resolution is required. Thus far, only the very long baseline interferometry (VLBI) is able to achieve an exceptionally high image resolution enough to image SMBHs. Figure 2.5 illustrates photon orbits around the Schwarzschild black hole as a function of the impact parameter $b = L/M$, where L is the angular momentum and E is the energy. The unstable circular photon orbit occurs at $r = 3r_g$. Photons with an impact parameter $b = 3\sqrt{3}GM$ are trapped in the circular orbit at $r = 3r_g$ (see subsection 2.2.1). The impact parameter of a light ray is approximately the same as the radius of the ring from a distance observer (Hartle 2003). This is called apparent boundary, a circle of apparent radius $r = 3\sqrt{3}r_g$. In a optically thin case, the photons on geodesics around the apparent boundary can orbit the black hole multiple times and enhance the brightness. Photons with the impact parameter $b < 3\sqrt{3}\,r_g$ will be captured by the gravity, it therefore results in a central dark area.

The right panel of Figure 2.5 depicts photon orbits around a Schwarzschild

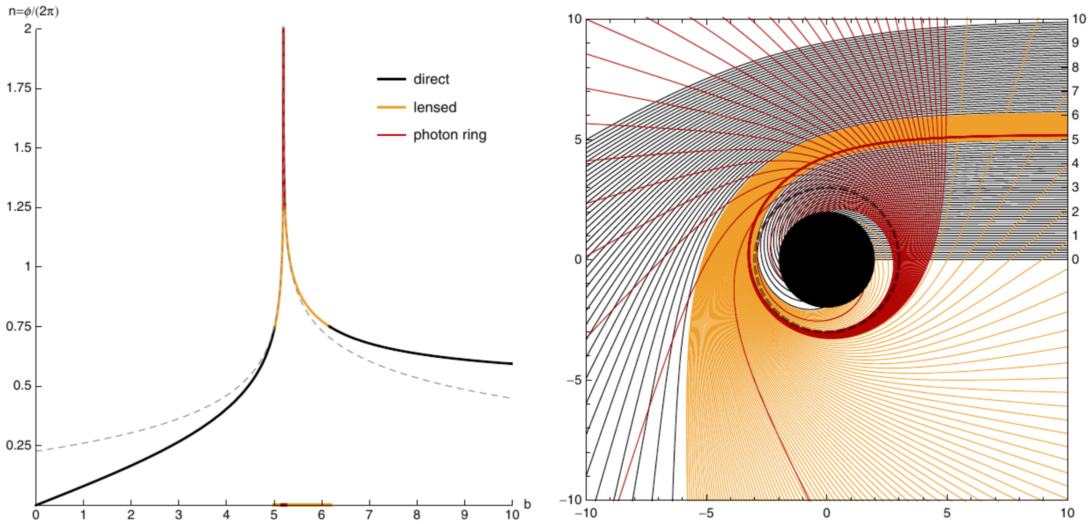

Figure 2.5: Bahavior of photons in the Schwarzschild spacetime as a function of the impact parameter b. n is the fractional number of orbits. The light rays from photon ring, lensed ring, and direct emission are colored red, gold, and black respectively. Figure taken from Gralla et al. (2019).

black hole, as seen by an observer (placed at large distances to the right of the plot). Following the argument in Gralla et al. (2019), we define the photon ring to consist of photon orbits intersect the equatorial plane of the disk three or more times. For the Schwarzschild black hole, the photon ring is at $5.19\,r_g < b < 5.23\,r_g$. We define the lensing ring ($5.02\,r_g < b < 6.17\,r_g$) to consist of photon orbits intersect the equatorial plane of the disk twice outside the horizon. For $b < 5.02\,r_g$ or $b > 6.17$, one would observe only the direct emission from the disk.

For a Kerr black hole case, the photon ring is approximately circular for all black hole spins and inclination (Johnson et al. 2020). It is worth noting that the characteristic features of the black hole shadow result from the location and properties of the emitting matter near the black hole, while direct emission from the photon ring may not be a dominant contribution (Gralla et al. 2019).

In 2017, EHT collaboration was able to observe the black hole shadow of two SMBHs Sagittarius A* (Sgr A*, where * denotes SMBH at the center) and M87* using a global array of 8 telescopes (see Figure 3.4). Figure 2.6 depicts a comparison of the sizes of two black holes.

2.3.1 Sagittarius A*

Our spiral galaxy Milky way hosts a SMBH Sgr A* with the mass $\mathrm{M} = (4.3 \pm 0.03) \times 10^6 M_\odot$ (GRAVITY Collaboration et al. 2022b) and the distance $8178 \pm 35\,\mathrm{pc}$ (GRAVITY Collaboration et al. 2019). Due to the proximity, the mass and distance of the Sgr A* were measured with high precision using the infrared in-

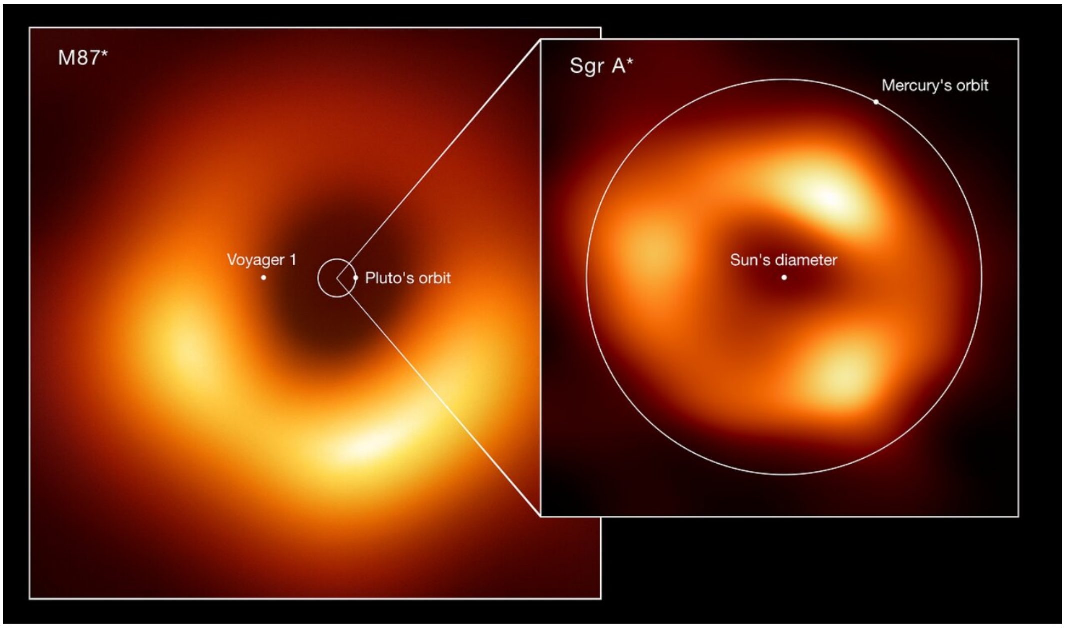

Figure 2.6: Comparison of the sizes of two black holes using EHT observations in 2017 at 1mm: M87* and Sgr A*. Credit: EHT collaboration (acknowledgment: Lia Medeiros, xkcd)

terferometer GRAVITY. However, the inclination angle is not well-constrained owing to the non-detection of the jet. Many studies assume that the inclination of the Sgr A* is face-on ($i \sim 0°$). For instance, Event Horizon Telescope Collaboration et al. (2022) reported that model comparisons disfavor scenarios that the black hole has high inclination ($i > 50°$).

Sgr A* has a low-bolometric luminosity $L_{\rm bol} \lesssim 10^{36}\,{\rm erg\,s^{-1}} \sim 100 L_{\odot}$, where $L_{\odot}$ is the bolometric luminosity of the sun. As a result, Sgr A* has extremely low Eddington ratio $\lambda_{\rm Edd}(L_{\rm bol}/L_{\rm Edd}) \sim 10^{-9}$, where the Eddington limit $L_{\rm Edd} = 4\pi\, c\, G\, M\, m_p/\sigma_T = 1.3 \times 10^{38}(M/M_{\odot}){\rm erg\,s^{-1}}$, m_p is the proton mass, σ_T is the Thomson cross section, and $M_{\odot}$ is the mass of the sun. The Eddington limit is the maximum luminosity when the radiation pressure and gravity are balanced, the low Eddington ratio therefore indicates that the radiation process is not efficient. Low luminosity AGNs can be explained by advection dominated accretion flow (ADAF, Narayan & Yi (1994)) model. According to the ADAF model, most of the gravitational potential energy by the infalling gas is lost by advection, it therefore results in a low luminosity.

Historically, Sgr A* has been one of the prime targets in mm-VLBI (Krichbaum et al. 1998; Doeleman et al. 2008; Issaoun et al. 2019). In 2017, EHT observations of Sgr A* at 230GHz with a nominal resolution of $\sim 25\,\mu as$ (Event Horizon Telescope Collaboration et al. 2022) revealed the black hole shadow of the SMBH at the center of our Galaxy with a diameter of $51.8 \pm 2.3\,\mu$as. The gravitational radius r_g of Sgr A* is about $5.1\,\mu$as, the diameter of the image therefore is consistent with the expected apparent boundary for black hole (diameter $\sim 6\sqrt{3}\, r_g$). However, a limitation of the snapshot imaging should be noted due to the high variability of Sgr A*. Due to the extreme variability, the azimuthal intensity distribution is not well-constrained and a small set of reconstructed images has diverse non-ring morphologies.

Sgr A* has a number of distinct characteristics. Flaring events from Sgr A* at most of the wavelengths, including optical and near-infrared regime with timescales as short as minutes, have been commonly reported (Genzel et al. 2003). The short timescales suggest that the flares are originated from the central engine within $\sim 10 r_g$. Recently, GRAVITY Collaboration et al. (2018) reported orbital motions of three flares. The orbital motions are clockwise typically on scales of 150μas and the period is a few tens of minutes corresponding to $\sim 0.3c$. It indicates a circular orbit of a compact polarized hot spot from infrared synchrotron emission. Wielgus et al. (2022) found an orbital motion at mm wavelengths using QU loop analysis from EHT ALMA only data.

Moreover, Sgr A* is a highly variable source. We can estimate the variability timescale of Sgr A* using the period of the innermost stable orbit (ISCO). For prograde orbits, the period ranges from 4 minutes ($4\pi t_g$) for maximal spin to 30 minutes ($12\sqrt{6}\pi t_g$) for zero spin, where $t_g \equiv GM/c^3$. For M87*, the period corresponds to 5 days to 1 month (Event Horizon Telescope Collaboration et al. 2022).

In addition, polarization of the Sgr A* has a unique characteristic compared to other AGNs. Event Horizon Telescope Collaboration et al. (2024) reported polarimetry of Sgr A* at 1mm with high polarized (with a peak linear polarization $\sim 40\%$ and a peak circular polarization $\sim 5-10\%$) ring with a prominent spiral electric vector position angle pattern. On the other hand, Sgr A* observations at centimeter wavelengths show significant circular polarization of about $\sim 1\%$ at 15 GHz and small linear polarization of less than 0.1% (Bower et al. 2002). Furthermore, Sgr A* observations in mm and sub-millimeter wavelengths show highly variable RM (Marrone et al. 2007; Wielgus et al. 2024). Numerous studies regarding Sgr A* imply that the near-event horizon accretion zone is magnetically dominated with a dominant poloidal field $B \sim 80-100$ gauss (Genzel et al. 2024). Given the strong magnetic field in the accretion zone, it is puzzling that we have not observed a relativistic jet from Sgr A*.

2.3.2 M87*

The giant elliptical galaxy Messier 87 (M87, NGC 4486, 3C 274) hosts a SMBH with the mass M $= (6.6\pm0.4)\times10^9 M_\odot$(Gebhardt et al. 2011) and the distance are

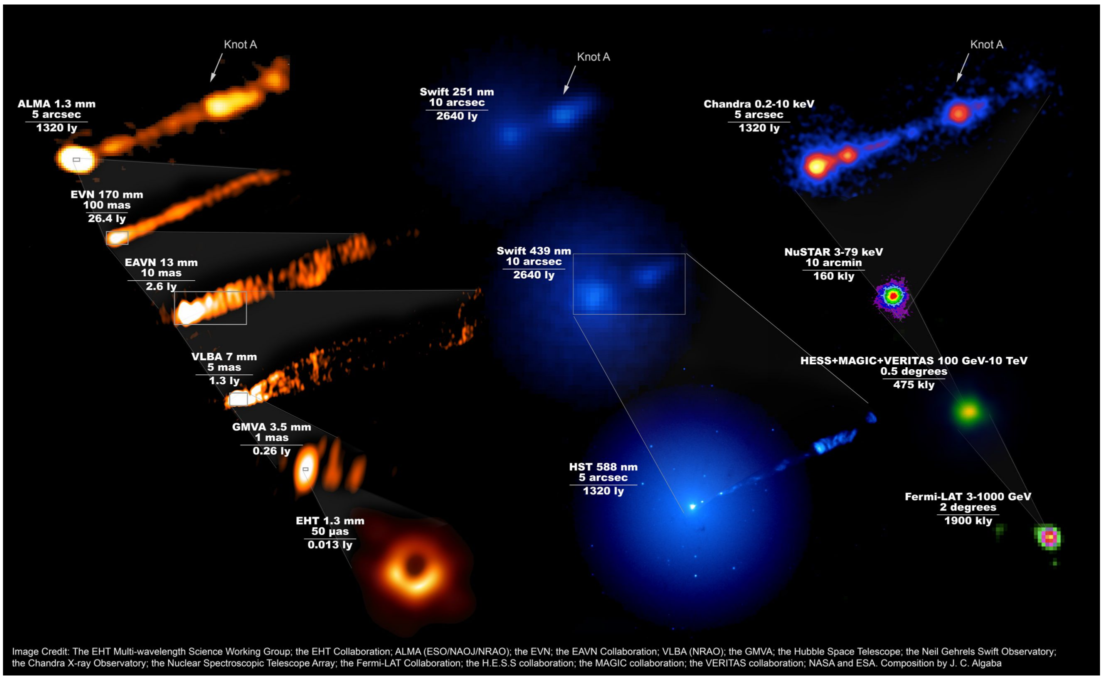

Image Credit: The EHT Multi-wavelength Science Working Group; the EHT Collaboration; ALMA (ESO/NAOJ/NRAO); the EVN; the EAVN Collaboration; VLBA (NRAO); the GMVA; the Hubble Space Telescope; the Neil Gehrels Swift Observatory; the Chandra X-ray Observatory; the Nuclear Spectroscopic Telescope Array; the Fermi-LAT Collaboration; the H.E.S.S collaboration; the MAGIC collaboration; the VERITAS collaboration; NASA and ESA. Composition by J. C. Algaba

Figure 2.7: Compilation of the quasi-simultaneous M87 images at various scales during the EHT 2017 campaign. Credit: EHT MWL science working group. Composition by J. C. Algaba.

$16.7 \pm 0.2\,$Mpc (Mei et al. 2007). Due to the large mass and proximity, M87* has the second largest apparent diameter of the observable SMBH at radio frequency after SgrA*. M87* has a bolometric luminosity $L_{bol} \approx 10^{42}$erg s^{-1}, that results in a low Eddington ratio $\lambda_{Edd} \gtrsim 10^{-5}$. Event Horizon Telescope Collaboration et al. (2019b) estimated an accretion rate of M87* ($\dot{M} \sim 2.7 \times 10^{-3} M_{\odot}$yr^{-1}) using a simple, spherical, one-zone model. As a result, the Eddington accretion ratio $\dot{M}/\dot{M}_{Edd}$ is $\sim 2.0 \times 10^{-5}$, where $\dot{M}_{Edd} = L_{Edd}/\epsilon c^2 = 137 M_{\odot}$yr^{-1} is the Eddington accretion rate with the efficiency $\epsilon = 0.1$. Henceforth, we use the mass of M87* of $6.2 \times 10^9 M_{\odot}$, the distance of 16.9 Mpc, and the inclination angle $\sim 17°$ (Walker et al. 2018) for the consistency with the EHT analysis (Event Horizon Telescope Collaboration et al. 2019a,b).

The gravitational radius of M87* is $3.8\,\mu$as and the apparent boundary for the Schwarzschild black hole (diameter $\sim 6\sqrt{3}\,r_g$) is 39.5μas. The estimated ring diameter of the EHT observation of M87* in 2017 is $42 \pm 3\,\mu$as, in agreement with the theoretical prediction of the photon ring diameter. However, it was challenging to estimate spin directly from the EHT M87* images in 2017 and 2018 since the photon ring with different spin at small inclination shows small deviation from a circular orbit in Kerr metric.

Event Horizon Telescope Collaboration et al. (2019b) analyzed M87* EHT observations in 2017 and argue that the EHT results are consistent with clockwise direction due to the asymmetric structure of the ring. The bright emission in the

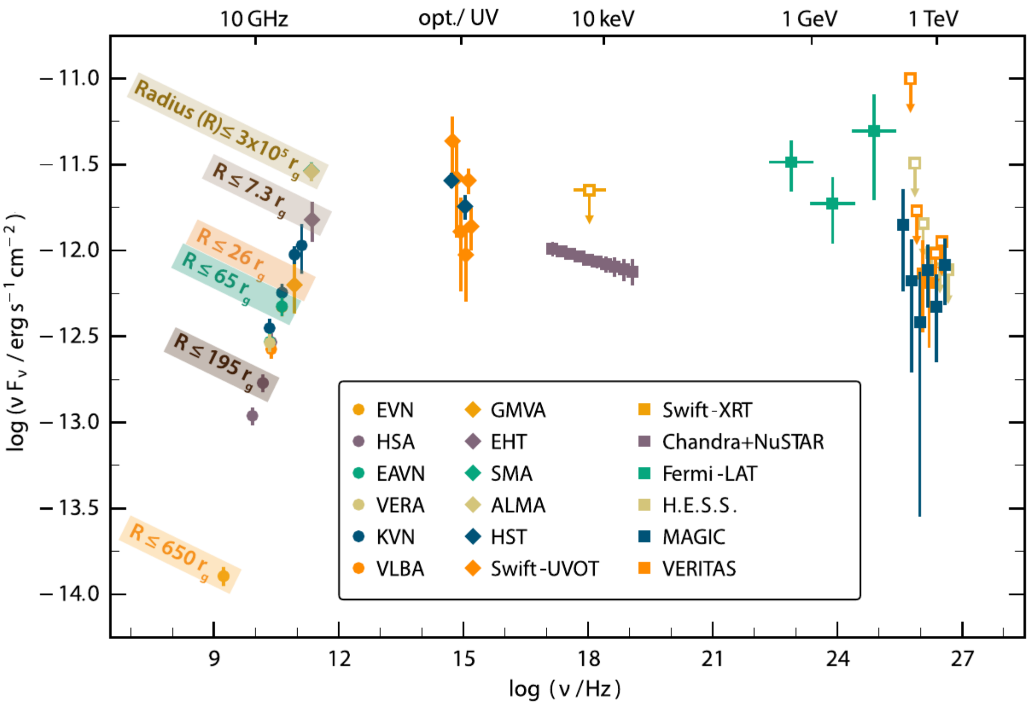

Figure 2.8: Broadband spectral energy distributions (SED) of M87 quasi-simultaneous observations between March 2017 and May. Fluxes measured by various instruments highlighted with different colors and markers. Figure taken from EHT MWL Science Working Group et al. (2021).

south can be explained by the Doppler beaming. If the motion of the accretion flow is clockwise, the plasma in the north is receding Earth and the plasma in the south is approaching and Doppler boosted. We note that the first dynamic image reconstruction of EHT M87 observation in 2017 shows counterclockwise motion (Arras et al. 2022).

Connecting the large scale jet structure and the central engine of the galaxy M87 is crucial to understand the energy extraction process and jet launching mechanism from SMBH. Figure 2.7 illustrates quasi-simultaneous M87 images at various scales (from $\sim 20\mu$as for EHT to $\sim 2^\circ$ for Fermi-LAT) in 2017 from radio to gamma ray. This figure shows that the galaxy M87 is one of the best candidates to study the jet launching mechanism from its central engine in different electromagnetic wavelength regimes. Figure 2.8 depicts broadband spectral energy distribution (SED) of M87 in 2017. One peak from radio to optical/UV are explained by the synchrotron emission and the second peak in the gamma ray regime is described by the Inverse Compton scattering. The SED model fitting results suggest that the gamma ray emission detected in 2017 likely originate from a region outside of EHT mm-band emission (EHT MWL Science Working Group et al. 2021). Furthermore, a comparison between EHT M87 observation in 2017 and the GRMHD simulation library suggests that non-spinning black

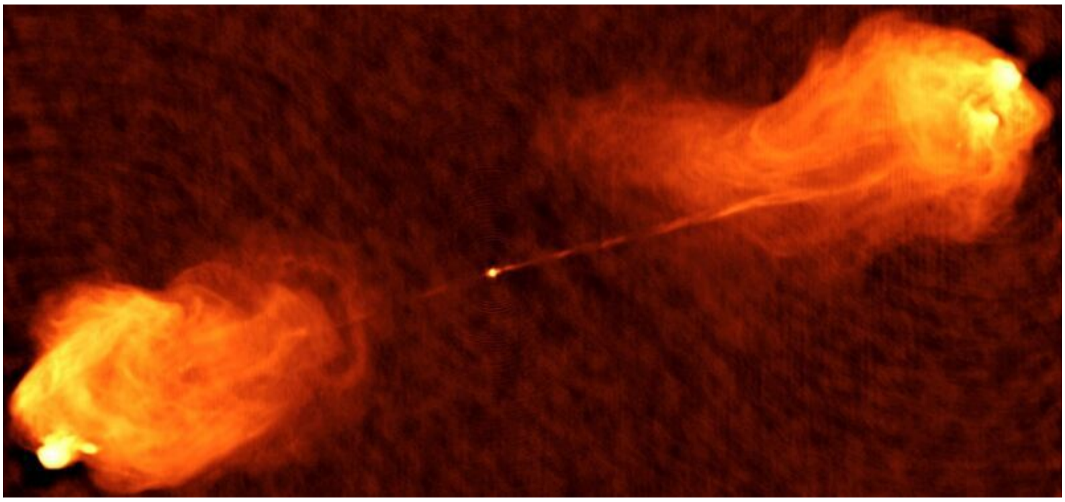

Figure 2.9: VLA observation of Cygnus A in 1983 at 5GHz. Credit: NRAO archive.

hole scenarios are inconsistent with the observations of M87 in 2017 because the Schwarzschild black hole cannot produce sufficiently powerful jets (Event Horizon Telescope Collaboration et al. 2019b).

In 2018, the M87* black hole shadow and relativistic jet were observed simultaneously using GMVA+ALMA observations at 86GHz (Lu et al. 2023). High sensitivity of GMVA+ALMA array and the characteristic of the spectral energy distribution of the optically thin jet from synchrotron radiation enabled the first simultaneous observation of M87* black hole shadow and the relativistic jet from the SMBH at 86 GHz. In chapter 6, we revisited the work in Lu et al. (2023) using Bayesian imaging software `resolve` and wavelet imaging method `DoG-HiT` in order to obtain images with improved resolution and estimate more precise measurement of ring parameters.

2.4 Jet launching mechanism

In 1918, *"A curious straight ray … apparently connected with the nucleus by a thin line of matter"* was observed from NGC 4486 (M87) by Heber Curtis, that is one of the first detection of the extragalactic jets (Curtis 1918). Figure 2.7 shows the observation of the kpc-scale jets of galaxy M87 from radio to X-ray. So far, numerous observations detected relativistic jets launching from the nucleus of active galaxies in various electromagnetic spectrum and scales and it is especially prominent in radio regime (Perley et al. 1984; Zensus et al. 1995; Walker et al. 2018; Lu et al. 2023). Those observations of the extragalactic jet from active galaxies indicate that there exists a mechanism that matter around the central engine can escape against gravitational force and be accelerated and collimated. As an example, Figure 2.9 shows a VLA observation of Cygnus A, revealing collimated radio jets with two-sided radio lobes extending about ~ 120 kpc from the core.

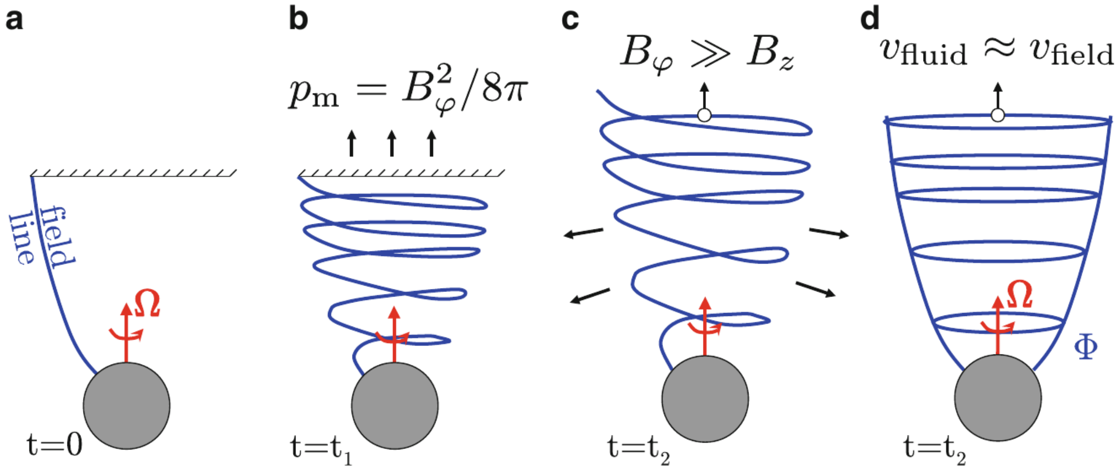

Figure 2.10: Schematic illustration of jet formation by magnetic fields. Figure taken from (Tchekhovskoy 2015).

In fact, black holes of all sizes can produce relativistic jets. Jet-producing accretion systems span from stellar-mass black holes to supermassive black holes, it suggests scale invariance in the jet launching mechanism (Tchekhovskoy 2015). Several theoretical models indicate that magnetic fields are essential for jet production (Blandford & Znajek 1977; Blandford & Payne 1982; Tchekhovskoy 2015). There are two most favored scenarios of jet launching: Blandford & Znajek (1977) introduced a mechanism extracting energy electromagnetically from Kerr black holes, which is called Blandford-Znajek (BZ) process. There is another mechanism to extract the energy from accretion flow (Blandford & Payne 1982), known as Blandford-Payne (BP) process. The BP process can be applied to stars and other objects since it does not require a black hole to be present in the system. Relativistic jets from AGNs may result from a combination of BZ and BP processes. The search for the observational evidence of the jet launching mechanism is still an active area of research in AGN studies.

Figure 2.10 illustrates the evolution of the magnetic field geometry to form a jet. In Figure 2.10, a perfectly conducting sphere and a ceiling represent the central compact object and the ambient medium respectively. A single poloidal field line in panel **a** gets twisted by a spinning sphere in panel **b**. The magnetic field can be twisted either by the frame-dragging effect from a spinning black hole or by the rotation of the accretion disk. This magnetic spring pushes against the ceiling with an effective pressure p_m due to the toroidal field B_{φ}. At some later time, t $=$ t$_2$, the toroidal field becomes stronger and the magnetic spring pushes away the ceiling and accelerates the plasma along the rotation axis, forming a jet

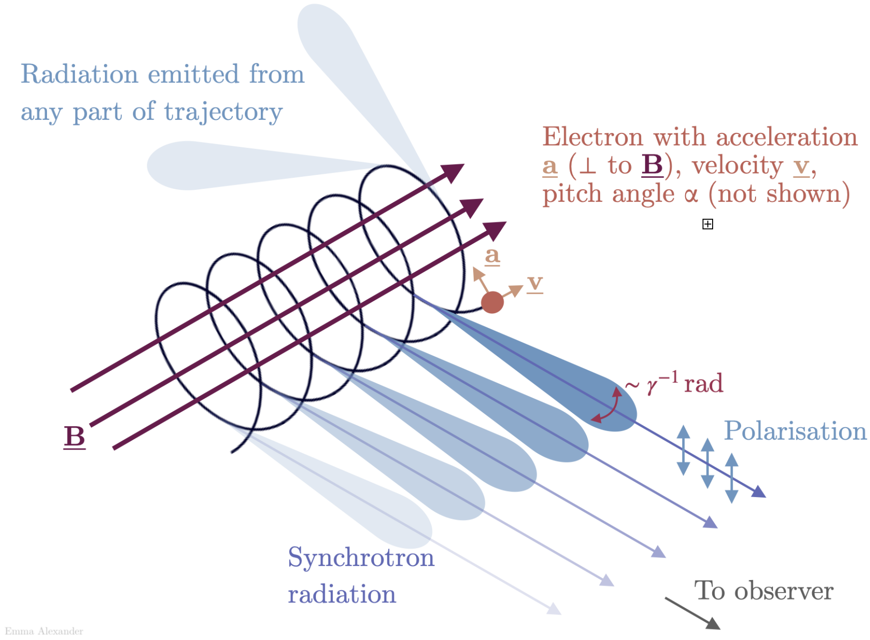

Figure 2.11: Illustration of synchrotron radiation from an electron in magnetic fields B. Credit: Emma L. Alexander.

in panel **c** and **d**. Toroidal magnetic fields from the twisted magnetic field lines may result in the collimated jet over large distances.

2.5 Synchrotron radiation

According to the Lorentz force law, charged particles in a magnetic field follow a helical trajectory around magnetic field lines (see Figure 2.11), gyrating at the gyrofrequency

$$\nu_g \equiv \frac{qB}{2\pi\gamma mc}, \tag{2.32}$$

where q is the particle charge, B is the magnetic field strength, $\gamma = 1/\sqrt{1 - v^2/c^2}$ is the Lorentz factor, m is the mass of the particle.

The gyrating particle emit the radiation at the gyrofrequency v_g. In a non-relativistic regime ($\gamma \approx 1$), it is called cyclotron radiation. The cyclotron emission can be utilized to measure magnetic field strengths around neutron stars: Truemper et al. (1978) reported a strong and narrow line feature at ~ 58 keV in the pulsed ($1.24s$) X-ray flux from X-ray binary star system Hercules X-1 using a balloon observation. This narrow peak at ~ 58 keV is the quantized electron cyclotron emission from the highly magnetized plasma at the magnetic poles of the rotating neutron star. The estimated magnetic field strength is 5.3×10^{12} gauss,

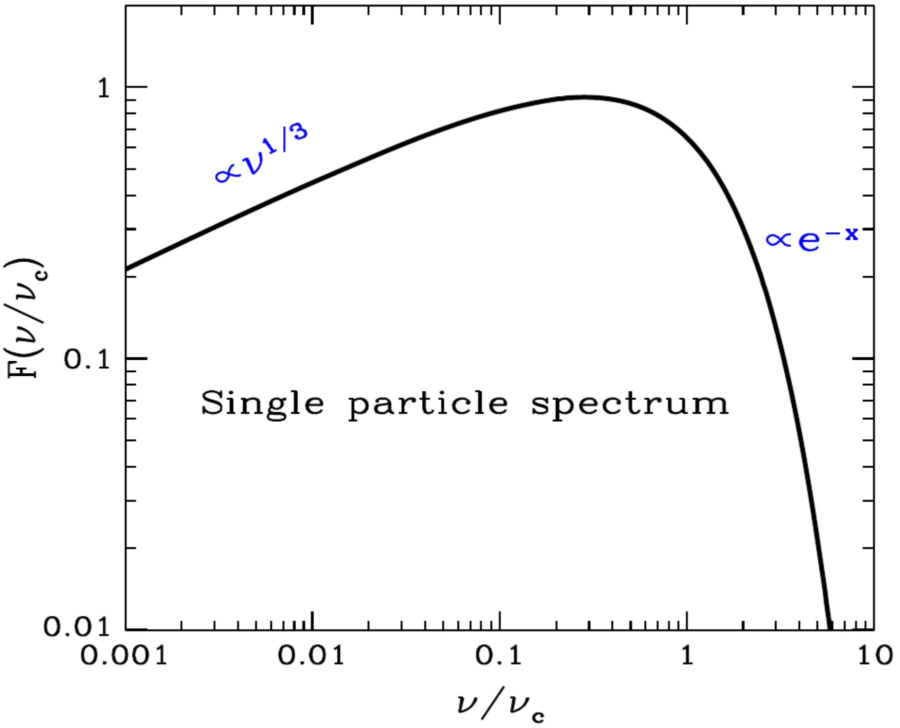

Figure 2.12: The function F(ν/ν_c) describing the synchrotron power emitted by the single electron. Figure taken from Ghisellini (2013).

which is 13 orders of magnitude larger compared to the magnitude of Earth's magnetic field at its surface (~ 0.5 gauss).

In the relativistic regime ($\gamma > 1$), the radiation is beamed from accelerated relativistic charged particles in magnetic fields (angular beam width $\sim 1/\gamma$ rad) in the direction of the particle motion (see Figure 2.11), called synchrotron radiation, also known as magnetobremsstrahlung (Ginzburg & Syrovatskii 1965; Rybicki & Lightman 1979; Ghisellini 2013). Since protons are heavier than electrons, the proton-synchrotron radiation power is scaled down by $\sim 3 \times 10^{-7}$ ($\sim (m_e/m_p)^2$), where m_e and m_p are the mass of the electron and proton, respectively. Therefore, we only consider electron-synchrotron radiation hereafter.

The synchrotron power of an electron (integration of the synchrotron emission over the solid angle and frequency) is

$$< P_s >= \frac{4}{3}\sigma_T c U_B \gamma^2 \beta^2, \tag{2.33}$$

where σ_T is the Thompson scattering cross section, $U_B = B^2/8\pi$ is the magnetic energy density, and $\beta = v/c$ is the ratio of velocity v to the speed of light c.

From the gyrating beamed radiation with the angular width $\sim 1/\gamma$, an observer will see the pulses with the time scale $\Delta t \sim 1/\gamma^3 \nu_g$. The inverse of this time is the typical synchrotron angular frequency $\nu_s = \gamma^3 \nu_g$. The frequency spectrum for a single relativistic ($\gamma \gg 1$) particle associated with those pulses becomes continuous with line broadening effect, compared to the cyclotron emission. The power per unit frequency emitted by an electron is given by (Rybicki & Lightman 1979; Ghisellini 2013):

$$P_s(\nu, \gamma, \alpha) = \frac{\sqrt{3}e^3 B\text{sin}\alpha}{m_e c^2} F(\nu/\nu_c) \tag{2.34}$$

$$F(\nu/\nu_c) \equiv \frac{\nu}{\nu_c} \int_{\nu/\nu_c}^{\infty} \mathbf{K}_{5/3}(y) dy \tag{2.35}$$

$$\nu_c \equiv \frac{3}{4\pi} \gamma^2 \frac{qB}{m_e c} \text{sin}\alpha, \tag{2.36}$$

where $\mathbf{K}_{5/3}(y)$ is the modified Bessel function of order $5/3$, α is the pitch angle between the velocity vector $\vec{v}$ and the magnetic field vector $\vec{B}$, and ν_c is the critical synchrotron radiation frequency.

The function $F(\nu/\nu_c)$ is shown in Figure 2.12. At $\nu \ll \nu_c$, it is well-approximated by a power law $\propto \nu^{1/3}$ and this broad spectrum extends to a frequency ν_c before decaying exponentially. The critical synchrotron radiation frequency ν_c is a factor γ^3 greater than the gyrating frequency ($\nu_c \sim \gamma^3 \nu_g \text{sin}\alpha$).

To calculate the spectral energy distribution (SED) of synchrotron radiation from electrons, we need electron number density. In equilibrium, the probability density f(v) for non-relativistic thermal particles follow the Maxwell-Boltzmann distribution:

$$f(v) = 4\pi v^2 \left(\frac{m}{2\pi k_B T}\right)^{3/2} \exp\left(-\frac{mv^2}{2\, k_B T}\right), \tag{2.37}$$

where v is the velocity and m is the mass, k_B is the Boltzmann constant, and T is the temperature.

In the relativistic case, the distribution of particle speeds follows the Maxwell-Jüttner distribution in equilibrium. Both distributions have an exponential cutoff, high kinetic energies therefore are suppressed.

On the other hand, in hot plasmas, the relaxation time required to go to equilibrium is long compared to the timescale of other processes, such as acceleration (Ghisellini 2013). As a result, the particle does not follow the Maxwell-Jüttner distribution. The number density of non-thermal particles where energies fall within the limits of an energy interval $E_{\text{min}} \leq E \leq E_{\text{max}}$, can be approximated as a power law (Rybicki & Lightman 1979; Ghisellini 2013):

$$N(E)dE = N_0 E^{-p} dE,\, E_{\text{min}} < E < E_{\text{max}}, \tag{2.38}$$

where $N_0 = N/\int_{E_{\rm min}}^{E_{\rm max}} E^{-p} dE$, N is the total number of electrons, and p is the particle distribution index.

When electrons are relativistic ($E = \gamma m_e c^2$, where c is the speed of light), the power-law electron number density with the Lorentz factor γ is written as (Rybicki & Lightman 1979; Ghisellini 2013):

$$N(\gamma)d\gamma = K\gamma^{-p}d\gamma, \ \gamma_{\rm min} < \gamma < \gamma_{\rm max}, \tag{2.39}$$

where $K = N/\int_{\gamma_{\rm min}}^{\gamma_{\rm max}} \gamma^{-p} d\gamma$.

Compared to the exponential cutoff in the Maxwell-Boltzmann distribution (Equation 2.37) for thermal particles, there is a high-energy tail for non-thermal particles due to the power law distribution. The power law number density generally results from the particle acceleration in a shock (Ghisellini 2013), which are common features of relativistic jets. The power law distribution of the non-thermal particle number density can be empirically justified by the power law distribution of the spectral energy density distribution (Equation 2.41) of the optically thin emission region.

The emissivity (power emitted by a unit volume for a unit solid angle) of the synchrotron radiation from an ensemble of electrons in the plasma under the assumption of isotropic emission is (Ghisellini 2013)

$$j_s(\nu, \alpha) = \frac{1}{4\pi} \int_{\gamma_{\rm min}}^{\gamma_{\rm max}} N(\gamma) P(\nu, \gamma, \alpha) d\gamma. \tag{2.40}$$

Changing variables of integration to $x \equiv \nu/\nu_c (\propto \nu/\gamma^2 B)$, the emissivity over a sufficiently broad energy range is

$$j_s \propto K B^{\frac{(p+1)}{2}} \nu^{-\frac{(p-1)}{2}} = K B^{1+\alpha} \nu^{-\alpha}, \tag{2.41}$$

where K is a constant from the electron number density in Equation 2.38, $\alpha = (p-1)/2$ is the spectral index of the radiation, namely $j_s \propto \nu^{-\alpha}$.

When the emission of an astronomical object results from the synchrotron radiation process, we can estimate the concentration and energy spectrum of the relativistic electrons in the emission sources (Ginzburg & Syrovatskii 1965). As an example, if the spectral index is $\alpha = 1/2$, the power-law particle number density has the power $p = 2$.

In a low radio frequency regime, the spectral behavior is different because of synchrotron self-absorption, in which a photon is absorbed by an interaction with a charged particle in magnetic fields. The absorption coefficient can be obtained using the relation between the Einstein coefficients under the assumption that $h\nu << E$, where h is the Planck constant (Rybicki & Lightman 1979):

$$\alpha_\nu = -\frac{c^2}{8\pi\nu^2}\int dEP(\nu,E)E^2\frac{\partial}{\partial E}\left[\frac{N(E)}{E^2}\right]. \tag{2.42}$$

The absorption coefficient for synchrotron emission from non-thermal electrons is

$$\alpha_\nu \propto B^{(p+2)/2}\nu^{-(p+4)/2}. \tag{2.43}$$

As a result, the source function in a low frequency regime is

$$S_\nu = j_\nu/\alpha_\nu \propto B^{-1/2}\,\nu^{5/2}. \tag{2.44}$$

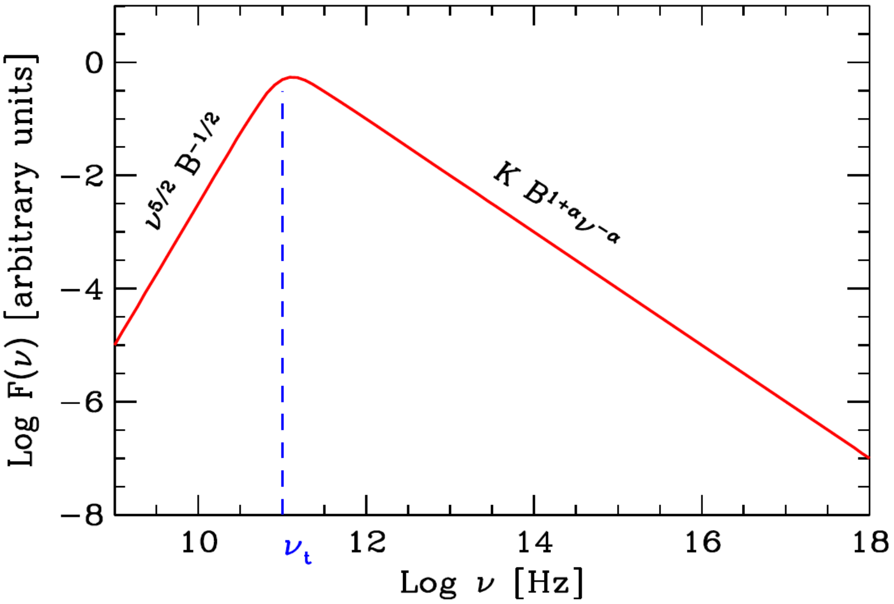

Figure 2.13: Synchrotron spectrum from a partially self-absorbed source. Figure taken from Ghisellini (2013).

We note that the absorption coefficient for synchrotron self-absorption is small at high frequencies. Furthermore, the spectral behavior is not dependent on the slope of the electron density distribution p since the more electron results in the more emission and absorption simultaneously. The slope of the synchrotron self-absorption spectrum ($\propto \nu^{5/2}$) is higher than the slope of the Raleigh-Jeans law ($\propto \nu^2$), which is the thermal emission when $h\nu >> kT$.

Figure 2.13 illustrates the synchrotron spectrum of a partially self-absorbed plasma. At a frequency ν_t, the transition from the optically thick to thin regime occurs when the synchrotron opacity is $\tau(\nu) = \alpha_\nu R \approx 1$, where R is the light travel distance.

The transition frequency ν_t is

$$\nu_t \propto [RKB^{(p+2)/2}]^{2/(p+4)}. \tag{2.45}$$

The transition frequency provides a good estimation of the magnetic field strength of a synchrotron-emitting source (Lobanov 1998a) and it is very close to the turn-over frequency from the observation.

Since the opacity varies with frequency, the location of the VLBI core, where the optical depth is $\tau \approx 1$, depends on the observing frequency. This phenomenon is known as core shift (Lobanov 1998b). The higher the observing frequency, the closer we observe to the central engine (see Figure 2.14). As a result, the core absolute position follows a power law:

$$r_{core} \propto \nu^{-1/k_r}, \tag{2.46}$$

where the power index k_r depends on the particle density distribution and the magnetic field.

It is worth noting that we can estimate the magnetic field strength using the core shift measurement from multi-frequency observations (Lobanov 1998b).

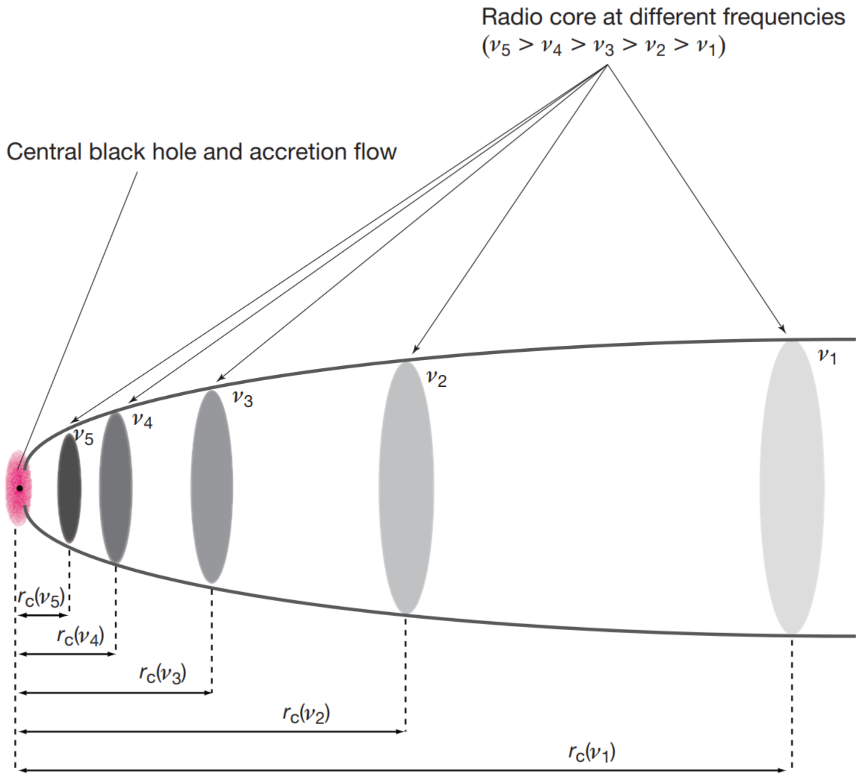

Figure 2.14: Schematic illustration of the radio core shift of a jet. Figure taken from Hada et al. (2011).

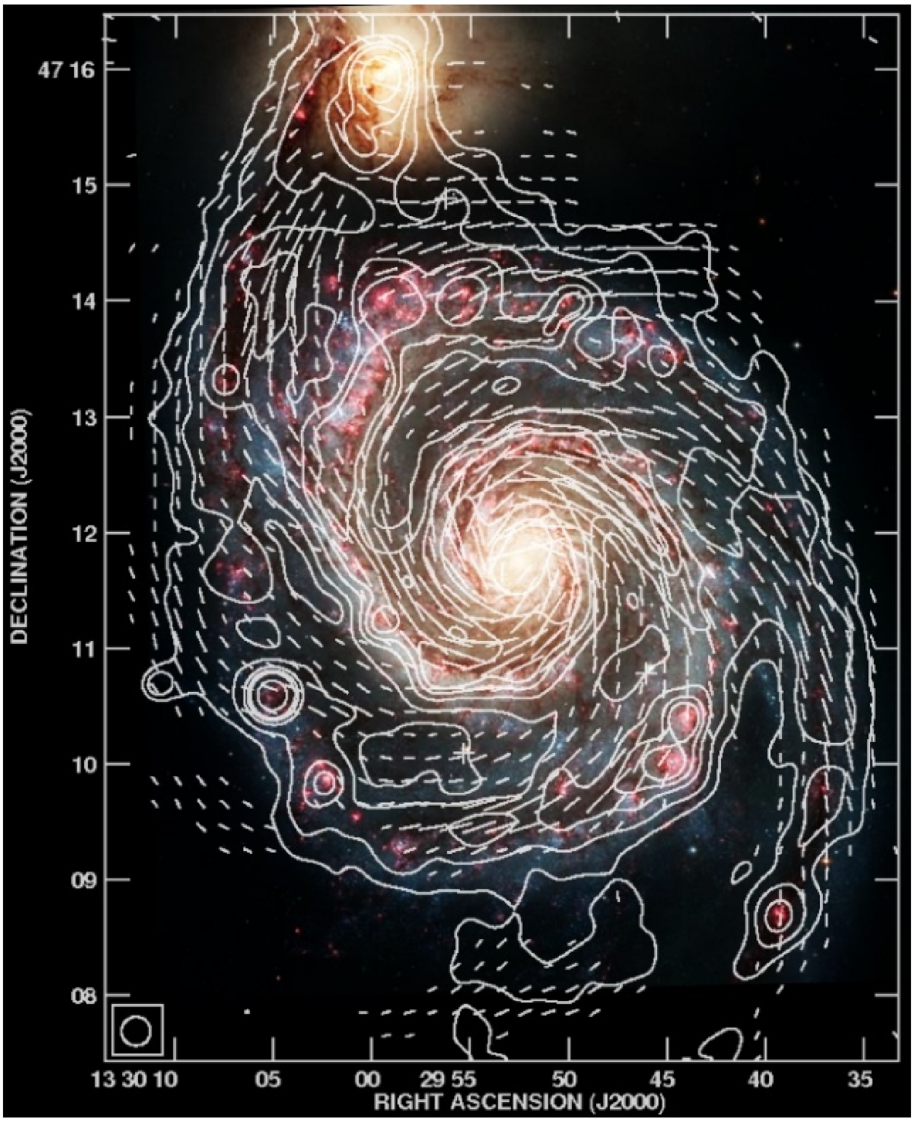

Figure 2.15: Contours of the total radio continuum emission of NGC 5194 (middle) and NGC 5195 (top) from VLA and Effelsberg observation at λ6 cm and magnetic field vectors with a length proportional to the polarized intensity (equivalent to the 90° rotated EVPA without Faraday rotation correction), overlaid on a Hubble Space Telescope optical image. Figure taken from Fletcher et al. (2011).

2.6 Polarization at radio frequency

The synchrotron radiation is linearly polarized since electrons responsible for the emission are accelerated perpendicular to the magnetic field (see Figure 2.11). The polarization observation at radio frequency provides invaluable information about the complex magnetic field structure and physical processes of corresponding astronomical object. Under the power law electron number density assumption (Equation 2.38), the degree of polarization of the synchrotron radiation in a homogeneous field is given by (Ginzburg & Syrovatskii 1965; Rybicki & Lightman

1979; Ghisellini 2013):

$$\Pi = \frac{p+1}{p+7/3}, \tag{2.47}$$

where p is the exponent in the power law electron number density.

The fractional polarization is $\sim 75\%$ for $p = 3$ and $\sim 69\%$ for $p = 2$. Due to the incoherent synchrotron emission from randomly oriented particle motions on microscopic scale, the upper limit on fractional linear polarization is 75% for an optically thin emission region. In the radio regime, the polarization is often considerably weakened, owing to the Faraday depolarization and synchrotron self-absorption where low-energy synchrotron photons emitted by relativistic electrons are reabsorbed by the electrons via inverse synchrotron processes. Furthermore, the finite resolution of the telescope results in depolarization.

The polarimetric information is a key to understand the magnetic fields of celestial objects. Since the electric vector position angle (EVPA) is perpendicular to the magnetic field, we can study the magnetic field geometry using the EVPA pattern from the observation. As an example, Figure 2.15 shows highly ordered spiral pattern magnetic field vectors of the face-on spiral galaxy M51 (NGC 5194). The radio emission at $\lambda 6$ cm is mainly originated from non-thermal synchrotron radiation since it is polarized (up to 40%) with negative spectral index $-1.2 < \alpha < -0.6$. We note that the compact and bright peaks of radio emission in the spiral arms with flatter spectral index ($\alpha \gtrsim -0.6$) coincide with H II regions and there is no corresponding peaks in polarized emission, indicating a significant proportion of these emission at cm-wavelength is thermal emission, originating from free-free emission (thermal bremsstrahlung). The estimated magnetic field strengths are $10 \sim 20 \mu G$ in the spiral arms and $\sim 30 \mu G$ at the core (Fletcher et al. 2011). It is noteworthy that there has been numerous studies regarding magnetic field structures in AGNs using polarimetric radio interferometric observations (Fernini et al. 1991; Homan & Wardle 1999; Lister & Homan 2005; Jorstad et al. 2005; Hada et al. 2016; Sebokolodi et al. 2020; Zhao et al. 2022; Event Horizon Telescope Collaboration et al. 2021, 2024).

2.6.1 Faraday rotation

The polarization angle χ of a radiation rotates when it propagates through a magnetized plasma owing to the difference in the refractive index of right and left circularly polarized emission in a plasma. This phenomenon is called Faraday rotation.

The basic model of Faraday rotation is

$$\chi = \chi_0 + \mathrm{RM}\,\lambda^2, \tag{2.48}$$

where χ_0 is the original polarization angle of the signal, RM is the rotation measure, and λ is the wavelength.

The magnitude and sign of RM relates to the magnetic field of a region observed parallel to the line-of-sight ($B_{\|}$) and the thermal electron column density (n_e) as

$$\mathrm{RM} = \mathcal{C} \int_{\mathrm{observer}}^{\mathrm{source}} n_e B_{\|} dl\,[\mathrm{rad\,m^{-2}}], \tag{2.49}$$

where dl is the incremental displacement along the line of sight measured in pc from the observer to the source, and $\mathcal{C}$ is a conversion constant, $\mathcal{C} \equiv e^3/2\pi m_e^2 c^4 \approx 0.812\,\mathrm{rad\,m^{-2}\,pc^{-1}\,cm^3\,\mu G^{-1}}$.

Since the Faraday rotation effect is proportional to the wavelength, the radio regime is the best candidate to study the Faraday rotation. From the multi-frequency polarimetric radio observation, we can estimate the rotation measure to study the foreground, namely Faraday screen, in front of the source. Observationally, the polarization angle is measured from the EVPA and the rotation measure can be estimated from the change of the EVPA over frequency. If the observed EVPA do not follow the λ^2 dependence in Equation 2.48, it indicates source-intrinsic Faraday rotation, namely an internal Faraday screen (Wielgus et al. 2024).

The Faraday rotation decreases the linear polarization due to different EVPA rotation from inhomogeneous RM distribution, called Faraday depolarization. A finite image resolution also results in depolarization.

It is worth noting that rotation measure analysis can probe the presence of helical and toroidal magnetic fields in the jet of AGNs (Asada et al. 2002; Gabuzda et al. 2004; Hovatta et al. 2012; Lisakov et al. 2021; Baidoo et al. 2023)

2.7 Inverse Compton scattering

The observed spectral energy distribution (SED) of the AGNs often show two peaks (see Figure 2.8). Especially, those two peaks are prominant in Blazars, a type of AGNs whose jets are pointing at us. The low-energy bump is originated from synchrotron radiation from radio to soft X-ray. However, we need another mechanism to explain the high-energy bump from hard X-ray to gamma ray. These high energy radiation can be emitted by a scattering process: A low-energy photon can gain energy by scattering off a high-energy electron, becoming a high energy (X-ray, gamma-ray) photon. This process is called inverse Compton scattering since it is the reverse of the direct Compton scattering, in which the photon gives the energy to the electron. If a majority of seed photons is produced by synchrotron process, it is referred to as synchrotron self-Compton (SSA).

The inverse Compton scattering power from an electron (the scattering energy loss rate per electron) is:

$$< P_s >= \frac{4}{3}\sigma_T c U_r \gamma^2 \beta^2, \tag{2.50}$$

where U_r is the initial photon energy density.

It is analogous to the synchrotron power of an electron in Equation 2.33. Furthermore, the single electron spectra from the inverse Compton scattering is peaked at a typical frequency $\nu' \approx \gamma^2 \nu$ boosted up by a factor γ^2, same as the synchrotron radiation.

Under the assumption that a power-law energy density distribution for the relativistic electrons, the inverse Compton emissivity ϵ_c shows a power law:

$$\epsilon_c \propto \nu^{-\alpha}, \ \alpha = \frac{p-1}{2}, \tag{2.51}$$

where p is the power law index in the electron energy density distribution.

It is important to note that the inverse Compton emissivity follows the same power law as for the synchrotron radiation.

Chapter 3

Radio interferometry

In optics, the angular resolution is linearly proportional to the wavelength λ and inversely proportional to the aperture diameter D. According to the Rayleigh criterion (Rayleigh 1879), the image resolution in radians is:

$$\theta_{\mathrm{res}} = 1.22\frac{\lambda}{D}. \tag{3.1}$$

It is noteworthy that the Rayleigh criterion is just a convention to define a resolution, there are many other criteria for the resolution.

High-resolution imaging has always been on demand in astrophysics because our targets are distant from us and exploring their internal structure is critical to understand the physical mechanism behind them. The resolution limit formula tells us there are two avenues to achieve high imaging resolution: increasing the aperture diameter, up to some physical limitation, and observing at higher frequency.

However, the Earth's atmosphere does not permit observing at frequency higher than visible light (or in many bands at lower frequency) on Earth due to the atmospheric opacity (see Figure 3.1). To observe at gamma rays, X-rays, and ultraviolet light, we need an expensive space mission.

Fortunately, we have an alternative to achieve higher resolution: aperture synthesis. We are able to combine radio telescopes and form a synthetic large aperture using interferometry (Ryle & Hewish 1960). Martin Ryle was awarded the Nobel Prize in Physics in 1974 for his observations and inventions of the aperture synthesis technique. In an radio interferometer, the longest baseline, which is the distance between telescopes, can be treated as a synthetic aperture diameter. In other words, we can achieve higher resolution by the radio interferometer with very long baselines without constructing a physically large aperture. To date, radio interferometry achieves the highest angular resolution ($\sim 20\,\mu$as at 1 mm) with the help of the aperture synthesis.

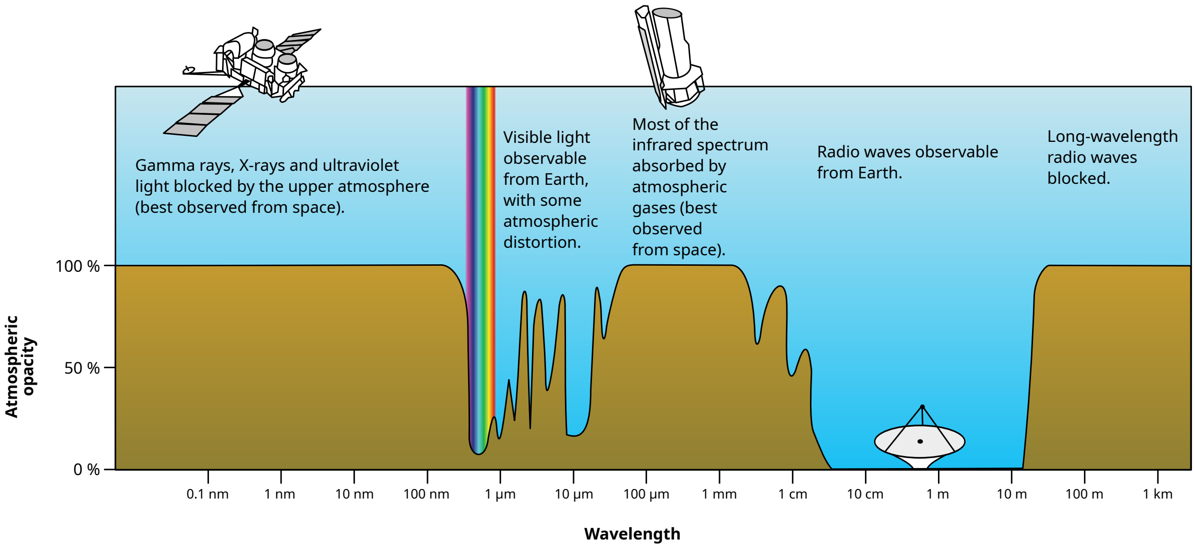

Figure 3.1: Earth's atmospheric opacity in wavelengths at different frequencies. Credit: NASA.

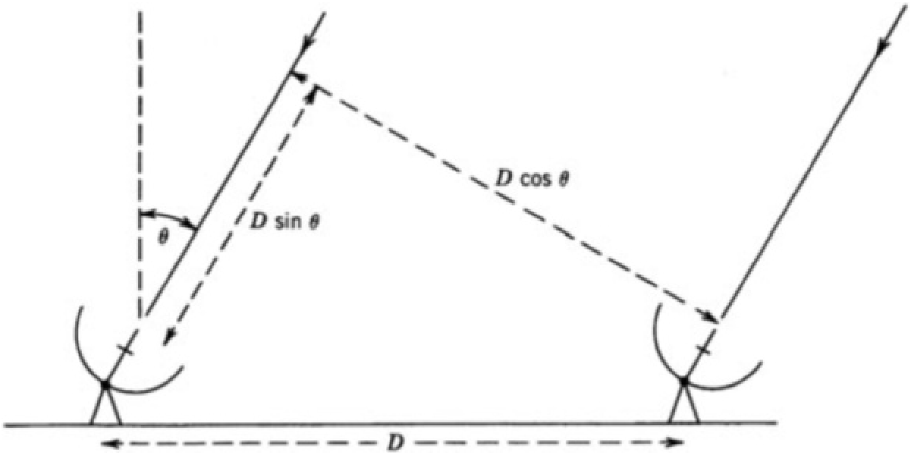

Figure 3.2: The path length difference between two radio telescopes. Figure taken from (Thompson et al. 2017).

3.1 Radio interferometer measurement equation

In this section, we derive a measurement equation for a radio interferometer. A radio interferometer, consisting of two radio telescopes, measures a response proportional to a Fourier component of the two-dimensional sky brightness distribution across the sky. Each individual radio telescope measures a voltage induced by the electric field, which carries the amplitude and phase information of the incoming electric field.

Figure 3.2 illustrates that there is a path length difference between two antennas when we observe a target in the sky:

$$c\,\tau_g = \mathbf{D}\,\cdot\,\mathbf{s} = D\sin\theta, \tag{3.2}$$

where c is the speed of light, τ_g is the geometric time delay, $\mathbf{D}$ is the baseline vector between two antennas, and $\mathbf{s}$ is the unit vector ($|\mathbf{s}| \equiv 1$) pointing toward the source.

The geometric path length difference $c\,\tau_g$ causes the phase difference:

$$\Delta\phi = \frac{2\pi\,\mathbf{D}\,\cdot\,\mathbf{s}}{\lambda}, \tag{3.3}$$

where λ is the wavelength of the signal.

To derive the radio interferometer measurement equation, let us consider quasi-monochromatic radiation from a point source. The voltage outputs corresponding to the electric fields for the antennas i and j are:

$$V_i(t) = E\cos(2\pi\nu t), \tag{3.4}$$

$$V_j(t) = E\cos(2\pi\nu t + \frac{2\pi\,\mathbf{D}\,\cdot\,\mathbf{s}}{\lambda}), \tag{3.5}$$

where E is the amplitude of the radiation and ν is the frequency.

For an averaging period $T \gg 1/\nu$, the output of the time-averaged correlation between the electric fields is:

$$R_C \ = < V_i(t)V_j(t) >_t = \ P\cos\left(\frac{2\pi\,\mathbf{D}\,\cdot\,\mathbf{s}}{\lambda}\right), \tag{3.6}$$

where $<>_t$ denotes time averaging and $P = E^2/2$ is the correlated power.

R_C is also called the cosine response, which is sensitive to the even (symmetric) structure (real part in the visibility). To recover the full signal, we need the sine response also, which is sensitive to the odd (asymmetric) structure, for the imaginary part in the visibility:

$$R_S \ = < e_i\left(t + \frac{\lambda}{4c}\right) e_j(t) >_t = \ P\sin\left(\frac{2\pi\,\mathbf{D}\,\cdot\,\mathbf{s}}{\lambda}\right). \tag{3.7}$$

Now we generalize the interferometric response for the full sky brightness distribution. Under the assumption that the radiation is incoherent (the emissions from different points have uncorrelated phases), we can exchange the expectation and integral. Therefore, the cosine and sine responses are

$$R_C = \int I(\mathbf{s})\cos\left(\frac{2\pi\,\mathbf{D}\,\cdot\,\mathbf{s}}{\lambda}\right)d\Omega, \tag{3.8}$$

$$R_S = \int I(\mathbf{s})\sin\left(\frac{2\pi\,\mathbf{D}\,\cdot\,\mathbf{s}}{\lambda}\right)d\Omega, \tag{3.9}$$

where $I(\mathbf{s})$ is the source intensity, namely the sky brightness distribution and $d\Omega$ is the solid angle.

Given the assumption of an ideal calibration without gain corruption, we define the interferometric visibility:

$$V = R_C - iR_S = \int I(\mathbf{s})\exp\left(-2\pi i\,\mathbf{D}\cdot\mathbf{s}/\lambda\right)d\Omega. \tag{3.10}$$

In the Cartesian sky coordinate system, let $\mathbf{D} = (\lambda u, \lambda v, \lambda w)$ be the coordinate axes measured in wavelengths and the unit vector ($|\mathbf{s}| = 1$) pointing toward the source is $\mathbf{s} = (l, m, n) = (l, m, \sqrt{1 - l^2 - m^2})$.

After removing the phase offset corresponding to the observation center $\mathbf{s}_0 = (0, 0, 1)$, the remaining path length difference is:

$$\mathbf{D}\cdot(\mathbf{s} - \mathbf{s}_0) = \lambda(ul + mv + w(\sqrt{1 - l^2 - m^2} - 1)). \tag{3.11}$$

As a result, the radio interferometer measurement equation stating the relation between the visibility and the sky brightness distribution is (Thompson et al. 2017):

$$V(u, v, w) = \int\int I(l, m, n)\exp^{(-2\pi i[ul+vm+w(\sqrt{1-l^2-m^2}-1)])}\frac{dldm}{\sqrt{1 - l^2 - m^2}}, \tag{3.12}$$

where (u, v, w) are the Fourier domain coordinates, (l, m, n) are the image domain coordinates, and $1/\sqrt{1 - l^2 - m^2}$ is originating from the Jacobian determinant for the coordinate transform from the spherical to Cartesian coordinates.

For a small field of view ($l, m \ll 1, n = \sqrt{1 - l^2 - m^2} \approx 1$), the measurement equation becomes a two-dimensional Fourier transformation between the visibility and the intensity:

$$V(u, v) = \int\int I(l, m)\exp^{(-2\pi i[ul+vm])}dldm = \mathcal{FT}[I(l, m)], \tag{3.13}$$

where $\mathcal{FT}$ denotes the Fourier transform operator.

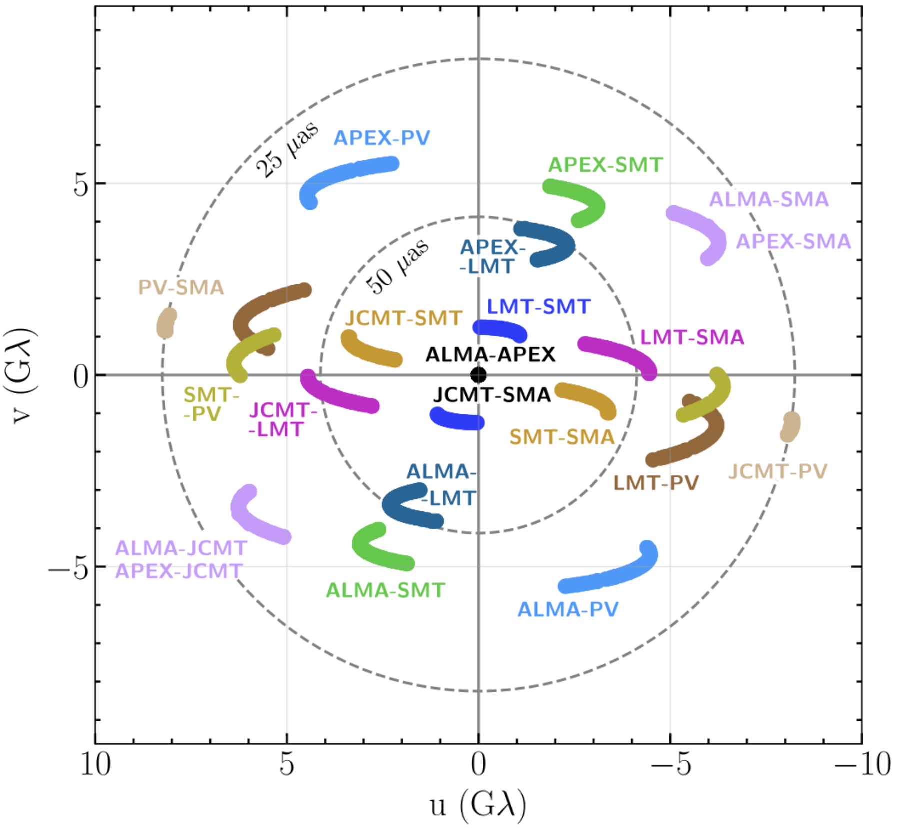

Figure 3.3: (u, v) coverage for M87* EHT observation in 2017. Figure taken from (Event Horizon Telescope Collaboration et al. 2019a).

In radio interferometry, we usually assume that our target source is static over time. Due to the Earth's rotation, we are able to sample the Fourier components in different locations of the (u, v) plane (Ryle 1962). However, we often have large gaps in the Fourier domain since the number of antenna is limited. In fact, there is a trade-off for the high resolution in aperture synthesis: sparsity of UV coverage. As an example, Figure 3.3 depicts the UV coverage of the M87* EHT observation in 2017 (see Figure 2.6). The coverage is extremely sparse since 8 antennas (over six geographic locations) cover the Earth's size synthetic aperture.

In Equation 3.13, to obtain an image, we need to infer the sky intensity from the visibility data. Therefore, the image reconstruction is an inverse problem. Since the interferometric data are incomplete, there is no unique solution, which means an ill-posed problem.

We can generalize the measurement equation for polarimetry with the data corruption using electric vectors with matrix multiplication (Hamaker et al. 1996; Smirnov 2011) and Jones matrices (Jones 1941). Following the derivation of (Smirnov 2011), consider a quasi-monochromatic signal from a single point source with z-axis in the direction of propagation. The electric field of the radio source can be described as a complex vector in a linear polarization basis:

$$\mathbf{e} = \begin{pmatrix} e_x \\ e_y \end{pmatrix}, \tag{3.14}$$

where e_x and e_y are amplitude and phase of the wave along the direction x and y respectively.

We assume that all transformations along the signal path are linear. This is a reasonable assumption in radio interferometry since most of the effects in the signal path, such as amplification, antenna leakage, and field rotation, can be approximated as a linear transformation. Then the output complex voltage vector for an antenna p from the electric field along the signal path can be described by the Jones matrices and electric field vector (Jones 1941; Smirnov 2011):

$$\mathbf{v}_p = \begin{pmatrix} v_{pa} \\ v_{pb} \end{pmatrix} = \mathbf{J}_n \mathbf{J}_{n-1} ... \mathbf{J}_1 \mathbf{e} = \mathbf{J}_p \mathbf{e}, \tag{3.15}$$

where a and b are two feeds (linear feeds or right/left circular feeds) and multiple effects along the signal propagation path are represented by a multiplication of different Jones matrices for antenna p, namely the total Jones matrix $\mathbf{J}_p$.

In an interferometer, the output signal of four correlations from two radio telescopes, namely the visibility matrix, is described by a matrix product of a column voltage vector for antenna p and a row voltage vector for antenna q:

$$\mathbf{V}_{pq} = 2 < \mathbf{v}_p \mathbf{v}_q^\dagger >= 2 \left\langle \begin{pmatrix} v_{pa} \\ v_{pb} \end{pmatrix} (v_{qa}^*, v_{qb}^*) \right\rangle = 2 \begin{pmatrix} < v_{pa} v_{qa}^* > & < v_{pa} v_{qb}^* > \\ < v_{pb} v_{qa}^* > & < v_{pb} v_{qb}^* >, \end{pmatrix} \tag{3.16}$$

where the angle bracket $<>$ denotes averaging over small time and frequency bin and $\dagger$ is the conjugate transpose.

Now we can obtain an equation for the visibility matrix from the electric field vector from Equation 3.15 and Equation 3.16:

$$\mathbf{V}_{pq} = 2\mathbf{J}_p < \mathbf{e}\mathbf{e}^\dagger > \mathbf{J}_q^\dagger = 2\mathbf{J}_p \begin{pmatrix} < e_x e_x^* > & < e_x e_y^* > \\ < e_y e_x^* > & < e_y e_y^* > \end{pmatrix} \mathbf{J}_q^\dagger = \mathbf{J}_p \, \mathbf{B} \, \mathbf{J}_q^\dagger, \tag{3.17}$$

where $\mathbf{B}$ is the brightness of the source.

In a linear polarization basis, the relation between the brightness of the source and Stokes parameters is:

$$\mathbf{B} = 2\begin{pmatrix} < e_x e_x^* > & < e_x e_y^* > \\ < e_y e_x^* > & < e_y e_y^* > \end{pmatrix} = \begin{pmatrix} I+Q & U+iV \\ U-iV & I-Q \end{pmatrix}. \tag{3.18}$$

In a circular polarization basis, the relation between the brightness of the source and Stokes parameters is:

$$\mathbf{B} = 2\begin{pmatrix} < e_r e_r^* > & < e_r e_l^* > \\ < e_l e_r^* > & < e_l e_l^* > \end{pmatrix} = \begin{pmatrix} I+V & Q+iU \\ Q-iU & I-V \end{pmatrix}. \tag{3.19}$$

Hereafter, we focus on the radio interferometer measurement equation in a circular polarization basis. To derive the full polarimetric sky brightness distribution, we start from a Jones matrix for antenna p consisting of the antenna gain matrix $\mathbf{G}$, the leakage matrix $\mathbf{D}$, the field rotation angle matrix $\mathbf{P}$:

$$\mathbf{J}_p = \mathbf{G}_p\mathbf{D}_p\mathbf{P}_p = \begin{pmatrix} g_p^r & 0 \\ 0 & g_p^l \end{pmatrix}\begin{pmatrix} 1 & D_p^r \\ D_p^l & 1 \end{pmatrix}\begin{pmatrix} e^{-i\phi_p} & 0 \\ 0 & e^{i\phi_p} \end{pmatrix}, \tag{3.20}$$

where g is the direction-independent antenna-based gain and D is the signal leakage, e.g., D_p^r is the signal leakage from left-hand circular polarization (LCP) to right-hand circular polarization (RCP) for antenna p, and ϕ_p is the antenna field rotation angle of the antenna p.

The antenna field rotation angle represents the rotation of the sky relative to the antenna coordinate system owing to Earth's rotation:

$$\phi = f_{\mathrm{el}}\theta_{\mathrm{el}} + f_{\mathrm{par}}\psi_{\mathrm{par}} + \phi_{\mathrm{off}}, \tag{3.21}$$

where θ_{el} is the elevation angle, ψ_{par} is the parallactic angle, and ϕ_{off} is a constant offset. The field rotation angle depends on the antenna mount. Alt-azimuth (ALT-AZ) mounts with Cassegrain focus have $f_{\mathrm{par}} = 1$ and $f_{\mathrm{el}} = 0$. ALT-AZ mounts with Nasmyth-Right type focus have $f_{\mathrm{par}} = 1$ and $f_{\mathrm{el}} = 1$, and ALT-AZ mounts with Nasmyth-Left type focus have $f_{\mathrm{par}} = 1$ and $f_{\mathrm{el}} = -1$.

If we assume that the radiation is incoherent (same as the derivation of Equation 3.12), we can derive the polarimetric radio interferometer measurement equation (RIME) for the full sky (continuous brightness distribution) represented by an integration over all possible directions with the Jones matrices and the phase shift (Equation 3.3) between signals from antenna p and q:

$$\mathbf{V}_{pq} = \int \mathbf{J}_p \, \mathbf{B} \exp\left(-2\pi i \, \mathbf{D} \cdot \mathbf{s}/\lambda\right) \, \mathbf{J}_q^{\dagger} \, d\Omega \tag{3.22}$$

$$= \mathbf{J}_p \left(\int\int \mathbf{B} \exp^{(-2\pi i [ul + vm + w(\sqrt{1-l^2-m^2}-1)])} \frac{dldm}{\sqrt{1-l^2-m^2}} \right) \mathbf{J}_q^{\dagger}. \tag{3.23}$$

If the field of view is small ($l, m \ll 1, n = \sqrt{1 - l^2 - m^2} \approx 1$), the polarimetric RIME equation can be simplified as:

$$\mathbf{V}_{pq} = \mathbf{G}_p \, \mathbf{D}_p \, \mathbf{P}_p \, \mathcal{FT}[\mathbf{B}] \, \mathbf{P}_q^{\dagger} \, \mathbf{D}_q^{\dagger} \, \mathbf{G}_q^{\dagger}, \tag{3.24}$$

where $\mathcal{FT}$ is the Fourier transform operator.

The Jones matrix formalism provides a neat mathematical framework to describe data corruption, that can be modeled as a linear process. We can use more complicated Jones matrices corresponding to particular effects in the signal path, e.g., band pass and ionospheric Faraday rotation. The order of the Jones matrices corresponds to the reverse order of the actual signal path.

In radio interferometry, calibration and imaging is equivalent to the inference of parameters in the RIME from the visibility data. As a result, calibration and imaging are degenerate inverse problems. The RIME provides a mathematical foundation to solve calibration and imaging problems.

3.2 Very long baseline interferometry

To achieve extremely high angular resolution, we can observe astronomical objects with radio interferometric arrays at millimeter wavelength with very long baselines. This technique is called very long baseline interferometry (VLBI). For instance, Figure 3.4 and Figure 3.5 show the Event Horizon Telescope (EHT) array at 1 mm in 2017 and the Global millimeter VLBI array (GMVA) at 3 mm in 2018 respectively.

VLBI has unique challenges to process the data since antennas do not have the same clock. It requires an additional step, called global fringe fitting (Schwab & Cotton 1983) for phase and delay calibration. Moreover, the extremely long baseline results in the sparsity of the UV coverage (see Figure 3.3). In other words, we have a very large synthetic aperture with poor sensitivity. VLBI observations at mm wavelength suffer from low signal to noise ratio (S/N) due to a short phase coherence time and low total flux from synchrotron radiation at mm wavelength. In addition, it is challenging to find a point-like static calibrator due to the high angular resolution. As an example, we perform the flux density calibration

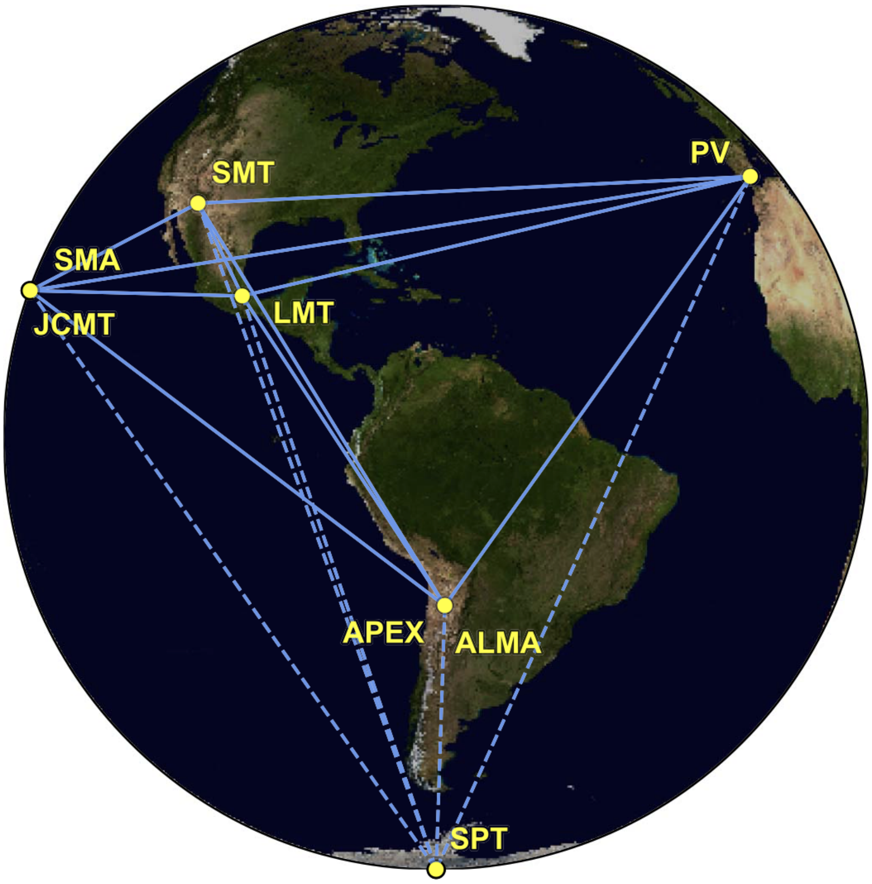

Figure 3.4: Eight stations of the EHT 2017 campaign over six geographic locations. Figure taken from (Event Horizon Telescope Collaboration et al. 2019a)

using the system temperature information instead of a flux density calibrator. Especially, in mm-VLBI, due to the lack of appropriate calibrators and short phase coherence time, we often use the target data itself in order to calibrate the data, namely self-calibration. Furthermore, we need to deal with different antenna characteristics and sensitivity when we form an array from different types of telescopes, e.g., Global millimeter VLBI array (GMVA) and Event Horizon Telescope (EHT). Heterogeneous antenna statistics from an inhomogeneous array cause complications in calibration and imaging.

As a result, we rely on additional assumptions, namely prior knowledge, to process the incomplete and noisy VLBI data since calibration and imaging in VLBI are highly underdetermined problems. Encoding appropriate prior knowledge about the instrument and target source is a key in VLBI data processing and it is one of the main goals in this thesis.

Figure 3.5: GMVA array for M87 observation in 2018. Credit: NAOJ

3.3 Probability density function of the visibility

In this section, we aim to derive the probability density function (PDF) of the visibility amplitude and phase. The noise in the visibility data is often described as an isotropic Gaussian. This assumption is justified by the central limit theorem, if the S/N of the data is sufficient and the thermal noise is the dominant noise process.

The sum of the visibility and the isotropic Gaussian noise $\vec{\mathbf{Z}} = \vec{\mathbf{V}} + \vec{\varepsilon}$, where $\vec{\mathbf{V}}$ is the visibility without noise and $\vec{\varepsilon}$ represents the error with components of independent Gaussian random variables with zero mean and variance σ^2. It is described by $\vec{\mathbf{Z}} = Ze^{i\phi}$, where Z is the visibility amplitude with noise and ϕ is the visibility phase with noise.

3.3.1 Probability distribution of the visibility amplitude

To derive the probability density function of the visibility amplitude $P(Z)$, we start from a complex-valued random variable $Z = X + iY$ with independent normally distributed variables $X \sim \mathcal{N}(m_x = |\vec{\mathbf{V}}|\cos\phi, \sigma^2)$, $Y \sim \mathcal{N}(m_y = |\vec{\mathbf{V}}|\sin\phi, \sigma^2)$.

The joint PDF is

$$P_{X,Y}(x,y) = \frac{1}{2\pi\sigma^2}\exp\left(-\frac{(x-m_x)^2+(y-m_y)^2}{2\sigma^2}\right). \tag{3.25}$$

Then we transform to polar coordinates $(R,\Phi) = (\sqrt{x^2+y^2}, \tan^{-1}(y/x))$ with the Jacobian determinant $|\frac{\partial(x,y)}{\partial Z,\phi}| = Z$. We can take $m_x = |\vec{\mathbf{V}}|$, $m_y = 0$ without loss of generality and marginalize over phase to obtain the amplitude PDF (Thompson et al. 2017):

$$\begin{aligned}
P(Z) &= \int_0^{2\pi} P_{R,\Phi}(Z,\phi)d\phi = \int_0^{2\pi} P_{X,Y}(Z\cos\phi, Z\sin\phi)Zd\phi & (3.26)\\
&= \frac{Z}{2\pi\sigma^2}\int_0^{2\pi}\exp\left(-\frac{(Z\cos\phi - |\vec{\mathbf{V}}|)^2+(Z\sin\phi)^2}{2\sigma^2}\right)d\phi & (3.27)\\
&= \frac{Z}{2\pi\sigma^2}\exp\left(-\frac{Z^2+|\vec{\mathbf{V}}|^2}{2\sigma^2}\right)\int_0^{2\pi}\exp\left(\frac{Z|\vec{\mathbf{V}}|\cos\phi}{\sigma^2}\right)d\phi & (3.28)\\
&= \frac{Z}{\sigma^2}\exp\left(-\frac{Z^2+|\vec{\mathbf{V}}|^2}{2\sigma^2}\right)I_0\left(\frac{Z|\vec{\mathbf{V}}|}{\sigma^2}\right), & (3.29)
\end{aligned}$$

where I_0 is the modified Bessel function of zero order ($\int_0^{2\pi}\exp(\frac{Z|\vec{\mathbf{V}}|\cos\phi}{\sigma^2})d\phi = 2\pi I_0(\frac{Z|\vec{\mathbf{V}}|}{\sigma^2})$).

Therefore, the probability distribution of the visibility amplitude follows a Rice distribution. Figure 3.6 shows the visibility amplitude PDF as functions of the S/N. For the high S/N case ($|\vec{\mathbf{V}}|/\sigma \gg 1$), the visibility amplitude PDF can be approximated as a Gaussian distribution: $P(Z) \approx \mathcal{N}(<Z>, \sigma_Z^2)$, where $<Z> \simeq |\vec{\mathbf{V}}|(1+\sigma^2/2|\vec{\mathbf{V}}|^2)$ and $\sigma_Z \simeq \sigma(1-\sigma^2/8|\vec{\mathbf{V}}|^2)$. For the low S/N case ($|\vec{\mathbf{V}}|/\sigma \ll 1$), the amplitude PDF becomes a skewed distribution. If $|\vec{\mathbf{V}}|/\sigma = 0$, it reduces to the Rayleigh distribution $P(Z) = Z/\sigma^2\exp(-Z^2/2\sigma^2)$ with the mean $<Z> = \sqrt{\pi/2}\sigma$ and the standard deviation $\sigma_Z = \sigma\sqrt{2-\pi/2}$ (Thompson et al. 2017).

3.3.2 Probability distribution of the visibility phase

Similar to the derivation of the amplitude PDF, the phase PDF can be derived by marginalizing over the radial coordinate r with $m_x = |\vec{\mathbf{V}}|$, $m_y = 0$ without loss of generality (Thompson et al. 2017):

$$\begin{aligned}
P(\phi) &= \int_0^\infty P_{R,\Phi}(Z,\phi)dZ = \int_0^\infty P_{X,Y}(Z\cos\phi, Z\sin\phi)ZdZ & (3.30)\\
&= \frac{1}{2\pi\sigma^2}\int_0^\infty Z\exp\left(-\frac{(Z\cos\phi - |\vec{\mathbf{V}}|)^2 + (Z\sin\phi)^2}{2\sigma^2}\right)dZ & (3.31)\\
&= \frac{1}{2\pi\sigma^2}\exp\left(-\frac{|\vec{\mathbf{V}}|^2}{2\sigma^2}\right)\int_0^\infty Z\exp\left(-\frac{Z^2 - 2Z|\vec{\mathbf{V}}|\cos\phi}{2\sigma^2}\right)dZ. & (3.32)
\end{aligned}$$

Then we perform a change of variables $u = \frac{Z - |\vec{\mathbf{V}}|\cos\phi}{\sqrt{2}\sigma}$,

$$\begin{aligned}
P(\phi) &= \frac{1}{2\pi\sigma^2}\exp\left(-\frac{|\vec{\mathbf{V}}|^2}{2\sigma^2}\right)\exp\left(\frac{|\vec{\mathbf{V}}|^2\cos^2\phi}{2\sigma^2}\right)\int_{-\frac{|\vec{\mathbf{V}}|\cos\phi}{2\sigma}}^\infty (\sqrt{2}\sigma u + |\vec{\mathbf{V}}|\cos\phi)\exp(-u^2)\sqrt{2}\sigma du & (3.33)\\
&= \frac{1}{2\pi}\exp\left(-\frac{|\vec{\mathbf{V}}|^2}{2\sigma^2}\right)\left\{1 + \sqrt{\frac{\pi}{2}}\frac{|\vec{\mathbf{V}}|\cos\phi}{\sigma}\exp\left(\frac{|\vec{\mathbf{V}}|^2\cos^2\phi}{2\sigma^2}\right)\left[1 + \mathrm{erf}\left(\frac{|\vec{\mathbf{V}}|\cos\phi}{\sqrt{2}\sigma}\right)\right]\right\}, & (3.34)
\end{aligned}$$

where $\mathrm{erf}(x) = \frac{2}{\sqrt{\pi}}\int_0^x \exp(-t^2)dt$ is the error function, which represents the probability that a normally distributed random variable with mean 0 and variance $\frac{1}{2}$ falls within the interval $[-x, x]$.

Figure 3.6 shows the visibility phase PDF as functions of the S/N. For the high S/N case ($|\vec{\mathbf{V}}|/\sigma \gg 1$), the visibility phase PDF can be approximated as a Gaussian distribution with standard deviation $\sigma/|\vec{\mathbf{V}}|$: $P(\phi) \approx \mathcal{N}(\phi, \sigma/|\vec{\mathbf{V}}|)$. For the low S/N case ($|\vec{\mathbf{V}}|/\sigma \ll 1$), the phase PDF becomes a fat-tailed distribution. If $|\vec{\mathbf{V}}|/\sigma = 0$, it is a uniform distribution $P(\phi) = 1/2\pi$ (Thompson et al. 2017).

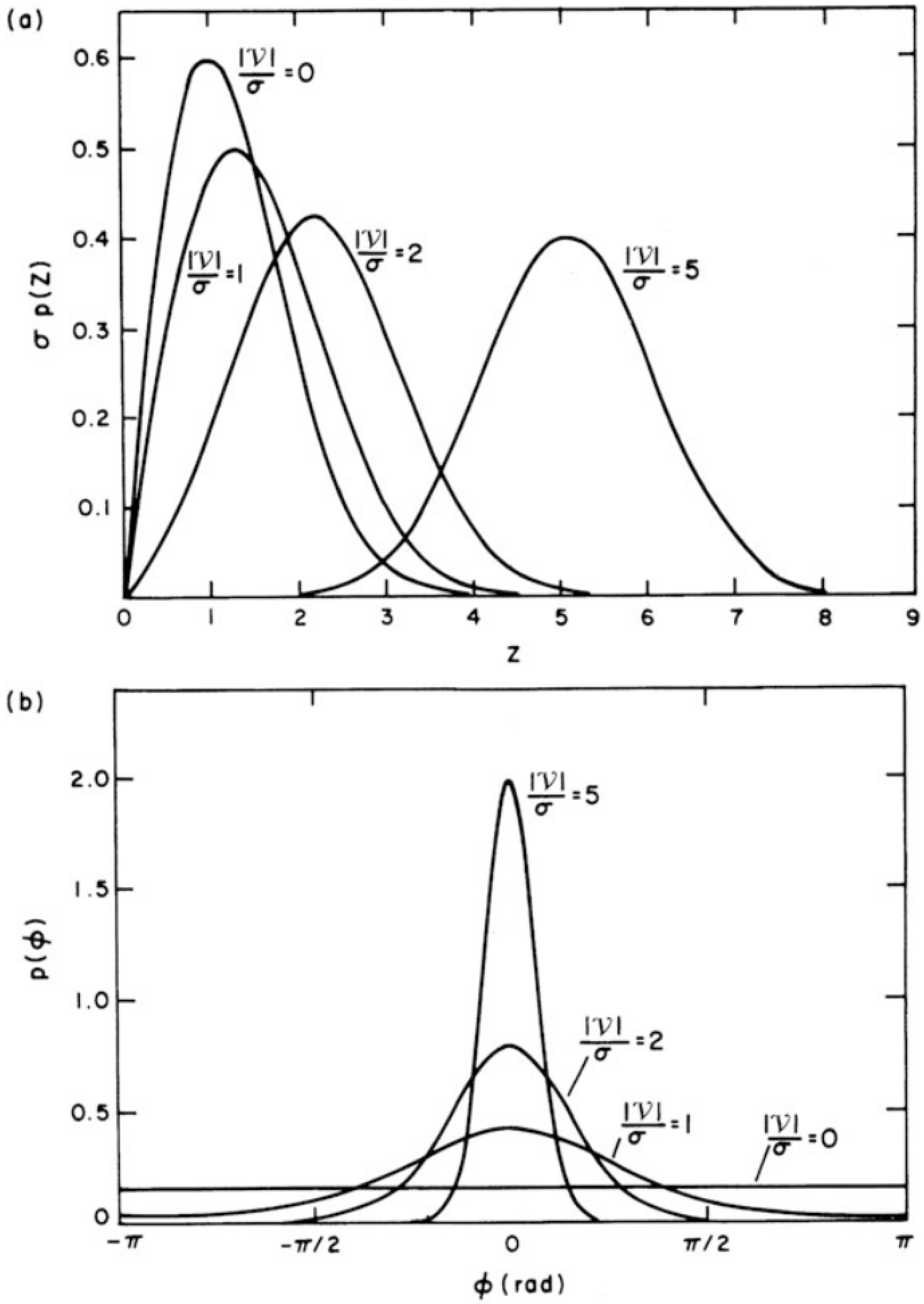

Figure 3.6: Probability distributions of (a) the amplitude visibility, (b) the phase visibility as functions of the S/N. Figure taken from (Thompson et al. 2017).

Chapter 4

Bayesian calibration and imaging

Image reconstruction is an ill-posed inverse problem, a unique solution therefore does not exist. In radio interferometry, the direct Fourier transform of the calibrated data, namely the dirty map, does not provide high-fidelity images due to the sparsity and noise in the data. Therefore, we require prior knowledge in the form of implicit or explicit regularization, or prior distributions, to obtain reliable images. There are different approaches to imaging, such as CLEAN (Högbom 1974; Clark 1980), Regularized Maximum Likelihood (RML) (Wiaux et al. 2009; Chael et al. 2016; Akiyama et al. 2017; Müller & Lobanov 2022), and Bayesian imaging (Junklewitz et al. 2016; Broderick et al. 2020a; Tiede 2022). This chapter introduces Bayesian imaging, which outperforms traditional `CLEAN`-based methods in terms of reconstruction accuracy. Then we discuss an extension to simultaneous calibration and imaging in a Bayesian framework. This is one of the main goals of this thesis: Incorporating calibration into image reconstruction in a probabilistic setup in order to infer more robust calibration solutions and images with uncertainty estimation.

4.1 Bayesian imaging

Bayesian imaging is a probabilistic approach to reconstruct samples of the possible images instead of a single image using Bayes' theorem. Our goal in Bayesian imaging is obtaining the posterior distribution of the image, that is consistent with our prior knowledge and the data. The Bayesian approach provides a neat probabilistic framework to infer signals based on our knowledge and data when the ground truth is unknown a priori. Historically, Bayesian approaches have been widely used to infer signals in astrophysics, typically for fewer than $\sim 10^2$ parameters due to the high computational cost.

The latest developments in optimization theory and computational resources enable the Bayesian method to be utilized in imaging with a large number of parameters. Bayesian imaging has a distinctive advantage: we can utilize our knowledge in a probabilistic setup explicitly. In other words, we are able to encode the prior knowledge about the instrument and source in the image reconstruction to obtain more reliable images. For instance, we are able to fit closure amplitudes and phases directly (Chael et al. 2018; Arras et al. 2022; Knollmüller et al. 2023) and the smoothness of the extended emission (Arras et al. 2021), and polarization constraints can be encoded in the prior model (Arras et al. 2025). The prior assumption is described by a probability distribution. Therefore, the uncertainty of our prior knowledge is taken into account in image reconstruction. This is specifically beneficial in radio interferometric imaging since our knowledge about the instrument and source can be utilized explicitly in order to obtain reliable images from incomplete data.

4.1.1 Bayes' theorem

In radio interferometry, a simplified version of the measurement equation (see section 3.1) is

$$V = RI + n, \tag{4.1}$$

where V is the visibility data, R is the response operator, which can be approximated as a Fourier transform operator assuming no calibration corruption with a small field of view, I is the image, and n is the noise.

In Bayesian imaging, we aim for reconstructing the posterior probability distribution of the image given the data $\mathcal{P}(I|V)$ based on our knowledge using Bayes' theorem:

$$\mathcal{P}(I|V) = \frac{\mathcal{P}(V|I)\,\mathcal{P}(I)}{\mathcal{P}(V)}, \tag{4.2}$$

where $\mathcal{P}(V|I)$ is the likelihood, $\mathcal{P}(I)$ is the prior, $\mathcal{P}(V) = \int \mathcal{D}I\,\mathcal{P}(V|I)\,\mathcal{P}(I)$ is the evidence acting as a normalization constant, and $\int \mathcal{D}I$ indicates a path integral over the space of all possible images.

Bayes' theorem is directly derived from the product rule of probability theory. Note that the Bayes' theorem resembles the Boltzmann distribution in statistical mechanics (Enßlin 2019):

$$\mathcal{P}(I|V) = \frac{e^{-\mathcal{H}(V,I)}}{\mathcal{Z}(V)}, \tag{4.3}$$

where $\mathcal{H}(V,I) = -\ln(\mathcal{P}(V,I))$ is the posterior information Hamiltonian, that is defined as the negative log posterior, and $\mathcal{Z}(V) = \int \mathcal{D}I\, e^{-\mathcal{H}(V,I)}$ is the partition function.

The negative log probability distribution, namely the Hamiltonian, is analogous to the energy. The Hamiltonian is beneficial to deal with numerically since multiplication and division are converted to addition and subtraction respectively.

4.1.2 Likelihood distribution

The likelihood distribution $\mathcal{P}(V|I)$ contains the full information that the measurements (data) are providing, it therefore can be interpreted as a data fidelity term. Most of radio interferometric imaging algorithms, such as `CLEAN` and RML methods, utilize the same likelihood term, but employ different prior assumptions (regularizers) in order to infer a plausible image from the data. As an example, `CLEAN` utilizes a simple prior assumption that the sky is a collection of point sources.

In order to construct the likelihood, we start from a Gaussian noise assumption:

$$n \curvearrowleft \mathcal{G}(n,N) = \frac{1}{\sqrt{|2\pi N|}} e^{-\frac{1}{2}n^\dagger N^{-1} n}, \tag{4.4}$$

where $|2\pi N|$ is the determinant of the noise covariance multiplied by 2π, the dagger $\dagger$ indicates the conjugate transposition, and N is the noise covariance.

If sufficient S/N is provided, the Gaussian noise is justified by the central limit theorem since the noise results from numerous contributions, such as atmospheric corruption and thermal noise. If the thermal noise is a predominant contribution, the noise can be approximated as an isotropic Gaussian distribution.

Under the assumption that the noise statistics is Gaussian, the likelihood distribution is derived as a Gaussian distribution by marginalization and the product rule:

$$\begin{aligned}\mathcal{P}(V|I) &= \int \mathcal{D}n\, P(V,n|I) = \int \mathcal{D}n\, P(V|n,I)P(n|I) \\ &= \int \mathcal{D}n\, \delta(V-(RI+n))\mathcal{G}(n,N) = \mathcal{G}(V-RI,N),\end{aligned} \tag{4.5}$$

where δ is the Dirac delta distribution.

Therefore, the likelihood Hamiltonian is

$$\begin{aligned}\mathcal{H}(V|I) &= -\ln(\mathcal{P}(V|I)) \\ &= \frac{1}{2}(V - RI)^{\dagger}N^{-1}(V - RI) + \frac{1}{2}\ln|2\pi N|.\end{aligned} \tag{4.6}$$

If the noise is spherical Gaussian distributed and uncorrelated, the likelihood Hamiltonian is the chi squared χ^2 describing the discrepancy between our model and the data:

$$\mathcal{H}(V|I) \; = \; \frac{1}{2}\sum_n \frac{|V_n - (RI)_n|^2}{\sigma_n^2} = \frac{1}{2}\,\chi^2. \tag{4.7}$$

In fact, most of imaging algorithms, such as `CLEAN`, RML methods, and Bayesian imaging, assume an isotropic Gaussian distributed likelihood with uncorrelated noise since it is numerically convenient to deal with. It is important to note that the isotropic Gaussian and uncorrelated noise assumption is not always valid. For instance, in mm-VLBI observations, the visibility phase is often not well-constrained compared to the visibility amplitude due to tropospheric phase corruption. In this case, the noise distribution is not isotropic Gaussian distributed.

A better parametrization of the non-isotropic Gaussian noise distribution and noise correlation may improve the image fidelity. However, implementing more sophisticated likelihoods increases numerical complexity. In many cases, uncorrelated spherical Gaussian noise is a fair assumption. If we perform time averaging of the data with respect to the phase coherence time, small correlation between the visibility data points therefore can be negligible. Unknown error contributions can be taken into account by adding a systematic error budget, proportional to the visibility amplitude (Event Horizon Telescope Collaboration et al. 2019c). This topic lies outside of the scope of this thesis and further investigation is left for future work.

Alternatively, we can utilize closure quantities directly for the likelihood. Closure phases ϕ_{abc} (Jennison 1958) and closure amplitudes A_{abcd} (Twiss et al. 1960) are invariant under the station-based antenna gain corruption:

$$\phi_{abc} = \arg(V_{ab}) + \arg(V_{bc}) - \arg(V_{ac}), \tag{4.8}$$

$$A_{abcd} = \left|\frac{V_{ab}V_{cd}}{V_{ac}V_{bd}}\right|, \tag{4.9}$$

where V is the visibility and a, b, c, and d are antenna labels.

Closure traces τ_{abcd} (Broderick & Pesce 2020) are insensitive to station-based antenna gain corruptions and polarimetric leakages:

$$\tau_{abcd} = \frac{1}{2} tr(\mathbf{V_{ab}} \mathbf{V_{cb}^{-1}} \mathbf{V_{cd}} \mathbf{V_{ad}^{-1}}), \tag{4.10}$$

where $tr()$ denotes the trace and $\mathbf{V}$ is the visibility matrix.

Closure amplitude and closure phase likelihoods can be employed for total intensity imaging from the data with high instrumental gain errors (Chael et al. 2018; Blackburn et al. 2020). For polarimetric imaging, a closure trace likelihood (Broderick & Pesce 2020; Müller 2024) can be utilized for data suffering from high instrumental gain and leakage corruptions. However, those closure quantities are degenerate and do not contain full information, e.g., there is no absolute flux density information in closure amplitudes and no absolute position information in closure phases.

4.1.3 Prior distribution

The prior distribution $\mathcal{P}(I)$ encodes our knowledge before we obtain the data. Different types of priors can be used in Bayesian imaging, e.g., Inverse Gamma prior for a point source (Arras et al. 2021), or Gaussian process prior for extended emission (Arras et al. 2022; Roth et al. 2023; Kim et al. 2024). We can also build more complex prior model using the combination of multiple priors, e.g., dynamic imaging (Arras et al. 2022; Knollmüller et al. 2023) or polarization imaging model (Arras et al. 2025).

In radio interferometric imaging, encoding appropriate prior knowledge for the sky (image) is essential due to the sparsity and uncertainty in the data. For instance, diffuse emission and point-like emission have different correlation length scales, this difference therefore should be taken into account in the prior model. The smoothness in diffuse emission can be modeled with correlation between pixels. We can model the covariance matrix of the image model for diffuse emission, that describes the two-point cross correlation between pixels. For point-like emission, we can use an uncorrelated prior, e.g., Inverse Gamma prior for the corresponding pixel.

The `CLEAN` algorithm also utilizes an implicit image prior, that the sky brightness distribution is composed of point sources, and perform a greedy search algorithm. The simple assumption in `CLEAN` has several advantages: The image reconstruction is fast and scalable and easier to converge numerically. However, the simple assumption (implicit prior) results in sub-optimal resolution and cannot provide reliable images for the continuous extended jet. Furthermore, `CLEAN` is not able to utilize closure quantities directly, it hinders to reconstruct a reliable image from mm-VLBI data. A detailed comparison between `CLEAN` assumptions and prior in Bayesian imaging can be found in (Arras et al. 2021).

4.1.4 Posterior distribution

According to Bayes' theorem (Equation 4.2), the posterior distribution of the image given the visibility data can be obtained from the likelihood, prior, and evidence distribution. In Bayesian inference, we often avoid calculating the evidence directly because of two reasons: first, the evidence is irrelevant to infer the posterior distribution of the model parameters under the assumption that a particular model is true (Mackay 2003). Second, the integration to obtain the evidence is prohibitively expensive for the high-dimensional inference problem. It is worth mentioning that the evidence can be utilized for the model selection (Mackay 2003).

In Bayesian imaging, we often use computationally efficient inference algorithms, that can estimate the posterior distribution without calculating the evidence, such as MCMC (Markov Chain Monte Carlo) (Mackay 2003; Broderick et al. 2020a,b), Hamiltonian Monte Carlo (HMC) (Betancourt 2017; Pesce 2021; Tiede 2022), and variational inference (VI) (Blei et al. 2016; Knollmüller & Enßlin 2019; Frank et al. 2021). MCMC method guarantees the recovery of the true posterior distribution with an infinite number of samples. However, it is computationally more expensive than HMC and VI, imaging with many pixels ($> 10^2$) therefore is not feasible. HMC can infer more parameters but still can reconstruct images with relatively small number of pixels (up to $\sim 10^4$) with small volume of the data sets, such as VLBI data sets.

In this thesis, we utilized variational inference methods since a joint inference of calibration solutions and imaging requires to explore a large number of parameters ($> 10^6$). Variational inference approximates the posterior as a parametric probability distribution by minimizing the Kullback-Leibler (KL) divergence (Kullback & Leibler 1951; Mackay 2003; Blei et al. 2016):

$$\mathrm{KL}(Q, P) = \int Q(x) \ln \left(\frac{Q(x)}{P(x)} \right) dx, \tag{4.11}$$

where Q is the approximating distribution and P is the true posterior distribution.

We can utilize KL divergence to quantify the information loss. It is commonly employed as a cost function in optimization problems. We note that the KL divergence is not symmetric ($\mathrm{KL}(Q, P) \neq \mathrm{KL}(P, Q)$). In fact, the optimal way to infer the approximating distribution is using $\mathrm{KL}(P, Q)$ (Leike & Enßlin 2017). However, we utilize $\mathrm{KL}(Q, P)$ for the inference, same as most of existing variational inference algorithms do, since the real distribution P is not accessible and minimizing $\mathrm{KL}(P, Q)$ therefore is not feasible.

In this work, we mainly used two variational inference methods, called metric Gaussian variational inference (MGVI) (Knollmüller & Enßlin 2019) and geometric variational inference (geoVI) (Frank et al. 2021) in order to explore the posterior of calibration solutions and images from radio interferometric data. In MGVI and geoVI, the prior distribution is reparametrized in normal coordinate system ξ with zero mean and unit covariance ($P(\xi) = \mathcal{N}(\xi; 0, \mathbf{1})$), our image prior model therefore is a generative model $I(\xi)$ (Knollmüller & Enßlin 2018). According to the reparametrization trick, the posterior takes the form (Frank et al. 2021):

$$P(\xi|V) = \frac{P(V|\xi)\mathcal{N}(\xi; 0, \mathbf{1})}{P(V)}. \tag{4.12}$$

The covariance of the posterior distribution $P(\xi|V)$ is parametrized by the inverse Fisher information metric. The Fisher information metric is defined as

$$M(\xi) = \left\langle \frac{\partial H(\xi|V)}{\partial \xi} \frac{\partial H(\xi|V)}{\partial \xi}^{\dagger} \right\rangle_{P(V|\xi)}, \tag{4.13}$$

where H is the negative logarithm of the probability distribution, namely the information Hamiltonian (see Equation 4.3).

We note that the Fisher metric is the inverse covariance if the posterior is a Gaussian distribution. For non-Gaussian posteriors, MGVI and geoVI are affected by an approximation error. The geoVI method is a non-linear generalization of MGVI (Frank et al. 2021) and non-Gaussian posteriors can be partially explored. It utilizes Riemannian geometry to estimate more complex probability distribution in order to mitigate the limitation of variational inference due to the parametrization of the posterior distribution to some extent. Estimating non-Gaussian posterior distributions in Bayesian imaging can provide more robust calibration and imaging. As an example, in chapter 7, geoVI method is able to describe the ellptical Gaussian leakage posterior distribution from mm-VLBI data. The detailed explanation regarding the MGVI and geoVI method can be found in (Knollmüller & Enßlin 2019; Frank et al. 2021)

4.2 Bayesian imaging software `resolve`

In this work, the Bayesian imaging software `resolve`[1] (**R**adio **E**xtended **SO**urces **L**ognormal deconvolution **E**stimator) is mainly utilized for calibration and imaging (Junklewitz et al. 2016; Arras et al. 2019b, 2021, 2022; Roth et al. 2023, 2024; Kim et al. 2024, 2025a,b). We use prior models and inference algorithms (MGVI, geoVI)(Knollmüller & Enßlin 2019; Frank et al. 2021) from the Bayesian inference numerical toolkit `NIFTy` (Selig et al. 2013; Steininger et al. 2019; Arras et al. 2019a; Edenhofer et al. 2024). `NIFTy` software is based on information field theory, which is Bayesian inference for fields (Enßlin 2019). `NIFTy` has been employed and validated with numerous high-dimensional inference problems, such as 3D tomography of galactic dust (Leike et al. 2020), infrared interferometry (GRAVITY Collaboration et al. 2022a), X-ray imaging (Westerkamp et al. 2024), and strong gravitational lensing (Rüstig et al. 2024). The variational inference methods enable the exploration of the posterior distribution of calibration solutions and images by using a parametric form to describes the posterior distribution. As a result, `resolve` is able to perform high-dimensional image reconstruction in a probabilistic framework with uncertainty estimation by balancing scalability and statistical integrity. In `resolve`, the spatial correlation between image pixels and temporal correlation between calibration solutions can be inferred by the data since non-parametric correlation kernels in Gaussian process prior model are inferred from the data. Detailed description about the `resolve` prior models can be found in (Arras et al. 2021, 2022).

4.3 Bayesian calibration

Calibration in radio interferometry is the process to identify the data corruption and remove the corruption from the data. In order to distinguish between the data corruption and source signal, we build a model M including calibration solution s_{cal} and source term s_{source}, which can explain the data d:

$$d = M(s_{cal},\, s_{source}) + n, \tag{4.14}$$

where n is the additive noise.

The calibration solution s_{cal} can be gains or leakages and the source term s_{source} can be a point source model or reconstructed images. As an example, the model M for self-calibration is $g_i g_j FT[I]$, which consists of gain calibration solutions s_{cal} and a Fourier-transformed reconstructed Stokes I image as s_{source}.

---

[1] https://gitlab.mpcdf.mpg.de/ift/resolve

Conventional calibration methods can be interpreted as maximum likelihood method with regularizers or maximum a-posteriori (MAP) estimation in the Bayesian language. In conventional methods, desired calibration solutions are estimated by minimizing the loss function containing data fidelity term and regularizers for the calibration solutions, e.g., the solution interval in antenna-based gain self-calibration. The source model is usually fixed in order to decrease the number of degrees of freedom in the model.

In Bayesian calibration, we are able to obtain the posterior distribution of the calibration solutions and source model simultaneously and the cross correlation between parameters can be explored. It is especially beneficial in radio interferometry since we often use reconstructed images as source models to estimate calibration solutions, e.g., antenna-based gain self-calibration and polarization calibration. Therefore, more reliable reconstructed images result in more robust calibration solutions and vice versa. Furthermore, the Bayesian approach allows the estimation of the uncertainty of calibration solutions and source model instead of point estimates. Therefore, we are able to quantify the reliability of reconstructed parameters.

Under the assumption that the noise distribution is Gaussian, the likelihood distribution in Bayesian calibration is:

$$P(d|M(s_{cal}, s_{source})) = \int \mathcal{D}n\, P(d, n|M) = \int \mathcal{D}n\, P(d|M, n)\, P(n|M) \tag{4.15}$$

$$= \int \mathcal{D}n\, \delta(d - (M + n))\, G(n, N) = G(d - M, N), \tag{4.16}$$

where δ is the Dirac delta distribution and N is the covariance of the noise n.

The likelihood is the data fidelity term, that describes the discrepancy between the data d and our model M. The likelihood Hamiltonian is:

$$\mathcal{H}(d|M) = -\log(P(d|M)) = \frac{1}{2}(d - M)^{\dagger} N^{-1}(d - M) + \frac{1}{2}\log(\sqrt{2\pi N}) \tag{4.17}$$

If the noise is uncorrelated, the likelihood Hamiltonian (the negative log likelihood) can be approximated as the chi squared χ^2:

$$\mathcal{H}(d|M) \approx \frac{1}{2}\sum_{i=1}^{m} \frac{|d_i - M_i(s_{cal},\, s_{source})|^2}{\sigma_i^2} = \frac{1}{2}\chi^2, \tag{4.18}$$

where m is the number of data points.

4.4 Pros and cons of Bayesian calibration and imaging

Bayesian approach reconstructs calibration solutions and images consistent with the data since we fit our model to the entire data sets in the visibility domain directly. In other words, calibration uncertainties are incorporated in the final results. On the other hand, in the conventional calibration and imaging methods, calibration and imaging are performed iteratively using a fraction of data and calibration uncertainty are not taken into account in the final image.

Another main advantage of the Bayesian approach is improved resolution, also known as super-resolution (Honma et al. 2014). The `CLEAN` algorithm assumes that the sky is a collection of point sources and convolve with the `CLEAN` beam to obtain an image. Convolving with a uniform `CLEAN` beam impose a conservative resolution, it therefore hinders to extract information from the data optimally. We note the multi-scale CLEAN (Cornwell 2008) can partially overcome this issue. On the other hand, in Bayesian imaging, we can utilize image prior that can describe multi-resolution. Therefore, we can reconstruct complex source structure with different correlation length scales. For instance, M87 reconstructions at 43GHz and 86GHz in chapter 5 and chapter 6 show that Bayesian imaging can achieve better resolution, especially in bright core regions. The direct fitting of the Gaussian process prior gain and sky model, incorporating correlation kernels and explicit prior knowledge such as smoothness of the diffuse emission and antenna-based gain solutions, results in super-resolution. In other words, `resolve` can infer the correlation structure between image pixels from the data using Gaussian process prior with non-parametric correlation kernel, different correlation structure in the core and jet therefore can be taken into account. Furthermore, the time-dependent gain solutions are inferred simultaneously with imaging without manual steering of gain constraints, such as gain solution interval.

In the Bayesian framework, we are able to incorporate calibrations into the image reconstruction naturally and the Bayesian method has been demonstrated to solve degenerate problems efficiently using more sophisticated inference algorithms than conventional calibration methods (Arras et al. 2019b; Roth et al. 2023; Kim et al. 2024, 2025b). Especially, in VLBI, the joint inference of calibration solutions and images is advantageous due to the lack of static and point-like calibrators and a short phase coherence time. In chapter 7, we demonstrate Bayesian polarization calibration and imaging in VLBI with examples of synthetic and real data.

Bayesian calibration and imaging allows us to obtain an ensemble of the possible reconstructions instead of a unique solution, that is more natural since radio interferometric data are noisy and incomplete. From the posterior samples, we can estimate the uncertainty of the reconstructed parameters. That is important to quantify the reliability of our reconstruction. As an example, in chapter 6, the posterior distribution of the image features (ring and jet) of the galaxy M87 is explored using posterior sample images. It is worth noting that we can estimate the correlation between reconstructed calibration solutions in Bayesian calibration (Natarajan et al. 2020).

Last but not least, the automated Bayesian calibration and imaging pipeline provides less biased and more reproducible results. In VLBI, Bayesian self-calibration and polarization calibration are less prone to flagging since the uncertainty in the data is taken into account in the image reconstruction and can be propagated to the calibration and image domain.

Bayesian calibration and imaging also has drawbacks: to date, it is not well-explored due to a high computational cost. It is more computationally demanding than conventional calibration and imaging methods since we reconstruct many calibration solutions and images instead of point estimates. The model complexity tends to be higher than the conventional method using an iterative approach. As a result, the large number of degrees of freedom in the model can cause difficulty in convergence.

Moreover, there is one of the main criticisms about the Bayesian statistics regarding the prior distribution: Our prior knowledge may be subjective and arbitrary. Indeed, we can take advantage of Bayes' theorem to reconstruct the results we want to obtain. If we use strongly biased prior, we can obtain the posterior distribution, that is almost similar to the prior. Therefore, having unbiased and flexible prior is crucial in Bayesian statistics. Furthermore, an extensive validation of the model with various types of synthetic/real data sets is required. In fact, this issue applies to all calibration and imaging methods in radio interferometry since our problem is an ill-posed inverse problem.

In conclusion, Bayes' theorem incorporates the certainty of our prior knowledge about the source and instrument and offers a robust framework to solve degenerate calibration and imaging problems in radio interferometry. However, care must be taken to use an unbiased and flexible prior in order to obtain a reliable and robust posterior distribution.

Chapter 5

Bayesian self-calibration and imaging in VLBI

The following chapter has been published in Astronomy & Astrophysics, for which I am the first author (Kim et al. 2024). I calibrated the data using `rPICARD` CASA-based pipeline (Janssen et al. 2019), implemented and performed self-calibration and image reconstructions using `resolve`. Aleksei Nikonov created synthetic data and performed `CLEAN` self-calibration and image reconstructions. I and Hendrik Mueller performed `ehtim` self-calibration and image reconstruction. Aleksei Nikonov and I tested and validated the method. All authors contributed to the writing and revision of the manuscript.

A&A, 690, A129 (2024)
https://doi.org/10.1051/0004-6361/202449663

Astronomy & Astrophysics

Bayesian self-calibration and imaging in very long baseline interferometry

Jong-Seo Kim[1,⋆], Aleksei S. Nikonov[1], Jakob Roth[2,3,4], Torsten A. Enßlin[2,3], Michael Janssen[1,5], Philipp Arras[2,4], Hendrik Müller[1,6], and Andrei P. Lobanov[1]

[1] Max-Planck-Institut für Radioastronomie, Auf dem Hügel 69, 53121 Bonn, Germany
[2] Max-Planck-Institut für Astrophysik, Karl-Schwarzschild-Str. 1, 85748 Garching, Germany
[3] Ludwig-Maximilians-Universität, Geschwister-Scholl-Platz 1, 80539 Munich, Germany
[4] Technische Universität München (TUM), Boltzmannstr. 3, 85748 Garching, Germany
[5] Department of Astrophysics, Institute for Mathematics, Astrophysics and Particle Physics (IMAPP), Radboud University, PO Box 9010, 6500 GL Nijmegen, The Netherlands
[6] Jansky Fellow of National Radio Astronomy Observatory, 1011 Lopezville Rd, Socorro, NM 87801, USA

Received 19 February 2024 / Accepted 17 July 2024

ABSTRACT

Context. Self-calibration methods with the `CLEAN` algorithm have been widely employed in very long baseline interferometry (VLBI) data processing in order to correct antenna-based amplitude and phase corruptions present in the data. However, human interaction during the conventional `CLEAN` self-calibration process can impose a strong effective prior, which in turn may produce artifacts within the final image and hinder the reproducibility of final results.

Aims. In this work, we aim to demonstrate a combined self-calibration and imaging method for VLBI data in a Bayesian inference framework. The method corrects for amplitude and phase gains for each antenna and polarization mode by inferring the temporal correlation of the gain solutions.

Methods. We use Stokes I data of M87 taken with the Very Long Baseline Array (VLBA) at 43 GHz, pre-calibrated using the rPICARD CASA-based pipeline. For antenna-based gain calibration and imaging, we use the Bayesian imaging software `resolve`. To estimate gain and image uncertainties, we use a variational inference method.

Results. We obtain a high-resolution M87 Stokes I image at 43 GHz in conjunction with antenna-based gain solutions using our Bayesian self-calibration and imaging method. The core with counter-jet structure is better resolved, and extended jet emission is better described compared to the `CLEAN` reconstruction. Furthermore, uncertainty estimation of the image and antenna-based gains allows us to quantify the reliability of the result.

Conclusions. Our Bayesian self-calibration and imaging method is able to reconstruct robust and reproducible Stokes I images and gain solutions with uncertainty estimation by taking into account the uncertainty information in the data.

Key words. methods: statistical – techniques: high angular resolution – techniques: image processing – techniques: interferometric – galaxies: active – galaxies: individual: M87

1. Introduction

Calibration and imaging are closely interconnected in radio interferometry which combines signals received at multiple antennas in order to form a virtual telescope with the aperture effectively determined by the largest projected distance between the participating antennas. The reconstruction of high-fidelity images from radio interferometric observations requires appropriate calibration of the data. In the standard calibration process, amplitude and phase corruptions are corrected, and data are flagged and averaged by a deterministic algorithm. After calibration, image reconstruction is required as radio interferometers measure incomplete Fourier components of the sky brightness distribution instead of observing an actual image. Image reconstruction in radio interferometry is an ill-posed problem. Therefore, a unique solution does not exist. Furthermore, the standard data reduction process in radio interferometry still leaves a large amount of uncertainty due to instrumental and atmospheric errors. A probabilistic approach can be beneficial to properly deal with the incompleteness and uncertainty of radio interferometric data.

In very long baseline interferometry (VLBI), the distance between ground-based telescopes reaches the size of the earth to achieve high resolution. The data obtained from this set of telescopes are highly sparse owing to limited number of antennas and observation time. Due to this sparsity, it is challenging to reconstruct high-fidelity images without additional assumptions about the source structure and instrument effects. This additional knowledge is called prior knowledge in Bayesian statistics. Encoding physically sensible prior knowledge results in robust and consistent image reconstructions from highly sparse VLBI data sets. In addition to the sparsity, the data reduction process in VLBI is complicated due to large gain uncertainties, and low S/N (signal-to-noise ratio) measurements (Janssen et al. 2022). Particularly, in millimeter VLBI, tropospheric effects cause significant visibility amplitude and phase errors. As a result, interpolating calibrator solutions to the science target is insufficient to correct time-dependent data corruption. Self-calibration

---

[⋆] Corresponding author; `jongkim@mpifr-bonn.mpg.de` methods within the CLEAN framework are the standard procedure to correct additional antenna-based gain corruption after the initial calibration.

The CLEAN algorithm (Högbom 1974; Clark 1980) is the de-facto standard for image reconstruction in radio interferometry due to its simplicity and interactivity. However, CLEAN suffers from several shortcomings (Arras et al. 2021). First, it cannot produce optimal results because the algorithm does not produce images consistent with the data. In CLEAN, the sky brightness distribution is assumed to be a collection of point sources, which is incorrect for diffuse emission. We note that multi-scale CLEAN (Cornwell 2008) is able to perform better than conventional CLEAN methods for extended emission. However, the conventional multi-scale CLEAN still does not compare the model with the data directly, the consistency between model and data therefore is not guaranteed. Furthermore, convolving with the CLEAN beam hinders achieving the optimal resolution. Second, it is difficult to modify the model. We cannot explicitly utilize existing knowledge, such as closure amplitudes and phases, the positivity of the flux, and polarization constraints in image reconstruction by CLEAN. Third, CLEAN requires the supervision of an experienced scientist. Hence, the results can be biased. For example, CLEAN windows and weighting schemes are user-dependent. Therefore, a strong effective prior is imposed onto the final image. Lastly, CLEAN does not provide an estimate of the uncertainties within an image. Due to these limitations, using CLEAN for self-calibration may have significant drawbacks. Human biases can be introduced into the final image during self-calibration since the data are modified by the inconsistent model image and flagged without objective criteria. Moreover, the simplicity of the CLEAN restricts the implementation of a more sophisticated optimization algorithm in self-calibration.

Forward modeling imaging algorithms can be utilized for more robust self-calibration in VLBI. The forward modeling approach interprets image reconstruction as an optimization problem. Forward modeling fits the model to the data directly, thus ensuring consistency between the image and the data. There exist traditional forward modeling approaches, such as the Maximum Entropy Method (MEM; Cornwell & Evans 1985; Narayan & Nityananda 1986). However, CLEAN-based algorithms have historically been favored due to the simplicity of implementation and the limited necessary computational resources. Recent developments in optimization theory and computer performance enable forward modeling algorithms to outperform CLEAN. There are a variety of different forward modeling methods, such as regularized maximum likelihood (RML) and Bayesian imaging.

The RML method (Wiaux et al. 2009; Akiyama et al. 2017; Chael et al. 2018; Müller & Lobanov 2022) is a forward modeling approach based on ridge regression. The image is reconstructed by minimizing an objective function containing data fidelity terms and regularizers. The algorithm can be faster than Bayesian approaches because one final image is generated instead of a collection of posterior sample images. It can be interpreted as the maximum a posteriori (MAP) estimation in Bayesian statistics. Recently, Dabbech et al. (2021) performed direction-dependent gain calibration and imaging jointly in the RML framework.

Bayesian imaging (Junklewitz et al. 2015; Broderick et al. 2020; Arras et al. 2021; Tiede 2022) in radio interferometry is a probabilistic approach that provides samples of potential images that are consistent with the data and prior assumptions within the noise statistics instead of one image. The samples can be interpreted as being drawn from the posterior probability distribution. In Bayesian statistics, the probability distribution of the reconstructed image is called the posterior, which is obtained from the prior distribution and the likelihood by Bayes' theorem.

Bayesian imaging has an intrinsic advantage: the prior knowledge can be encoded explicitly into the image reconstruction. Knowledge about the source and instrument, such as closure quantities, can be utilized directly to obtain robust images from sparse VLBI data sets (Arras et al. 2022). Moreover, uncertainty estimation can be obtained as a by-product of image reconstruction. The reliability of the results can be quantified by the uncertainty estimation. Arras et al. (2019b) performed calibration and imaging jointly in the Bayesian framework with Very Large Array (VLA) data. Recently, Roth et al. (2023) proposed Bayesian direction-dependent calibration and imaging with VLA data.

Building on the works of Arras et al. (2019b), we propose a novel Bayesian self-calibration and imaging method for VLBI data sets. For our method, we require pre-calibrated data that have not undergone manual flagging in order to reduce human biases. Instead of the iterative procedure in the CLEAN self-calibration approach, our method infers the Stokes I image and antenna-based gain terms simultaneously. The spatial correlation between pixels in the sky model is inferred by the non-parametric Gaussian kernel following Arras et al. (2021). Furthermore, time-dependent antenna-based amplitude and phase gain terms are inferred by considering the temporal correlation between points in time-dependent gain solutions. We estimate the uncertainty of reconstructed parameters by the variational inference method (Blei et al. 2016; Knollmüller & Enßlin 2019). Estimated uncertainty of the image and antenna-based gain terms can provide valuable information about the image and each antenna condition.

This paper is structured as follows. In Section 2, we describe the measurement equation in radio interferometry and interpretation of image reconstruction problem in Bayesian framework. In Section 3, we describe our self-calibration and imaging prior model in VLBI and inference algorithm. We validate the Bayesian self-calibration and imaging with real VLBA M87 data at 43 GHz in Section 4 and synthetic data in Section 5. In Section 6, we summarize our results.

2. Image reconstruction in radio interferometry

2.1. Radio interferometer measurement equation (RIME)

The mapping from a given sky brightness distribution to the data measured by the radio interferometer is represented by the radio interferometer measurement equation (RIME) and will be defined in this subsection. The two-point correlation function of the electric field is equivalent to the Fourier components of the sky brightness distribution by the van Cittert–Zernike theorem (Hamaker et al. 1996; Smirnov 2011; Thompson et al. 2017). A radio interferometer can obtain this correlation function called visibility $V(u, v)$. In VLBI, due to the small field of view, the relationship between the visibility $V(u, v)$ and sky brightness distribution $I(x, y)$ can be approximated with a two-dimensional Fourier transform (Thompson et al. 2017):

$$\mathcal{V}(u, v) = \mathbb{F} I := \int_{-\infty}^{\infty} \int_{-\infty}^{\infty} I(x, y) e^{-2\pi i(ux+vy)} dx\, dy, \tag{1}$$

where $\mathbb{F}$ is the Fourier transform, $(u, v) =: \boldsymbol{k}$ are the Fourier and (x, y) the image domain coordinates.

In an observation, a visibility data point from antenna pair i, j at a time t is the visibility at the Fourier space location

$\boldsymbol{k}_{ij}(t) := (u, v)_{ij}(t) = \boldsymbol{b}_{\perp,ij}(t)/\lambda$, with $\boldsymbol{b}_{\perp,ij}(t)$ representing the vector baseline between the antenna pair at time t projected orthogonal to the line of sight, and λ being the observing wavelength.

The measured visibility, corrupted by errors in direction-independent antenna gains (g_i, g_j), and thermal noise, n_{ij} is

$$V_{ij}(t) = g_i(t)\, g_j^*(t)\, \mathcal{V}(\boldsymbol{k}_{ij}(t)) + n_{ij}(t), \tag{2}$$

where * denotes complex conjugation.

The measurement equation can be written in shorthand notation:

$$V_{ij}(t) = R^{(g,t)} I + n_{ij}(t) := g_i(t)\, g_j^*(t)\, B(t)[\mathbb{F}\, I] + n_{ij}(t), \tag{3}$$

with $R^{(g,t)}$ describing the measurement operator that is composed of sampling of the measured baseline visibilities for each sampled time t, $B(t)[\mathcal{V}]_{ij} := \mathcal{V}(\boldsymbol{k}_{ij}(t))$, and the application of the antenna gains g.

We note that a straightforward inverse Fourier transform cannot produce high-fidelity images because the data are measured at sparse locations in the (u, v) grid, corrupted by gains, and contain uncertainty from thermal noise. Due to incompleteness and uncertainty in the data, multiple possible image reconstructions can be obtained that would be consistent with the same data. To address this problem, image reconstruction in radio interferometry aims to infer for example the most plausible image $I(x, y)$ from incomplete, distorted, and noisy data $V_{ij}(t)$.

2.2. Bayesian imaging

Bayes' theorem provides a statistical framework to construct the posterior probability distribution for the sky $I(x, y)$ from the incomplete visibility data $V_{ij}(t)$. Instead of computing a single final image, Bayesian imaging provides the probability distribution over possible images, called the posterior distribution. The posterior distribution of the image I given the data V can be calculated via Bayes' theorem:

$$\mathcal{P}(I|V) = \frac{\mathcal{P}(V|I)\,\mathcal{P}(I)}{\mathcal{P}(V)}, \tag{4}$$

where $\mathcal{P}(V|I)$ is the likelihood, $\mathcal{P}(I)$ is the prior, and $\mathcal{P}(V) = \int \mathcal{D}I\, \mathcal{P}(V|I)\,\mathcal{P}(I)$ the evidence acting as a normalization constant. In the case of Bayesian image reconstruction, the evidence involves an integral over the space of all possible images, hence $\int \mathcal{D}I \ldots$ indicates a path integral.

Bayes' theorem follows directly from the product rule of probability theory. It can be rewritten to resemble the Boltzmann distribution in statistical mechanics by introducing the information Hamiltonian (Enßlin 2019):

$$\mathcal{P}(I|V) = \frac{e^{-\mathcal{H}(V,I)}}{\mathscr{Z}(V)}, \tag{5}$$

where $\mathcal{H}(V, I) = -\ln(\mathcal{P}(V, I))$ is the information Hamiltonian, which is the negative log probability, and $\mathscr{Z}(V) = \int \mathcal{D}I\, e^{-\mathcal{H}(V,I)}$ is the partition function.

For imaging with a large number of pixels, the posterior distribution of the image $\mathcal{P}(I|V)$ will be high dimensional. Due to the high dimensionality, it is not feasible to visualize the full posterior probability distribution. Thus, we compute and analyze summary statistics as the posterior mean

$$m = \langle I \rangle_{\mathcal{P}(I|V)} \tag{6}$$

and standard deviation

$$\sigma_I = \sqrt{\langle (I - m)^2\, \rangle_{\mathcal{P}(I|V)}}, \tag{7}$$

where $\langle f(I) \rangle_{\mathcal{P}(I|V)} := \int \mathcal{D}I\, f(I)\, \mathcal{P}(I|V)$ denotes the posterior average of $f(I)$.

In Bayesian imaging, we can design the prior model to encode the desired prior knowledge, such as the positivity of flux density and the polarization constraints. The use of this additional prior information about the source and the instrument stabilizes the reconstruction of the sky image. For instance, diffuse emission can be well described by a smoothness prior on the brightness of nearby pixels. The details of our prior assumption are discussed in Section 3.

Furthermore, the mean and standard deviation of any parameter in the model can be estimated. The standard deviation can be utilized to quantify the uncertainty of reconstructed parameters. In other words, we can propagate the uncertainty information in the data domain into other domains, such as the image or the antenna gain.

For this, the set of quantities of interest that are to be inferred need to be extended, for example to include the sky intensity I and all antenna gains g. The gains enter the measurement equation by determining the response, $R \equiv R^{(g)}$, and thereby the likelihood, which becomes $\mathcal{P}(V|g, I)$.

The joint posterior distribution for gains and sky is again obtained by Bayes' theorem,

$$\mathcal{P}(g, I|V) = \frac{\mathcal{P}(V|g, I)\,\mathcal{P}(g, I)}{\mathcal{P}(V)}, \tag{8}$$

where $\mathcal{P}(V) = \int \mathcal{D}I \int \mathcal{D}g\, \mathcal{P}(V, g, I)$ is the joint evidence and $\mathcal{P}(g, I) = \mathcal{P}(g)\,\mathcal{P}(I)$ the joint prior, here assumed to be decomposed into independent sky and gain priors, $\mathcal{P}(I)$ and $\mathcal{P}(g)$ respectively.

By marginalization of the joint posterior over the sky degrees of freedom, $\int \mathcal{D}I\, \mathcal{P}(I, g|V) =: \mathcal{P}(g|V)$, a gain (only) posterior can be obtained. From this, the posterior mean $\langle g_i \rangle_{\mathcal{P}(g|V)}$ and standard deviation σ_{g_i} can be calculated for any antenna i. As a result, each antenna gain corruption mean and uncertainty can be inferred from the data by obtaining the joint posterior distribution. Uncertainty estimation is a distinctive feature of Bayesian imaging.

2.3. Likelihood distribution

For compact notation, we define the signal vector $s = (g, I)$ containing the gain g and the image I that carries all their components. The visibilities V are in our case the data d. The likelihood distribution $\mathcal{P}(d|s)$ largely determines the resulting Bayesian imaging algorithm since it contains the information on the measurement process that will be inverted by the algorithm.

The probability distribution of the noise n in the measurement equation (Eq. (3)) can often be approximated to be Gaussian distribution. From a statistical point of view, the effective noise level is a sum of many noise contributions and it can be approximated as Gaussian distribution by the central limit theorem, if sufficient S/N is provided.

We therefore assume that the noise n is drawn from a Gaussian distribution with covariance N,

$$n \curvearrowleft \mathscr{G}(n, N) = \frac{1}{\sqrt{|2\pi N|}} e^{-\frac{1}{2} n^\dagger N^{-1} n} \tag{9}$$

where $|2\pi N|$ is the determinant of the noise covariance (multiplied by 2π) and $\dagger$ indicates the conjugate transpose of a vector or matrix.

Under this assumption, the likelihood $\mathcal{P}(d|s)$ is a multivariate Gaussian distribution:

$$\mathcal{P}(d|s) = \mathscr{G}(V - R^{(g)}I, N). \tag{10}$$

The likelihood Hamiltonian

$$\begin{aligned}\mathcal{H}(d|s) &= -\ln(\mathcal{P}(d|s)) \\ &= \frac{1}{2}(V - R^{(g)}I)^{\dagger}N^{-1}(V - R^{(g)}I) + \frac{1}{2}\ln|2\pi N|\end{aligned} \tag{11}$$

is then of quadratic form in I, but of fourth order in g, as $R^{(g)}$ is already quadratic in g. This renders the joint imaging and calibration problem in radio interferometry a challenging undertaking.

Furthermore, we assume that the noise is not correlated with time and different baselines. Time and baseline correlation of the noise could be inferred as well, similar to the inference of the signal angular power spectrum. However, this would be another algorithmic advancement in image reconstruction since it is significantly increasing the complexity of the algorithm. Therefore, we use the approximation that the noise is uncorrelated with time and different baselines, which is current standard in radio imaging. In other words, the noise covariance $N_{ij} = \delta_{ij}\,\sigma_i^2$ is diagonal. Under the assumption, denoting here with n any datum in the data vector (that was previously indexed by the two antenna identities and a time stamp, (i, j, t)), the likelihood Hamiltonian can be interpreted as the data fidelity term:

$$\mathcal{H}(d|s) \;=\; \frac{1}{2}\sum_{n}\frac{|V_n - (R^{(g)}I)_n|^2}{\sigma_n^2} = \frac{1}{2}\,\chi^2. \tag{12}$$

2.4. Posterior distribution

Bayesian imaging aims to calculate the posterior distribution $\mathcal{P}(s|d)$ from the visibility data $d = V$ and the prior $\mathcal{P}(s)$. Obtaining the posterior distribution $\mathcal{P}(s|d)$ is equivalent to calculating the posterior information Hamiltonian $\mathcal{H}(s|d)$. The information Hamiltonian contains the same information as the probability density it derives from, but it is numerically easier to handle since the multiplication of two probability distributions is converted to an addition. The joint data and signal information Hamiltonian is composed of a likelihood and prior information term, $\mathcal{H}(s)$ and $\mathcal{H}(d|s)$, respectively, which are just added,

$$\mathcal{H}(d, s) = \mathcal{H}(d|s) + \mathcal{H}(s). \tag{13}$$

The posterior information Hamiltonian

$$\mathcal{H}(s|d) \equiv -\ln(\mathcal{P}(s|d)) = \mathcal{H}(d|s) + \mathcal{H}(s) - \mathcal{H}(d) \tag{14}$$

differs from this only by the subtraction of $\mathcal{H}(d)$, the evidence Hamiltonian.

There are numerous algorithms that explore the posterior, such as Markov chain Monte Carlo (MCMC) and Hamiltonian Monte Carlo (HMC) methods. Those are, however, computationally very expensive for the ultra-high dimensional inference problems we are facing in imaging. Another method to obtain a signal estimate is to calculate the maximum a posteriori (MAP) estimation. The posterior Hamiltonian is minimized to calculate the MAP estimator of a signal

$$s_{\mathrm{MAP}} := \mathrm{argmin}_s \mathcal{H}(s|d). \tag{15}$$

The evidence term is independent of the signal and therefore has no influence on the location of the minimum in signal space. Thus, equivalently the joint information Hamiltonian $\mathcal{H}(d, s)$ of the signal and data can be minimized, as it only differs from the posterior information $\mathcal{H}(s|d)$ by the signal independent evidence $\mathcal{H}(d)$. MAP estimation is computationally much faster than sampling the entire posterior density, enabling high-dimensional inference problem. However, MAP does not provide any uncertainty quantification on its own (Knollmüller & Enßlin 2019). We note that RML methods can be interpreted as MAP estimation in Bayesian framework. The interpretation of RML method in terms of Bayesian perspective can be found in Appendix B.

Bayesian inference ideally explores the structure of the posterior around its maximum the MAP method focuses on. In case this has a nontrivial, non-symmetric structure, the MAP estimate can be highly biased w.r.t. the more optimal posterior mean, which is optimal from an expected squared error functional perspective. In general, in Bayesian inference, one wants to be able to calculate expectation values for any interesting function $f(s)$ of the signal, be it the sky intensity, $f(s) = I$, its uncertainty dispersion $f(s) = (I - \overline{I})^2$, power spectrum $f(s) = P_I(\boldsymbol{k}) = |\mathbb{F}\,I|^2(\boldsymbol{k})$, or any function of the gains. Thus,

$$\overline{f} := \langle f(s)\rangle_{(s|d)} \tag{16}$$

should somehow be accessible. For non-Gaussian posteriors, but also for non-linear signal functions, this will in general differ from $f(s_{\mathrm{MAP}})$, and the difference can be substantial (Enßlin & Frommert 2011).

A good compromise between efficiency (like that given by MAP) and accuracy (as HMC can provide) is variational inference method. These fit a simpler probability distribution to the posterior, one from which a set $S = \{s_1, \ldots\}$ of posterior samples can be drawn. The estimate of any posterior average of a signal function can then be approximated by the sample average

$$\overline{f} \approx \frac{1}{|S|}\sum_{s\in S} f(s), \tag{17}$$

where $|S| = \sum_{s\in S} 1$ denotes the size of the set. To estimate the posterior distribution of the sky and gains, Metric Gaussian Variational Inference method (MGVI, Knollmüller & Enßlin 2019) is utilized in this work. For further details on the used variational inference scheme, see Section 3.5.

2.5. Self-calibration in VLBI

Before imaging, correlated radio interferometric data need to be calibrated to correct for data corruption. For calibration, the target source of an observation and calibrator sources, which are commonly bright and point-like, are observed alternately. By comparing expected properties of the calibrators and observed data, instrumental effects can be identified. The calibrator solution, correcting instrumental effects, is then applied to the data of the target source. However, residual errors still exist after the initial calibration due to the time dependence of amplitude and phase corruptions and the angular separation between the target source and calibrators.

With a sufficient S/N, the target source itself can be used as a calibrator. Using the target source itself for calibration is called self-calibration (Cornwell & Wilkinson 1981; Brogan et al. 2018). Following the initial calibration, the conventional self-calibration method, iteratively correcting the antenna-based gain corruptions, works as follows: First, a model image is reconstructed from the target data $V_{ij}^{(m)}$. The image can be reconstructed by `CLEAN` or forward modeling algorithms. Second, the residual gains g are estimated by minimizing the cost function (Cornwell & Wilkinson 1981; Taylor et al. 1999):

$$S = \sum_k \sum_{i,j}^{i \neq j} \frac{|V_{ij}^{(m)}(\boldsymbol{k}_{ij}(t_k)) - g_i(t_k) g_j^*(t_k) M_{ij}(\boldsymbol{k}_{ij}(t_k))|^2}{\sigma_{ij}^2(t_k)}, \tag{18}$$

where $g_i(t_k)$ is the complex gain of the antenna i at the time t_k, $M_{ij}(\boldsymbol{k}_{ij}(t_k))$ is the Fourier component at $\boldsymbol{k}_{ij}(t_k)$ of the model image, and σ_{ij} is the noise standard deviation of the visibility data V_{ij}.

The cost function contains the difference between the data V_{ij} and the Fourier-transformed model image M_{ij} with gains g. Gains g are free parameters in the minimization. Simple minimization schemes, such as the least-squares method, are utilized to infer the gains g with a solution interval, which is the correlation constraint. Then the estimated residual gain corruption g is removed from the data. The m-th iteration of self-calibration is

$$V_{ij}^{(m)}(t_k) = \frac{V_{ij}^{(m-1)}(t_k)}{g_i(t_k)\, g_j^*(t_k)}. \tag{19}$$

There are different ways to propagate the error in CLEAN self-calibration. As an example, in `DIFMAP` (Shepherd 1997) software, phase self-calibration does not change the errors and amplitude self-calibration corrects errors by treating gains as constant within the solution interval. As a result, error of the self-calibrated data is

$$\sigma_{ij,self} = \frac{\sigma_{ij}}{|g_i|\,|g_j|}, \tag{20}$$

where σ_{ij} is the error of the data before self-calibration.

We note that the S/N of the data is conserved in self-calibration, if the gains are treated as constant in error propagation. If the reported noise estimates are correct, it is a reasonable assumption. In `DIFMAP`, there is also an option to fix the weights to prevent the amplitude corrections from being applied to the visibility errors.

In conclusion, self-calibration consists of three steps: model image reconstruction from the data, residual gain estimation from the minimization, and modification of the data by removing estimated residual gains. Those three steps are continued iteratively until some stopping criterion is met.

Self-calibration works as long as the effective number of degrees of freedom for the visibility data for N stations ($N(N-1)/2$) is larger than the degrees of freedom of antenna gains (amplitude: N, phase: $N-1$). The system of equations to obtain antenna-based gains from the data is over-determined. As a result, with a sufficient S/N and number of antennas, we can estimate the gains from the visibility data. The closure amplitude and phase are invariant under the antenna-based gain calibration. Therefore, we can calibrate antenna gains by self-calibration while conserving relative intensity information and relative position about the source.

While self-calibration is required to obtain a high-fidelity VLBI image, it does have shortcomings. Strong biases might be imposed during the self-calibration due to the use of inconsistent model image from `CLEAN` reconstruction and manual setting of the solution interval for gain estimation. Furthermore, self-calibration hinders the reproduction of the result due to the human interactions in imaging. Some fraction of the data points are often flagged during the self-calibration, either manually or on the basis of non-convergence of the gain solutions. The flagging is however prone to errors, as it is difficult to distinguish between a bad data point and a data point inconsistent with the model image.

In this paper, self-calibration and imaging are combined into a joint inference problem. In other words, the inference of gains and image is performed simultaneously. Data flagging is performed solely by the calibration pipeline. It is a generalized version of conventional self-calibration, as it combines image reconstruction and gain inference by the minimization of the data fidelity term. We note that the posterior distribution of gains are explored in Bayesian self-calibration instead of computing a point estimate in conventional iterative self-calibration approaches. Originally, the joint antenna-based calibration and imaging approach was presented in Arras et al. (2019b) and extended to also include direction-dependent effects in Roth et al. (2023). The Bayesian self-calibration and imaging allow us to reconstruct less-biased reproducible images with the help of sophisticated prior model and minimization scheme.

3. The algorithm

3.1. `resolve`

The self-calibration approach developed in this paper is realized using the package `resolve`[1], which is an open-source Bayesian imaging software for radio interferometry. It is derived and formulated in the language of information field theory (Enßlin 2019). The first version of the algorithm was presented by Junklewitz et al. (2015, 2016). Arras et al. (2019b) added imaging and antenna-based gain calibration with Very Large Array (VLA) data. Dynamic imaging with closure quantities was implemented in Arras et al. (2022). In `resolve`, imaging and calibration are treated as a Bayesian inference problem. Thus from the data, `resolve` estimates the posterior distribution for the sky brightness distribution and calibration solutions. To obtain the posterior distribution and to define prior models, `resolve` builds on the a Python library NIFTy[2] (Arras et al. 2019a). In NIFTy, variational inference algorithms such as Metric Gaussian Variational Inference (Knollmüller & Enßlin 2019, MGVI) and geometric Variational Inference (Frank et al. 2021b, geoVI), as well as Gaussian process priors, are implemented.

3.2. rPICARD

For the signal stabilization and flux density calibration, we use the fully automated end-to-end rPICARD pipeline (Janssen et al. 2019). Using the input files[3], our data calibration can be reproduced exactly with rPICARD version 7.1.2, available as Singularity or Docker container[4].

---

[1] `https://gitlab.mpcdf.mpg.de/ift/resolve`

[2] `https://gitlab.mpcdf.mpg.de/ift/nifty`

[3] `https://zenodo.org/uploads/10190800`

[4] `https://hub.docker.com/r/mjanssen2308/casavlbi`
The container corresponding to v7.1.2 is tagged as ec77b9874a6de7d071c8a1d8b3816702d4c6fd9f.

3.3. Sky brightness distribution prior model

We expect the Stokes I sky brightness distribution $I(\boldsymbol{x})$ to be positive, spatially correlated, and to vary over several orders of magnitude. We encode these prior assumptions into our sky brightness prior model. More specifically, to encode the assumption of positivity and variations over several orders of magnitude, we model the sky as

$$I(\boldsymbol{x}) = \exp(\psi(\boldsymbol{x})), \tag{21}$$

where $\psi(\boldsymbol{x})$ is the logarithmic sky brightness distribution.

To also encode the spatial correlation structure into our prior model we generate the log-sky ψ from a Gaussian process

$$\psi \curvearrowleft \mathscr{G}(\psi, \Psi), \tag{22}$$

where Ψ is the covariance matrix of the Gaussian process.

The covariance matrix Ψ represents the spatial correlation structure between pixels. Since the correlation structure of the source is unknown, we want to infer the covariance matrix Ψ, also called the correlation kernel, from the data. However, estimating the full covariance matrix for high-dimensional image reconstructions is computationally demanding since storing the covariance matrix scales quadratically with the number of pixels. To overcome this issue, the prior log-sky ψ is assumed to be statistically isotropic and homogeneous. According to the Wiener-Khinchin theorem (Wiener 1949; Khinchin 1934), the spatial covariance S of a homogeneous and isotropic Gaussian process becomes diagonal in Fourier space, and is described by a power spectrum $P_\Psi(|\boldsymbol{k}|)$,

$$\Psi(\boldsymbol{k}, \boldsymbol{k}') = \langle \psi(\boldsymbol{k}) \psi(\boldsymbol{k}')^\dagger \rangle = (2\pi)^{d_k} \delta(\boldsymbol{k} - \boldsymbol{k}') P_\Psi(|\boldsymbol{k}|), \tag{23}$$

where d_k is the dimension of the Fourier transform.

The power spectrum $P_\Psi(|\boldsymbol{k}|)$ scales linearly with the number of pixels. Thus, inference of the covariance matrix assuming isotropy and homogeneity is computationally feasible for high-dimensional image reconstructions. In our sky prior model, the power spectrum is falling with $|\boldsymbol{k}|$, typically showing a power law shape. The falling power spectrum encodes smoothness in the sky brightness distribution I. Small-scale structures in the image I are suppressed since high-frequency modes have small amplitudes due to the falling power spectrum. The correlation kernel in the prior can be interpreted as a smoothness regularizer in the RML method and vice versa.

The log-normal Gaussian process prior is encoded in `resolve` in the form of a generative model (Knollmüller & Enßlin 2018). This means that independently distributed Gaussian random variables $\xi = (\xi_\Psi, \xi_k)$ are mapped to the correlated log-normal distribution:

$$I(\boldsymbol{x}) = \exp(\psi(\boldsymbol{x})) = \exp(\mathbb{F}[\sqrt{P_\Psi(\xi_\Psi)} \xi_k]) = I(\xi), \tag{24}$$

where $\mathbb{F}$ is the Fourier transform operator, all ξ are standard normal distributed, $P_\Psi(\xi_\Psi)$ is the spatial correlation power spectrum of log-sky ψ, and $I(\xi)$ is the standardized generative model.

In `resolve`, the power spectrum model P_Ψ is modeled non-parametrically. In the image reconstruction, the posterior parameters ξ_Ψ modeling the power spectrum are inferred simultaneously with the actual image. More details regarding the Gaussian process prior model in `resolve` can be found in the methods section of Arras et al. (2022).

We note that we can mitigate strong biasing since the reconstruction of the correlation kernel is a part of the inference process instead of assuming a fixed correlation kernel or a specific sky prior model. As an example, in `CLEAN`, the sky brightness distribution is assumed to be a collection of point sources. However, it is not a valid assumption for diffuse emission, and it therefore might create imaging artifacts, such as discontinuous diffuse emission with blobs. In `resolve`, the correlation structure in the diffuse emission can be learned from the data. As a result, the diffuse emission can be well described by the sky prior model. Furthermore, the Gaussian process prior model with non-parametric correlation kernel can also be used for the inference of other parameters, such as amplitude and phase gain corruptions, in order to infer the temporal correlation structure and to encode smoothness in the prior.

3.4. Antenna-based gain prior model

In this paper, we assume that the residual data corruptions can be approximately represented as antenna-based direction-independent gain corruptions. The measurement equation (Eq. (3)) can be generalized for polarimetric visibility data with sky brightness distribution matrix including right-hand circular polarization (RCP) and left-hand circular polarization (LCP) antenna-based gain corruptions for antenna pair i, j (Hamaker et al. (1996), Smirnov (2011)):

$$\mathbf{V}_{ij} = G_i(t) \left(\int_{-\infty}^{\infty} \int_{-\infty}^{\infty} \mathbf{I}(x, y)\, e^{-2\pi i (u_{ij} x + v_{ij} y)} dx\, dy \right) G_j^\dagger(t) + \mathbf{N}_{ij}, \tag{25}$$

where $\mathbf{V}_{ij}$ is the visibility matrix with four complex correlation functions by the right-hand circularly polarized signal R and the left-hand circularly polarized signal L:

$$\mathbf{V}_{ij} = \begin{pmatrix} R_i R_j^* & R_i L_j^* \\ L_i R_j^* & L_i L_j^* \end{pmatrix}, \tag{26}$$

$\mathbf{I}(x, y)$ is the sky brightness distribution matrix of the four Stokes parameters (namely, I, Q, U, and V):

$$\mathbf{I} = \begin{pmatrix} I + V & Q + iU \\ Q - iU & I - V \end{pmatrix}, \tag{27}$$

$\mathbf{N}_{ij}$ is the additive Gaussian noise matrix, and $G_i(t)$ is the antenna-based gain corruption matrix:

$$G_i(t) = \begin{pmatrix} g_i^R(t) & 0 \\ 0 & g_i^L(t) \end{pmatrix}. \tag{28}$$

We model the complex gain $g(t)$ via the Gaussian process prior model described in the previous section. For instance, the ith antenna RCP gain $g_i^R(t)$ can be represented by two Gaussian process priors λ and ϕ:

$$g_i^R(t) = \exp(\lambda_i^R(t) + i\phi_i^R(t)), \tag{29}$$

where λ is the log amplitude gain, and ϕ is the phase gain.

The Gaussian process priors λ and ϕ are generated from multivariate Gaussian distributions with covariance matrices Λ and Φ:

$$\lambda \curvearrowleft \mathscr{G}(\lambda, \Lambda)\,, \phi \curvearrowleft \mathscr{G}(\phi, \Phi). \tag{30}$$

The temporal correlation kernels Λ and Φ are inferred from the data in the same way as the inference of spatial correlation of the log-sky ψ (see Section 3.3). The gain prior g is represented in the form of a standardized generative model

$$g(\xi) = \exp\left(\mathbb{F}\left[\sqrt{P_\lambda(\xi_\Lambda)}\xi_{k'} + i\sqrt{P_\phi(\xi_\Phi)}\xi_{k''} \right]\right), \tag{31}$$

where $\xi = (\xi_\Lambda, \xi_{k'}, \xi_\Phi, \xi_{k''})$ are standard normal distributed random variables, $P_\lambda(\xi_\Lambda)$ is the temporal correlation power spectrum for log amplitude gain λ, and $P_\phi(\xi_\Phi)$ is the temporal correlation power spectrum for phase gain ϕ.

As we discussed before, in `resolve`, power spectra are modeled in a non-parametric fashion. Therefore, the temporal correlation structure of the amplitude and phase gains is determined automatically from the data. In `CLEAN` self-calibration, the solution interval of the amplitude and phase gain solutions characterizes the temporal correlation. However, a fixed solution interval is chosen by the user without objective criteria; it might induce biases and create imaging artifacts from the noise in the data (Martí-Vidal & Marcaide 2008; Popkov et al. 2021). This issue can be mitigated in Bayesian self-calibration by inferring the temporal correlation kernels for amplitude and phase gains from the data.

In this paper, only the total intensity image is reconstructed. Therefore, non-diagonal terms in the visibility, which are related to linear polarization can be ignored. The visibility matrix is approximated as

$$\mathbf{V}_{ij} \approx \begin{pmatrix} R_i R_j^* & 0 \\ 0 & L_i L_j^* \end{pmatrix}. \tag{32}$$

Similarly, Stokes Q, U, and V can be ignored in the sky brightness distribution:

$$\mathbf{I}(\boldsymbol{x}) \approx \begin{pmatrix} I(\boldsymbol{x}) & 0 \\ 0 & I(\boldsymbol{x}) \end{pmatrix}. \tag{33}$$

Therefore, the visibility matrix model is

$$\tilde{\mathbf{V}}_{ij}(t) = \begin{pmatrix} g_i^R(t) & 0 \\ 0 & g_i^L(t) \end{pmatrix} B(t) \left[\mathbb{F}\begin{pmatrix} I(\boldsymbol{x}) & 0 \\ 0 & I(\boldsymbol{x}) \end{pmatrix}\right] \begin{pmatrix} g_j^R(t) & 0 \\ 0 & g_j^L(t) \end{pmatrix}^{\dagger}, \tag{34}$$

where $B(t)$ is the sampling operator (see Eq. (3)).

The visibility matrix model $\tilde{\mathbf{V}}_{ij}(t)$ can be calculated from the standardized generative sky model $I(\xi)$ and the gain model $g(\xi)$. We note that we aim to fit the model $\tilde{\mathbf{V}}_{ij}(t)$ in Eq. (34) containing the RCP and LCP gains and Stokes I image to the visibility matrix data $\mathbf{V}_{ij}$ in Eq. (32) directly in a probabilistic setup. As a result, we can perform self-calibration (gain inference) and imaging simultaneously. In the next section, we describe the variational inference algorithm we use to approximate the posterior distribution of the gain and sky parameters given the data.

3.5. Inference scheme

Bayes' theorem allows us to infer the conditional distribution of the model parameters $\xi = (\xi_\Psi, \xi_k, \xi_\Lambda, \xi_{k'}, \xi_\Phi, \xi_{k''})$, also called posterior distribution, from the observed data. From the posterior distribution of ξ, we can obtain the correlated posterior distributions with inferred correlation kernels for the sky emission $I = I(\xi)$ and the gains $G = G(\xi)$. In order to estimate the posterior distribution for the high-dimensional image reconstruction, the MGVI algorithm (Knollmüller & Enßlin 2019) is used. In MGVI, the posterior distribution $\mathcal{P}(\xi|V)$ is approximated as a multivariate Gaussian distribution $\mathscr{G}(\xi - \bar{\xi}, \Xi)$ with the inverse Fisher information metric Ξ as a covariance matrix.

The posterior distribution is obtained by minimizing the Kullback-Leibler (KL) divergence between the approximate Gaussian distribution and the true posterior distribution:

$$D_{KL}(\mathscr{G}(\xi - \bar{\xi}, \Xi) || \mathcal{P}(\xi|V)) = \int d\xi\, \mathscr{G}(\xi - \bar{\xi}, \Xi) \ln\left(\frac{\mathscr{G}(\xi - \bar{\xi}, \Xi)}{\mathcal{P}(\xi|V)} \right). \tag{35}$$

The KL divergence measures the expected information gain from the posterior distribution to the approximated Gaussian posterior distribution. By minimizing the KL divergence, we can find the closest Gaussian approximation to the true posterior distribution in the variational inference sense.

The KL divergence in the MGVI algorithm can be represented by the information Hamiltonians:

$$D_{KL} = \langle \mathcal{H}(\xi|V) \rangle_{\mathscr{G}(\xi-\bar{\xi},\Xi)} - \langle \mathcal{H}(\xi - \bar{\xi}, \Xi) \rangle_{\mathscr{G}(\xi-\bar{\xi},\Xi)}, \tag{36}$$

where $\mathcal{H}(\xi|V)$ is the posterior Hamiltonian and $\mathcal{H}(\xi - \bar{\xi}, \Xi)$ is the approximated Gaussian posterior Hamiltonian.

We can express the posterior Hamiltonian in terms of the likelihood and prior Hamiltonians (see Eq. (14)):

$$D_{KL} \cong \langle \mathcal{H}(V|\xi) + \mathcal{H}(\xi) \rangle_{\mathscr{G}(\xi-\bar{\xi},\Xi)}. \tag{37}$$

The evidence Hamiltonian $\mathcal{H}(V)$ can be ignored because it is independent of the hyperparameters for the prior model. We note that the KL divergence contains the likelihood Hamiltonian, which is equivalent to the data fidelity term (see Section 2.3), ensuring the consistency between the final image and the data.

The MGVI algorithm infers samples ξ of the normal distributed approximate posterior distribution. The posterior mean and standard deviation of the sky I and the gain G can be calculated from the samples of the normal distributed posterior distribution and those sky and gain posterior are consistent with the data. We note that MGVI allows us to capture posterior correlations between parameters ξ, although multimodality cannot be described, and the uncertainty values tend to be underestimated since it provides a local approximation of the posterior with a Gaussian (Frank et al. 2021a). In conclusion, high-dimensional image reconstruction can be performed by the MGVI algorithm by striking a balance between statistical integrity and computational efficiency. A detailed discussion is provided in Knollmüller & Enßlin (2019).

4. Image reconstruction: real data

4.1. M87 VLBA 7 mm data

To validate the Bayesian self-calibration and imaging method on the real data, we applied it to a Very Long Baseline Array (VLBA) observation of M87 in 2013 at 43 GHz (7 mm). The project code from the NRAO archive is BW098. A detailed

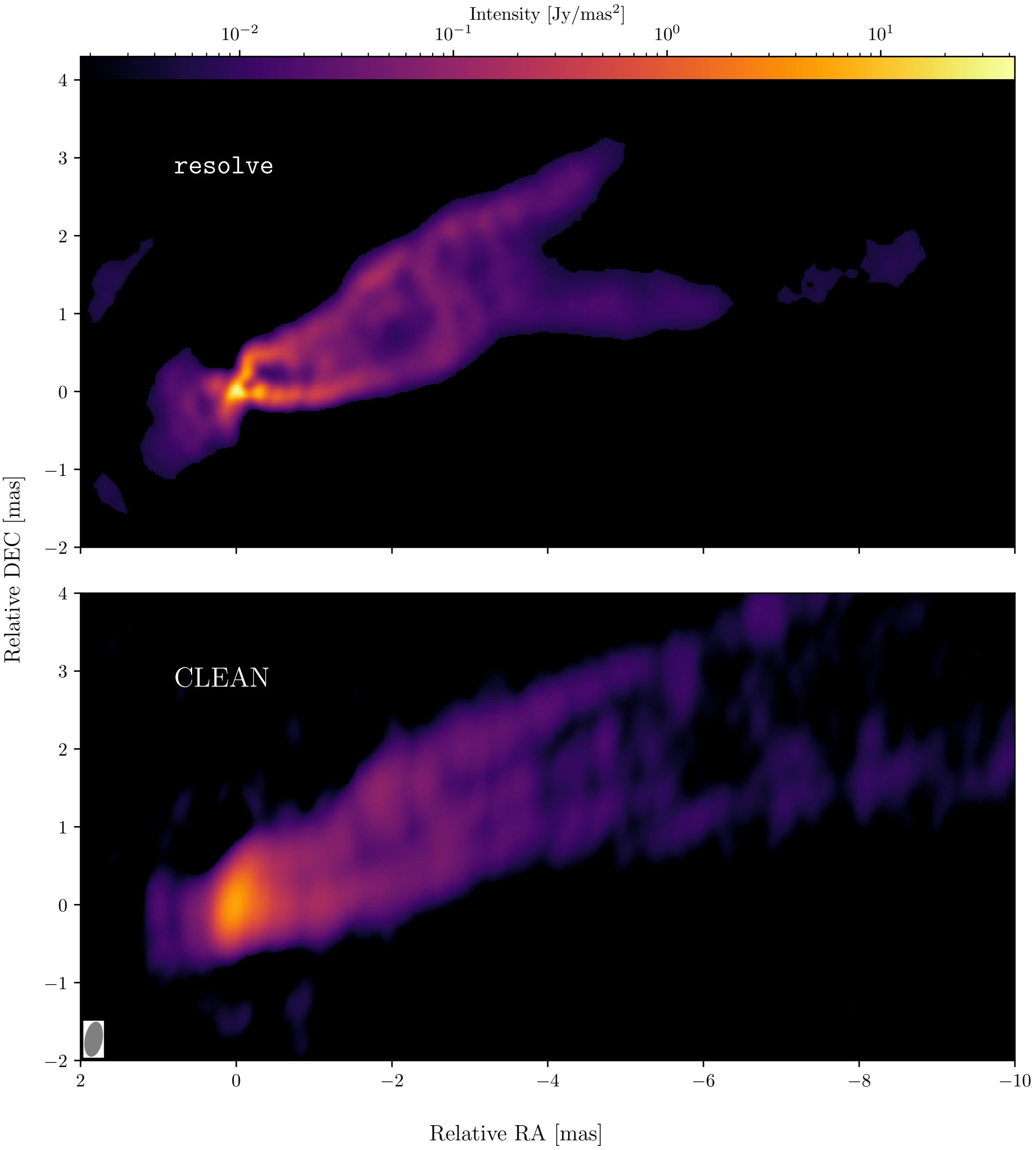

Fig. 1. M87: the posterior mean image by Bayesian self-calibration (top) and the self-calibrated `CLEAN` image (bottom) reconstructed from the same a-priori calibrated visibility data of VLBA observations at 43 GHz. In the figure, intensities higher than $3\sigma_{\mathrm{rms}}$ (root mean square) of corresponding reconstruction were shown. The image obtained by `resolve` has $I_{\mathrm{max}} = 35\,\mathrm{Jy\,mas^{-2}}$ with the noise level of $\sigma_{\mathrm{rms}} = 2\,\mathrm{mJy\,mas^{-2}}$ which is calculated from the top left empty region in the posterior mean image. The `CLEAN` image restoring beam shown in the lower-left corner is 0.5×0.2 mas, Position angle (P.A.) = −11°. The `CLEAN` image has $I_{\mathrm{max}} = 6\,\mathrm{Jy\,mas^{-2}}$ with the noise level of $\sigma_{\mathrm{rms}} = 0.6\,\mathrm{mJy\,mas^{-2}}$.

description of the project can be found in Walker et al. (2018). The M87 VLBA data are chosen because it is a full track data set and the source has complex structures and a high-dynamic range. Therefore, we are able to test the performance of the Bayesian self-calibration algorithm in order to improve the image fidelity. We used correlated raw data from the NRAO archive and complete an a-priori and signal stabilization calibration using the rPICARD pipeline (Janssen et al. 2019). All data and image fits files are archived on zenodo[5].

4.2. Reconstruction by `CLEAN`

We used `DIFMAP` (Shepherd 1997) software to reconstruct a Stokes I image using hybrid mapping in combination with super-uniform, uniform and natural weighting with a pixel size of 0.03 milliarcsecond (mas) in Figure 1. Gain solutions from `CLEAN` self-calibration are shown in Figure C.2 and Figure C.3. The resulting image corresponds to the result obtained by Walker et al. (2018). To facilitate a direct comparison with the results obtained by the `resolve` software, we convert the standard `CLEAN` image intensity unit, originally in Jy/beam, to Jy mas^{-2}. This conversion involved dividing the `CLEAN` output in Jy/beam by the beam area, which is calculated as $\frac{\pi}{4\log 2} \cdot \mathrm{BMAJ} \cdot \mathrm{BMIN}$,

---

[5] `https://zenodo.org/uploads/10190800`

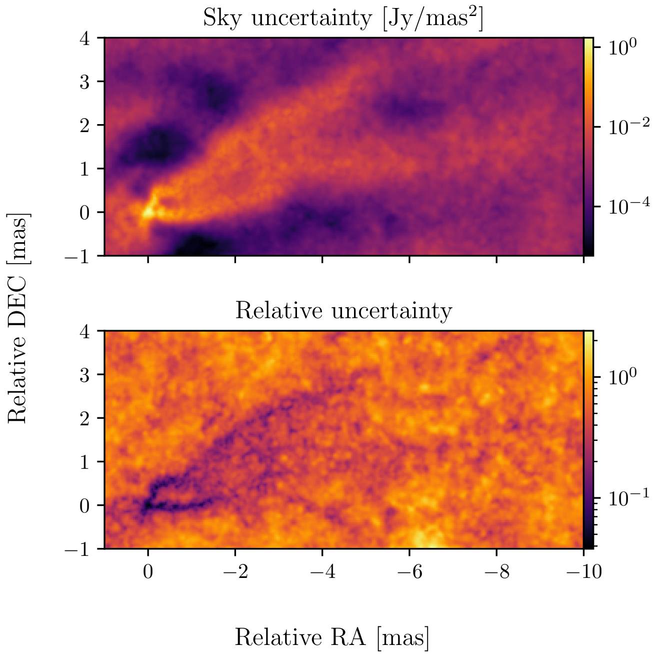

Fig. 2. M87: sky posterior pixel-wise standard deviation (top) and relative uncertainty, which is the sky posterior standard deviation normalized by the posterior mean (bottom) by `resolve` reconstruction from the top panel of Figure 1.

where BMAJ and BMIN represent the major and minor axes of the beam, respectively. The noise level σ_{rms} = 67 μJy/beam was calculated 1 arcsecond from the phase center to minimize the influence of the bright VLBI core. Since `CLEAN` uses a conventional beam size, which does not always coincide with the effective resolution of the image, we display the `CLEAN` image convolved with 0.18 mas circular beam to show the resolved high flux density region. This "over-resolved" image is presented at the bottom of Figure F.2. The image helps to compare `CLEAN` result of high flux density region with the `resolve` result.

4.3. Reconstruction by `resolve`

In Figure 1, the `resolve` posterior mean sky image is displayed. The `resolve` image is reconstructed with a spatial domain of 2048 × 1024 pixels and a field of view of 30 mas × 15 mas. The visibilities were time-averaged with a time interval of 10 seconds and frequency-averaged over 8 intermediate frequencies. For the `resolve` reconstruction, the number of data points is $\approx 1.5 \times 10^5$ (RR and LL components) and we used 20 samples for the posterior estimation. As a result, the reduced χ^2 value of the final result is 1.2, which ensures the consistency between the reconstruction results and the data. The wall-clock time for `resolve` run is 2h 40min on a single node of MPCDF Raven cluster with 20 MPI (Message Passing Interface) tasks.

In addition to the posterior mean image, the uncertainty of the image can be estimated from the sky posterior samples in `resolve`. In Figure 2, the shown relative uncertainty is the pixel-wise posterior standard deviation normalized by the sky posterior mean. We note that low relative uncertainty values are estimated in the core and limb-brightened jet regions.

During a conventional self-calibration for mm-VLBI data, low S/N data points and outliers are often flagged. However, it is often challenging to identify bad data points from data points inconsistent with the model image in self-calibration, and we therefore rely on expert's experience. Data flagging without objective criteria hinders the reproducibility of results and biased prior knowledge might be imposed in image reconstruction owing to the manual data flagging. For the `resolve` self-calibration and imaging, data were only flagged by the rPICARD pipeline during pre-calibration and not flagged manually during Bayesian self-calibration and imaging in order to minimize human interaction. In Bayesian imaging, high uncertainty in low S/N data points is taken into account naturally during image reconstruction. Therefore, high-fidelity images can be reconstructed without manual data flagging in Bayesian framework, if adequate information of the noise level is available. Three percent of the visibility amplitude was added in the visibility noise as a systematic error budget, e.g., related to the uncalibrated polarimetric leakage (Event Horizon Telescope Collaboration 2019a).

The hyperparameter setup for log-sky ψ, log amplitude gain λ, and phase gain ϕ priors is described in Appendix C. Four temporal correlation kernels (amplitude gain and the phase gain for RCP and LCP mode respectively) are inferred under the assumption that antennas from homogeneous array have similar amplitude and phase gain correlation structures per polarization mode. We chose a resolution of 7054 pixels for the temporal domain of λ and ϕ and the time interval per each pixel is 10 seconds. We note that the time interval in gains is not directly related to the solution interval in `CLEAN` self-calibration method since the correlation structure is learned from the data automatically instead of using a fixed solution interval in `resolve`. We infer gain terms with two times of the observation time interval and crop only the first half since the Fast Fourier Transforms (FFT), which assumes periodicity, is utilized. The number of pixels for gain corrections is $7054 \times 10 \times 2 \times 2 \approx 2.8 \times 10^5$ (2× observation interval × number of VLBI antennas × (phase, amplitude) × (RCP, LCP)). As a result, the degrees of freedom (DOF) for the inference are $2048 \times 1024 + 7054 \times 40 +$ power spectrum DOF $\approx 2.9 \times 10^6$.

The posterior mean and standard deviation of amplitude and phase gains per each antenna and polarization mode are shown in Figures 3 and 4. The uncertainty of the amplitude and phase gain solutions is estimated by the posterior samples. Therefore, we can quantify the reliability of the amplitude and phase gain solutions by Bayesian self-calibration method. In order to validate the result, self-calibration solutions from `CLEAN` algorithm and an RML method by `ehtim` software (Chael et al. 2018) are shown in Appendices D and E. We note that `resolve`, `CLEAN`, and `ehtim` self-calibration solutions are comparable qualitatively, although different imaging methods and minimization schemes are employed. In Figures C.2 and C.3, there is no gain solution when we do not have data (BR: 7–8 h, HN: >8 h, MK: <2 h, NL: >9 h, and SC: >7 h). Gain solutions in those time intervals cannot be constrained by the data, standard deviations of the gain amplitude in Figure 3 are therefore increased.

Figures 5 and 6 show LCP and RCP gain solutions for Los Alamos (LA) and Saint Croix (SC) antenna, respectively. The amplitude and phase gain solutions are assumed to be smooth and to not very much. The amplitude gains vary up to 20% and the phase gains deviate up to 30 degrees. Considering temporal correlation in amplitude gain and phase gain solutions for this data is reasonable because the amplitude and phase coherence time of the VLBI array at 43 GHz is higher than 10 seconds.

Figure 1 shows two image reconstructions by the `resolve` and `CLEAN`. In the `resolve` image, better resolution is achived in the core and limb-brightened regions and the counter jet is more clear than `CLEAN` image. In Figure F.2, even the over-resolve `CLEAN` image cannot achieve the high resolution comparable

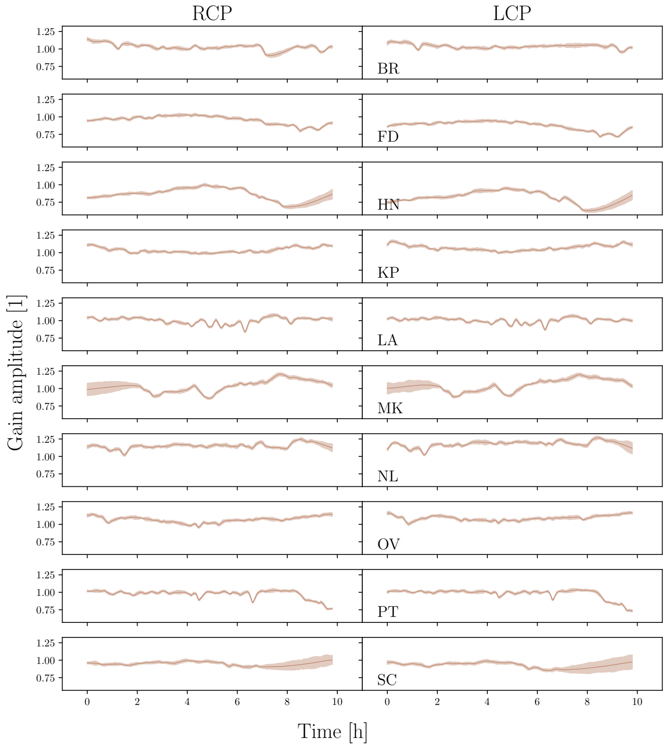

Fig. 3. M87: reconstructed posterior amplitude gains. The gain as a function of time is illustrated as a thin line with a semi-transparent standard deviation. The left and right columns of the figure show gains from the right (RCP) and left (LCP) circular polarizations correspondingly. Each row represents an individual antenna, whose abbreviated name is indicated in the bottom left corner of each LCP plot.

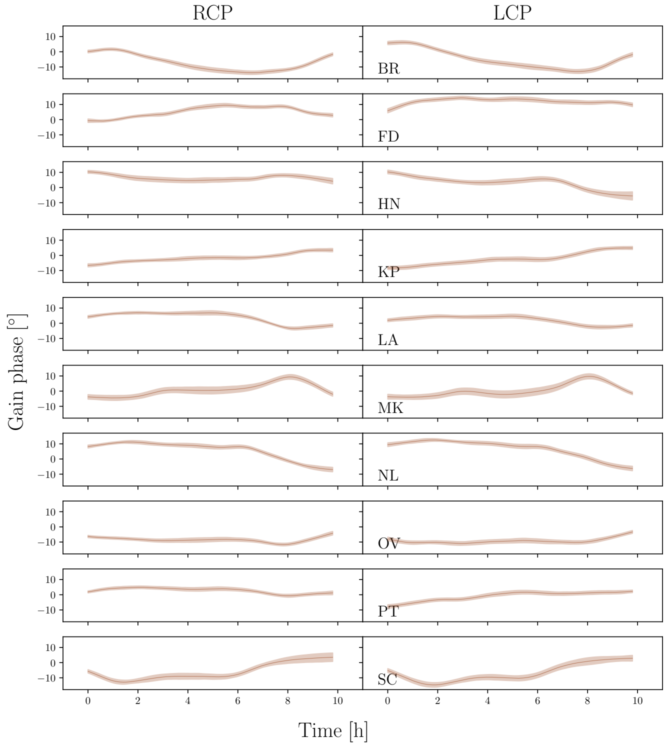

Fig. 4. M87: Reconstructed posterior phase gains. The gain as a function of time is illustrated as a thin line with a semi-transparent standard deviation. The left and right columns of the figure show gains from the right (RCP) and left (LCP) circular polarizations correspondingly. Each row represents an individual antenna, whose abbreviated name is indicated in the bottom left corner of each LCP plot.

with the `resolve` image. The extended jet emission looks more consistent in `resolve` image since the correlation structure between pixels are inferred by the Gaussian process prior with correlation kernel in `resolve`. Furthermore, the `resolve` image does not have negative flux because the positivity of the flux is enforced in the log-normal sky prior.

For the residual gain inference by `resolve`, the correlation structure between the gain solutions is inferred by the data. In other words, we do not need to choose solution interval of the gains manually but rather amplitude and phase gain solutions can be estimated by the Gaussian process prior model and more sophisticated inference scheme than the conventional `CLEAN` self-calibration. The consistency between data and the image with gain solutions is ensured since we fit the model to the data directly.

In order to obtain high-fidelity image, it is crucial to distinguish the uncertainty of gains and image from the VLBI data. From the perspective of statistical integrity, self-calibration and imaging should be performed simultaneously. Conventional iterative self-calibration estimates gain as a point and often flag outliers manually. This can impose a strong effective prior and thereby hinder proper accounting of the uncertainty information in the data. Furthermore, a variety of different images result from different ways `CLEAN` boxes are placed or different solution interval are chosen for amplitude and phase gains. Bayesian self-calibration and imaging can reduce such biases and provides reasonable uncertainty estimation of the gain solutions and image. This example with VLBA data set demonstrates that `resolve` is not only able to reconstruct images from real VLBI data but perform robust joint self-calibration and image reconstruction from sparse VLBI data set without iterative manual procedures.

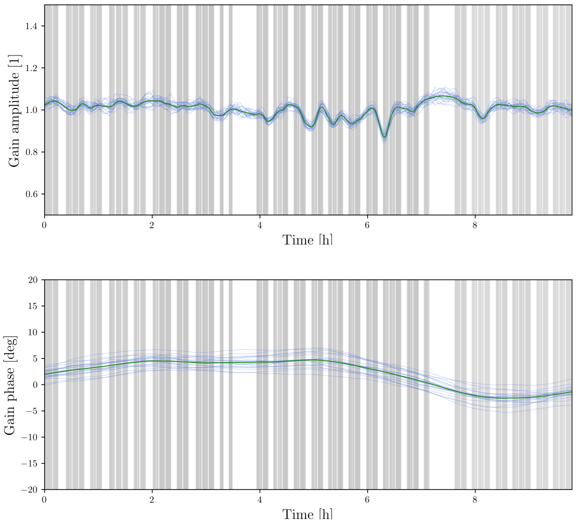

Fig. 5. M87: LCP amplitude (top) and phase (bottom) gain posterior mean and posterior samples for LA antenna by the Bayesian self-calibration. The thick green solid line represents the posterior mean value, while the thin blue solid lines depict individual samples. Grey vertical shades indicate areas with available data points.

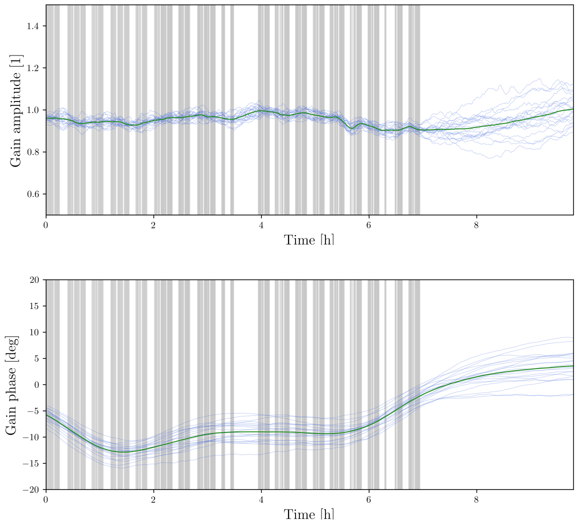

Fig. 6. M87: RCP amplitude (top) and phase (bottom) gain posterior mean and posterior samples for SC antenna by the Bayesian self-calibration. The thick green solid line represents the mean value, while the thin blue solid lines depict individual samples. Grey vertical shades indicate areas with available data points.

5. Image reconstruction: synthetic data

5.1. Synthetic data

In order to validate the method, it is crucial to test the Bayesian self-calibration algorithm by applying it to synthetic visibility data with a known ground truth image. The synthetic data test is conducted in a semi-blind way. The metadata, including *uv*-coverage, frequency, and the error associated with each visibility point, was imported from the real observation data discussed in Section 4. For the ground truth image, we chose the 15 GHz intensity image obtained by `resolve` using full-track VLBA May 2009 observations used in Nikonov et al. (2023). The ground truth image shows a great variety of scales from small and bright filaments to extended faint structures. To align the ground truth image with the real 43 GHz data, we scaled it down linearly to ensure that the jet lengths roughly correspond to each other. The resulting ground truth image is displayed in Figure 7. The *uv*-data was created from this image using `ehtim` software (Chael et al. 2019). To simulate the atmospheric, pointing and other antenna-based errors, we corrupted the data with periodic time-dependent complex antenna gains using CASA software. The periods of the gain functions for an individual antenna are defined between 1 and 12 hours to mimic inhomogeneous statistics, which is commonly found in data from inhomogeneous arrays. The degree of gain variation was chosen based on the real observations, where one can observe the change of amplitude gain approximately 20% and for the phase around 10°.

5.2. Reconstruction by `CLEAN` and `resolve`

The `CLEAN` and `resolve` images with the synthetic data are depicted in Figure 7 and sky uncertainty maps are shown in Figure 8. The iterative self-calibration and image reconstruction setup by `CLEAN` are similar to the one discussed in Section 4.2. For Bayesian self-calibration and imaging by `resolve`, the hyper parameters of the log-sky prior ψ, log-amplitude gain prior λ, and phase gain prior ϕ for the synthetic data are the same as the reconstruction for the real data (in Tables C.1 and C.2). However, for all the antenna and their polarization modes, individual temporal correlation kernels for the amplitude and phase gains were employed for the synthetic data in order to infer gain corruptions with different correlation structures.

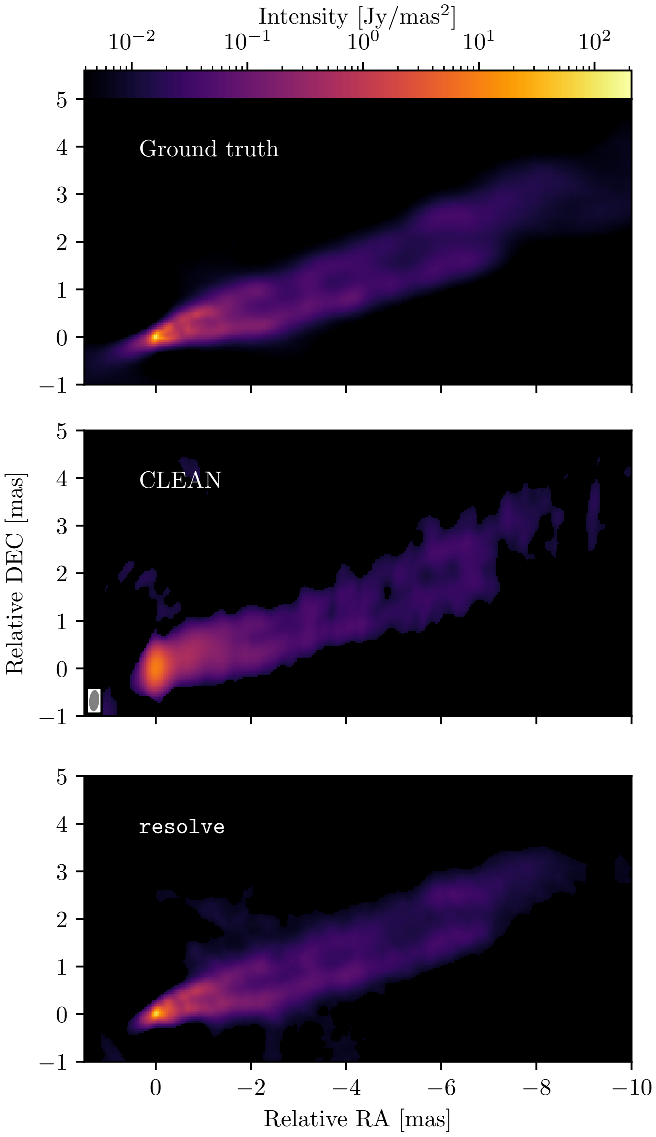

Fig. 7. Synthetic data: ground truth (top) and reconstructed images obtained using `CLEAN` (middle) and `resolve` (bottom) self-calibration. The restoring `CLEAN` beam illustrated in the bottom left corner of the plot is 0.5 × 0.2 mas, PA = −5°. All images in the figure were masked at $3\sigma_{\rm rms}$ level of a corresponding image. The unified color bar on the top of the figure shows an intensity range of the ground truth (GT) image, where maximum intensity is $I^{\rm GT}_{\rm max} = 209\,{\rm Jy\,mas^{-2}}$, the rms noise level is $\sigma^{\rm GT}_{\rm rms} = 1\,{\rm mJy\,mas^{-2}}$. The noise level of the reconstructed images are $\sigma^{\rm CLEAN}_{\rm rms} = 3\,{\rm mJy\,mas^{-2}}$, $\sigma^{\rm resolve}_{\rm rms} = 2\,{\rm mJy\,mas^{-2}}$. Maximum intensity values are $I^{\rm CLEAN}_{\rm max} = 10\,{\rm Jy\,mas^{-2}}$, $I^{\rm resolve}_{\rm max} = 111\,{\rm Jy\,mas^{-2}}$ correspondingly.

We choose a resolution of 2048 × 1024 pixels for the Stokes I image with a field of view 30 mas × 15 mas. The reduced χ^2 of the `resolve` reconstruction with the synthetic data is 0.6.

Figure 7 shows a comparison of images of ground truth, `CLEAN` reconstruction, and `resolve` reconstruction. The `CLEAN` algorithm tends to reconstruct blobby extended structure since `CLEAN` reconstructs a collection of delta components and the delta components are convolved with the `CLEAN` beam to visualize the image. Furthermore, the core region is not optimally

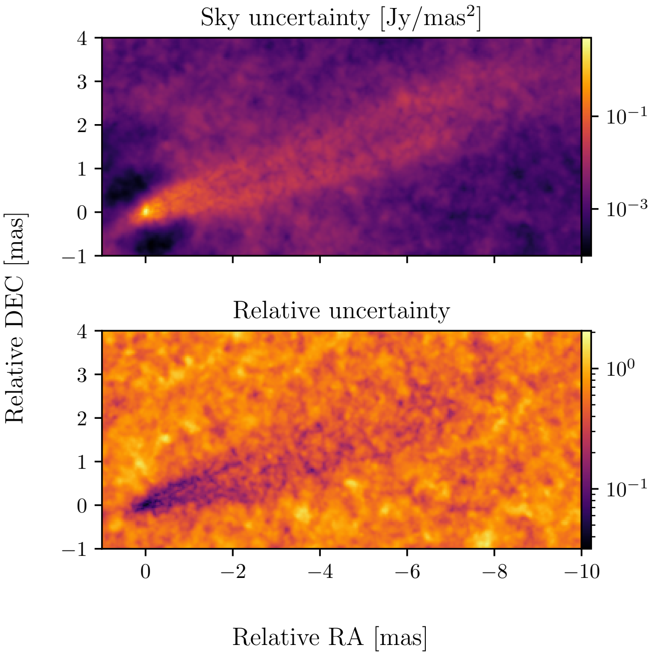

Fig. 8. Synthetic data: sky posterior pixel-wise standard deviation (top) and relative uncertainty, which is the sky posterior standard deviation normalized by the posterior mean (bottom) by `resolve` reconstruction from the bottom panel of Figure 7.

resolved even with over-resolved beam in Figure F.1. We note that multi-scale `CLEAN` might be able to recover the extended jet structure with better-resolved core, but iterative user-dependent self-calibration steps are still required in order to obtain high fidelity images. In the `resolve` image, the core and the extended jet structure in the ground truth image are recovered better than the `CLEAN` reconstruction.

The ground truth gain corruption and recovered `resolve` gain solution figures for the synthetic data are archived on zenodo[6]. The reconstructed amplitude and phase gain solutions by the Bayesian self-calibration in the time coverage with data are reasonably consistent with the ground truth.

In conclusion, this example illustrates that a high fidelity image with robust amplitude and phase gain solutions with different correlation structure can be reconstructed from the corrupted synthetic data set by the Bayesian self-calibration and imaging method. Bayesian self-calibration may be utilized for inhomogeneous arrays, such as global mm-VLBI array (GMVA) and EVN (European VLBI network) to reconstruct reliable image and gain solutions with uncertainty estimation in the future.

6. Conclusion

We have presented the Bayesian self-calibration and imaging method by `resolve` and applied it to real and synthetic VLBI data. VLBA M87 data at 43 GHz were pre-calibrated by the rPICARD CASA-based pipeline and imaging with self-calibration was performed by Bayesian imaging software `resolve`. The data flagging was done by rPICARD pipeline without manual flagging and the image and gain solutions with uncertainty estimation were reconstructed jointly in the `resolve` framework.

Self-calibration solutions by `resolve` from real data are consistent with the conventional `CLEAN` and an RML method `ehtim`, despite the fact that different imaging approaches and gain inference schemes are utilized. In Bayesian self-calibration, we do not have to choose the solution interval of gain solutions but rather the time correlation structure of the gain solutions is inferred from the data. The synthetic data test shows that the Bayesian self-calibration method is able to infer different correlation structure of gain solutions per antenna and polarization mode, which is common in inhomogeneous VLBI arrays. Furthermore, in `resolve`, the uncertainty estimation of the gain solutions and image is provided on top of the posterior mean gains and image, which is important for the scientific analysis. On the other hand, in `CLEAN` self-calibration, residual gains are estimated and removed iteratively by using the `CLEAN` reconstructed model images as prior. Therefore, inconsistencies in the CLEAN model image resulting from user choices in the manual setting of `CLEAN` windows, weighting schemes, data flagging, and solution intervals for gain solutions may introduce bias. In RML-based `ehtim` self-calibration, the model image for self-calibration is consistent with the data since the model fits the data directly. However, solution interval is still chosen manually and only a point estimate of the antenna gain temporal evolution is provided, lacking any uncertainty information on the provided gain solution.

As a result, our example with the VLBA M87 data shows that we are able to reconstruct a robust image and antenna-based gain solutions with uncertainty estimation by taking into account the uncertainty information in the data. The VLBA M87 `resolve` image has better resolved core and counter jet, and consistent extended jet emission than the one provided by the conventional `CLEAN` reconstruction. This demonstrates the potential of the proposed method also for applications to other data sets. From our perspective, future work is needed on testing Bayesian self-calibration and imaging method on more challenging VLBI data, such as from sparse and inhomogeneous antenna array, and at high frequencies, and to incorporate polarization calibration in the `resolve` framework.

Data availability

The reduced image of M87 is available at the CDS via anonymous ftp to `cdsarc.cds.unistra.fr` (`130.79.128.5`) or via `https://cdsarc.cds.unistra.fr/viz-bin/cat/J/A+A/690/A129`
Supplementary material is available at `https://zenodo.org/uploads/10190800`

Acknowledgements. We thank the anonymous referee who suggested the validation with an RML-based method and constructive comments, Jack Livingston for feedback on drafts of the manuscript, Jakob Knollmüller for discussions on resolve software and feedback, Thomas Krichbaum and Martin Shepherd for discussions on `CLEAN` algorithm and `DIFMAP` software. J.K. and A.N. received financial support for this research from the International Max Planck Research School (IMPRS) for Astronomy and Astrophysics at the Universities of Bonn and Cologne. This work was supported by the M2FINDERS project funded by the European Research Council (ERC) under the European Union's Horizon 2020 Research and Innovation Programme (Grant Agreement No. 101018682). J.R. acknowledges financial support from the German Federal Ministry of Education and Research (BMBF) under grant 05A23WO1 (Verbundprojekt D-MeerKAT III). P.A. acknowledges financial support from the German Federal Ministry of Education and Research (BMBF) under grant 05A20W01 (Verbundprojekt D-MeerKAT). The National Radio Astronomy Observatory is a facility of the National Science Foundation operated under cooperative agreement by Associated Universities, Inc.

References

Akiyama, K., Ikeda, S., Pleau, M., et al. 2017, AJ, 153, 159
Arras, P., Baltac, M., Ensslin, T. A., et al. 2019a, NIFTy5: Numerical Information Field Theory v5, Astrophysics Source Code Library [record `ascl:1903.008`]

---

[6] `https://zenodo.org/uploads/10190800`

Arras, P., Frank, P., Leike, R., Westermann, R., & Enßlin, T. A. 2019b, A&A, 627, A134
Arras, P., Bester, H. L., Perley, R. A., et al. 2021, A&A, 646, A84
Arras, P., Frank, P., Haim, P., et al. 2022, Nat. Astron., 6, 259
Blei, D. M., Kucukelbir, A., & McAuliffe, J. D. 2016, arXiv e-prints [arXiv:1601.00670]
Broderick, A. E., Gold, R., Karami, M., et al. 2020, ApJ, 897, 139
Brogan, C. L., Hunter, T. R., & Fomalont, E. B. 2018, arXiv e-prints [arXiv:1805.05266]
Carrillo, R. E., McEwen, J. D., & Wiaux, Y. 2012, MNRAS, 426, 1223
Chael, A. A., Johnson, M. D., Bouman, K. L., et al. 2018, ApJ, 857, 23
Chael, A. A., Bouman, K. L., Johnson, M. D., et al. 2019, ehtim: Imaging, analysis, and simulation software for radio interferometry, Astrophysics Source Code Library [record ascl:1904.004]
Clark, B. G. 1980, A&A, 89, 377
Cornwell, T. J. 2008, IEEE J. Sel. Top. Signal Process., 2, 793
Cornwell, T. J., & Evans, K. F. 1985, A&A, 143, 77
Cornwell, T. J., & Wilkinson, P. N. 1981, MNRAS, 196, 1067
Dabbech, A., Repetti, A., Perley, R. A., Smirnov, O. M., & Wiaux, Y. 2021, MNRAS, 506, 4855
Enßlin, T. A. 2019, Ann. Phys., 531, 1800127
Enßlin, T. A., & Frommert, M. 2011, Phys. Rev. D, 83, 105014
Event Horizon Telescope Collaboration (Akiyama, K., et al.) 2019a, ApJ, 875, L3
Event Horizon Telescope Collaboration (Akiyama, K., et al.) 2019b, ApJ, 875, L4
Event Horizon Telescope Collaboration (Akiyama, K., et al.) 2024, A&A, 681, A79
Frank, P., Leike, R., & Enßlin, T. A. 2021a, Ann. Phys., 533, 2000486
Frank, P., Leike, R., & Enßlin, T. A. 2021b, Entropy, 23, 853
Fuentes, A., Gómez, J. L., Martí, J. M., et al. 2023, Nat. Astron., 7, 1359
Hamaker, J. P., Bregman, J. D., & Sault, R. J. 1996, A&AS, 117, 137
Högbom, J. A. 1974, A&AS, 15, 417
Janssen, M., Goddi, C., van Bemmel, I. M., et al. 2019, A&A, 626, A75
Janssen, M., Radcliffe, J. F., & Wagner, J. 2022, Universe, 8, 527
Junklewitz, H., Bell, M. R., & Enßlin, T. 2015, A&A, 581, A59
Junklewitz, H., Bell, M. R., Selig, M., & Enßlin, T. A. 2016, A&A, 586, A76
Khinchin, A. 1934, Math. Ann., 109, 604
Knollmüller, J., & Enßlin, T. A. 2018, arXiv e-prints [arXiv:1812.04403]
Knollmüller, J., & Enßlin, T. A. 2019, arXiv e-prints [arXiv:1901.11033]
Kosogorov, N. A., Kovalev, Y. Y., Perucho, M., & Kovalev, Y. A. 2024, MNRAS, 528, 1697
Martí-Vidal, I., & Marcaide, J. M. 2008, A&A, 480, 289
Müller, H., & Lobanov, A. P. 2022, A&A, 666, A137
Müller, H., Mus, A., & Lobanov, A. 2023, A&A, 675, A60
Müller, H., Massa, P., Mus, A., Kim, J.-S., & Perracchione, E. 2024, A&A, 684, A47
Mus, A., Müller, H., & Lobanov, A. 2024, A&A, 688, A100
Narayan, R., & Nityananda, R. 1986, ARA&A, 24, 127
Nikonov, A. S., Kovalev, Y. Y., Kravchenko, E. V., Pashchenko, I. N., & Lobanov, A. P. 2023, MNRAS, 526, 5949
Paraschos, G. F., Debbrecht, L. C., Kramer, J. A., et al. 2024, A&A, 686, L5
Pashchenko, I. N., Kravchenko, E. V., Nokhrina, E. E., & Nikonov, A. S. 2023, MNRAS, 523, 1247
Popkov, A. V., Kovalev, Y. Y., Petrov, L. Y., & Kovalev, Y. A. 2021, AJ, 161, 88
Roth, J., Arras, P., Reinecke, M., et al. 2023, A&A, 678, A177
Shepherd, M. C. 1997, in Astronomical Society of the Pacific Conference Series, 125, Astronomical Data Analysis Software and Systems VI, eds. G. Hunt, & H. Payne, 77
Smirnov, O. M. 2011, A&A, 527, A106
Taylor, G. B., Carilli, C. L., & Perley, R. A. 1999, Astronomical Society of the Pacific Conference Series, 180, Synthesis Imaging in Radio Astronomy II
Terris, M., Dabbech, A., Tang, C., & Wiaux, Y. 2023, MNRAS, 518, 604
The Event Horizon Telescope Collaboration 2023, arXiv e-prints [arXiv:2311.09479]
Thompson, A. R., Moran, J. M., & Swenson, George W., J. 2017, Interferometry and Synthesis in Radio Astronomy, 3rd edn (Springer Cham)
Tiede, P. 2022, J. Open Source Softw., 7, 4457
Walker, R. C., Hardee, P. E., Davies, F. B., Ly, C., & Junor, W. 2018, ApJ, 855, 128
Wiaux, Y., Jacques, L., Puy, G., Scaife, A. M. M., & Vandergheynst, P. 2009, MNRAS, 395, 1733
Wiener, H. 1949, Extrapolation, Interpolation, and Smoothing of Stationary Time Series, with Engineering Applications (MIT Press)
Wilber, A. G., Dabbech, A., Jackson, A., & Wiaux, Y. 2023, MNRAS, 522, 5558
Zhao, G.-Y., Gómez, J. L., Fuentes, A., et al. 2022, ApJ, 932, 72

Appendix A: Weighting scheme in `resolve`

The statistics of the posterior sky distribution determined by Bayesian inference has some analogy to robust weighting in the `CLEAN` algorithm. The posterior distribution will include Fourier scales with high signal-to-noise, while Fourier scales with low signal-to-noise will be damped with the signal-to-noise ratio. This has some analogy to the `CLEAN` algorithm with robust weighting where Fourier scales with high signal-to-noise are uniformly weighted and scales with low signal-to-noise are weighted naturally. Nevertheless, in contrast to the `CLEAN` algorithm, this behavior of the resulting sky reconstruction is intrinsic to Bayesian inference or other methods following some form of regularized maximum likelihood approach.

In the appendix A.4 of Junklewitz et al. (2016), this analogy between robust weighting in `CLEAN` and the posterior obtained from Bayesian inference was made more explicit. More specifically, Junklewitz et al. (2016) derived the Bayesian Wiener Filter operation for estimating sky brightness, finding that it takes the same mathematical form of robust weighting when expressed in Fourier space. Thereby the robust parameter, which in the case of `CLEAN` needs to be chosen by the user is determined by the prior distribution for the sky brightness.

Appendix B: Bayesian perspective on regularized maximum likelihood (RML) method

In this subsection, we aim to investigate the RML method from a Bayesian perspective. In the RML method, an objective function $J(d, s)$ is to be minimized w.r.t. to the unknown signal s. Therefore, the RML estimator is

$$s_{\mathrm{RML}} := \mathrm{argmin}_s J(d, s). \tag{B.1}$$

The objective function consists of a data fidelity term $\chi^2(d, s)$ and a regularizing term $r(s, \beta)$ that should prevent irregular solutions (Chael et al. 2018):

$$J(d, s) = \chi^2(d, s) + r(s, \beta), \tag{B.2}$$

where β denotes the set of parameters the regularizer might depend on, including a potential parameter determining the relative weight of the regularization w.r.t. the data fidelity term.

The data fidelity term $\chi^2(d, s)$ is equivalent to the likelihood Hamiltonian $\mathcal{H}(d|s)$ in Bayesian inference up to irrelevant additive and multiplicative constants (see Eq. 12). In other words, the data fidelity term is the negavie log likelihood $\chi^2(d, s) = -\ln \mathcal{P}(d|s) + \mathrm{const.}$. It is natural to regard the regularizing term $r(s, \beta)$ as the negative log prior $r(s, \beta) = -\ln \mathcal{P}(s|\beta) + \mathrm{const.}$. In this case, the RML estimator would be identical to the Bayesian maximum a posteriori (MAP) estimator for the corresponding signal prior $\mathcal{P}(s|\beta)$, with fixed hyperparameters β.

Therefore, RML method can be regarded as Bayesian methods in which the regularizing term $r(s, \beta)$ specifies the prior assumption on the signal and that exploits the MAP approximation. From this perspective, the regularization terms can be translated into prior assumptions, via

$$\mathcal{P}(s|\beta) = e^{-\mathcal{H}(s|\beta)} \equiv \frac{e^{-r(s,\beta)}}{\int \mathcal{D}s\, e^{-r(s,\beta)}}. \tag{B.3}$$

Here, the denominator in the last expression ensures proper normalization and would be essential to a Bayesian determination of the parameters β of the regularizer, which, however, is usually done in RML practice by trial and error and visual inspection of the results. We note that Müller et al. (2023) employed the genetic algorithm in order to automate the parameter β selection.

In RML methods, several regularizers are often combined in order to encode different prior knowledge about the source. Let us therefore revisit some of the commonly used regularizers in RML methods, such as the entropy, total variation (TV), and total squared variation (TSV) regularization and interpretation from the Bayesian perspective:

Entropy regularization of a discretized intensity field $s(x, y) = I(x, y)$, with $x, y \in \mathbb{Z}$, is given by

$$r_{\mathrm{entropy}}(I, \beta) = T \sum_{x,y} I_{x,y} \ln \frac{I_{x,y}}{M_{x,y}}\,, \tag{B.4}$$

with $\beta = (T, M)$ consisting of a "temperature" T that determines the strength of the regularization and a reference image M, with respect to which this relative entropy like expression is evaluated. Converting this to a prior according to Eq. B.3 yields

$$\mathcal{P}(I|\beta) \propto e^{-T \sum_{x,y} I_{x,y} \ln \frac{I_{x,y}}{M_{x,y}}} = \prod_{x,y} e^{-T\, I_{x,y} \ln \frac{I_{x,y}}{M_{x,y}}}$$
$$= \prod_{x,y} \left(\frac{I_{x,y}}{M_{x,y}}\right)^{-T\, I_{x,y}} =: \prod_{x,y} \mathcal{P}(I_{x,y}|\beta). \tag{B.5}$$

This means that all pixels are assumed to be uncorrelated, since the prior is a direct product of individual pixel priors

$$\mathcal{P}(I_{x,y}|\beta) \propto \left(\frac{I_{x,y}}{M_{x,y}}\right)^{-T\, I_{x,y}}. \tag{B.6}$$

These assign nearly constant probabilities for any flux value for which $I_{x,y} \ll 1/T$ and a sharper than exponential cut off of the prior probabilities for intensities beyond $I_{x,y} = 1/T$. High flux values are therefore strongly suppressed by the entropy regularizer as was already pointed out by (Junklewitz et al. 2016).

Here, we would like to point out in addition to this that the reference image has a very mild effect on the results, as this super exponential cut off is fully determined by T. Approximately, the entropy regularization therefore corresponds to assuming the intensity field to be white noise with values roughly uniformly distributed between 0 and $1/T$. For these reasons, the entropy RML is not expected to provide improved images for most radio astronomical observations of diffuse sources. The reputation of the entropy RML method to produce smooth images results probably from the usage of a large T parameter, which strongly discourages extreme brightnesses and therefore encourages the neighboring pixel of a strong flux location to explain the flux of that. A good feature of the entropy RML method is, however, that negative intensities are excluded by it a priori.

The **total squared variation regularization**

$$r_{\mathrm{TSV}}(I, \beta) = \alpha \sum_{x,y} \left[\left(I_{x+1,y} - I_{x,y}\right)^2 + \left(I_{x,y+1} - I_{x,y}\right)^2 \right], \tag{B.7}$$

can be regarded in the continuum limit as requesting intensity gradients to be minimal

$$r_{\mathrm{TSV}}(I, \beta) \equiv \alpha' \int dx \int dy \left[\left(\frac{\partial I(x, y)}{\partial x}\right)^2 + \left(\frac{\partial I(x, y)}{\partial y}\right)^2 \right] \tag{B.8}$$
$$= \alpha' \int dx \int dy\, |\nabla I(x, y)|^2\,, \tag{B.9}$$

where $\beta = \alpha$ in the discrete case and $\beta = \alpha'$ in the corresponding continuum case determine the strength of the regularization.

The total squared variation regularization corresponds certainly to a more appropriate prior for diffuse emission, as it couples nearby locations and enforces some smoothness of the reconstruction.

This regularization actually becomes diagonal in Fourier space, with

$$r_{\rm TSV}(I,\beta) = \alpha' \int \frac{dk^2}{(2\pi)^2}\, |\boldsymbol{k} I(\boldsymbol{k})|^2 \,. \tag{B.10}$$

This turns out to be exactly (up to negligible additive terms) the log prior of a statistical homogeneous and isotropic Gaussian random field

$$\mathcal{G}(I, P_I(k)) \propto \exp\left(-\frac{1}{2}\int \frac{dk^2}{(2\pi)^2} \frac{|I(\boldsymbol{k})|^2}{P_I(k)}\right), \tag{B.11}$$

with an intensity power spectrum

$$P_I(k) = \frac{1}{2\alpha'}\, k^{-2} \,. \tag{B.12}$$

In one dimension, a Gaussian process with such a power spectrum would be equivalent to a Wiener process, which is known to produce continuous, but rough structures.

Changing to the **total variation regularizer**, in the continuum representation written as

$$r_{\rm TV}(I,\beta) \equiv \alpha' \int dx \int dy\, |\nabla I(x,y)| \,, \tag{B.13}$$

enhances the tendency to allow rough structures, but it favors roughness to be more localized. This is because the L_1 norm underlying the TV regularizer is more tolerant to few large intensity gradients and the L_2 norm underlying the TSV regularizer instead prefers many, smaller gradients. We note that the TSV regularizer does not have a simple Fourier space representation. Both, TV and TSV, regularizers are utilized to consider the correlation between neighboring pixels. However, they do not enforce the positivity of the sky intensity and tend to generate rough structures.

Appendix C: Hyperparameter setup for sky and gain priors

Table C.1. Hyper parameters for the log-sky prior ψ.

	ψ mean	ψ std
Offset	35	—
Zero mode variance	1	0.1
Fluctuations	3	1
Flexibility	1.2	0.4
Asperity	0.4	0.4
Average slope	-3	1

Notes. All hyperparameters are unitless. Detailed description of each parameter can be found in Section 3.4 of Arras et al. (2021).

The hyperparameter setup for the log-sky prior ψ is listed in Table C.1. The offset mean represents the mean value of the log-sky ψ; thus the mean of prior sky model $\exp(\psi)$ is $\exp(35) \approx 10^{15}$ Jy/sr ($\approx 10^{-2}$ Jy/mas^2). The value is allowed to vary two e-folds up and down in one standard deviation (std) of the prior. The zero mode variance mean describes the standard deviation of the offset and its standard deviation is therefore the standard deviation of the offset standard deviation.

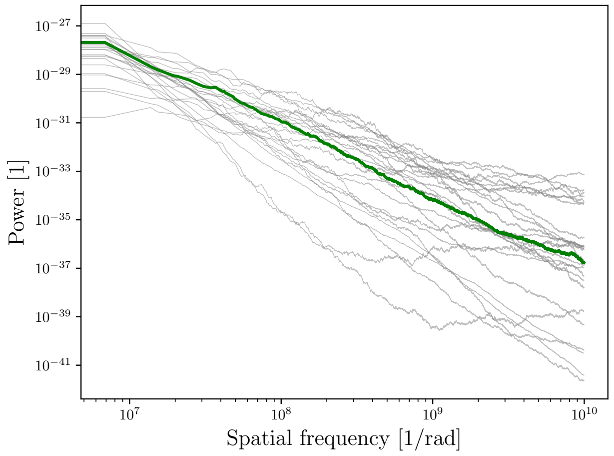

Fig. C.1. M87: posterior and prior power spectra of logarithmic sky brightness distribution ψ. The green line denotes posterior mean power spectrum; grey lines denote prior power spectrum samples.

Table C.2. Hyper parameters for the log-amplitude gain prior λ and the phase gain prior ϕ.

	λ mean	λ std	ϕ mean	ϕ std
Offset	0	—	0	—
Zero mode variance	0.2	0.1	1e-3	1e-6
Fluctuations	0.2	0.1	0.2	0.1
Flexibility	0.5	0.2	0.5	0.2
Asperity	None	None	None	None
Average slope	-3	1	-3	1

Notes. All hyperparameters are unitless. Detailed description of each parameter can be found in Section 3.4 of Arras et al. (2021).

The next four hyperparameters are model parameters for the spatial correlation power spectrum $P_\Psi(\xi_\Psi)$ in Eq. 24. The posterior and prior power spectra of the log-sky ψ are in Figure C.1. The average slope mean and std denote the mean and standard deviation of the slope for amplitude spectrum, which is the square root of the power spectrum. In Figure C.1, the prior power spectrum samples (grey lines) follow a power law with slope mean -6 and standard deviation 2. A steep prior power spectrum is chosen to suppress small scale structure in the early self-calibration stages. This prevents imprinting imaging artifacts from the noise to the final image. A relatively high standard deviation of the power spectrum is chosen to ensure flexibility of the prior model. Fluctuations and flexibility are non-trivial hyperparameters controlling the Wiener process and integrated Wiener process in the model, which determine fluctuation and flexibility of the power spectrum in a nonparametric fashion. Nonzero asperity can generate periodic patterns in the image. Thus, we used relatively small asperity parameters for our log-sky model ψ. We note that the power spectrum model is flexible enough to capture different correlation structures. As a result, the flexibility of the prior model can reduce biases from strong prior assumptions.

For the self-calibration of the real data (see Section 4.3), four temporal correlation kernels (amplitude gain and the phase gain for RCP and LCP mode respectively) are inferred under the assumption that antennas from homogeneous array have similar

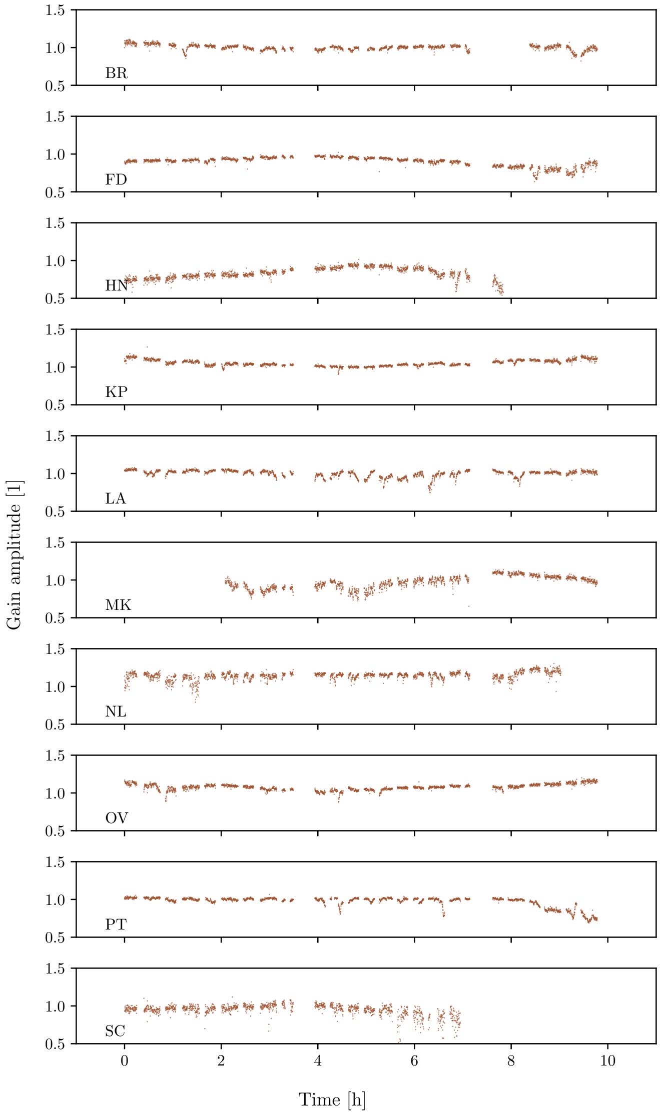

Fig. C.2. Real data: Amplitude gain solutions by the `CLEAN` self-calibration method.

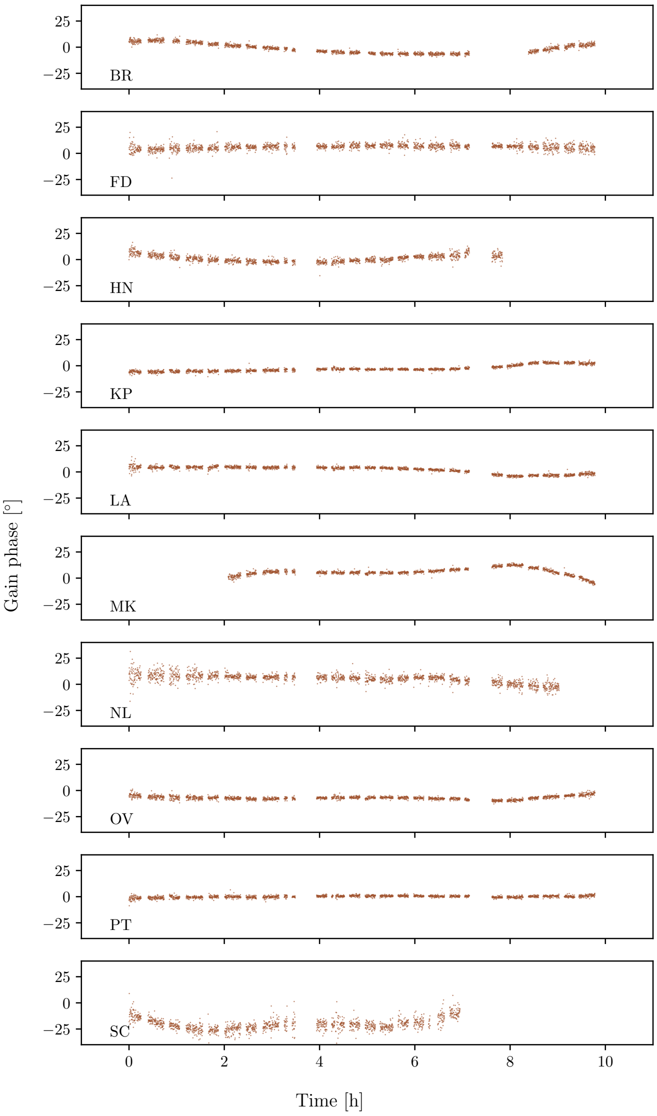

Fig. C.3. Real data: Phase gain solutions by the `CLEAN` self-calibration method.

amplitude and phase gain correlation structures per polarization mode. For the self-calibration of the synthetic data (see Section 5.2), 40 individual temporal correlation kernels for the amplitude and phase gains are inferred, one per antenna and polarization mode, as the ground truth gain corruptions were generated with individual correlation structures. The mean of the amplitude gain prior model is obtained by exponentiating the offset mean of λ, which is $\exp(0) = 1$ and the mean of the phase gain prior model is the offset mean of ϕ, which is 0 radians. Model parameters for the zero mode variance, fluctuations, and flexibility are chosen to be small to suppress extremely high gain corrections. Asperity mean and std hyper parameters are set to None since the gain solutions are not periodic. The average slope mean is -3 for log-amplitude and phase gain, therefore the slope mean for the power spectrum is -6 with the standard deviataion 2. The broad range of the average slope parameter allows the prior model to describe different temporal correlation structures. As a result, the gain prior model is flexible enough to learn the temporal correlation structure from the data automatically. More details about prior model parameters are explained in Arras et al. (2021).

Appendix D: `CLEAN` self-calibration solutions: real data

Figure C.2 and Figure C.3 show the `CLEAN` self-calibration solutions for the real VLBI M87 data at 43GHz by DIFMAP software. One amplitude and one phase gain solution per each antenna are obtained because `CLEAN` image in Figure 1 is produced by the Stokes I data averaging the RR and LL components. Since the Stokes V emission is negligible in the data, `resolve` gain solutions for RCP and LCP are very similar in Figure 3 and Figure 4. Therefore, a high-fidelity total intensity image can be reconstructed by estimating one gain solution per each antenna in `CLEAN` self-calibration.

We can compare self-calibration solutions from `CLEAN` and `resolve`. The gain solutions from `CLEAN` and `resolve` with scans are consistent qualitatively. As an example, the abrupt variation of the `resolve` gain amplitude for LA antenna (6h - 6.5h) in Figure 5 is due to the discrepancy of amplitude between scans. Figure C.2 shows a similar behavior in the `CLEAN` gain amplitude for LA antenna (6h - 6.5h). We note that the data were flagged manually during `CLEAN` self-calibration. Outliers

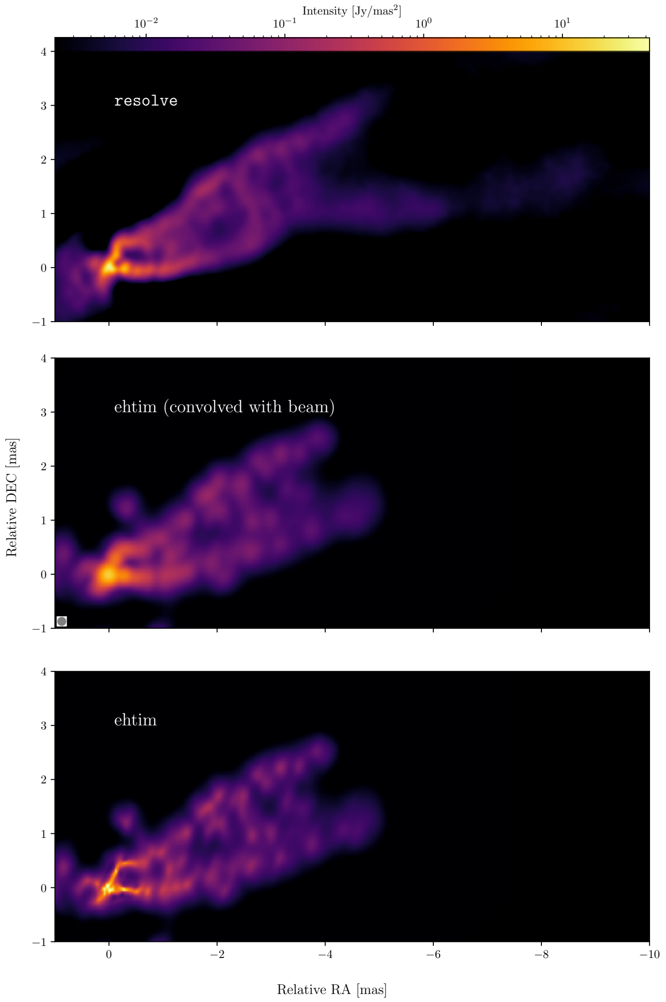

Fig. E.1. Real data: `resolve` image (top), `ehtim` image convolved with the beam (0.167mas × 0.167mas, middle), and `ehtim` image (bottom). The beam-convolved `ehtim` image (middle) has $I_{\max}$ = 14 Jy mas^{-2} and `ehtim` image (bottom) has $I_{\max}$ = 73 Jy mas^{-2}.

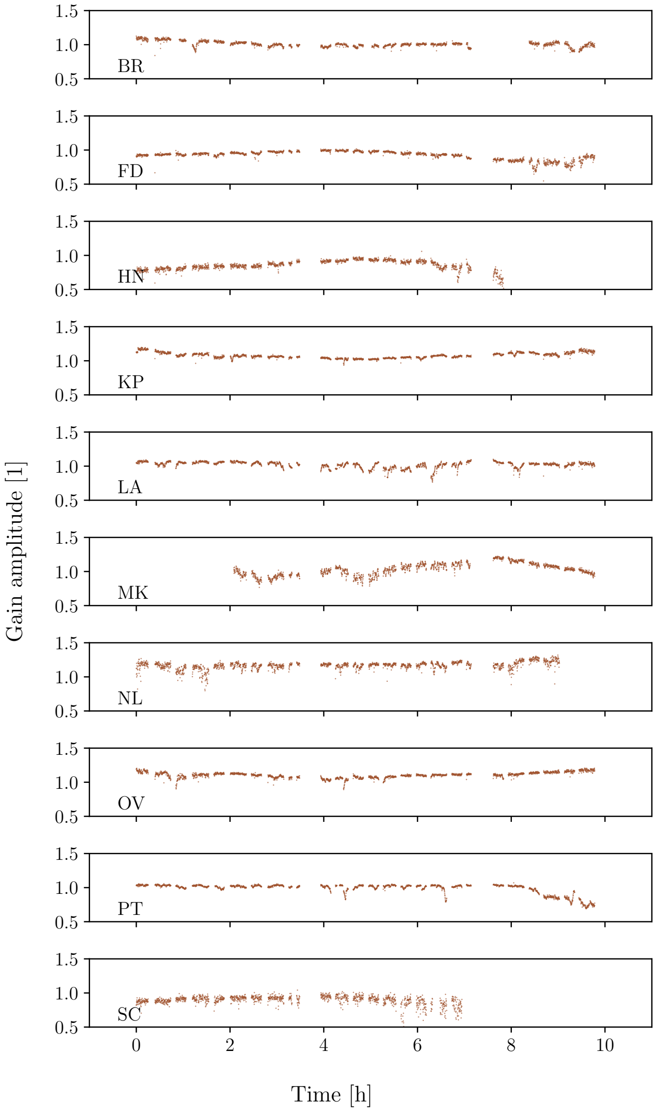

Fig. E.2. Real data: Amplitude gain solutions by the `ehtim` self-calibration method.

are often flagged during iterative `CLEAN` self-calibration and the data flagging relies on user's experience. On the other hand, in `resolve` self-calibration, the whole data after pre-calibration are used for imaging without manual flagging.

Appendix E: `ehtim` image and self-calibration solutions: real data

`ehtim` (Chael et al. 2018) is a widely used RML imaging software for VLBI data, e.g. by the Event Horizon Telescope at 230 GHz (e.g. Event Horizon Telescope Collaboration 2019b; The Event Horizon Telescope Collaboration 2023; Event Horizon Telescope Collaboration 2024), for observations with the global Millimeter VLBI Array (GMVA) at 86 GHz (e.g. Zhao et al. 2022), observations with European VLBI network (EVN), the Very Long Baseline Array (VLBA), and the space VLBI mission RadioAstron at smaller frequencies (e.g. recently Kosogorov et al. 2024; Paraschos et al. 2024; Fuentes et al. 2023), and even for related inverse problems outside of radio astronomy (Müller et al. 2024). To validate the `resolve` self-calibration and imaging method, we compare it to RML self-calibration and imaging performed by `ehtim`. The comparison of `resolve` and `ehtim` image is shown in Figure E.1. `ehtim` minimizes a weighted sum of data terms (chosen to be χ^2-terms based on visibilities), and regularization terms (entropy, TV, TSV, l_1-norm, total flux constraint). To navigate this large number of parameters, usually either a parameter survey (e.g. Event Horizon Telescope Collaboration 2019b; Fuentes et al. 2023) or metaheuristics (Müller et al. 2023; Mus et al. 2024) are applied to `ehtim`. Performing a full exploration of the parameter space would exceed the scope of this comparison. Hence, for this work, we rather chose the regularization weights by manual exploration to the best of our efforts.

In `ehtim`, the self-calibration procedure is similar to `CLEAN` self-calibration. First, a model image is reconstructed by the given data. Second, residual gains are estimated by minimizing a cost function (Eq. 18) based on the Fourier components of the model image. Then new data are generated by removing the estimated residual gain corruption. These procedures are continued iteratively until the desired image quality is achieved. In contrast to the `CLEAN` self-calibration, the model images computed by `ehtim` can be consistent with data since the model fits the data directly in the visibility domain.

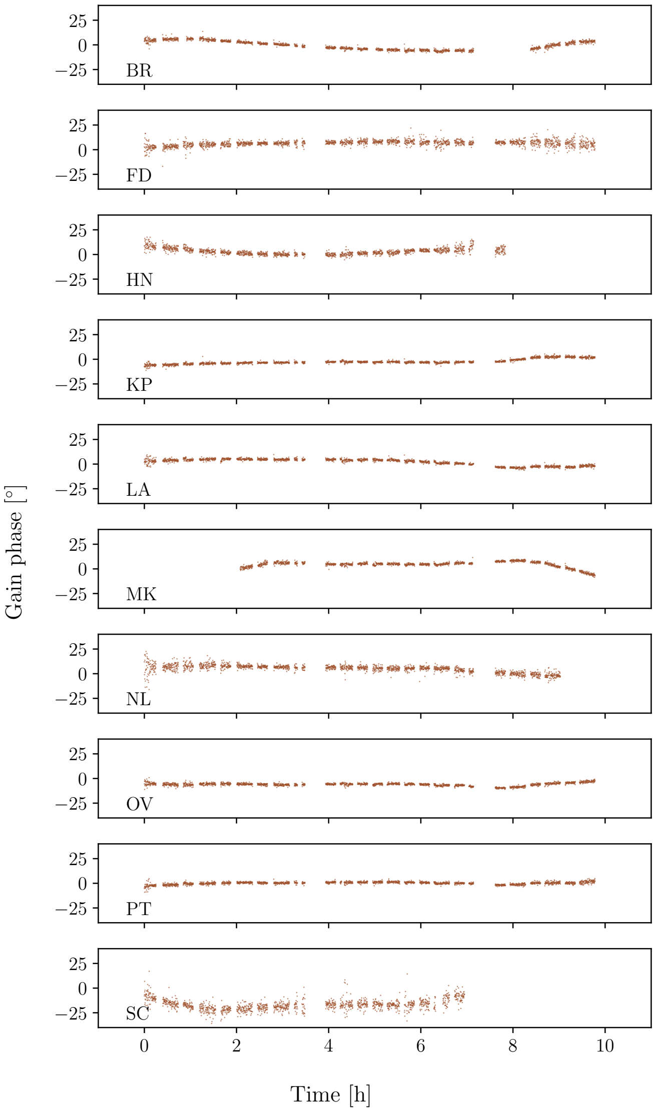

Fig. E.3. Real data: Phase gain solutions by the `ehtim` self-calibration method.

The `ehtim` image in Figure E.1 achieves better resolution compared to `CLEAN` image in Figure 1. The core regions show even sharper edge-brightening and counter jet than `resolve` image. However, the image contains sharper artifacts in the core region and the extended jet emission looks discontinuous. Therefore, we convolved `ehtim` image with the beam (0.167mas × 0.167mas) to show an image at a conservative resolution. The core, counter jet, and extended jet emission in `resolve` and beam-convolved `ehtim` images look consistent. We note that the smoothness of the image is enforced by the TV and TSV regularizers in `ehtim` reconstruction. However, since TV and TSV regularizers tend to produce rough structures (see Appendix B), these regularizers may not be optimal for recovering extended jet emission as `ehtim` was developed for the high-resolution reconstruction of compact emission. It has been demonstrated in the past that the use of extended basis functions, rather than regularizers acting in the pixel basis, may offer an advantage for these cases in RML methods (see the SARA family Carrillo et al. 2012; Terris et al. 2023; Wilber et al. 2023).

Figure E.2 and Figure E.3 show the amplitude and phase gain solutions by `ehtim` self-calibration. Self-calibration by `ehtim` is performed alternating with the deconvolution. For the self-calibration of real M87 data, no temporal correlation between gain solutions is considered and small gain tolerance of (0.01, 0.05) is used to correct the gain incrementally. This means that both, gains smaller than 0.01 and larger than 0.05, are disfavored by the prior. We detect gain phase and amplitude trends that are consistent with the results obtained with `resolve` and `CLEAN`.

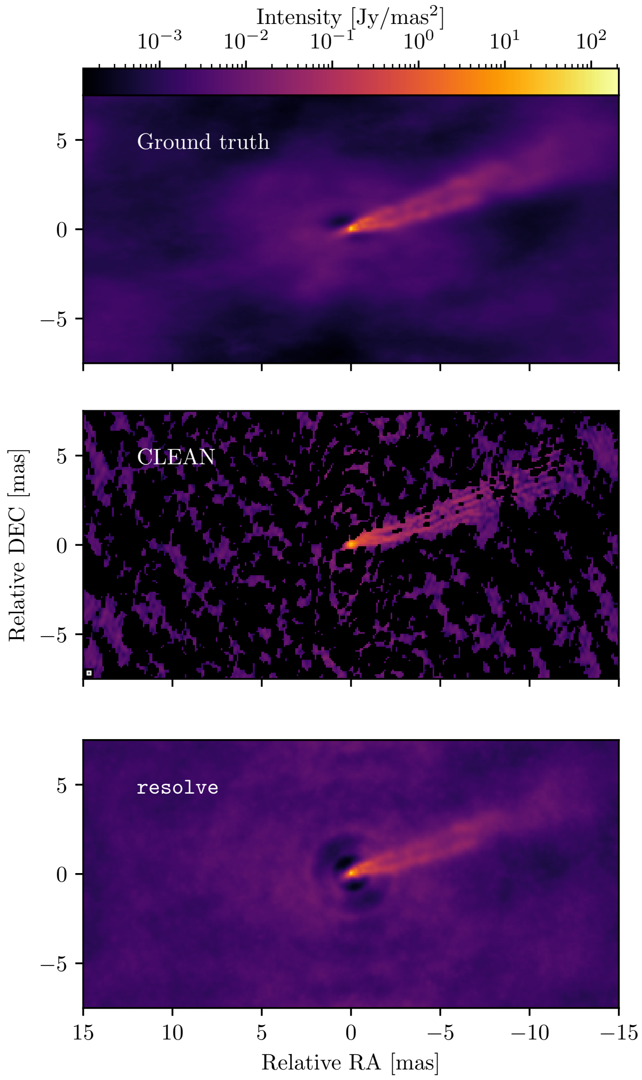

Fig. F.1. Synthetic data: ground truth (top) and reconstructed images obtained using `CLEAN` (middle) and `resolve` (bottom) self-calibration. The circular 0.15 mas `CLEAN` beam is illustrated in the bottom left corner of the plot. The `CLEAN` image was masked at the lowest positive value. The unified color bar on the top of the figure shows an intensity range of the ground truth image, where maximum intensity is $I^{\mathrm{GT}}_{\mathrm{max}} = 209\,\mathrm{Jy\,mas^{-2}}$, the minimum value is $I^{\mathrm{GT}}_{\mathrm{min}} = 137\,\mu\mathrm{Jy\,mas^{-2}}$. Maximum intensity values of reconstructed images are $I^{\mathrm{CLEAN}}_{\mathrm{max}} = 34\,\mathrm{Jy\,mas^{-2}}$, $I^{\mathtt{resolve}}_{\mathrm{max}} = 111\,\mathrm{Jy\,mas^{-2}}$ correspondingly.

Appendix F: Comparison of `resolve` and over-resolved `CLEAN` image

Figure F.1 and Figure F.2 show the comparison between `CLEAN` image with over-resolved beam and `resolve` image with saturated color bar for synthetic and real data respectively. In Figure F.1, the `CLEAN` algorithm is not able to recover small scale structures in the core of the ground truth image even with over-resolved beam. Furthermore, the extended jet in `CLEAN` image is discontinuous due to the small size of the `CLEAN` beam. In `resolve` image, the extended jet and bright core are relatively well recovered. We note that a prominent central spine in extended jet is reconstructed in `CLEAN` image. It is not pronounced in the ground truth image, can therefore be `CLEAN` artifacts (Pashchenko et al. 2023). In Figure F.2, the structure of core and limb-brightened region is consistent in `resolve` and `CLEAN` reconstruction with over-resolved beam. The central spine in extended jet is pronounced in the `CLEAN` image again, same as the `CLEAN` reconstruction from the synthetic data.

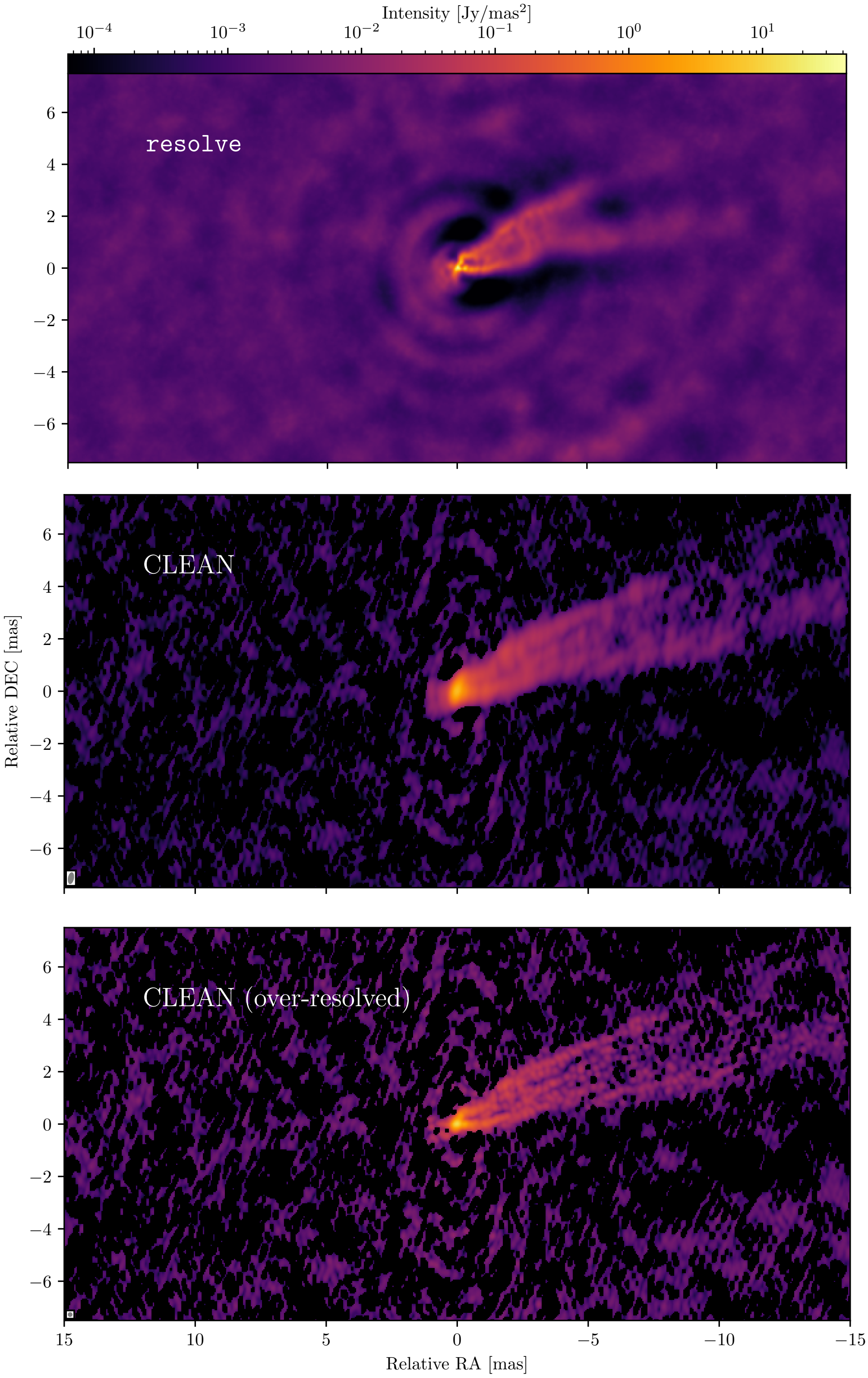

Fig. F.2. M87: the posterior mean image by Bayesian self-calibration (top), the self-calibrated `CLEAN` image (middle) and the over-resolved `CLEAN` image (bottom) reconstructed from the same a-priori calibrated visibility data of VLBA observations at 43 GHz. The unified color bar shows an intensity range from the minimum intensity up to the maximum intensity of the `resolve` image. The image obtained by the Bayesian approach has a maximum intensity $I_{\mathrm{max}} = 35\,\mathrm{Jy\,mas^{-2}}$ with a minimum value of $I_{\mathrm{min}} = 8\,\mu\mathrm{Jy\,mas^{-2}}$. The `CLEAN` image (middle) restoring beam shown in the lower-left corner of the plot is 0.5×0.2 mas, P.A. = −11°. The maximum intensity of the `CLEAN` reconstruction is $I_{\mathrm{max}} = 6\,\mathrm{Jy\,mas^{-2}}$. The over-resolved `CLEAN` image (bottom) circular restoring beam shown in the lower-left corner of the plot is 0.18 mas. The maximum intensity of the over-resolved `CLEAN` image is $I_{\mathrm{peak}} = 13\,\mathrm{Jy\,mas^{-2}}$.

Chapter 6

Imaging a ring-like structure and the extended jet of M87 at 86GHz

The following chapter has been published in Astronomy & Astrophysics, for which I am the first author (Kim et al. 2025a). We revisited Lu et al. (2023) using `resolve` and `DoG-HiT` software. I performed `resolve` image reconstruction and carried out image feature analysis with the `resolve` posterior samples. Hendrik Mueller reconstructed the `DoG-HiT` image and contributed to the validation of the substructure of ring and central spine in M87. Aleksei Nikonov did the jet transverse profile analysis with `resolve` posterior samples. Ru-Sen Lu calibrated the data using `AIPS` software. Jakob Knollmueller contributed to the `resolve` image reconstruction and the posterior plot of ring measurements using `VIDA` software. All authors contributed to the writing of the manuscript.

A&A, 696, A169 (2025)
https://doi.org/10.1051/0004-6361/202452038

Astronomy & Astrophysics

Imaging a ring-like structure and the extended jet of M87 at 86 GHz

Jong-Seo Kim[1,⋆], Hendrik Müller[1,2], Aleksei S. Nikonov[1], Ru-Sen Lu[3,4,1], Jakob Knollmüller[5], Torsten A. Enßlin[6,7], Maciek Wielgus[8,1], and Andrei P. Lobanov[1,9]

[1] Max-Planck-Institut für Radioastronomie, Auf dem Hügel 69, 53121 Bonn, Germany
[2] Jansky Fellow of National Radio Astronomy Observatory, 1011 Lopezville Rd, Socorro, NM 87801, USA
[3] Key Laboratory of Radio Astronomy and Technology, Chinese Academy of Sciences, A20 Datun Road, Chaoyang District, Beijing 100101, PR China
[4] Shanghai Astronomical Observatory, Chinese Academy of Sciences, Shanghai, PR China
[5] Radboud University, Heyendaalseweg 135, 6525 AJ Nijmegen, The Netherlands
[6] Max-Planck-Institut für Astrophysik, Karl-Schwarzschild-Str. 1, 85748 Garching, Germany
[7] Ludwig-Maximilians-Universität, Geschwister-Scholl-Platz 1, 80539 Munich, Germany
[8] Instituto de Astrofísica de Andalucía-CSIC, Glorieta de la Astronomía s/n, 18008 Granada, Spain
[9] Institut für Experimentalphysik, Universität Hamburg, Luruper Chaussee 149, 22761 Hamburg, Germany

Received 28 August 2024 / Accepted 24 February 2025

ABSTRACT

Context. The galaxy M87 is one of the prime targets for high resolution radio imaging to investigate the ring-like "shadow" of its supermassive black hole, the innermost regions of accretion flow, and the formation of the relativistic jet. However, it remains challenging to observe them jointly due to the sparsity of the UV coverage and limited array sensitivity. In 2018, global mm-VLBI array (GMVA)+ALMA observations at 86 GHz enabled the simultaneous reconstruction of a ring structure and the extended jet emission. In order to analyze the ring and jet of M87, conventional `CLEAN` algorithms were mainly employed alongside the regularized maximum likelihood method `SMILI` in previous work.

Aims. To test the robustness of the reconstructed structures of M87 GMVA+ALMA observations at 86 GHz, we estimate the ring diameter, width, and the extended jet emission with the possible central spine by two different novel imaging algorithms: `resolve` and `DoG-HiT`.

Methods. We performed Bayesian self-calibration and imaging with uncertainty estimation using `resolve`. In addition, we reconstructed the image with `DoG-HiT`, using only interferometric closure quantities.

Results. Overall, reconstructions are consistent with the `CLEAN` and `SMILI` images. The ring structure of M87 is resolved at a higher resolution and the posterior distribution of M87 ring features is explored. The `resolve` images show that the ring diameter is 60.9 ± 2.2 μas and its width is 16.0 ± 0.9 μas. The ring diameter and the ring width measured from the `DoG-HiT` image are 61.0 μas and 20.6 μas, respectively. The ring diameter is therefore in agreement with the estimation (64^{+4}_{-8} μas) by `SMILI` image reconstructions and visibility domain model fitting. Two bright spots in the ring are reconstructed by four independent imaging methods. Therefore, the substructure in the ring most likely results from the data. A consistent limb-brightened jet structure is reconstructed by `resolve` and `DoG-HiT`, albeit with a less pronounced central spine.

Conclusions. Modern data-driven imaging methods confirm the ring and jet structure in M87, and complement traditional VLBI methods with novel perspectives on evaluating the significance of the recovered features. They confirm the result of the previous report.

Key words. methods: statistical – techniques: high angular resolution – techniques: image processing – techniques: interferometric – galaxies: active – galaxies: individual: M87

1. Introduction

Continued improvements in instruments and algorithms for very long baseline interferometry (VLBI) enable us to image and analyze radio emission from near to supermassive black holes (SMBH) and inside the formation zone of relativistic jet in active galactic nuclei (AGNs). The recent Event Horizon Telescope (EHT) observations captured the black hole "shadow" in M87* and SgrA* (Event Horizon Telescope Collaboration 2019a, 2022), and the Global mm-VLBI Array (GMVA) and Very Long Baseline Array (VLBA) observations provided high fidelity images of the extended jet emission in radio-loud AGNs (Walker et al. 2018; Kim et al. 2018; Okino et al. 2022). The nearby galaxy M87, with a SMBH mass of $6.5 \times 10^9 M_\odot$ (Event Horizon Telescope Collaboration 2019b) and a redshift of $z = 0.004283$ (Cappellari et al. 2011), provides a unique opportunity to study the black hole accretion disk and jet launching mechanism simultaneously due to the large angular scales of 0.08 pc or 260 R_g (where $R_g = GM/c^2$) per milliarcsecond. So far, the black hole shadow and relativistic jet of M87 at radio frequencies have been observed independently due to instrumental limitations and the characteristics of the source in different frequency regimes.

Observations of M87 with the GMVA, the phased Atacama Large Millimeter/Submillimeter Array (ALMA), and the

---

[⋆] Corresponding author; `jongkim@mpifr-bonn.mpg.de`

Greenland Telescope (GLT) in 2018 enabled the central ring-like structure and the extended jet to be imaged simultaneously. Lu et al. (2023) employed a `CLEAN` (Högbom 1974; Clark 1980) self-calibration and imaging method in order to reconstruct the ring and jet structures in M87 with a large field of view. Additionally, the ring in M87 was reconstructed with a smaller field of view using a regularized maximum likelihood (RML)-based imaging software `SMILI` (Akiyama et al. 2017). GMVA observations at 86 GHz play a significant role in resolving the core and extended jet emission of M87. Prior to the EHT M87 observation in 2017 (Event Horizon Telescope Collaboration 2019a), the GMVA M87 observation in 2014 and 2015 (Kim et al. 2018) provided the core and edge-brightened jet of M87 image down to 13 R_g. The GMVA observations with ALMA in 2018 facilitated the detection of the ring with extended jet emission since ALMA provides the longest north-south baselines with improved sensitivity. For the first time, these finding connected the central ring-like feature, which presumably corresponds to the compact accretion flow, with the innermost jet. This work was accompanied by recent groundbreaking observations of the jet in M87 on a variety of scales, ranging from the (full polarimetric results on) horizon scales (Event Horizon Telescope Collaboration 2019a, 2021a, 2023, 2024), to the strongly edge-brightened innermost jet (Walker et al. 2018; Kim et al. 2018, 2023), as well as to the triple-peaked, helical structure and dynamics in the large scale jet (Asada et al. 2016; Hada 2017; Nikonov et al. 2023; Cui et al. 2023). It is imperative to connect the compact scale structures of M87* to the large scale structures to understand AGN jet formation. The observations presented by Lu et al. (2023) play a significant role in connecting horizon scales to jet scales.

However, the data reduction process of GMVA+ALMA is challenging due to the sparsity of the UV coverage, tropospheric phase corruption at millimeter wavelengths, a low signal-to-noise ratio (S/N), and inhomogeneous antenna statistics due to the different sensitivity of antennas. This difficulty jeopardizes the interpretation of some of the features in the reconstruction, namely the ring-like structure (two brighter spots) and the jet (inner ridge line). Imaging with the conventional `CLEAN` method is not able to reconstruct a robust ring-like structure due to suboptimal resolution. Furthermore, the simple assumption in `CLEAN` that the sky brightness distribution is a collection of point sources is not an optimal prior to describe the extended continuous jet emission. An independent assessment of the robustness of these features is needed to facilitate a much-awaited scientific interpretation.

The latest advancement in forward modeling imaging algorithms enables us to generate more robust results from sparse millimeter-VLBI data sets. As an example, Bayesian imaging is a probabilistic approach that reconstructs the posterior distribution using Bayes' theorem. Hence, Bayesian imaging is able to use posterior samples to estimate the uncertainty of parameters, such as image features and instrumental gains. However, image reconstruction is computationally demanding compared to other imaging methods since a collection of possible images is reconstructed instead of a single image. RML methods reconstruct an image by minimizing an objective function, which consists of a data fidelity term and regularizers that favor certain image structures such as smoothness or sparsity. Contrary to `CLEAN`, forward modeling methods fit the model to the data directly in the visibility domain. We can fit closure quantities directly or calibration can be incorporated in the image reconstruction. Furthermore, we are able to encode knowledge about the source and measurement setup explicitly in the prior distribution and regularizers. As a result, both of the imaging approaches outperform the traditional inverse modeling `CLEAN` algorithm and we can reconstruct reproducible images with improved resolution in a less supervised fashion. A detailed comparison between `CLEAN` and forward modeling approaches can be found in Chael et al. (2016); Arras et al. (2021); Müller et al. (2024).

In this work, we reconstruct images using two imaging algorithms: we perform Bayesian self-calibration and imaging jointly using the Bayesian imaging software `resolve` (Junklewitz et al. 2016; Arras et al. 2022; Roth et al. 2023; Kim et al. 2024) and we reconstruct an image with closure amplitudes and closure phases only (Chael et al. 2018) using the RML-based `DoG-HiT` software (Müller & Lobanov 2022, 2023a,b). These two independent imaging methods are utilized in order to estimate the robustness of the M87 ring and extended jet emission from the GMVA+ALMA observation in 2018. They quantify the robustness of the recovered features from two alternative, supplementary perspectives, by self-calibration and imaging from a probabilistic point of view and by imaging with closure quantities only without a potential self-calibration bias.

This article is structured as follows. In Sect. 2, we explain the `resolve` and `DoG-HiT` image reconstruction methods. In Sect. 3, we show two image reconstruction results and then analyze the robustness of the M87 ring structure and jet emission. In Sect. 4, we summarize our results.

2. Method

2.1. Bayesian self-calibration and imaging by `resolve`

`resolve`[1] is an open-source Bayesian imaging software for radio interferometric data (Junklewitz et al. 2016; Arras et al. 2022; Roth et al. 2023; Kim et al. 2024). In `resolve`, samples of potential images and antenna-based gain solutions that are consistent with the data are reconstructed by Bayes' theorem in a variational inference sense (Blei et al. 2016; Knollmüller & Enßlin 2019; Frank et al. 2021). In this paper, we used the metric Gaussian variational inference method (Knollmüller & Enßlin 2019, MGVI) to estimate the posterior distribution of the sky brightness distribution and antenna-based gains. The MGVI method enables us to perform high-dimensional Bayesian inference with affordable computational resources. The probabilistic approach could be advantageous for the M87 GMVA+ALMA observations due to the sparse UV coverage, and large and heterogeneous data uncertainties. For details of the M87 GMVA+ALMA data, we refer to Sects. 1 and 2 of the supplementary information in Lu et al. (2023).

We reconstructed the `resolve` image in Fig. 1 with a spatial domain of 2048 × 1024 pixels and a field of view of 4 mas × 2 mas from a priori calibrated (without self-calibration) data. The Bayesian self-calibration is performed simultaneously with the imaging. The number of posterior samples was 100 and the reduced χ^2 value of the final result was 1.1. The wall-clock time for the `resolve` reconstruction was 5.5 hours on a single node of the MPIfR cluster with 25 MPI (Message Passing Interface) tasks.

Since the GMVA+ALMA array is highly inhomogeneous, it is a reasonable assumption that each antenna gain has a different temporal correlation structure. In `resolve`, we utilized a Gaussian process prior with a nonparametric correlation kernel in the NIFTy software[2] for the sky brightness distribution (image) and gain prior model. The spatial correlation between

---

[1] https://gitlab.mpcdf.mpg.de/ift/resolve

[2] https://gitlab.mpcdf.mpg.de/ift/nifty

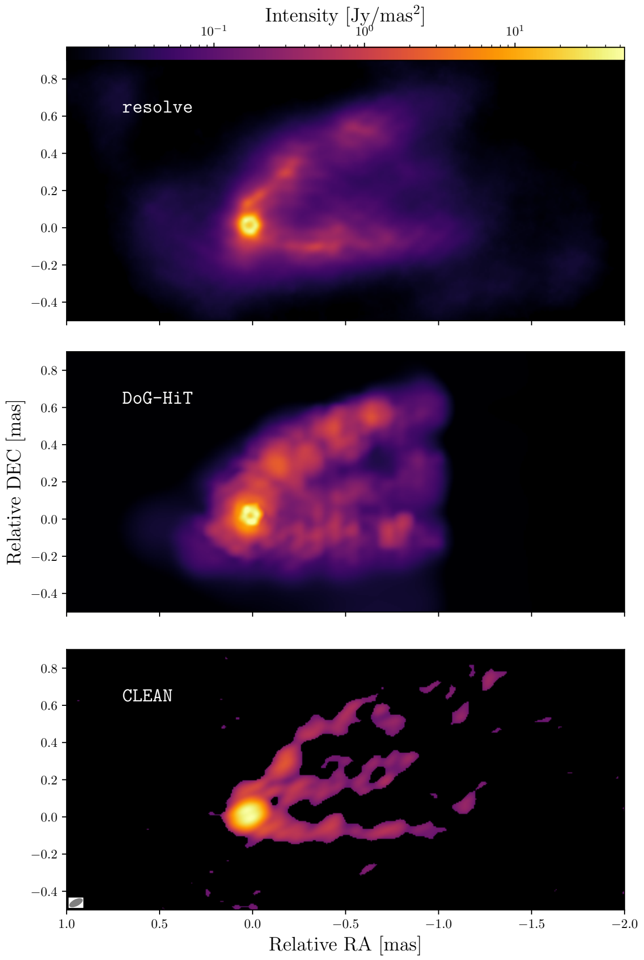

Fig. 1. Image reconstructions of GMVA+ALMA M87 at 86 GHz. Each image presents results obtained by a different algorithm. The top posterior mean image was reconstructed using the `resolve` Bayesian self-calibration and imaging method. The middle image was obtained using `DoG-HiT` closure amplitudes and closure phases only imaging. The bottom image was obtained using the `CLEAN` self-calibration and imaging in Lu et al. (2023). The `CLEAN` image is convolved with an elliptical beam, which is represented as an ellipse with sizes 79 × 37 µas, PA = −63° in the bottom-left corner.

image pixels and temporal correlation between gains can therefore be inferred from the data without manual steering of the gain solution interval constraints (see Fig. A.2). The amplitude gain prior is assumed to be correlated and different correlation kernels are inferred per antenna. Gain amplitudes for right-hand circular polarization (RCP) and left-hand circular polarization (LCP) are assumed to have the same correlation structure to stabilize the self-calibration and image reconstruction. The phase gain is assumed to be uncorrelated since the phase coherence time in GMVA observations is comparable with the data averaging time (ten seconds) and it can be even shorter under poor weather conditions.

Furthermore, the posterior distribution of model parameters, such as each pixel in the image and antenna-based gain solutions, can be explored in `resolve`. In other words, the reliability of the reconstructed parameters and the image features, such as the ring structure and extended jet emission, can be quantified by estimated uncertainties from posterior samples. As an example, if one antenna is problematic, then it would result in a high uncertainty in its gain solution. As a result, in Bayesian imaging, the high uncertainty of these data points can be self-consistently taken into account in the image reconstruction. More details about the Bayesian self-calibration and imaging method for VLBI data and validation with synthetic data can be found in Kim et al. (2024).

2.2. Imaging with closure quantities by `DoG-HiT`

`DoG-HiT` is a regularized maximum likelihood (RML) imaging algorithm that reconstructs the image using multiscalar wavelet basis functions (Müller & Lobanov 2022). The basis functions are fitted to the UV coverage, offering a neat separation between covered and noncovered Fourier coefficients, that is, gaps in the UV coverage (for more details on the wavelets, we refer the reader to Müller & Lobanov 2023a). The image is recovered by a sparsity promoting forward-backward splitting framework that effectively calculates the multiresolution support. In other words, the image is represented by the set of all statistically significant wavelet scales. It has been demonstrated that the multiresolution support is beneficial prior information that enables reconstruction even for sparse and weakly constrained settings (Müller & Lobanov 2022, 2023b).

In this work, we aim to validate the results presented in Lu et al. (2023) using closure-only imaging pioneered by Chael et al. (2018). Closure-only imaging is a self-calibration independent technique. As a result, we are able to estimate the robustness of the recovered features against the gain calibration. We represent the `DoG-HiT` image (see Fig. 1) in a square field of view of 4096 µas by 512 × 512 pixels. The reconstruction was run on a CPU (11th generation Intel core i7) with 32 GB RAM for roughly thirty minutes. The reduced χ^2 to the closure phases was 1.36 and to the closure amplitudes was 1.1. For the reconstruction with `DoG-HiT`, we first select a set of wavelet basis functions, called a dictionary, fitted to the UV coverage of the observation. Then we run `DoG-HiT` with all large scale wavelets that were significant to fit the extended, diffuse jet emission. Then we use this image as an initial guess and add all small-scale wavelets that are relevant to represent the central ring, and minimize the χ^2-metric to the closure phases and closure amplitudes.

In this framework, we directly fit to the self-calibration independent closure amplitudes and closure phases. For a given number of antennas, more closure quantities can be constructed than visibilities. However, not all the measurements are independent since they can be represented as linear combinations of other closure triangles and quadrilaterals (Twiss et al. 1960; Blackburn et al. 2020; Thyagarajan et al. 2022). Since the number of statistically independent closure phases and amplitudes is therefore smaller than the number of independent visibilities, which effectively leads to a number of degeneracies such as lost information of the total flux density and the absolute source position, we have to account for the larger freedom in the models. There are two opposite strategies to achieve this. We could either try to explore the multimodality and degeneracies inherent to closure quantities, for example using recently proposed multiobjective optimization schemes (Müller et al. 2023; Mus et al. 2024a,b), or we could utilize a more constraining piece of prior information that resolves the degeneracies. For the purpose of the latter approach, multiresolution support proved successful and was implemented in `DoG-HiT`.

3. Results

The M87 GMVA+ALMA images at 86 GHz by `resolve`, `DoG-HiT`, and `CLEAN` (Lu et al. 2023) are shown in Fig. 1.

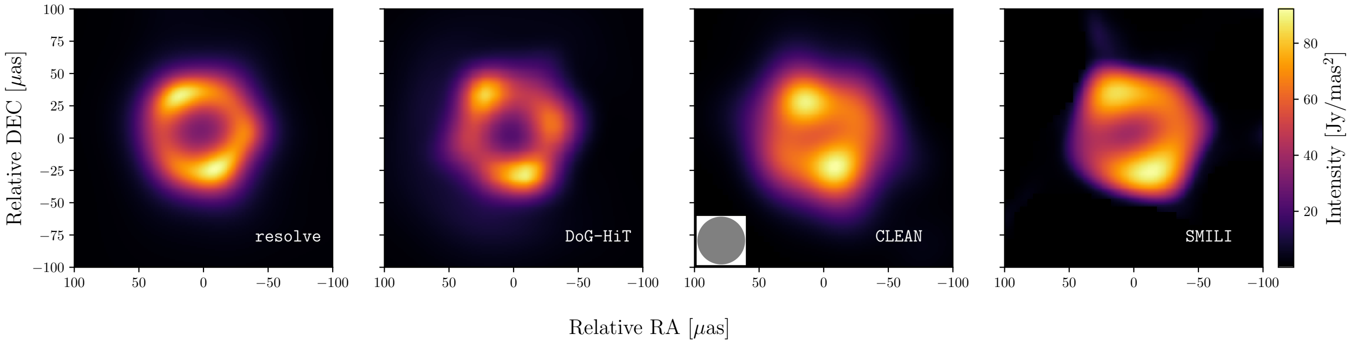

Fig. 2. Ring of the M87 image reconstructions at 86 GHz from Fig. 1. The color shows intensity in Jy mas^{-2} according to the linear color bar located at the right of the figure. Each image presents results obtained by a different algorithm, whose names are indicated in the lower right corners. The left image is the `resolve` posterior mean image using the Bayesian self-calibration and imaging method. The left-center image is the `DoG-HiT` reconstruction using closures only imaging. The right-center image represents the `CLEAN` reconstruction with the over-resolved 37 μas circular beam in Lu et al. (2023). The right image shows the `SMILI` reconstruction in Lu et al. (2023). All images were processed by a Gaussian interpolation.

`resolve` and `DoG-HiT` image fits and results are archived in zenodo[3].

3.1. Estimation of ring-like features in M87

A zoom-in on the central compact emission region is presented in Fig. 2. In the visibility domain, the presence of the visibility null amplitude at around 2.3 Gλ and the phase jump around the null amplitude (see Fig. S2 in Lu et al. 2023) is analogous to EHT M87 observations in 2017 and 2018 (Event Horizon Telescope Collaboration 2019a, 2024), which is strong evidence of the M87 ring structure. Figure 5 (middle panel) shows the visibility domain representation of `resolve` and `DoG-HiT` images, namely the posterior mean model visibility amplitudes by `resolve` and the amplitudes of the Fourier-transformed `DoG-HiT` image. The visibility null amplitudes in `resolve` and `DoG-HiT` are located at around 2.3 Gλ, which is consistent with the results in Lu et al. (2023). The visibility null amplitudes are shorter than the M87 EHT observation in 2017 and 2018 (at around 3.4 Gλ).

The disagreement of visibility null amplitudes between 3 mm and 1 mm implies that the diameter of the observed ring at 3 mm is larger than that of the ring at 1 mm, since the baseline location of the visibility null amplitude scales inversely with the ring diameter (Lu et al. 2023). For comparison, in Sagittarius A*, the intrinsic (descattered) size of the compact horizon-scale source changes by about a factor of 2 between 1 mm and 3 mm emission (Issaoun et al. 2019; Event Horizon Telescope Collaboration 2022). The M87 ring diameter at 86 GHz was estimated in Lu et al. (2023) to be (64$^{+4}_{-8}$ μas), based on the circular ring fitting with the optimal set of `SMILI` images and visibility domain model fitting. Furthermore, they found that the thick ring is preferred over a thin ring using image analysis and model fitting.

In this article, the posterior distribution of the M87 ring diameter, width, and ellipticity is estimated using the `variational image domain analysis` (`VIDA`) software (Tiede et al. 2022). To validate the robustness of the ring structure, `resolve` provides more reliable error estimates than the previous report since the uncertainty is estimated from posterior sample images, and not from the selected top-set of images. `VIDA` is an image feature extraction tool that treats each image as a probability distribution and compares the image to the geometrical model image (template) by utilizing Kullback–Leiber (KL) or Bhattacharyya (Bh) divergences as the objective function. Using the corresponding template, the ring features of each posterior sample image are estimated. In this analysis, we used the `CosineRingwFloor` template, and the azimuthal intensity distribution is described by a cosine expansion.

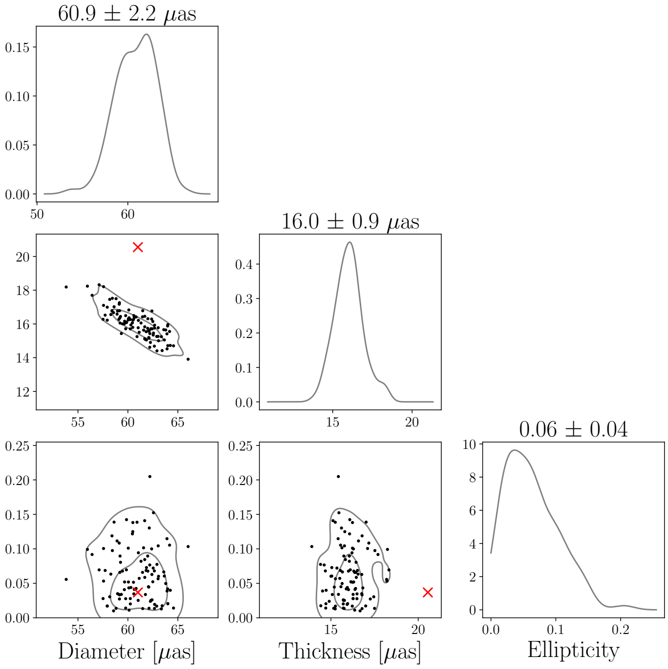

Fig. 3. Posterior distribution of the M87 ring diameter, thickness, and ellipticity estimated from 100 `resolve` posterior sample images. Contours show 1σ and 2σ cumulative regions. The probability density function is obtained using Gaussian kernel density estimation. Each black dot marks the estimated ring parameter from the `resolve` posterior sample images. The red marks correspond to the estimation of the ring diameter and ring thickness obtained by the `DoG-HiT` reconstruction (diameter: 61.0 μas, thickness: 20.6 μas, ellipticity: 0.04).

Figure 3 shows that the M87 ring diameter estimated from the `resolve` images is 60.9 ± 2.2 μas and is 61.0 μas from the `DoG-HiT` image. The estimated ring diameter using `resolve` and `DoG-HiT` is within the errors of the estimation (64$^{+4}_{-8}$ μas) in Lu et al. (2023). The width is 16.0 ± 0.9 μas using `resolve` and 20.6 μas using `DoG-HiT`. The discrepancy in the ring width

---

[3] https://zenodo.org/uploads/13348953

between resolve and DoG-HiT results from the sparse UV coverage beyond the first visibility null amplitude. The visibility domain model fitting (see Fig. S10 in Lu et al. 2023) shows that the UV coverage beyond the first null is crucial to determine the best fitting model. However, the thick ring and thin ring models show similar reduced χ^2 due to the limited UV coverage beyond the first null. As a result, the ring width is not well constrained by the data. Furthermore, we note that the ring diameter and width show anti-correlation, which is due to the finite resolution of the telescope array. The effective radius of the ring decreases with a larger ring width (see Appendix G of Event Horizon Telescope Collaboration 2019c), which explains the dependence between the estimated diameter and width. This anti-correlation is also shown by SMILI reconstructions (see Fig. S14 in Lu et al. 2023). The ellipticity of the ring, τ, is defined as $\tau = 1 - b/a$, where a is the semimajor axis lengths and b is the semiminor axis lengths of the elliptical ring. The τ is 0.06 ± 0.04 by resolve and 0.04 by DoG-HiT, which means there is no significant ellipticity of the M87 ring. A detailed description of the VIDA.jl software can be found in Tiede et al. (2022).

The observation by GMVA+ALMA M87 on 2018, April 14 was conducted a week before the EHT M87 observation (2018, April 21 and 25), which is shorter than the expected timescale for decorrelation of the emission pattern (Georgiev et al. 2022). The flux density of the compact region 200 μas × 200 μas) at 1 mm is 0.5 ± 0.1 Jy by DIFMAP, eht-imaging, and SMILI softwares (see Table 2 in Event Horizon Telescope Collaboration 2024). We note that the compact region flux density constraints from EHT 2018 data were challenging due to the lack of short baseline coverage (Event Horizon Telescope Collaboration 2024). The total flux density at 3 mm is 0.57 ± 0.03 Jy on mas scales, and the flux density of the compact region[4] at 3 mm is 0.33 ± 0.02 Jy by resolve. DoG-HiT images estimate 0.43 Jy in the compact field of view. As a result, the spectral index α of the M87 compact region is slightly positive $\alpha \sim 0.4$. This implies a mixed optical depth in the core, under a caveat that the emitting region at 3 mm is larger than at 1 mm, following the ring diameter analysis. The observed ratio of flux densities is reasonably consistent with the predictions of the numerical models, which typically indicate an inhomogeneous optical depth in the compact region (Event Horizon Telescope Collaboration 2019d, 2021b; Palumbo et al. 2024).

3.2. Extended jet emission of M87

Our reconstructions of the limb-brightened M87 jet structure broadly agree with the one described in Lu et al. (2023): we see an edge-brightened jet anchored to the vicinity of the ring-like feature. One peculiar feature in the image reported by Lu et al. (2023) is the presence of a bright spine along the jet axis. This central ridge line may be related to the triple-helix structure in the jet of M87 that has been observed at larger scales (Nikonov et al. 2023).

However, it is questionable whether this feature of the image represents a real structure on-sky, or appears as a consequence of imaging artifacts. Particularly, it has been recently demonstrated that CLEAN deconvolution errors are prone to produce inner ridge lines for edge-brightened jet configurations (Pashchenko et al. 2023). In fact, the central spine is less prominent in the DoG-HiT and resolve reconstructions.

DoG-HiT and resolve allow the robustness of the central spine to be quantified from two independent perspectives: by calibration-independent imaging with a minimal human bias in DoG-HiT, and by uncertainty estimation in resolve. For DoG-HiT, the small scale structure and the large scale (diffuse) structure are represented by different wavelets, which are ultimately expressed by the multiresolution support. This allows us to estimate the robustness of the central ridge by a jackknife test, that is, we cut the diffuse emission at the location of the central spine and recalculate the fit statistics to the (calibration-independent) closure quantities. To this end, we applied the following strategy. We flagged long baselines of more than 2 $G\lambda$ (to focus the analysis on the diffuse emission), then we fitted the closure phases and closure amplitudes with DoG-HiT, only varying coefficients in the multiresolution support, and calculated the updated fit statistics. Next, we masked out the diffuse, central spine from the multiresolution support, and refit the closure quantities. Finally, we compared the scoring with a central spine and without a central spine.

This strategy resembles a standard strategy in VLBI, which is often applied in the discussion of the existence of a counter-jet. However, we note some key advantages of the strategy applied by us, compared to CLEAN. First, DoG-HiT directly fits closure quantities, hence the conclusions that we can draw are less dependent on the phase and amplitude self-calibration. Second, we perform the jackknife test on a multiscalar domain, which allows us to divide the emission more clearly into small and large scale structures. Finally, DoG-HiT directly fits a model to the data that is composed of diffuse and compact emission and does not need a final convolution with the beam, as opposed to the point source model of CLEAN (e.g., see the discussion in Müller & Lobanov 2023a). Hence, we compare the fit quality of the approximated on-sky representation rather than an unphysical list of CLEAN components (which would question the interpretability of the χ^2-statistics).

We obtain $\chi^2_{\mathrm{cph}} = 1.104$, $\chi^2_{\mathrm{cla}} = 1.494$ when fitting the data with a central spine, and $\chi^2_{\mathrm{cph}} = 1.061$, $\chi^2_{\mathrm{cla}} = 1.592$ when fitting without a central spine. Neither mode is strongly favored. From this study, we cannot report the conclusive detection of a central spine in the image.

An alternative perspective on the robustness of image features is offered by the built-in uncertainty quantification in resolve. In Fig. 4, the transverse flux intensity profiles of the M87 jet emission are depicted. The mean and standard deviation of the transverse jet profile can be obtained from 100 posterior sample images by resolve. The intensity profile of the jet at 0.25, 0.5, 0.75 mas shows that the edge-brightened structure (two peaks) is prominent, however a significant central spine structure is not seen. In Fig. 4, the standard deviation of the pixel fluxes at the central spine is not particularly higher than the limb-brightened feature. In Fig. 1, the DoG-HiT image shows a central spine, which however is fainter than that of the CLEAN reconstruction. Therefore, the central spine in the images obtained by CLEAN in Lu et al. (2023) may be a consequence of CLEAN artifacts resulting from the CLEAN windows and sparsity-promoting CLEAN sky model. Further observations with additional short baseline antennas are required to conclude the detection of the central spine. The edge-brightened morphology that we recover is both consistent with the earlier observations at 86 GHz (Kim et al. 2018) and well-motivated theoretically (e.g., Yang et al. 2024). The counter jet is not detected consistently in the three images, it is therefore not discussed further in this work.

---

[4] Defined as the 200 μas (or about 50 R_g) field of view centered on the ring.

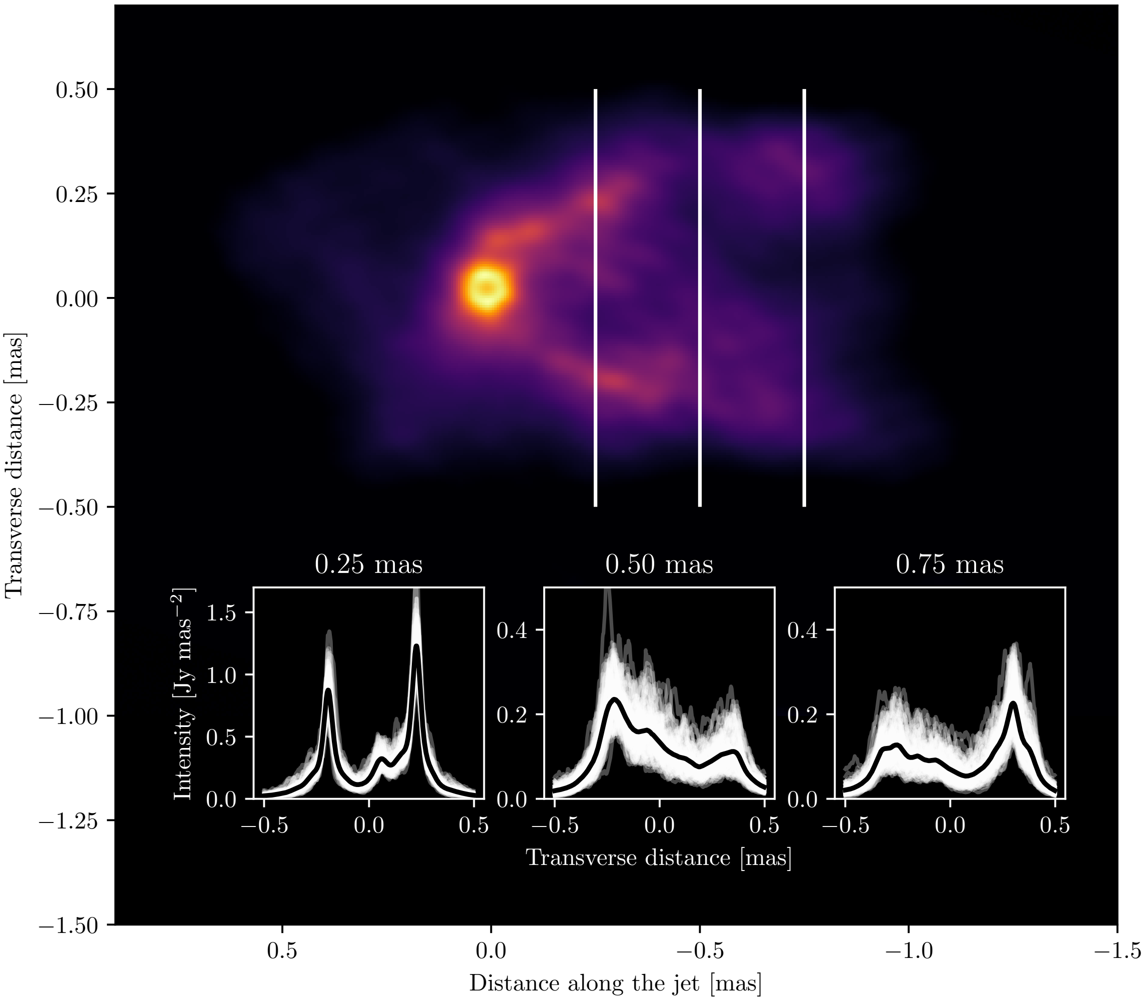

Fig. 4. Galaxy M87 jet transverse profiles and intensity map obtained by `resolve`. Intensity in the map is represented by false color according to the color bar used in Fig. 1 in logarithmic scale. The image is rotated 18° clockwise. Intensity plots at the bottom of the figure show flux density profiles of the jet at 0.25, 0.5 and 0.75 mas from the phase center. Each vertical line corresponds to a location where profiles were extracted.

3.3. Substructure of the M87 ring

A feature that appears consistent across all four different imaging algorithms (`SMILI`, `CLEAN`, `resolve`, and `DoG-HiT`) are the two bright blobs in the ring. While images are recovered with various resolutions, the recovered ring emission always shows the double structure within the ring toward the top and the bottom, at consistent positions across different imaging methods. We note that the limb-brightened structures that are recovered by `resolve` close to the ring seem to connect to the ring exactly at the positions where the brighter blobs within the ring occur consistently for all four reconstructions. Hence, it may be natural to interpret the double pattern in the ring as a physical phenomenon. In this subsection we present some discussion on how real these features may be.

First, it is noticeable that these brighter regions in the ring form a double structure that is point-symmetric to the center of the ring. That supports the interpretation of these structures as an imaging artifact, especially due to the sparse coverage at long baselines. In fact, Lu et al. (2023) have tested `SMILI` and `CLEAN` reconstructions on synthetic data and found that similar structures are artificially introduced by the imaging procedure (compare Sect. 4 and particularly Fig. S8 in Lu et al. 2023).

Multiple well-understood artifacts may cause such a double structure. Here, we discuss the three most natural scenarios. First, it could be caused by specific choices of the regularization assumption inherent to the respective imaging algorithm. Second, the structure could be introduced artificially by residual gain effects. Finally, the structure may be described by a residual sidelobe structure, which would make it essentially a consequence of the sparsity of the UV coverage. In what follows, we will discuss each of these concerns individually.

Four imaging methods that were utilized here approach the image reconstruction from four vastly different perspectives: `CLEAN` recovers the structure in an inverse modeling framework essentially processing a sparsity-promoting regularization approach (sky brightness distribution is represented by a collection of delta components) (Lannes et al. 1997), `SMILI` approaches the image by a weighted sum of multiple handcrafted data and regularization terms in a RML framework (Akiyama et al. 2017); `DoG-HiT` processes multiscale functions in the context of compressive sensing (Müller & Lobanov 2022); and `resolve` estimates the posterior distribution of the image and gains from the prior model encoding source and instrument information and likelihood (i.e., the data; Kim et al. 2024). We note that the prior in Bayesian imaging can be interpreted as regularizers in RML methods, and vice versa (Kim et al. 2024). The multiscale functions in `DoG-HiT` and the Gaussian process prior in `resolve` are flexible and do not ask for the double structure in the ring as prior knowledge. The fact that all four independent methods that use a variety of prior information (regularization) lead to a similar structure challenges the interpretation of the double structure as an artifact from the assumptions and prior information applied by the imaging procedure.

The structure may be a consequence of unsolved gain residuals. In fact, it is a possible issue that the alternating self-calibration and cleaning procedure produce "phantom" structures point symmetric to the origin that has been reported in practice for a long time. We note, however, that the double feature also appears in the `DoG-HiT` reconstruction that are independent from gain corruptions (closure-only imaging), which makes a potential cause by the calibration of the phases less likely. This claim is supported by the `resolve` reconstruction which solves for the self-calibration with imaging simultaneously in a probabilistic setup.

Finally, we ask whether the double structure could be introduced by the sparsity of UV coverage. That is a possibility that can never be eradicated completely, simply because the observation fundamentally misses relevant visibilities through the gaps in the UV coverage. Consequently, there is missing information. In fact, the Fourier domain representation of a double source is a fringe pattern (compare Fig. 5), which is exactly the kind of artifact that not fully cleaned residuals may introduce. This issue has been identified through synthetic data tests by Lu et al. (2023). They generated synthetic data sets with artificial baselines from symmetric ring ground truth images to understand the importance of the long west-east baselines. `CLEAN` and `SMILI` reconstructions from the synthetic data with additional baselines were able to reconstruct the ground truth. From the synthetic data with original UV coverage, `SMILI` reconstructions could recover symmetric ring ground truth images reasonably well, but `CLEAN` reconstructions tended to generate asymmetric ring structures. The occurrence of the double structure may be related to the lack of long west-east baselines. Nevertheless, we argue that the recovered double structure is represented by the measured visibilities. In Fig. 5, we show the central ring image (top panels) and the amplitudes of the full Fourier transform of the reconstructions (middle panels) for `DoG-HiT` (left panels) and `resolve` (right panels). A ring feature is identified in the Fourier domain by a first zero that is clearly covered by observations (compare, e.g., to the model fitting discussions in Lu et al. 2023). Moreover, the visibility domain representations of `DoG-HiT` and `resolve` show the ellipticity of the null visibility amplitude points in Fig. 5 (middle panel). We note that the location of the null visibility points in the UV domain is elliptical, with an elongation in the direction of the jet. This may result in bright spots in the image aligned perpendicularly to the jet, related to the stretch of the image domain ring. The data from multiple antennas (EF, KP, OV, PV, and YS) at the longest west-east baselines imply that the ellipticity of the null visibility points originates from the data.

To analyze the UV-coverage sparsity that corresponds to the M87 ring substructure, we subtract a uniform ring feature from the images (defined by 60% of the respective emission peak) to extract the double feature on top of the ring. The resulting double patterns are depicted in the bottom panels of Fig. 5, and their respective amplitudes in the Fourier domain in the last row. The observed UV points are overplotted with red crosses. Observations span the main fringe and the first side-lobe uniformly, the

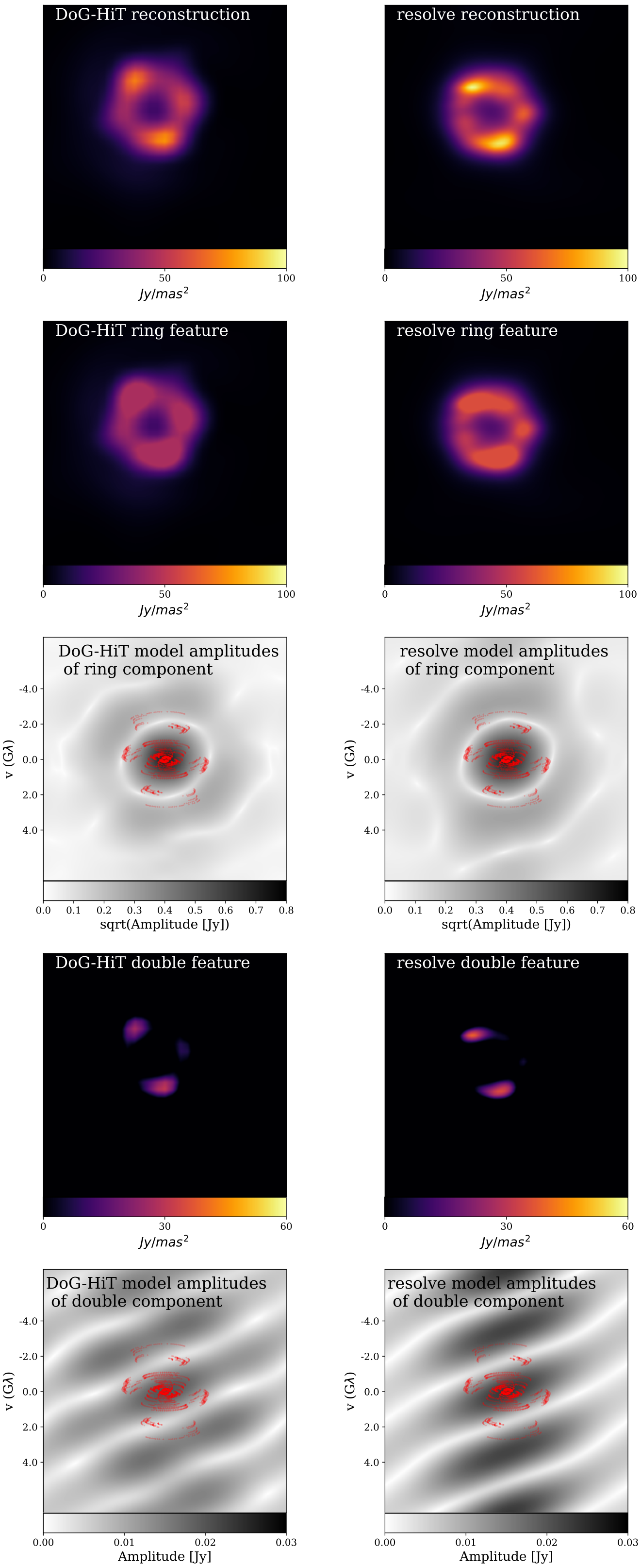

Fig. 5. Reconstructions of the central feature by `DoG-HiT` (left panels) and `resolve` (right panels). Top panels: reconstructions of the compact emission. Top-middle panels: the central ring feature. Middle panels: The recovered amplitudes of the central feature, with the UV coverage overplotted (red points). Middle-bottom panels: the central ring feature, cut at 60% of the respective peak brightness, which showcases the double blob pattern on top of the ring. Bottom panels: the amplitudes and the UV coverage of the double pattern alone.

fringes are not produced exclusively in the gaps in the UV coverage. These findings, as well as the striking similarity between multiple imaging approaches, constitute a convincing argument for the physical nature of bright spots along the ring. However, a definitive answer cannot be given with the quality of the existing data set, particularly in the presence of the synthetic data tests performed by Lu et al. (2023), and follow-up observations are needed.

If the emission that forms the ring image is dominated by the accretion disk, elongation in the direction perpendicular to the ring may be a simple geometric effect for the inclined observer. While the 230 GHz ring image is strongly asymmetric with respect to the jet axis (Event Horizon Telescope Collaboration 2024), our 86 GHz reconstructions exhibit a high degree of symmetry. In numerical general relativistic magnetohydrodynamic (GRMHD) simulations of accretion within the EHT library (Dhruv et al. 2025), consistent behavior appears for some retrograde accretion models (negative black hole spins). In that case, 230 GHz image asymmetry is driven primarily by the spin effects (Event Horizon Telescope Collaboration 2019d), which are dominant very near the event horizon. In the 86 GHz image, which is formed by a more extended emission, these effects are balanced by the Doppler boost that enhances brightness on the opposite side of the black hole, which results in a ring structure elongated perpendicularly to the jet axis, with bright spots on both sides of the central brightness depression.

4. Conclusions

Lu et al. (2023) present observations of the core and jet in M87 observed with the GMVA+ALMA at 86 GHz. The image contains a ring-like feature that looks similar to the one reported by the EHT (Event Horizon Telescope Collaboration 2019a, 2024), but with an approximately 1.5 times larger ring diameter resulting from the null visibility points and phase jump at 2.3 $G\lambda$. For the first time, this ring feature is connected to an innermost jet in the same image, possibly providing constraints on the launching mechanism of the jet. Furthermore, the recovered image contains several fainter features that may be of great importance for a scientific interpretation, especially in the context of recent works on the large scale jet structure in M87 (Kim et al. 2018; Cui et al. 2023; Nikonov et al. 2023; Kim et al. 2023).

To validate the results reported in Lu et al. (2023), we apply two more imaging algorithms specially designed to study the robustness of the recovered features: by Bayesian self-calibration and imaging with `resolve`, and by closure-only imaging with `DoG-HiT`. The distinctive features of `resolve` and `Dog-HiT`, namely the probabilistic approach and the multiscale wavelet-based deconvolution algorithm, allow us to quantify the robustness of the recovered M87 ring and extended jet emission. We obtained the posterior distribution of the ring diameter, width, and ellipticity by analysis of the `resolve` posterior sample images. We confirm the M87 ring-like structure at 86 GHz with a diameter of 60.9 ± 2.2 μas, a thickness of 16.0 ± 0.9 μas, and an ellipticity of 0.06 ± 0.04 by `resolve`, and a diameter of 61.0 μas, a thickness of 20.6 μas, and an ellipticity of 0.04 by `DoG-HiT`. The estimated ring diameter is consistent with the estimate (64^{+4}_{-8} μas) in Lu et al. (2023).

Furthermore, image reconstructions using `resolve` and `DoG-HiT` show that the ring is embedded in a strongly edge-brightened large scale jet structure, which agrees with the findings reported in Lu et al. (2023). Among the upper and lower arm of the edge-brightened jet, the `CLEAN` reconstruction presented in Lu et al. (2023) features a third, central spine that may be interpreted together with a triple-helix structure at larger scales (Nikonov et al. 2023). However, the central spine structure in the `resolve` and `DoG-HiT` reconstructions is less prominent compared to the `CLEAN` reconstruction. Our analysis shows that this central spine is neither necessary to fit the data, nor supported by the uncertainty quantification by `resolve` in the image domain. The validation by two independent imaging methods implies that the central spine is fainter than previously reported.

Finally, all utilized imaging algorithms coincide on the same substructure in the ring consisting of two bright spots to the north and the south, co-located with inner anchor points on the edge-brightened jet to the horizon scale. Stemming from a coincidence of this phenomenon across a variety of imaging algorithms, and its representation in the Fourier domain, we argue that is more likely that this substructure of the ring results from the data, and not an imaging or self-calibration artifact, although an artifact that originates from sparse UV coverage is not ruled out. The potential physical origin of these structures is unclear. If real, they might be transient emission structures during the observational period, however, their alignment perpendicular to the jet suggests otherwise. They might also be permanent structures potentially linked to the disk-jet transition, as their location within the disk seems to coincide with the position the jet edges point to. Finally, they may be a result of an interplay of Doppler boost and black hole spin effects, as seen in numerical simulations of retrograde accretion. Investigating the size and asymmetry of the 86 GHz emission ring in the EHT M87 simulation library could be a fruitful path toward understanding the detailed physics responsible for the morphology of our image.

Acknowledgements. We thank Jae-Young Kim for helpful suggestions and feedback on drafts of the manuscript, Jack Livingston and Thomas Krichbaum for comments and informative discussions. J. K. and A. N. received financial support for this research from the International Max Planck Research School (IMPRS) for Astronomy and Astrophysics at the Universities of Bonn and Cologne. This work was supported by the M2FINDERS project funded by the European Research Council (ERC) under the European Union's Horizon 2020 Research and Innovation Programme (Grant Agreement No. 101018682). R.-S.L. is supported by the National Science Fund for Distinguished Young Scholars of China (Grant No. 12325302) and the Shanghai Pilot Program for Basic Research, CAS, Shanghai Branch (JCYJ-SHFY-2021-013). M.W. is supported by a Ramón y Cajal grant RYC2023-042988-I from the Spanish Ministry of Science and Innovation. This research has made use of data obtained with the Global Millimeter VLBI Array (GMVA), which consists of telescopes operated by the MPIfR, IRAM, Onsala, Metsahovi, Yebes, the Korean VLBI Network, the Greenland Telescope, the Green Bank Observatory and the Very Long Baseline Array (VLBA). The VLBA and the GBT are facilities of the National Science Foundation operated under cooperative agreement by Associated Universities, Inc. The Greenland Telescope (GLT) is operated by the Academia Sinica Institute of Astronomy and Astrophysics (ASIAA) and the Smithsonian Astrophysical Observatory (SAO). The data were correlated at the correlator of the MPIfR in Bonn, Germany.

References

Akiyama, K., Kuramochi, K., Ikeda, S., et al. 2017, ApJ, 838, 1
Arras, P., Bester, H. L., Perley, R. A., et al. 2021, A&A, 646, A84
Arras, P., Frank, P., Haim, P., et al. 2022, Nat. Astron., 6, 259
Asada, K., Nakamura, M., & Pu, H.-Y. 2016, ApJ, 833, 56
Blackburn, L., Pesce, D. W., Johnson, M. D., et al. 2020, ApJ, 894, 31
Blei, D. M., Kucukelbir, A., & McAuliffe, J. D. 2016, arXiv e-prints, [arXiv:1601.00670]
Cappellari, M., Emsellem, E., Krajnović, D., et al. 2011, MNRAS, 413, 813
Chael, A. A., Johnson, M. D., Narayan, R., et al. 2016, ApJ, 829, 11
Chael, A. A., Johnson, M. D., Bouman, K. L., et al. 2018, ApJ, 857, 23
Clark, B. G. 1980, A&A, 89, 377
Cui, Y., Hada, K., Kawashima, T., et al. 2023, Nature, 621, 711
Dhruv, V., Prather, B., Wong, G., & Gammie, C. F. 2025, ApJS, 277, 16
Event Horizon Telescope Collaboration (Akiyama, K., et al.) 2019a, ApJ, 875, L1

Event Horizon Telescope Collaboration (Akiyama, K., et al.) 2019b, ApJ, 875, L6

Event Horizon Telescope Collaboration (Akiyama, K., et al.) 2019c, ApJ, 875, L4

Event Horizon Telescope Collaboration (Akiyama, K., et al.) 2019d, ApJ, 875, L5

Event Horizon Telescope Collaboration (Akiyama, K., et al.) 2021a, ApJ, 910, L12

Event Horizon Telescope Collaboration (Akiyama, K., et al.) 2021b, ApJ, 910, L13

Event Horizon Telescope Collaboration (Akiyama, K., et al.) 2022, ApJ, 930, L12

Event Horizon Telescope Collaboration (Akiyama, K., et al.) 2023, ApJ, 957, L20

Event Horizon Telescope Collaboration (Akiyama, K., et al.) 2024, A&A, 681, A79

Frank, P., Leike, R., & Enßlin, T. A. 2021, Entropy, 23, 853

Georgiev, B., Pesce, D. W., Broderick, A. E., et al. 2022, ApJ, 930, L20

Hada, K. 2017, Galaxies, 5, 2

Högbom, J. A. 1974, A&AS, 15, 417

Issaoun, S., Johnson, M. D., Blackburn, L., et al. 2019, ApJ, 871, 30

Junklewitz, H., Bell, M. R., Selig, M., & Enßlin, T. A. 2016, A&A, 586, A76

Kim, J. Y., Krichbaum, T. P., Lu, R. S., et al. 2018, A&A, 616, A188

Kim, J.-Y., Savolainen, T., Voitsik, P., et al. 2023, ApJ, 952, 34

Kim, J.-S., Nikonov, A. S., Roth, J., et al. 2024, A&A, 690, A129

Knollmüller, J., & Enßlin, T. A. 2019, arXiv e-prints [arXiv:`1901.11033`]

Lannes, A., Anterrieu, E., & Marechal, P. 1997, A&AS, 123, 183

Lu, R.-S., Asada, K., Krichbaum, T. P., et al. 2023, Nature, 616, 686

Müller, H., & Lobanov, A. P. 2022, A&A, 666, A137

Müller, H., & Lobanov, A. P. 2023a, A&A, 673, A151

Müller, H., & Lobanov, A. P. 2023b, A&A, 672, A26

Müller, H., Mus, A., & Lobanov, A. 2023, A&A, 675, A60

Müller, H., Massa, P., Mus, A., Kim, J.-S., & Perracchione, E. 2024, A&A, 684, A47

Mus, A., Müller, H., & Lobanov, A. 2024a, A&A, 688, A100

Mus, A., Müller, H., Martí-Vidal, I., & Lobanov, A. 2024b, A&A, 684, A55

Nikonov, A. S., Kovalev, Y. Y., Kravchenko, E. V., Pashchenko, I. N., & Lobanov, A. P. 2023, MNRAS, 526, 5949

Okino, H., Akiyama, K., Asada, K., et al. 2022, ApJ, 940, 65

Palumbo, D. C. M., Bauböck, M., & Gammie, C. F. 2024, ApJ, 970, 151

Pashchenko, I. N., Kravchenko, E. V., Nokhrina, E. E., & Nikonov, A. S. 2023, MNRAS, 523, 1247

Roth, J., Arras, P., Reinecke, M., et al. 2023, A&A, 678, A177

Thyagarajan, N., Nityananda, R., & Samuel, J. 2022, Phys. Rev. D, 105, 043019

Tiede, P., Broderick, A. E., & Palumbo, D. C. M. 2022, ApJ, 925, 122

Twiss, R. Q., Carter, A. W. L., & Little, A. G. 1960, The Observatory, 80, 153

Walker, R. C., Hardee, P. E., Davies, F. B., Ly, C., & Junor, W. 2018, ApJ, 855, 128

Yang, H., Yuan, F., Li, H., et al. 2024, Sci. Adv., 10, eadn3544

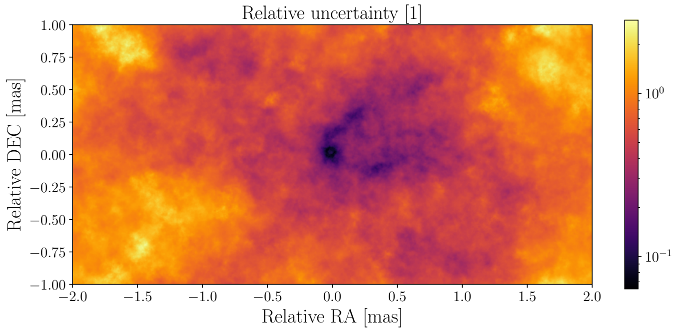

Fig. A.1. `resolve` image pixel-wise relative uncertainty, which is the sky brightness posterior standard deviation normalized by the posterior mean from the `resolve` reconstruction in the top panel of Fig. 1.

Appendix A: Uncertainty estimation by `resolve`

Figure A.1 shows the pixel-wise relative uncertainty of the `resolve` image in Fig. 1. The relative uncertainty is defined as the sky brightness posterior standard deviation normalized by the posterior mean from 100 posterior sample images. Lower relative uncertainty values of the M87 ring emission and limb-brightened are estimated, that means they are well-constrained by the data. However, the relative uncertainty values in the central spine are higher compared to the limb-brightened jet emission. Figure A.2 depicts the `resolve` posterior amplitude gains. ALMA (AA) amplitude gain solutions show smooth behavior with lower posterior standard deviations compared to other arrays due to the high sensitivity of ALMA array. The gain amplitudes with high uncertainties result from the absence of the data (BR: <4h, EF: >6h, GB: <4h, KP: <3h, LA: <3h, PT: <3h, and YS: RCP gains). For instance, the RCP gain amplitudes for YS antenna have uniformly distributed high uncertainties since only single polarization mode (LCP) was observed for YS antenna.

Appendix B: Contour plots

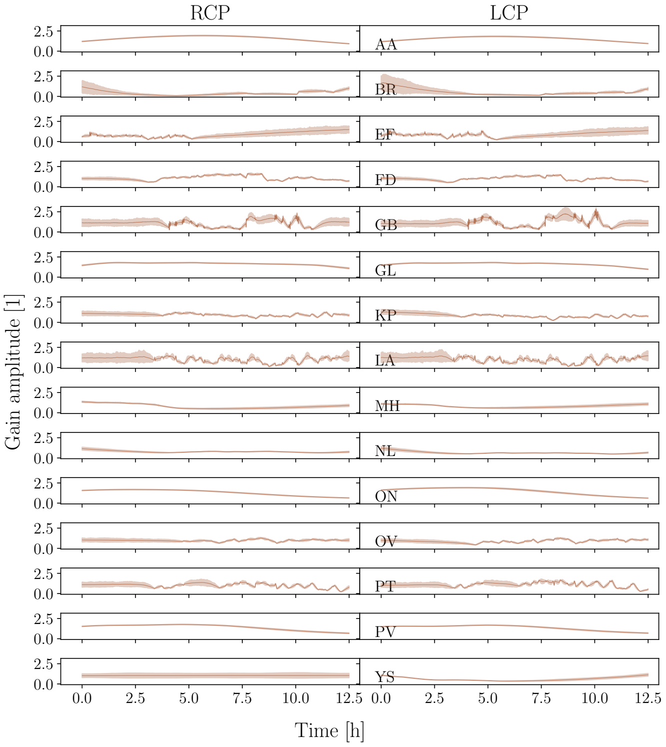

Fig. A.2. `resolve` posterior amplitude gains. The gain as a function of time is illustrated as a thin line with a semi-transparent standard deviation. The left and right columns of the figure show gains from the right (RCP) and left (LCP) circular polarizations correspondingly. Each row represents an individual antenna, whose abbreviated name is indicated in the bottom left corner of each LCP plot.

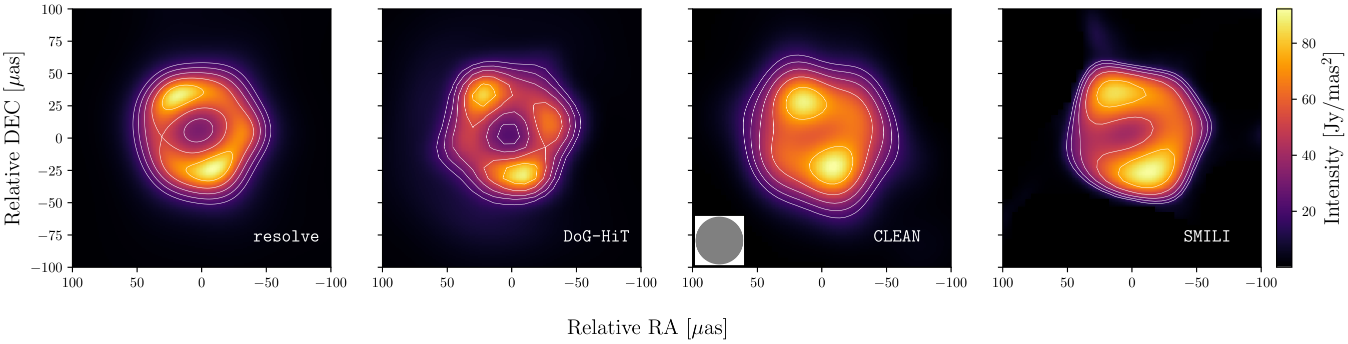

Fig. B.1. Same as Fig. 2 , but overlaid with successive contours that increase by a factor of $\sqrt{2}$, starting from 20% of the peak.

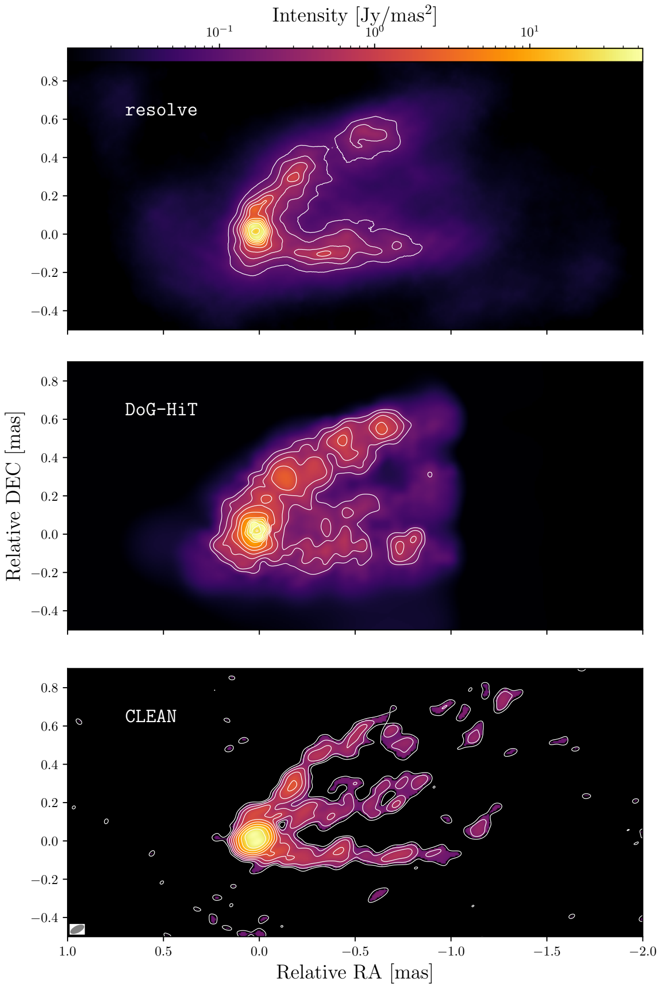

Fig. B.2. Same as Fig. 1, but overlaid with successive contours that increase by a factor of 2, starting from 0.2% of the peak. The starting level was chosen based on the structure of the `CLEAN` image.

Chapter 7

Bayesian polarization calibration and imaging in VLBI

The following chapter is based on a paper currently under review: (Kim et al. 2025b), submitted for publication, arXiv:2511.16556. I am the first author of this work. I implemented the Bayesian polarization calibration and imaging method in `resolve` and performed image reconstructions using `resolve`. Jakob Roth and Jongho Park contributed to implementing the Bayesian polarization calibration and imaging method. All authors contributed to the writing and revision of the manuscript.

Astronomy & Astrophysics manuscript no. main
November 21, 2025

Bayesian polarization calibration and imaging in very long baseline interferometry

Jong-Seo Kim[1,⋆], Jakob Roth[2,3], Jongho Park[4], Jack D. Livingston[1], Philipp Arras[2], Torsten A. Enßlin[2,5], Michael Janssen[1,6], J. Anton Zensus[1], and Andrei P. Lobanov[1,7]

[1] Max-Planck-Institut für Radioastronomie, Auf dem Hügel 69, D-53121 Bonn, Germany
[2] Max-Planck-Institut für Astrophysik, Karl-Schwarzschild-Str. 1, 85748 Garching, Germany
[3] Technische Universität München (TUM), Boltzmannstr. 3, 85748 Garching, Germany
[4] School of Space Research, Kyung Hee University, 1732, Deogyeong-daero, Giheung-gu, Yongin-si, Gyeonggi-do 17104, Republic of Korea
[5] Ludwig-Maximilians-Universität, Geschwister-Scholl-Platz 1, 80539 Munich, Germany
[6] Department of Astrophysics, Institute for Mathematics, Astrophysics and Particle Physics (IMAPP), Radboud University, P.O. Box 9010, 6500 GL Nijmegen, The Netherlands
[7] Institut für Experimentalphysik, Universität Hamburg, Luruper Chaussee 149, 22761, Hamburg, Germany

Received 20 November 2025 / accepted —

ABSTRACT

Context. Extracting polarimetric information from very long baseline interferometry (VLBI) data is demanding but vital for understanding the synchrotron radiation process and the magnetic fields of celestial objects, such as active galactic nuclei (AGNs). However, conventional `CLEAN`-based calibration and imaging methods provide suboptimal resolution without uncertainty estimation of calibration solutions, while requiring manual steering from an experienced user.
Aims. We present a Bayesian polarization calibration and imaging method for VLBI data sets, that explores the posterior distribution of antenna-based gains, polarization leakages, and polarimetric images jointly from pre-calibrated data.
Methods. We reconstructed the posterior distribution of Stokes images, gains, and leakages from real and synthetic data sets in the framework of Bayesian imaging software `resolve` using variational inference methods. Polarization constraints are enforced in the model. Furthermore, polarization calibration with several sources and multiple intermediate frequencies (IFs) is supported in order to maximize the parallactic angle coverage and identify instrumental corruptions per IF.
Results. We demonstrate our calibration and imaging method with observations of the quasar 3C273 with the Very Long Baseline Array (VLBA) at 15 GHz and the blazar OJ287 with the Global Millimeter VLBI Array (GMVA) + Atacama Large Millimeter/Submillimeter Array (ALMA) at 86 GHz. Compared to the `CLEAN` method, our approach provides physically realistic images that satisfy positivity of flux and polarization constraints and can reconstruct complex source structures composed of various spatial scales. In contrast to conventional imaging and calibration methods, our method systematically accounts for calibration uncertainties in the final images and provides uncertainties of Stokes images and calibration solutions.
Conclusions. Our Bayesian polarization calibration and imaging method explores the posterior distribution of calibration solutions and reconstruct physically plausible high-resolution images from VLBI data. The automated Bayesian approach for calibration and imaging will be able to obtain high-fidelity polarimetric images using high-quality data from next-generation radio arrays. The pipeline developed for this work is publicly available.

Key words. techniques: interferometric - techniques: image processing - techniques: high angular resolution - methods: statistical - polarization - galaxies: active - galaxies: jets

1. Introduction

Polarization provides valuable information about astronomical objects and the ambient medium in astronomy, as it is one of the most direct ways to access information about astrophysical magnetic fields. In conjunction with very long baseline interferometry (VLBI), which is able to achieve nominal resolutions of $\sim 20\,\mu$as at 1 mm (Event Horizon Telescope Collaboration et al. 2019) and $\sim 15\,\mu$as at 345 GHz (Raymond et al. 2024), we have the ability to probe extreme magneto-ionic environments.

Polarimetric studies with VLBI have revealed the presence of helical and toroidal magnetic fields in the jet of AGN (Asada et al. 2008; Hovatta et al. 2012; Gabuzda et al. 2017), the magnetic field of the supermassive black holes M87* and Sgr A* (Event Horizon Telescope Collaboration et al. 2021, 2024; Event Horizon Telescope Collaboration 2025), and an alignment between polarization and the jets of AGN, suggesting the presence of magnetizing shocks in AGN jets (Lister & Homan 2005; Pushkarev et al. 2023). However, polarization calibration of VLBI data is challenging, as polarization signals typically have signal-to-noise ratios (S/N) that are an order of magnitude lower than for total intensity.

Polarized data after pre-calibration can still have significant residual corruption from leakage between one polarization feed to another, known as polarization leakage or 'D-terms'. Moreover, the complex source structure of calibrators in VLBI, especially at mm-wavelengths, hinders the estimation of this polarization leakage. The conventional polarization calibration approach in radio interferometry is observing a static and point-

---

[⋆] jongkim@mpifr-bonn.mpg.de

like calibrator with known polarization properties and identifying leakage corruptions by using the information about the calibrator and disentangling source polarization from the instrumentation contributions that are being solved by the time-varying polarization of the feed angle rotation. However, due to the high angular resolution, it is unusual to find static point-like calibrators for polarization calibration in VLBI (Cotton 1993).

Leppanen et al. (1995) introduced the `LPCAL` software to infer polarization leakage corruptions in VLBI data sets. `LPCAL` utilizes a polarization prior model with a set of components which assumes that the linear polarization of a component is proportional to the total intensity of the corresponding component, known as the similarity approximation (Cotton 1993; Leppanen et al. 1995). The simple and effective prior is advantageous in order to determine leakage corruption from sparse and noisy VLBI data sets due to the small number of degrees of freedom in the model.

However, the similarity approximation in `LPCAL` is not valid for sources with complex polarization structure (Cotton 1993). Furthermore, multi-source calibration is not directly supported (see Lister & Homan 2005, for an example of a multi-source method with `LPCAL`.) and D-terms are considered both static in time and frequency for each intermediate frequency (IF) as default in `LPCAL`. Recently, the new `CLEAN`-based polarization calibration software packages `GPCAL` (Park et al. 2021b) and `PolSolve` (Martí-Vidal et al. 2021) are able to employ reconstructed Stokes Q and U images as priors in leakage calibration, a technique called polarization self-calibration. These software support multi-source models to increase parallactic angle coverage, and are able to solve for D-terms that vary with time and frequency.

Nevertheless, `GPCAL` and `PolSolve` still rely on the conventional `CLEAN` deconvolution algorithm, which has limitations. The `CLEAN` algorithm is supervised and user-dependent. As a result, CLEAN windows and weighting schemes may induce biases in the final results. Furthermore, `CLEAN` assumes that the sky is a collection of point sources (usually of the size of the synthesized beam) or Gaussian blobs in multi-scale `CLEAN` (Cornwell 2008), but has no explicit notion of an extended structure. This results in suboptimal resolution, as the potential of radio interferometric observations to super-resolve sources (in the high S/N regime) is not exploited. Consequently, the CLEAN image model for the leakage calibration is not suitable for radio interferometric data with complex source structure. Moreover, the conventional `CLEAN`-based self-calibration is performed iteratively with switching between flagging and manually choosing gain solution intervals that results in inconsistent calibration solutions (Martí-Vidal & Marcaide 2008; Popkov et al. 2021) and a lack of reproducibility. Lastly, calibration uncertainties are not taken into account in the final results and uncertainty estimation is not supported.

Modern forward modeling imaging algorithms provide us a new approach to overcome the limitations of `CLEAN`-based polarization calibration methods (Birdi et al. 2020; Pesce 2021; Event Horizon Telescope Collaboration et al. 2021, 2024). Explicit regularizers and prior assumptions in forward modeling algorithms enable us to infer more robust leakage solutions from sparse VLBI data sets. For example, polarization constraints can be enforced in the polarization imaging model to avoid unphysical polarimetric images (Birdi et al. 2018). Recent instrumental advancement in VLBI accomplishes significantly improved S/N and more wide-band observations. Additionally, the latest algorithmic developments offer methods to solve highly degenerate inverse problems efficiently. A modern polarization calibration and imaging pipeline that utilizes the full potential of the data is highly desirable.

In this work, we introduce a novel Bayesian calibration and imaging method using the Bayesian imaging software `resolve`. The posterior distribution of antenna-based gains, D-terms, and Stokes images are explored jointly using variational inference algorithms (Knollmüller & Enßlin 2019; Frank et al. 2021). Recently, the polarization constraint ($I \geq \sqrt{Q^2 + U^2 + V^2}$) is encoded in the the `resolve` polarization imaging model (Arras et al. 2025). We utilize this polarization imaging model and incorporate polarization calibration and gain self-calibration directly into the imaging process. Furthermore, multi-source and multi-IF polarization calibration are supported in a probabilistic framework.

This article is structured as follows. In section 2, we explain the conventional `CLEAN`-based polarization calibration method and our Bayesian method. In section 3 and section 4, we validate the method with synthetic and real data sets respectively. We summarizes our results in section 5.

2. Method

2.1. Radio Interferometer measurement equation (RIME)

A radio interferometer measures Fourier components of the sky brightness distribution instead of imaging the sky directly. According to the van Cittert-Zernike theorem, the two-point correlation function of the signals recorded by two antennas, i and j, called the visibility data V_{ij}, is given by the Fourier transformed sky brightness distribution I for total intensity under the assumption that the field of view is small (Hamaker et al. 1996; Smirnov 2011; Thompson et al. 2017):

$$V(u, v)_{ij} = \int_{-\infty}^{\infty} \int_{-\infty}^{\infty} I(x, y)\, e^{-2\pi \mathbf{i}(ux+vy)} dx\, dy = \mathbb{FT}[I], \tag{1}$$

where (u, v) are the Fourier domain coordinates, (x, y) are the image domain coordinates, and $\mathbb{FT}$ is the Fourier transform operator.

Since the observed data is incomplete and corrupted by atmospheric and instrumental effects, we obtain a low-fidelity image, also known as the dirty map, from a direct Fourier transform of the visibility data. Inferring the real source structure from radio interferometric data is an ill-posed inverse problem, and therefore a unique solution does not exist. Thus, additional assumptions, prior knowledge, or other regularizers of the solution space are required to obtain high-fidelity images from radio interferometric data in image reconstruction.

The measurement equation (Eq. 1) can be generalized for full polarization observation, and the instrumental and atmospheric data corruption can be described by Jones matrices (Jones 1941). As a result, the radio interferometer measurement equation (RIME) for the full polarimetric visibility matrix $\mathbf{V}$ in the circular polarization basis is given by(Smirnov 2011):

$$\mathbf{V}_{ij} = \mathbf{J}_i \left(\int_{-\infty}^{\infty} \int_{-\infty}^{\infty} \mathbf{I}(x, y)\, e^{-2\pi \mathbf{i}(ux+vy)} dx\, dy \right) \mathbf{J}_j^{\dagger} + \mathbf{N}_{ij}, \tag{2}$$

where $\mathbf{V}_{ij}$ is the visibility matrix consisting of four complex correlation functions by the signal from the right-hand circular polarization (RCP) R and the signal from the left-hand circular polarization (LCP) L:

$$\mathbf{V}_{ij} = \begin{pmatrix} R_i R_j^* & R_i L_j^* \\ L_i R_j^* & L_i L_j^* \end{pmatrix}, \tag{3}$$

where the asterisk $*$ denotes a complex conjugate,
$\mathbf{J}_i$ is the Jones matrix describing the data corruption of the antenna i by instrumental and atmospheric effects:

$$\mathbf{J}_i = \mathbf{G}_i\,\mathbf{D}_i\,\mathbf{P}_i = \begin{pmatrix} g_i^R & 0 \\ 0 & g_i^L \end{pmatrix} \begin{pmatrix} 1 & D_i^R \\ D_i^L & 1 \end{pmatrix} \begin{pmatrix} e^{-\mathbf{i}\phi_i} & 0 \\ 0 & e^{\mathbf{i}\phi_i} \end{pmatrix}, \tag{4}$$

where $\mathbf{G}_i$ is the antenna-based gain matrix, $\mathbf{D}_i$ is the leakage (D-term) matrix describing the signal leakage between polarizers (e.g., D_i^R is the signal leakage from LCP to RCP for antenna i), $\mathbf{P}_i$ is the field rotation angle matrix, † denotes conjugate transposition, $\mathbf{N}_{ij}$ is the additive noise, and $\mathbf{I}$ is the polarimetric sky brightness distribution matrix, consisting of Stokes I, Q, U, and V:

$$\mathbf{I} = \begin{pmatrix} I + V & Q + \mathbf{i}U \\ Q - \mathbf{i}U & I - V \end{pmatrix}. \tag{5}$$

The antenna field rotation angle ϕ, representing the rotation of the receiver polarization feeds with respect to the source due to Earth's rotation, is defined as $\phi = f_{\rm el}\theta_{\rm el} + f_{\rm par}\psi_{\rm par} + \phi_{\rm off}$, where $\theta_{\rm el}$ is the elevation angle, $\psi_{\rm par}$ is the parallactic angle, and $\phi_{\rm off}$ is a constant offset. The field rotation angle depends on the antenna mount. Alt-azimuth (ALT-AZ) mounts with a Cassegrain focus have $f_{\rm par} = 1$ and $f_{\rm el} = 0$. ALT-AZ mounts with a Nasmyth-Right type focus have $f_{\rm par} = 1$ and $f_{\rm el} = 1$, and ALT-AZ mounts with a Nasmyth-Left type focus have $f_{\rm par} = 1$ and $f_{\rm el} = -1$. More details regarding the antenna mount types can be found in the Appendix C of Janssen et al. (2019).

The polarization calibration and imaging model with the polarimetric visibility matrix data $\mathbf{V}$, Jones matrices $\mathbf{J_i}$, $\mathbf{J_j}$ for antennas, i and j, and model visibilities ($\mathcal{RR}$, $\mathcal{RL}$, $\mathcal{LR}$, and $\mathcal{LL}$) from Stokes images is

$$\begin{aligned}
R_iR_j^* &= g_i^R\, g_j^{R*}[e^{-\mathbf{i}\phi_i}\,\mathcal{RR}\,e^{\mathbf{i}\phi_j} + D_i^R\,e^{\mathbf{i}\phi_i}\,\mathcal{LR}\,e^{\mathbf{i}\phi_j} \\
&\quad + e^{-\mathbf{i}\phi_i}\,\mathcal{RL}\,e^{-\mathbf{i}\phi_j}\,D_j^{R*} + D_i^R e^{\mathbf{i}\phi_i}\,\mathcal{LL}e^{-\mathbf{i}\phi_j}\,D_j^{R*}] \\
R_iL_j^* &= g_i^R\, g_j^{L*}[e^{-\mathbf{i}\phi_i}\,\mathcal{RR}\,e^{\mathbf{i}\phi_j}D_j^{L*} + D_i^R\,e^{\mathbf{i}\phi_i}\,\mathcal{LR}\,e^{\mathbf{i}\phi_j}\,D_j^{L*} \\
&\quad + e^{-\mathbf{i}\phi_i}\,\mathcal{RL}\,e^{-\mathbf{i}\phi_j} + D_i^R e^{\mathbf{i}\phi_i}\,\mathcal{LL}e^{-\mathbf{i}\phi_j}] \\
L_iR_j^* &= g_i^L\, g_j^{R*}[D_i^L\,e^{-\mathbf{i}\phi_i}\,\mathcal{RR}\,e^{\mathbf{i}\phi_j} + e^{\mathbf{i}\phi_i}\,\mathcal{LR}\,e^{\mathbf{i}\phi_j} \\
&\quad + D_i^L\,e^{-\mathbf{i}\phi_i}\,\mathcal{RL}\,e^{-\mathbf{i}\phi_j}\,D_j^{R*} + e^{\mathbf{i}\phi_i}\,\mathcal{LL}e^{-\mathbf{i}\phi_j}\,D_j^{R*}] \\
L_iL_j^* &= g_i^L\, g_j^{L*}[D_i^L\,e^{-\mathbf{i}\phi_i}\,\mathcal{RR}\,e^{\mathbf{i}\phi_j}\,D_j^{L*} + e^{\mathbf{i}\phi_i}\,\mathcal{LR}\,e^{\mathbf{i}\phi_j}\,D_j^{L*} \\
&\quad + D_i^L\,e^{-\mathbf{i}\phi_i}\,\mathcal{RL}\,e^{-\mathbf{i}\phi_j} + e^{\mathbf{i}\phi_i}\,\mathcal{LL}e^{-\mathbf{i}\phi_j}],
\end{aligned} \tag{6}$$

where the model visibility matrix consists of Stokes images:

$$\mathbf{V}_{model} = \begin{pmatrix} \mathcal{RR} & \mathcal{RL} \\ \mathcal{LR} & \mathcal{LL} \end{pmatrix} = \mathbb{FT}\left[\begin{pmatrix} I + V & Q + \mathbf{i}U \\ Q - \mathbf{i}U & I - V \end{pmatrix}\right]. \tag{7}$$

Polarization calibration and imaging is equivalent to estimating the gains g, D-terms D, Stokes images I, Q, U, and V from the visibility data $\mathbf{V}$. In the conventional `CLEAN`-based method, this polarimetric calibration and imaging problem in VLBI is solved in an iterative fashion since the problem is highly degenerate. In this work, we infer the gains g, leakages D, Stokes I, Q, U, and V jointly from pre-calibrated visibility matrix data $\mathbf{V}$ in a probabilistic approach.

2.2. `CLEAN`-based polarization calibration method

The `CLEAN`-based polarization calibration method assumes that the antenna gains have already been calibrated during the data pre-processing and imaging/self-calibration procedures. It also assumes that the antenna's field rotation angles have been corrected during the data pre-processing phase (see Park et al. 2021b, 2023; Martí-Vidal et al. 2021 for more details). With these assumptions, the cross-hand visibilities consist of both the source's intrinsic linear polarization terms and the terms associated with the antenna's polarimetric leakages and field rotation angles.

Determining the leakages is not straightforward, as they need to be disentangled from the source polarization terms. One of the most widely used methods in the past assumes that the source's linear polarization emission is proportional to the total intensity structure within each "sub-model", which consists of a group of neighboring total intensity CLEAN components. This method is known as the "similarity approximation" (Cotton 1993; Leppanen et al. 1995) and is implemented in `LPCAL`, a task within the Astronomical Image Processing System (`AIPS`; Greisen (2003)).

While generally a good approximation, the similarity method faces challenges when dealing with very weakly polarized sources (e.g., Park et al. 2021a), particularly when utilizing global VLBI observations at millimeter wavelengths, which provide ultra-high angular resolution. In such cases, the source's linear polarization structures are often complex, and the similarity approximation may not hold well (e.g., Event Horizon Telescope Collaboration et al. 2021, 2024; Zhao et al. 2022).

To overcome this limitation, two methods have been developed: `GPCAL` (Park et al. 2021b), based on `AIPS` and `Difmap`, and `PolSolve` (Martí-Vidal et al. 2021), based on `CASA` (CASA Team et al. 2022). These methods conduct calibration as follows:

1. They derive the leakages using the similarity approximation, like LPCAL, and remove them from the data.
2. They perform imaging with `CLEAN` using the leakage-corrected data to obtain the source's Stokes Q and U CLEAN models.
3. They use the original data to derive the leakage solutions again, this time using the source's linear polarization models obtained in the previous step, and remove the leakages using the updated solutions.
4. They iteratively update the source's linear polarization models and leakage solutions by repeating steps 2 and 3 until the solutions converge.

These methods can also simultaneously utilize data from multiple calibrator sources, which typically leads to improved leakage calibration accuracy, as the leakage solutions are not expected to vary between sources.

2.3. Bayesian imaging software `resolve`

The open-source Bayesian imaging software `resolve`[1] treats radio interferometric imaging and calibration (Eq. 2) as an inverse problem and computes a probabilistic solution for it. Thus, `resolve` computes the probability distribution of the sky brightness $\mathbf{I}$ given the measured visibilities. In Arras et al. (2019b), a joint calibration and imaging approach was introduced, computing a posterior probability distribution for the sky brightness $\mathbf{I}$ and the antenna gains $\mathbf{G}$. Roth et al. (2023) extended this approach, incorporating direction-dependent effects in the antenna

---

[1] `https://gitlab.mpcdf.mpg.de/ift/resolve`

gains. A further extension to `resolve` was made in Arras et al. (2025), enabling full Stokes imaging. In Roth et al. (2024), the idea of major and minor cycles used in `CELAN` based algorithms was adapted in a Bayesian version for the `resolve` framework.

Building on the full Stokes imaging capabilities, this work introduces polarization calibration and imaging to `resolve`. Thus, we compute the posterior distribution of the full Stokes sky brightness matrix $\mathbf{I}$ jointly with the posterior distributions of the antenna-based gain matrix $\mathbf{G}$, and leakage matrix $\mathbf{D}$. The posterior distribution can be expressed via Bayes' theorem

$$\mathcal{P}(\mathbf{G},\mathbf{D},\mathbf{I}|\mathbf{V}) = \frac{\mathcal{P}(\mathbf{V}|\mathbf{G},\mathbf{D},\mathbf{I})\,\mathcal{P}(\mathbf{G},\mathbf{D},\mathbf{I})}{\mathcal{P}(\mathbf{V})}, \tag{8}$$

in terms of the likelihood $\mathcal{P}(\mathbf{V}|\mathbf{G},\mathbf{D},\mathbf{I})$ and the prior $\mathcal{P}(\mathbf{G},\mathbf{D},\mathbf{I})$. In the following section 2.4, we discuss the likelihood model. In section 2.5, we outline the prior models and in section 2.6, we describe the algorithm for approximating the posterior distribution given the likelihood and prior.

2.4. Likelihood distribution

As outlined in Section 2.3, we approach the polarization calibration and imaging problem as a Bayesian inference task. This entails defining the prior and likelihood to compute the posterior distribution, which represents the result of the Bayesian imaging/inference process.

Following the framework established by Knollmüller & Enßlin (2018), we employ a coordinate transformation, or reparametrization trick (also known as inverse transform sampling), to introduce new parameters ξ. This transformation ensures that the prior follows a standard normal distribution $\mathcal{P}(\xi) = \mathcal{G}(\xi, \mathbb{1})$, integrating all prior knowledge into the likelihood component $\mathcal{P}(V|\xi)$.

The likelihood $\mathcal{P}(V|\xi)$ is composed of two components: $\mathcal{P}(\mathbf{V}|\mathbf{G},\mathbf{D},\mathbf{I})$ and a function of mapping ξ to specific values of $\mathcal{G}$, $\mathcal{D}$, and $\mathcal{I}$. The former component describes the data aspect of the likelihood while the latter incorporates the prior information for the gains g, the leakages D, and the Stokes images I, Q, U, and V. This section elaborates on the first component while the following section will deal with the second.

Our data model integrates gain matrices $\mathbf{G}$, leakage matrices $\mathbf{D}$, field rotation angle matrices $\mathbf{P}$, and the polarization imaging model $\mathbf{I}$. Upon setting $\mathbf{G}$, $\mathbf{D}$, $\mathbf{P}$, and $\mathbf{I}$, the visibility data $\mathbf{V}$ can be formulated as follows:

$$\mathbf{V}_{ij} = \mathbf{G}_i\,\mathbf{D}_i\,\mathbf{P}_i\,\mathbb{FT}\,[\,\mathbf{I}\,]\,\mathbf{P}_j^\dagger\,\mathbf{D}_j^\dagger\,\mathbf{G}_j^\dagger. \tag{9}$$

By encapsulating Jones matrices into the response function, the model can be simplified:

$$\mathbf{V}_{ij} = \mathbf{J}_i\,\mathbb{FT}\,[\,\mathbf{I}\,]\,\mathbf{J}_j^\dagger = \mathbf{R}^{(g,D)}[\mathbf{I}]\,, \tag{10}$$

where $\mathbf{R}^{(g,D)}$ is the response function consisting of the Fourier operator and Jones matrices.

It is important to note that field rotation angle matrices $\mathbf{P}$ are often pre-corrected during pre-calibration to stabilize the phase calibration in VLBI. However, the field rotation angle matrix $\mathbf{P}$ and the D-term matrix $\mathbf{D}$ are not commutative. Consequently, our model for pre-corrected field rotation angle data is:

$$\mathbf{V}_{ij}^{\phi\,\mathrm{cor.}} = \mathbf{P}_i^{-1}\mathbf{G}_i\,\mathbf{D}_i\,\mathbf{P}_i\,\mathbb{FT}\,[\,\mathbf{I}\,]\,\mathbf{P}_j^\dagger\,\mathbf{D}_j^\dagger\,\mathbf{G}_j^\dagger\,(\mathbf{P}_j^\dagger)^{-1}. \tag{11}$$

This means we must reverse the pre-correction of the field rotation angle in pre-calibrated data before adequately solving the Jones matrices, given the non-commutative properties of matrices $\mathbf{G}$, $\mathbf{D}$, and $\mathbf{P}$.

Assuming additive Gaussian noise on the radio interferometric data, justified by the central limit theorem, the likelihood given noise covariance $\mathbb{N}$ is expressed as:

$$\mathcal{P}(\mathbf{V}|\mathbf{I},\mathbf{G},\mathbf{D}) = \mathcal{G}(\mathbf{V} - \mathbf{R}^{(g,D)}[\mathbf{I}], \mathbb{N}). \tag{12}$$

In this work, the noise covariance is assumed to have a diagonal covariance; thus, the noise is uncorrelated. This likelihood formulation underscores how our method, unlike `CLEAN`-based polarization calibration methods, facilitates the simultaneous inference of calibration solutions and Stokes images. Consequently, the uncertainty estimation of Stokes images inherently reflects uncertainties from the calibration, data noise and incomplete uv-coverage.

Table 1. List of prior distributions in the Bayesian polarization calibration and imaging model.

Model	Description	Prior
s	Polarization imaging model	2D $\mathcal{GP}(\xi_s)$
q	Polarization imaging model	2D $\mathcal{GP}(\xi_q)$
u	Polarization imaging model	2D $\mathcal{GP}(\xi_u)$
v	Polarization imaging model	2D $\mathcal{GP}(\xi_v)$
λ	Log-normal amplitude gain	1D $\mathcal{GP}(\xi_\lambda)$
ϕ	Phase gain	1D $\mathcal{GP}(\xi_\phi)$
		or $\mathcal{N}(0, \sigma_\phi^2)$
a	Log-normal amplitude D-term	$\mathcal{N}(m_a, \sigma_a^2)$
b	Phase D-term	$\mathcal{N}(0, \sigma_b^2)$

2.5. Polarization calibration and imaging prior model

As detailed in Section 2.4, we transform the imaging problem such that the formal prior distribution is a standard normal distribution: $\mathcal{G}(\xi, \mathbb{1})$. Using this reparametrization method, specifying the prior translates to defining generative models, which use standard-normal distributed parameters as inputs to generate the variables of interest, such as the full Stokes sky model $\mathbf{I}$, the gain matrices $\mathbf{G}$, and the leakage matrices $\mathbf{D}$.

Generative model for polarization imaging prior $\mathbf{I}$ The generative model for the Stokes sky emission $\mathbf{I}$ closely follows the model presented in Arras et al. (2025). Regarded as a complex 2×2 matrix, $\mathbf{I}$ is defined by:

$$\mathbf{I} = \begin{pmatrix} \langle E_{i,r}E_{j,r}^*\rangle & \langle E_{i,r}E_{j,l}^*\rangle \\ \langle E_{i,l}E_{j,r}^*\rangle & \langle E_{i,l}E_{j,l}^*\rangle \end{pmatrix} = \begin{pmatrix} I+V & Q+\mathbf{i}U \\ Q-\mathbf{i}U & I-V \end{pmatrix}, \tag{13}$$

within the circular basis (Smirnov 2011). Here, E is the electric field, and indices i, j denote antenna labels and r, l refer to the respective circular feeds. The matrix must meet specific constraints: (1) $\mathbf{I}$ is positive definite and Hermitian, (2) strictly positive total flux $I > 0$, and (3) an upper bound on polarized emission $I^2 \geq Q^2 + U^2 + V^2$ (Hamaker et al. 1996; Smirnov 2011).

Arras et al. (2025) identifies the matrix exponential as a fitting parametrization for the polarized sky brightness distribution:

$$\mathbf{I} = e^{x} := \exp\begin{pmatrix} s+v & q+\mathbf{i}u \\ q-\mathbf{i}u & s-v \end{pmatrix}, \tag{14}$$

where s, q, u, and v are real numbers for each pixel, in particular they can be both positive and negative.

Stokes I, Q, U, and V can be obtained from the two dimensional fields s, q, u, and v:

$$\begin{aligned} I &= e^{s}\cosh p, & Q &= \frac{q}{p}e^{s}\sinh p, \\ U &= \frac{u}{p}e^{s}\sinh p, & V &= \frac{v}{p}e^{s}\sinh p, \end{aligned} \tag{15}$$

where $p := \sqrt{q^2 + u^2 + v^2}$.

The total flux I is strictly positive in Equation 15 and $\mathbf{I}$ is Hermitian since the matrix exponential and the Hermitian conjugate commute. Furthermore, $\mathbf{I}$ is positive definite because the eigenvalues of a Hermitian matrix are real and the eigenvalues of the matrix exponential are the exponential of the eigenvalues. The determinant of $\mathbf{I}$ is the product of the eigenvalues, which is positive:

$$0 < \det \mathbf{I} = I^2 - Q^2 - U^2 - V^2. \tag{16}$$

Thus, it proves that this parametrization satisfies all three conditions of $\mathbf{I}$.

To complete the generative model for $\mathbf{I}$, we need to define the models generating the 2-dimensional (2D) fields s, q, u, and v. We model each of those fields using a Gaussian process ($\mathcal{GP}$) with a non-parametric correlation kernel, captured through generative models that convert standard-normal distributed latent parameters ξ_s, ξ_q, ξ_u, ξ_v into the Gaussian process values $s(\xi_s)$, $q(\xi_q)$, $u(\xi_u)$, $v(\xi_v)$ (following methods in Arras et al. (2021)). In our polarization imaging prior model, the spatial correlation between pixels and the correlation between Stokes images are taken into account since the correlation kernels of s, q, u, and v are inferred from the data. The exact mathematical definition of the generative Gaussian process model can be found in Arras et al. (2021, Sec. 3.4).

Generative model for gain prior g The antenna based gain prior consists of two Gaussian process models is

$$g(t) = \exp(\lambda(t) + \mathbf{i}\phi(t)), \tag{17}$$

where log-normal amplitude gain λ and phase gain ϕ are 1-dimensional (1D) Gaussian process priors.

For the gain prior, we use the same generative Gaussian process model in the imaging prior. Thus, the log-normal amplitude gain $\lambda(\xi_\lambda)$ and phase gain $\phi(\xi_\phi)$ can be described by standard-normal distributed model parameters ξ_λ and ξ_ϕ. For mm-VLBI data with short phase coherence time, we can use an uncorrelated normal-distribution $\phi \curvearrowleft \mathcal{N}(0, \sigma_\phi^2)$ for the phase gain prior.

In `resolve`, the temporal correlation structures in gain solutions are inferred from the data. In order words, we determine the gain solution interval from the data without manual steering and we are even able to infer solution interval per antennas, which can be advantageous for data from a heterogeneous VLBI array (Kim et al. 2025). More details about the antenna-based gain calibration in `resolve` can be found in (Arras et al. 2019b; Kim et al. 2024).

Generative model for D-term prior D The D-term (leakage) prior model is given by:

$$D = \exp(a + \mathbf{i}b), \tag{18}$$

where $a \curvearrowleft \mathcal{N}(m_a, \sigma_a^2)$ and $b \curvearrowleft \mathcal{N}(0, \sigma_b^2)$ are normal distributed priors, m_a is the mean of the log-normal amplitude D-term, and σ_b and σ_b are the standard deviations of the log-normal amplitude and phase D-term respectively.

Therefore, the D-term amplitude is log-normal distributed and the D-term phase is normal distributed. A summary table in Table 1 describes our calibration and imaging prior models.

2.6. Posterior distribution

The posterior distribution of all unknowns given the visibility data in Equation 8 is a very high dimensional object including the Stokes images, gains, and D-terms. Due to the high number of dimensions and the complicated relations between all the involved quantities, any representation of this probability function needs an approximation. One way of representing a posterior distribution is via a set of samples drawn from it. Be $\mathbf{s} = (\mathbf{I}, \mathbf{G}, \mathbf{D})$ denotes the quantities to be inferred and $\mathbf{d} = \mathbf{V}$ denotes the data, then the samples $\mathbf{s}_i \hookleftarrow \mathcal{P}(\mathbf{s}|\mathbf{d})$ with $i \in \{1, \ldots N\}$ are an approximative representation of the posterior $\mathcal{P}(\mathbf{s}|\mathbf{d})$ as any expectation with respect to some function $f(\mathbf{s})$ can be calculated from those approximately,

$$\langle f(\mathbf{s}) \rangle_{(\mathbf{s}|\mathbf{d})} := \int \mathcal{D}\mathbf{s}\, f(\mathbf{s})\, \mathcal{P}(\mathbf{s}|\mathbf{d}) \approx \frac{1}{N}\sum_{i=1}^{N} f(\mathbf{s}_i), \tag{19}$$

where $\int \mathcal{D}\mathbf{s}$ indicates a path integral.

In this work, we utilized two variational inference algorithms (MGVI, geoVI) (Knollmüller & Enßlin 2019; Frank et al. 2021) as implemented in the `NIFTy` software package (Selig et al. 2013; Arras et al. 2019a) to explore the posterior distribution of the Stokes images and calibration solutions. In the variatioanl inference method, the posterior distribution is approximated as a parametrized distribution by minimizing the Kullback-Leibler (KL) divergence as a cost function. The KL divergence measures the information gain between two probability distributions.

These variational inference methods scale quasi-linearly in computational complexity with the problem size; therefore, they enable to solve high-dimensional calibration and imaging problems. Specifically, geoVI, an extension of the MGVI algorithm, can describe non-Gaussian posteriors by constructing a coordinate transformation between the latent space, in which the prior was Gaussian, but the posterior is not, to another latent space, in which the posterior becomes approximate Gaussian. More details about MGVI and geoVI can be found in (Knollmüller & Enßlin 2019; Frank et al. 2021).

From the posterior samples, the posterior mean of the fractional linear polarization is

$$\langle P_{\mathrm{frac}}(\mathbf{s}) \rangle_{(\mathbf{s}|\mathbf{d})} := \int \mathcal{D}\mathbf{s} \left(\frac{Q(\mathbf{s})^2 + U(\mathbf{s})^2}{I(\mathbf{s})^2} \right) \mathcal{P}(\mathbf{s}|\mathbf{d}) = \left\langle \frac{Q^2 + U^2}{I^2} \right\rangle. \tag{20}$$

We note that the posterior mean of the fractional linear polarization is not equal to $(\langle Q \rangle^2 + \langle U \rangle^2)/\langle I \rangle^2$, where $\langle I \rangle$, $\langle Q \rangle$, and $\langle U \rangle$

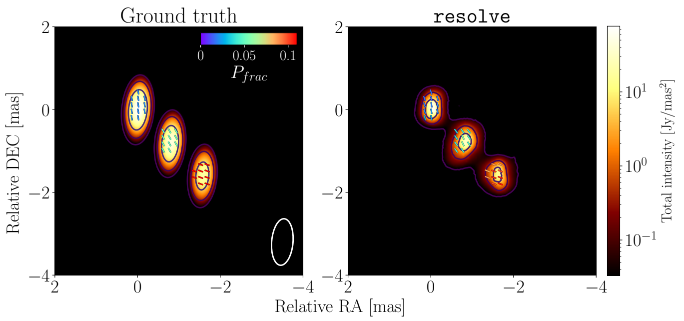

Fig. 1. Comparison between the ground truth image (left panel) convolved with the nominal CLEAN beam with the uniform weighting and the posterior mean resolve polarization reconstruction (right panel) with EVPAs with colors corresponding to the fractional linear polarization P_{frac}. The contours represent the total intensity of corresponding images.

are the posterior mean Stokes images, because of the non-linear dependence of P_{frac} on the Stokes parameters.

As another example, the posterior mean of the electric vector position angle (EVPA) is

$$\langle \Phi \rangle_{(\mathbf{s}|\mathbf{d})} := \int \mathcal{D}\mathbf{s}\, \frac{1}{2} \arctan\left(\frac{U(\mathbf{s})}{Q(\mathbf{s})}\right) \mathcal{P}(\mathbf{s}|\mathbf{d}) = \left\langle \frac{1}{2} \arctan\left(\frac{U}{Q}\right) \right\rangle. \quad (21)$$

3. Application to synthetic data

In VLBI, polarization calibration using multiple calibrators at different declinations helps to reconstruct more robust leakage solutions, which break the degeneracy between the field rotation angle matrix **P** and the leakage matrix **D** (Park et al. 2021b; Martí-Vidal et al. 2021). In order to validate the Bayesian polarization calibration method with multiple calibrators, we tested our method with three of the synthetic VLBA data sets presented in Park et al. (2021b). Synthetic data sets were produced using `PolSimulate` in the `CASA` software (McMullin et al. 2007) with OJ287, 3C273, BLLac uv-coverage at 15GHz by 10 VLBA antennas. More details regarding the synthetic data can be found in Park et al. (2021b). The ground truth image consists of three point sources. The ground truth image colvolved with the nominal CLEAN beam with the uniform weighting is in Figure 1. We assume that there is no gain corruption in the data.

The polarization calibration with synthetic data was performed as follows. First of all, initial D-term estimates were obtained by the maximum a-posteriori (MAP) method using all three calibrator data sets. Then, the posterior distribution of Stokes images and D-term was reconstructed with 3C273 synthetic data using the geoVI method (Frank et al. 2021) starting from estimated MAP D-terms as the initial condition. Figure 1 shows the resolve total intensity image and EVPAs with colors corresponding to the fractional linear polarization (right panel). We chose a spatial domain of 256 × 256 pixels and a field of view of 10 mas × 10mas. The resolve image was able to recover three linearly polarized components (with the fractional linear polarization 2%, 5%, and 11% respectively).

Figure 2 represents a comparison between the resolve D-term posterior distribution and the ground truth D-terms. The resolve posterior distribution is obtained from 100 posterior samples using Gaussian kernel density distribution in `Scipy` Python library (Virtanen et al. 2020). Overall, the reconstructed D-term posterior distributions using `resolve` are consistent with the ground truth D-terms within the 2σ errors. This results demonstrate that the resolve polarization calibration and imaging method is able to reconstruct reliable D-term solutions and Stokes images using multiple calibrator data sets.

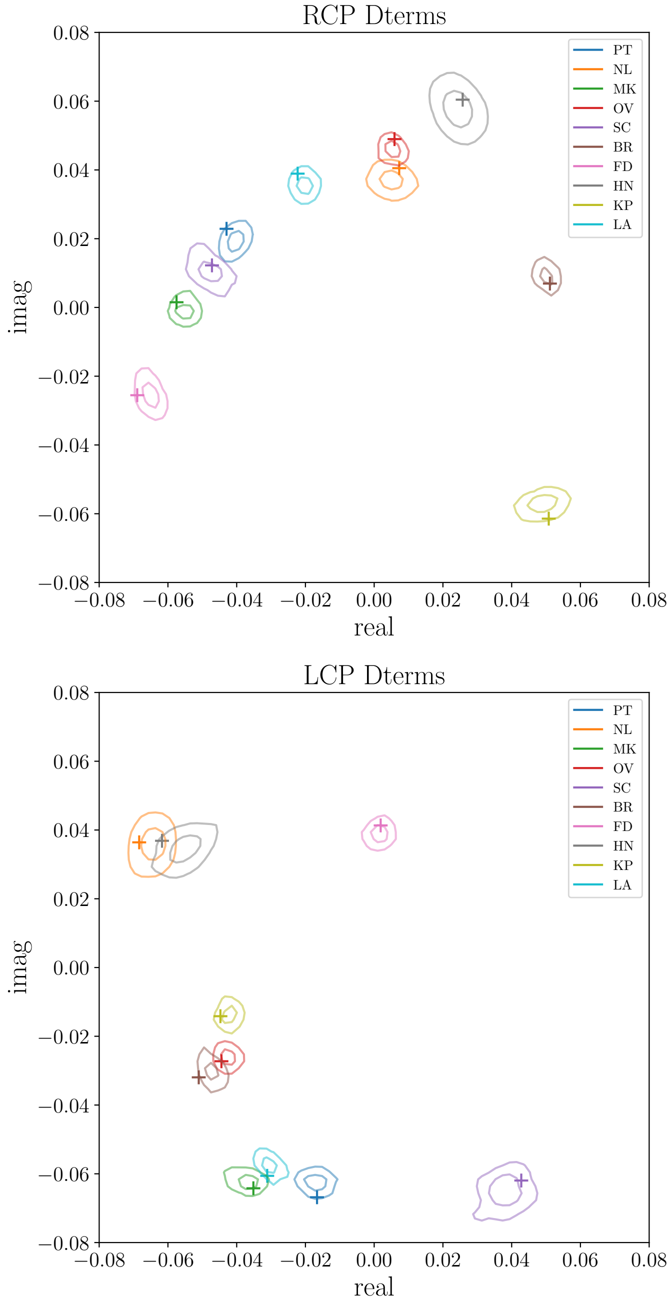

Fig. 2. Comparison between the D-term posterior using `resolve` and ground truth D-terms from the synthetic data. Contours show 1σ and 2σ cumulative regions of resolve posterior D-terms using Gaussian kernel density estimation. The plus signs correspond to the ground truth D-terms.

4. Application to real data

4.1. 3C273 VLBA observation at 15 GHz

We applied our Bayesian polarization calibration and imaging method to pre-calibrated (without self-calibration and D-term calibration) 3C273 VLBA MOJAVE survey data at 15 GHz on

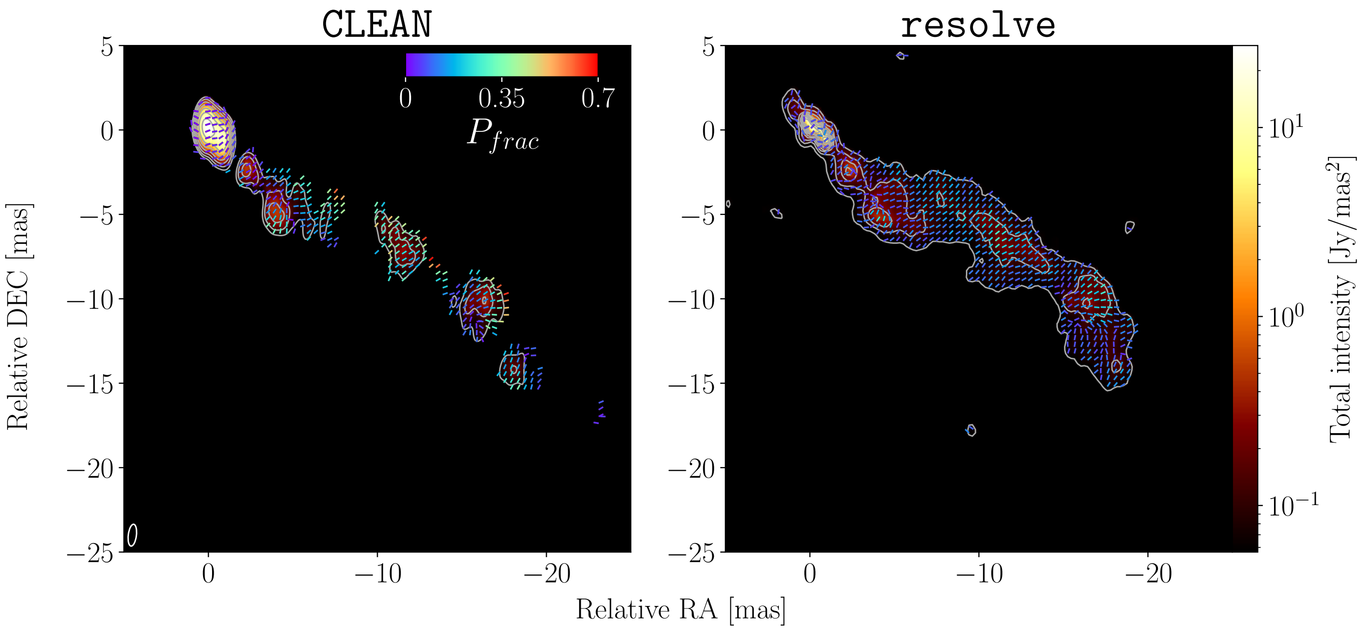

Fig. 3. Comparison between the 3C273 VLBA CLEAN and resolve posterior mean linear polarization reconstructions at 15 GHz. Colored ticks indicate EVPAs, with colors corresponding to the fractional linear polarization P_{frac}. The contours representing the total intensity of corresponding images increase by a factor of 2, starting from 1% of the peak CLEAN total intensity.

28 January 2017 (Lister et al. 2018) in order to demonstrate that `resolve` is able to infer D-terms per intermediate frequency (IF) from a source with complex structure. The data have 8 IFs (32MHz each) and the total bandwidth is 256MHz.

We reconstructed the resolve Stokes images with a spatial domain of 256 × 256 and a field of view of 50 mas × 50 mas. For the resolve reconstruction, we added a 10 % systematic error budget in the data. The reduced χ^2 of the resolve reconstruction was 1.2, and the number of posterior samples was 20. The wall-clock time for the resolve reconstruction was around 5 hours on a single node of the MPIfR cluster with 10 MPI (Message Passing Interface) tasks.

We assumed that Stokes images do not vary over frequencies due to the narrow bandwidth (256 MHz), and performed antenna gain self-calibration and leakage calibration per IF. For the absolute EVPA calibration, we applied the same correction value from the MOJAVE team for the CLEAN reconstruction. The model parameters for polarization imaging prior, gain prior, and D-term prior for the 3C273 VLBA data can be found in Table A.1 and Table A.2.

Figure 3 shows a comparison of linear polarization reconstructions from CLEAN and the resolve posterior mean. EVPA colors correspond to the fractional linear polarization, and contours represent the total intensity of the corresponding images. The CLEAN images are taken from the MOJAVE archive[2]. For the CLEAN reconstruction, the MOJAVE team performed self-calibration and image reconstruction using the `DIFMAP` software (Shepherd 1997) and the `LPCAL` task (Leppanen et al. 1995) in the `AIPS` software (Greisen 2003) for polarization calibration. The D-term solutions using `LPCAL` are the median solution values from all sources in the epoch after removing obvious outliers (Lister & Homan 2005).

In the core region, the resolve image shows improved resolution compared to the core in the CLEAN image. The extended total intensity emission in the resolve image is overall consistent with the CLEAN reconstruction but it looks more continuous since the spatial correlations between pixels are inferred from the data in `resolve`. We note that it is also possible to use an over-resolved CLEAN beam to obtain a CLEAN image with higher resolution. However, an image convolved with an over-resolved CLEAN beam cannot adequately describe the continuous extended jet and it may result in unrealistic fractional linear polarization ($I < \sqrt{Q^2 + U^2 + V^2}$). In contrast to `CLEAN`, `resolve` can describe complex source structure spanning a range of spatial scales using the Gaussian process sky prior we described, which is aware of spatial correlations of the polarized flux while ensuring the polarization constraints at each image pixel individually.

The linear polarization comparison between `CLEAN` and `resolve` shows noticeable differences. The fractional linear polarization on the edges of linearly polarized emission in the CLEAN reconstruction is relatively higher than that in the resolve reconstruction. The discrepancy may result from the lack of a polarization constraint in the CLEAN imaging prior or biases from the similarity approximation in `CLEAN`-based polarization calibration. Encoding the polarization constraint that the maximum linear polarization is 100 % in the prior facilitates physically sensible reconstruction consistent with the theoretical fractional linear polarization for optically thin synchrotron radiation from non-thermal electrons with a power law distribution of energies (up to 75 %; Rybicki & Lightman (1979)).

The EVPA pattern is generally consistent except for the core region due to the improved resolution in the resolve image. Both images show the rotational EVPA structure at the core but the resolve image exhibits thinner emission structures that show more abrupt changes. Figure D.1 shows the 3C273 resolve EVPA standard deviation. We note that a robust rotation measure can be estimated using the Bayesian approach (Vogt & Enßlin 2005). A detailed investigation of Bayesian rotation measure analysis using our method is left for future work.

For the leakage calibration, a total of 160 D-terms (2 polarization modes × 10 antennas × 8 IFs) are inferred since the D-terms in MOJAVE observations with VLBA at 15 GHz tend to be

---

[2] `https://www.cv.nrao.edu/MOJAVE/`

different per IF. This approach of reconstructing D-terms per IF is highly desirable, especially for wide-band observations, as the signal path for each IF is different which can result in changes to the D-terms for each IF separately. We also note that base-band boundaries can cause jumps in leakage that will also differ for the individual IFs (Martí-Vidal et al. 2021).

In Figure C.1, the resolve D-term posterior means and D-terms obtained using the `LPCAL` software are shown to be consistent with each other, as they are strongly correlated. It is important to note that the resolve D-term solutions are from 3C273 data only and D-terms using `LPCAL` are the median values of D-term solutions from multiple sources. The results indicate that our Bayesian polarization calibration method is able to estimate reliable D-terms from data with complex source structures. A more detailed analysis with additional data sets is deferred to future work.

4.2. OJ287 GMVA+ALMA observation at 86 GHz

Zhao et al. (2022) report the GMVA+ALMA observation of the blazar OJ 287 at 86 GHz on 2. April 2017. The blazar OJ 287 is a supermassive binary black hole candidate showing quasiperiodic optical outbursts with a period of about 12 years (Sillanpaa et al. 1988). GMVA observations jointly with the phased ALMA provide high fidelity images due to the improved sensitivity and long north-south baselines (Issaoun et al. 2019; Zhao et al. 2022; Lu et al. 2023; Kim et al. 2025). However, polarization calibration and imaging for mm-VLBI observations are demanding due to the low S/N of the polarized signals, tropospheric phase corruption, and heterogeneous antenna statistics, such as in GMVA+ALMA data.

We revisit the GMVA+ALMA observation of the blazar OJ 287 at 86 GHz in Zhao et al. (2022) to validate our Bayesian polarization calibration and imaging method using pre-calibrated data. For polarization calibration, robust gain self-calibration is required due to the degeneracy between D-terms and gains. Kim et al. (2024, 2025) validate the `resolve` self-calibration methods with mm-VLBI data sets. Reconstructed antenna gain solutions from the VLBA M87 observation in 2013 at 43GHz indicate that gain solutions from a homogeneous array with high S/N are consistent among `CLEAN`, `ehtim`, and `resolve` methods (Kim et al. 2024). However, `CLEAN` self-calibration utilizes a crude regularizer (e.g., a uniform solution interval for different antenna gain solutions) and often flags a significant fraction of the data. Therefore, those limitations may hinder robust self-calibration for mm-VLBI observations.

To mitigate this issue, we employed different correlation kernels for antenna gain amplitude solutions in order to take into account heterogeneous array sensitivity. For the gain phase prior, we utilized uncorrelated normally distributed phases due to the short phase coherence time in GMVA observations at 86 GHz (Kim et al. 2025). Employing a different gain amplitude kernel per antenna is analogous to setting up different solution interval constraints per antenna in self-calibration. In `resolve`, the time correlations in the gain solutions are inferred from the data in an automated fashion and the large uncertainties of particular data points are taken into account naturally in the Bayesian framework. Therefore, we are able to perform more robust self-calibration without flagging a significant number of the data points compared to `CLEAN`-based self-calibration methods. Furthermore, the large gain uncertainties inherent to mm-VLBI observations are explicitly accounted for and propagated into the image domain. As a result, the reliability of calibration and imaging is quantified through uncertainty estimation.

Polarization calibration for mm-VLBI data sets presents several additional challenges. In mm-VLBI, we often use the target data for D-term calibration due to a lack of point-like calibrators. Polarization leakages tend to be higher in mm-VLBI than in cm-VLBI, and the high resolution often reveals complex source polarization structures. Thus, precise D-term calibration is crucial to obtain reliable polarimetric images, and accurate polarimetric images, in turn, improve D-term calibration. However, in conventional polarization calibration methods, utilizing the similarity approximation or CLEAN images as a prior hinders the reconstruction of complex polarization structures since a few sub-components in the similarity approximation and the collection of delta components in the CLEAN reconstruction cannot accurately represent the extended emission and complex source structures that are smaller than the CLEAN beam. On the other hand, in `resolve`, polarization imaging models with complex source structures, satisfying the polarization constraint and consistent with the data, are utilized for more robust polarization calibration.

The data are time-averaged with 15 seconds and frequency-averaged for `ehtim` and `resolve` software, since the antenna leakages in the data are similar over frequencies (Zhao et al. 2022). For the CLEAN image, self-calibration and image reconstruction were performed using the `DIFMAP` software and the `LPCAL` method of the `AIPS` software was used for leakage calibration using 4 individual intermediate frequencies (IFs). For the ehtim reconstruction, self-calibration and polarization calibration were performed in an iterative fashion using the `ehtim` software. The details regarding the CLEAN and ehtim polarization calibration and image reconstructions can be found in Zhao et al. (2022).

For the resolve reconstruction, Stokes I, Q, U, and V images with a spatial domain of 256×256 piexels and a field of view of $500\,\mu$as $\times$ $500\,\mu$as, as well as gain solutions with a time interval of 15 seconds and leakage solutions, are inferred simultaneously. The reduced χ^2 of the resolve reconstruction was 1.2, and the number of posterior samples was 100. The wall-clock time for the resolve reconstruction was around 8.5 hours on a single node of the MPIfR cluster with 25 MPI tasks. The model parameters for polarization imaging prior, gain prior, and D-term prior for the OJ287 GMVA+ALMA data can be found in Table A.3 and Table A.4.

Figure 4 depicts the total intensity with EVPAs of the blazar OJ287 at 86 GHz using three different imaging algorithms: `CLEAN`, `ehtim` from Zhao et al. (2022), and `resolve`. All three image reconstructions show three main components in the total intensity and diverging EVPAs in the north-west component. Furthermore, the curved jet (middle component) from the core (south-east component) is recognizable only in the ehtim and resolve images. In contrast, `CLEAN` has limitations in reconstructing smaller scale structures than the CLEAN beam. The ehtim and resolve images show better resolution than the CLEAN image because forward modeling permits partial removal of the observational point spread function during the data inversion process. The ehtim image exhibits higher resolution than the resolve image, since the sparsity promoting regularizers in `ehtim` tend to produce extremely sharp structures.

For polarization imaging, polarization constraints are encoded in `resolve` and `ehtim`. We performed the absolute EVPA calibration using the reported integrated EVPA of ALMA-only OJ287 image at 86 GHz in Goddi et al. (2021). The details of the absolute EVPA calibration method can be found in Appendix B. In Figure 4, the EVPAs in the north-west jet component diverge in all three images. The fractional linear polarization along

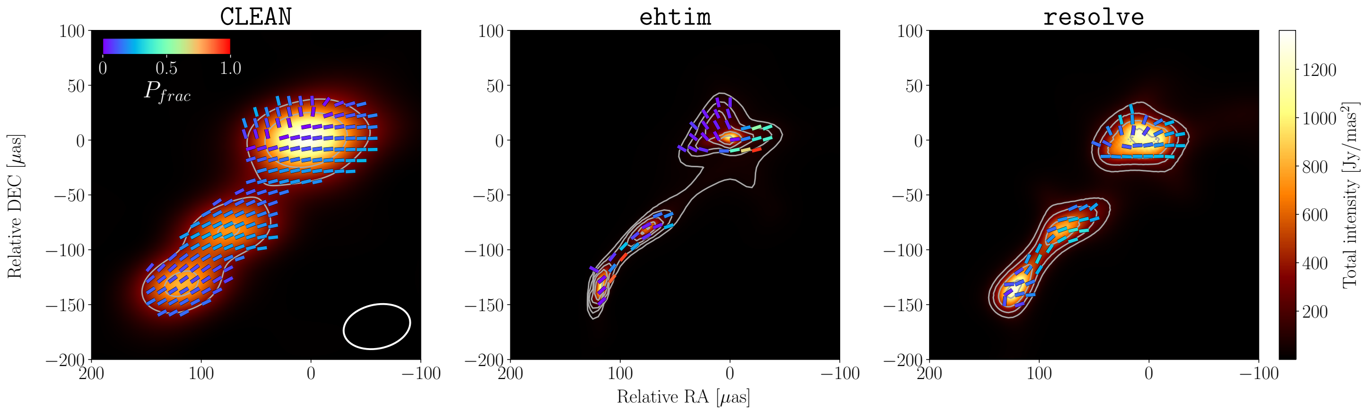

Fig. 4. Comparison among the OJ287 GMVA+ALMA CLEAN, ehtim, and resolve posterior mean linear polarization reconstructions at 86 GHz. Colored ticks indicate EVPAs, with colors corresponding to the fractional linear polarization $P_{\rm frac}$. The contours representing the total intensity of the corresponding images increase by a factor of 2, starting from 10% of the peak resolve posterior mean total intensity. All images were processed by Gaussian interpolation.

the north-east direction in the diverging jet component increases gradually in the images from `CLEAN` and `resolve`, whereas the ehtim image shows a nearly monotonous fractional linear polarization. In the ehtim image, there are extremely highly polarized pixels ($P_{\rm frac} > 99$ %) that may be imaging artifacts caused by the sparsity regularizers. A high fractional linear polarization (> 75 %) indicates optically thin synchrotron radiation from a uniform magnetic field and the absence of Faraday depolarization. However, such a scenario is unrealistic, since the EVPA reconstruction of OJ287 shows complex structure indicating a non-uniform magnetic field. We note that the Faraday rotation of OJ287 from the ALMA-only observation is $3.05 \pm 0.62 \times 10^3\,{\rm rad\,m^{-2}}$ (Goddi et al. 2021), which is relatively small, Faraday depolarization therefore can be negligible.

The south-east core component and the middle jet component show EVPAs along the jet direction. This indicates toroidal magnetic fields, given that the relatively small rotation measure from the ALMA observation (Goddi et al. 2021). In the ehtim and resolve images, we see bending EVPA patterns, and the pattern is more wiggling in the resolve image. The diverging EVPA pattern in the north-west jet component can be explained by oblique or recollimation shocks (Zhao et al. 2022). Figure D.2 shows the OJ287 resolve EVPA posterior standard deviation.

Figure 5 shows the amplitude gain posterior distribution. Different correlation kernels per antenna are employed to infer different temporal correlation structure arising from the heterogeneous antenna sensitivities. We utilized a uncorrelated phase gain prior since the phase coherence time is comparable to the averaging time (15 seconds).

Figure 6 depicts a comparison between the resolve D-term posterior distributions and reconstructed D-terms using `ehtim`. The resolve and ehtim D-terms are broadly consistent. In Figure C.2, cross correlation plots between resolve posterior D-terms and ehtim reconstructed D-terms are shown. They exhibit strong positive correlations, but some antennas (e.g., PT) show weaker positive correlations. This discrepancy between `resolve` and `ehtim` results from the highly corrupted phases at 3mm and the different self-calibration and flagging routines used. For polarization calibration and imaging, `ehtim` used 8 antennas out of 13, whereas `resolve` utilized all antennas (YS observed only single polarization; therefore, we show the resolve D-terms for 12 antennas). In `resolve`, non-Gaussian leakage posterior distributions were obtained using the geoVI method. A few antennas (e.g., BR and ON) exhibit higher uncertainty in the D-term phase due to highly corrupted visibility phases. The ehtim D-terms are overall consistent with D-terms obtained from the `LPCAL` software (Zhao et al. 2022). In conclusion, the D-term solutions are in good agreement across the `resolve`, `ehtim`, and `LPCAL` methods.

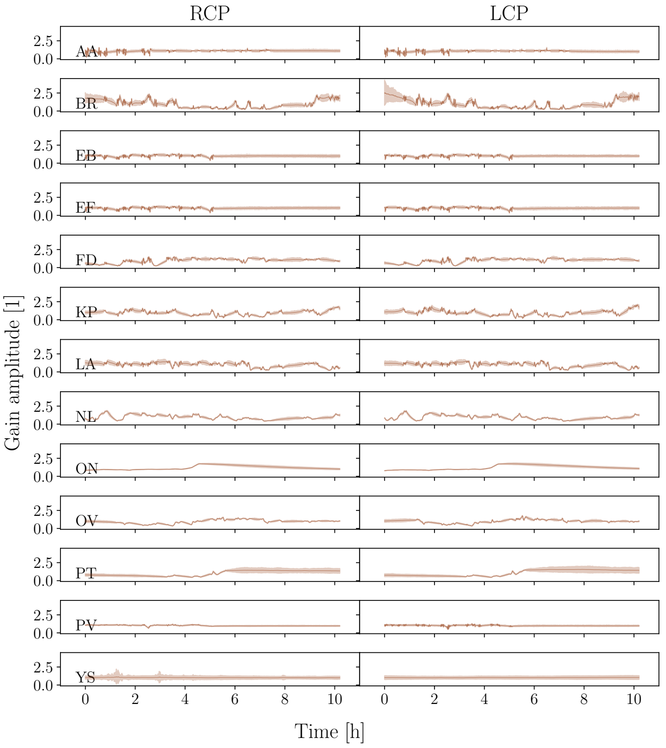

Fig. 5. Posterior amplitude gains of the OJ287 GMVA+ALMA observation using `resolve`. The solid line represents the amplitude gain posterior mean with a semi-transparent standard deviation. Each row represents an individual antenna with corresponding abbreviated name in the bottom left corner of each RCP plot.

We note that RML methods can be interpreted as maximum a-posteriori (MAP) estimation in Bayesian language (Kim et al. 2024). However, the point estimation cannot represent calibration solutions with high uncertainties well, and the MAP estimation is prone to overfitting the data. Furthermore, `ehtim` does not support multi-scale bases functions. In contrast to `resolve`,

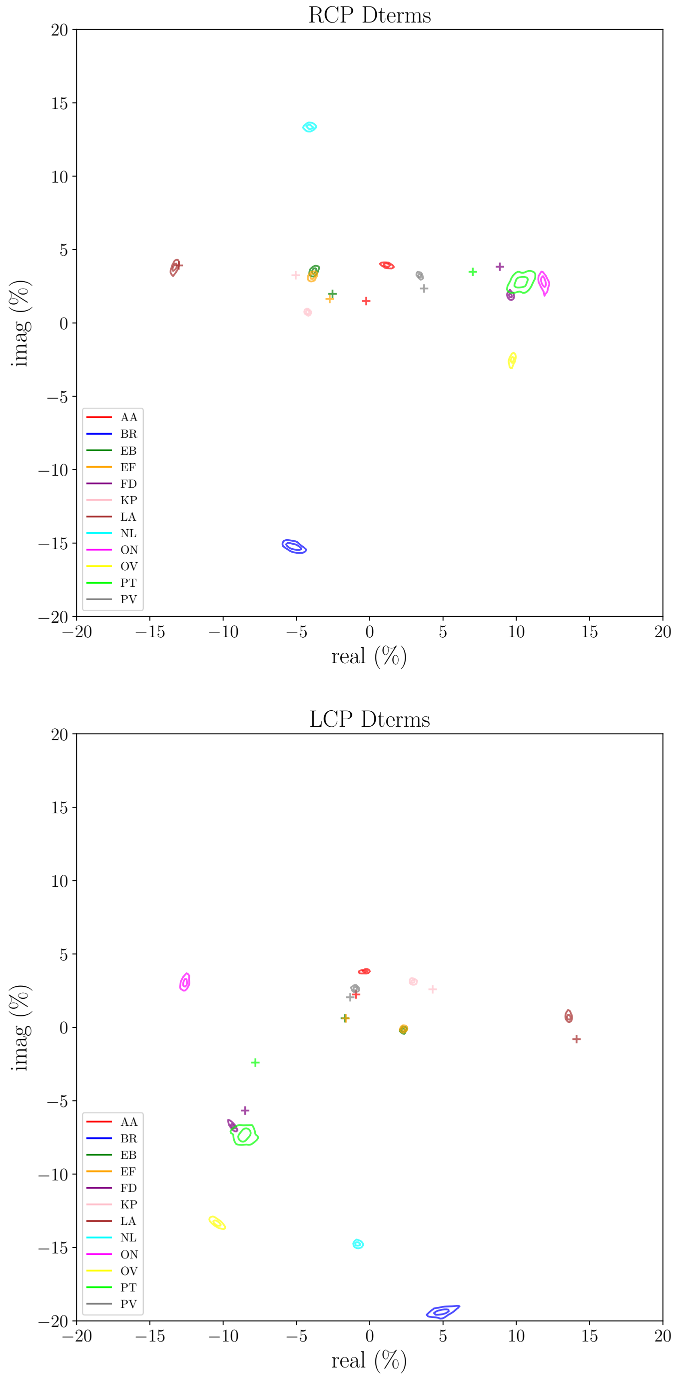

Fig. 6. Comparison between OJ287 GMVA+ALMA D-term posterior distributions using `resolve` and D-term solutions using `ehtim`. Contours show 1σ and 2σ cumulative regions of resolve posterior D-terms using Gaussian kernel density estimation. The plus signs correspond to the reconstructed D-terms using `ehtim`.

it tends to produce extremely sharp features. Different correlation structures between the core and jet cannot be adequately described due to the sparsity promoting priors, such as the l_1-norm, total variation (TV), and total squared variation (TSV). Employing extremely sharp images as a model in polarization calibration may result in biased D-terms and polarization images. A more detailed discussion of the Bayesian interpretation of regularizers in RML method can be found in the Appendix B of Kim et al. (2024).

In short, the resolve reconstructions of 3C273 at 15 GHz OJ 287 at 86 GHz demonstrate that our Bayesian polarization calibration and imaging pipeline can obtain reliable super-resolution polarimetric images, D-terms and gain solutions from VLBI data. Reconstructed Stokes images are utilized as a polarization calibration model, enabling to obtain more complex polarization structures than conventional `CLEAN`-based methods. Uncertainty estimation of reconstructed images and calibration solutions in `resolve` is especially beneficial in mm-VLBI due to the high calibration uncertainties from tropospheric phase corruptions and antenna leakages. In our method, calibration uncertainties are accounted for in our reconstructed images and we are able to quantify the reliability of Stokes images and calibration solutions.

5. Conclusions

In this work, we have presented a novel Bayesian polarization calibration and imaging method using the `resolve` algorithm. Our method can simultaneously reconstruct high-resolution polarimetric images satisfying the polarization constraint ($I \geq \sqrt{Q^2 + U^2 + V^2}$), antenna-based gains, and polarization leakages from the entire data set. The polarization calibration is based on the reconstructed Stokes images instead of the similarity approximation used in traditional approaches, which does not hold for complex polarized emission patterns. Therefore, we can reconstruct reliable polarimetric images with complex structures and more robust calibration solutions, consistent with the entire data set. Moreover, multi-source and multi-IF polarization calibration is supported owing to the scalability of `resolve`, achieved through variational inference methods (Knollmüller & Enßlin 2019; Frank et al. 2021).

We have demonstrated our method with synthetic and real observations. Examples using the quasar 3C273 MOJAVE VLBA data at 15 GHz and the blazar OJ287 GMVA+ALMA observation at 86 GHz show that `resolve` can reconstruct polarimetric images with super-resolution (Honma et al. 2014), revealing structures below the synthesized beam, which is the resolution limit of the conventional `CLEAN`-based methods. The fractional linear polarization in resolve images is consistent with the theoretical estimation for synchrotron radiation ($< 75\%$) in AGN jets.

Reconstructed D-terms obtained with `resolve` are consistent with those from the conventional `CLEAN`-based method and the RML-based method `ehtim`. Furthermore, our RIME-based Bayesian polarization calibration and imaging method is able to reconstruct D-term solutions from target data with complex source structure without using calibrators.

Validation with synthetic and real data sets indicates that incorporating polarization calibration into imaging is beneficial for sparse and noisy VLBI data sets in order to estimate reliable and reproducible calibration solutions and images. Calibration uncertainties are explicitly taken into account in our final resolve results, and the reliability of the gain and leakage solutions was estimated. For future work, the EVPA posterior distribution can be utilized for rotation measure analysis, and frequency-dependent D-term calibration within the Bayesian framework should be investigated for wide-band radio interferometric observations. The pipeline is publicly accessible at `https://github.com/JongseoKim/resolve_polcal`

Acknowledgements. We thank Yuri Kovalev for comments on the manuscript and providing the MOJAVE data, Guang-Yao Zhao and Jose Gomez for providing the GMVA+ALMA OJ287 data. J. K. received financial support for this research from the International Max Planck Research School (IMPRS) for Astronomy and Astrophysics at the Universities of Bonn and Cologne. This work was supported by the M2FINDERS project funded by the European Research Council (ERC) under the European Union's Horizon 2020 Research and Innovation Programme (Grant Agreement No. 101018682). J. R. acknowledges financial support from the German Federal Ministry of Education and Research (BMBF) under grant 05A23WO1 (Verbundprojekt D-MeerKAT III)

References

Arras, P., Baltac, M., Enßlin, T., et al. 2019a, NIFTy5: Numerical Information Field Theory v5
Arras, P., Bester, H. L., Perley, R. A., et al. 2021, Astronomy & Astrophysics, 646, A84
Arras, P., Frank, P., Leike, R., Westermann, R., & Enßlin, T. A. 2019b, A&A, 627, A134
Arras, P., Roth, J., Reinecke, M., et al. 2025, arXiv e-prints, arXiv:2504.00227
Asada, K., Inoue, M., Kameno, S., & Nagai, H. 2008, ApJ, 675, 79
Birdi, J., Repetti, A., & Wiaux, Y. 2018, MNRAS, 478, 4442
Birdi, J., Repetti, A., & Wiaux, Y. 2020, MNRAS, 492, 3509
CASA Team, Bean, B., Bhatnagar, S., et al. 2022, PASP, 134, 114501
Cornwell, T. J. 2008, IEEE Journal of Selected Topics in Signal Processing, 2, 793
Cotton, W. D. 1993, AJ, 106, 1241
Event Horizon Telescope Collaboration. 2025, arXiv e-prints, arXiv:2509.24593
Event Horizon Telescope Collaboration, Akiyama, K., Alberdi, A., et al. 2024, ApJ, 964, L25
Event Horizon Telescope Collaboration, Akiyama, K., Alberdi, A., et al. 2019, ApJ, 875, L1
Event Horizon Telescope Collaboration, Akiyama, K., Algaba, J. C., et al. 2021, ApJ, 910, L12
Frank, P., Leike, R., & Enßlin, T. A. 2021, Entropy, 23, 853
Gabuzda, D. C., Roche, N., Kirwan, A., et al. 2017, MNRAS, 472, 1792
Goddi, C., Martí-Vidal, I., Messias, H., et al. 2021, ApJ, 910, L14
Greisen, E. W. 2003, in Astrophysics and Space Science Library, Vol. 285, Information Handling in Astronomy - Historical Vistas, ed. A. Heck, 109
Hamaker, J. P., Bregman, J. D., & Sault, R. J. 1996, A&AS, 117, 137
Hamaker, J. P., Bregman, J. D., & Sault, R. J. 1996, Astronomy and Astrophysics Supplement Series, 117, 137
Honma, M., Akiyama, K., Uemura, M., & Ikeda, S. 2014, PASJ, 66, 95
Hovatta, T., Lister, M. L., Aller, M. F., et al. 2012, AJ, 144, 105
Issaoun, S., Johnson, M. D., Blackburn, L., et al. 2019, ApJ, 871, 30
Janssen, M., Goddi, C., van Bemmel, I. M., et al. 2019, A&A, 626, A75
Jones, R. C. 1941, Journal of the Optical Society of America (1917-1983), 31, 488
Kim, J.-S., Müller, H., Nikonov, A. S., et al. 2025, A&A, 696, A169
Kim, J.-S., Nikonov, A. S., Roth, J., et al. 2024, A&A, 690, A129
Knollmüller, J. & Enßlin, T. A. 2019, arXiv e-prints, arXiv:1901.11033
Knollmüller, J. & Enßlin, T. A. 2018, Encoding prior knowledge in the structure of the likelihood
Leppanen, K. J., Zensus, J. A., & Diamond, P. J. 1995, AJ, 110, 2479
Lister, M. L., Aller, M. F., Aller, H. D., et al. 2018, ApJS, 234, 12
Lister, M. L. & Homan, D. C. 2005, AJ, 130, 1389
Lu, R.-S., Asada, K., Krichbaum, T. P., et al. 2023, Nature, 616, 686
Martí-Vidal, I. & Marcaide, J. M. 2008, A&A, 480, 289
Martí-Vidal, I., Mus, A., Janssen, M., de Vicente, P., & González, J. 2021, A&A, 646, A52
McMullin, J. P., Waters, B., Schiebel, D., Young, W., & Golap, K. 2007, in Astronomical Society of the Pacific Conference Series, Vol. 376, Astronomical Data Analysis Software and Systems XVI, ed. R. A. Shaw, F. Hill, & D. J. Bell, 127
Park, J., Asada, K., & Byun, D.-Y. 2023, ApJ, 958, 27
Park, J., Asada, K., Nakamura, M., et al. 2021a, ApJ, 922, 180
Park, J., Byun, D.-Y., Asada, K., & Yun, Y. 2021b, ApJ, 906, 85
Pesce, D. W. 2021, AJ, 161, 178
Popkov, A. V., Kovalev, Y. Y., Petrov, L. Y., & Kovalev, Y. A. 2021, AJ, 161, 88
Pushkarev, A. B., Aller, H. D., Aller, M. F., et al. 2023, MNRAS, 520, 6053
Raymond, A. W., Doeleman, S. S., Asada, K., et al. 2024, AJ, 168, 130
Roth, J., Arras, P., Reinecke, M., et al. 2023, A&A, 678, A177
Roth, J., Frank, P., Bester, H. L., et al. 2024, A&A, 690, A387
Rybicki, G. B. & Lightman, A. P. 1979, Radiative processes in astrophysics
Selig, M., Bell, M. R., Junklewitz, H., et al. 2013, A&A, 554, A26
Shepherd, M. C. 1997, in Astronomical Society of the Pacific Conference Series, Vol. 125, Astronomical Data Analysis Software and Systems VI, ed. G. Hunt & H. Payne, 77
Sillanpaa, A., Haarala, S., Valtonen, M. J., Sundelius, B., & Byrd, G. G. 1988, ApJ, 325, 628
Smirnov, O. M. 2011, A&A, 527, A106
Smirnov, O. M. 2011, Astronomy & Astrophysics, 527, A106
Thompson, A. R., Moran, J. M., & Swenson, Jr., G. W. 2017, Interferometry and Synthesis in Radio Astronomy, 3rd Edition
Virtanen, P., Gommers, R., Oliphant, T. E., et al. 2020, Nature Methods, 17, 261
Vogt, C. & Enßlin, T. A. 2005, A&A, 434, 67
Zhao, G.-Y., Gómez, J. L., Fuentes, A., et al. 2022, ApJ, 932, 72

Appendix A: Hyperparameter setup

Appendix B: Absolute EVPA calibration

Most VLBI observations use circular polarization feeds. Therefore, we need to constrain the arbitrary phase difference between the right and left circular polarization feeds (RCP and LCP) at each frequency in the fully station based approach to polarization classification and calibration (Cotton 1993; Leppanen et al. 1995). This process is called absolute EVPA calibration. The simplest approach to determining this phase offset is to use a trusted external observation as an 'anchor'. External anchors are typically observations with a single dish, an interferometer with linear polarization feeds, or an observation that has already calibrated the phase difference between RCP and LCP independently. This method relies on the assumption that the signal of a 'target' observation is similar to that of the anchoring observation, in both time and the physical structure of the emission. As such, the best calibrated sources for absolute EVPA calibration have the following three characteristics;

1. The source has sufficient linear polarization in both the target observation and anchor observation.
2. The source is not highly variable in time; as such does not vary between the two observations.
3. The source is compact; this is particularly relevant when comparing a target VLBI observation against single dish or unresolved non-VLBI observations as we assume the emission from both observations comes from the same physical structure of the source.

To compute the RCP-LCP phase correction we take twice the EVPA offset between the target and anchor observations. Typically, the EVPA offset is found by calculating the integrated Stokes Q and U flux density of both observations and calculating an integrated EVPA as $\mathrm{EVPA} = 0.5 \arctan[\mathrm{U}/\mathrm{Q}]$. This can be done by only considering Stokes Q and U emission that is co-spatial with Stokes I emission to ensure a direct comparison between the target and anchor.

For our reconstruction of OJ287 in Figure 4, we calculated the integrated EVPA of our reconstructed resolve image of Stokes Q and U and compared it to ALMA observations with the EVPA - 69.69° at 86.3 GHz in Goddi et al. (2021). From this we found an EVPA correction of -16.07° based on the OJ287 resolve integrated EVPA and ALMA-only EVPA.

Appendix C: D-term cross correlation plots

Appendix D: EVPA posterior standard deviation plots

Table A.1. Model parameters for the resolve 3C273 polarization imaging priors s, q, u, and v.

	s mean	s std	q, u mean	q, u std	v mean	v std
Offset	35.0	—	0.0	—	0.0	—
Zero mode variance	1.0	0.1	0.01	0.01	0.001	0.001
Fluctuations	3.0	1.0	0.05	0.05	0.005	0.005
Flexibility	1.2	0.4	0.1	0.1	0.1	0.1
Asperity	—	—	—	—	—	—
Average slope	-3.0	1.0	-3.0	1.0	-3.0	1.0

Table A.2. Model parameters for the resolve 3C273 log-amplitude gain prior λ, phase gain prior ϕ, log-amplitude D-term prior a, and phase D-term prior b.

	λ mean	λ std	ϕ mean	ϕ std		a	b
Offset	0.0	—	0.0	—	Mean	-2.5	0.0
Zero mode variance	0.1	0.01	0.2	0.1	Std	1.0	3.0
Fluctuations	0.2	0.1	0.2	0.1			
Flexibility	0.5	0.2	0.5	0.2			
Asperity	None	None	None	None			
Average slope	-3.0	1.0	-3.0	1.0			

Table A.3. Model parameters for the resolve OJ287 polarization imaging priors s, q, u, and v.

	s mean	s std	q, u mean	q, u std	v mean	v std
Offset	38.0	—	0.0	—	0.0	—
Zero mode variance	1.0	0.1	0.01	0.01	0.001	0.001
Fluctuations	3.0	1.0	0.05	0.05	0.005	0.005
Flexibility	1.2	0.4	0.1	0.1	0.1	0.1
Asperity	—	—	—	—	—	—
Average slope	-3.0	0.5	-3.0	0.5	-3.0	0.5

Table A.4. Model parameters for the resolve OJ287 log-amplitude gain prior λ, phase gain prior ϕ, log-amplitude D-term prior a, and phase D-term prior b.

	λ mean	λ std		ϕ	a	b
Offset	0.0	—	Mean	0.0	-2.5	0.0
Zero mode variance	1e-3	1e-6	Std	2.0	0.5	3.0
Fluctuations	0.2	0.1				
Flexibility	0.5	0.2				
Asperity	None	None				
Average slope	-3.0	1.0				

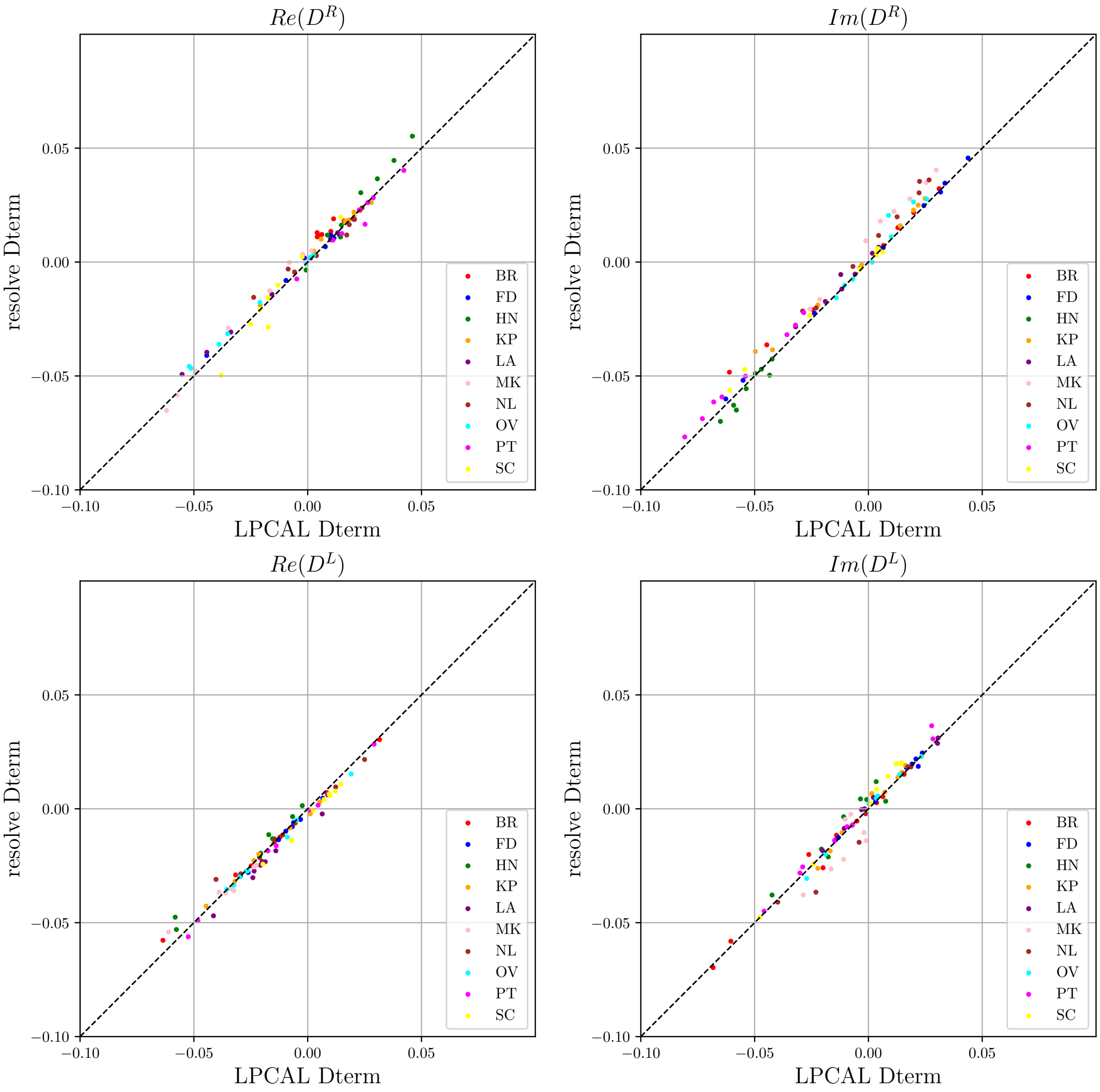

Fig. C.1. Cross correlation plots between 3C273 resolve posterior mean D-terms and LPCAL D-terms.

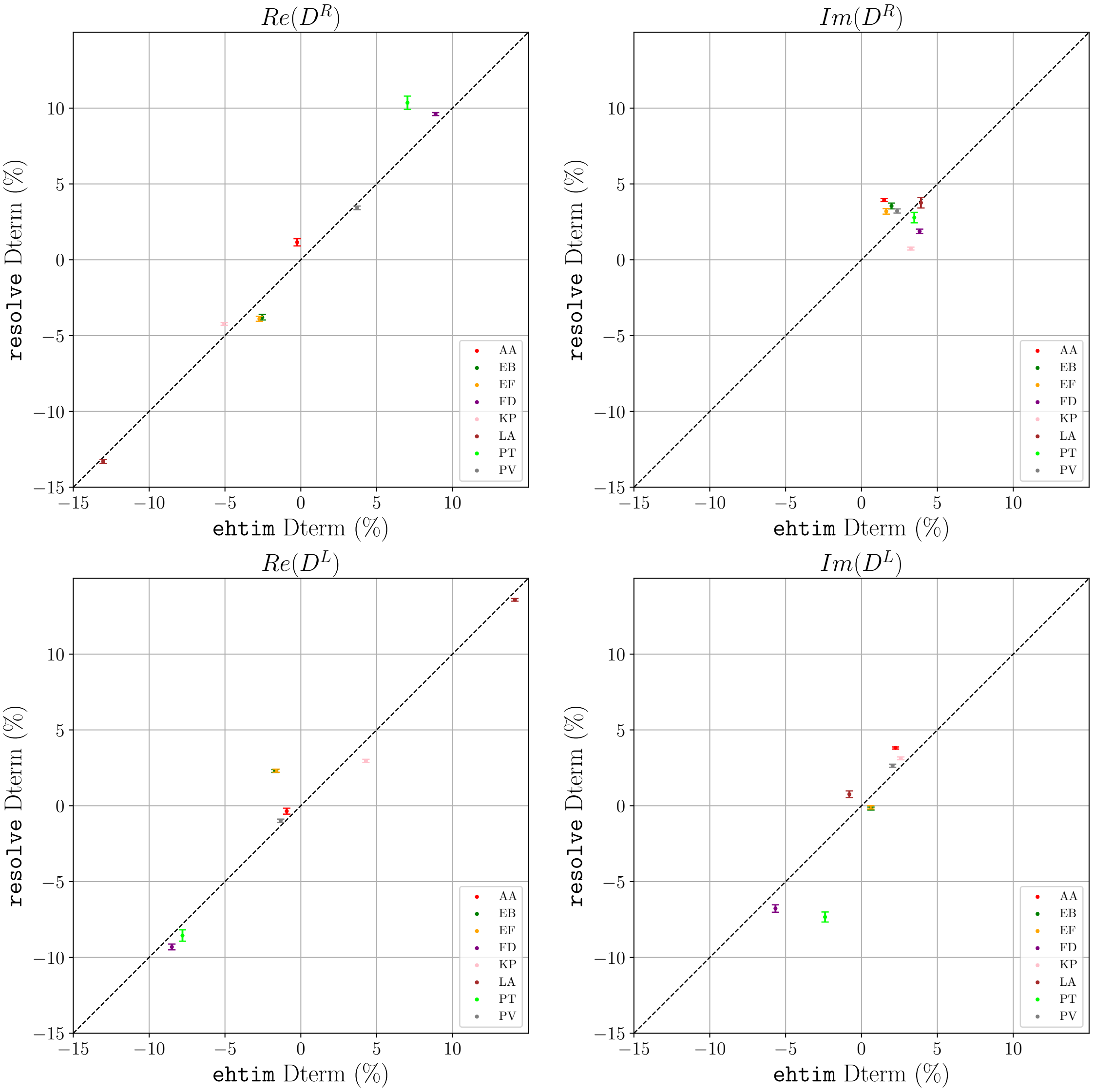

Fig. C.2. Cross correlation plots between OJ287 GMVA+ALMA D-term posterior means using `resolve` and D-term solutions using `ehtim`.

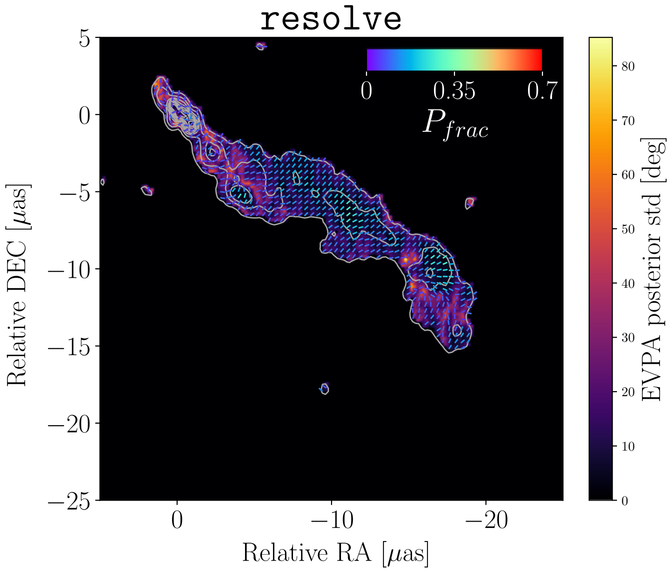

Fig. D.1. EVPA posterior standard deviation map of the 3C273 observation at 15GHz using `resolve`. The contours representing the total intensity resolve posterior mean image increase by a factor of 2, starting from 1% of the peak CLEAN total intensity.

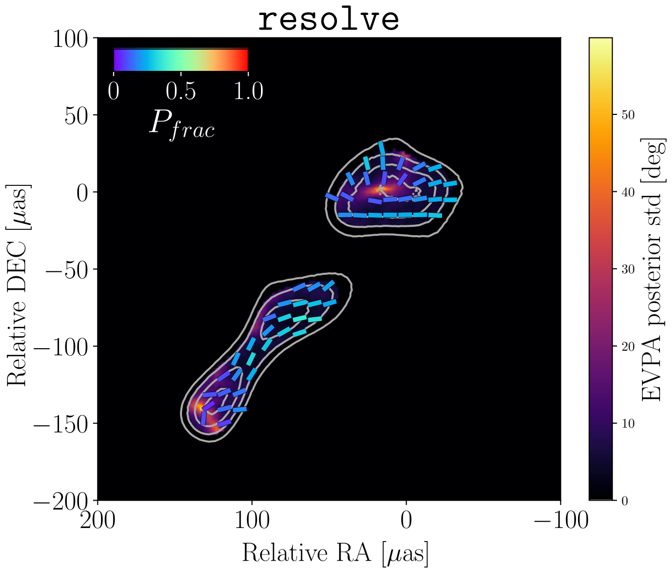

Fig. D.2. EVPA posterior standard deviation map of the OJ287 GMVA+ALMA observation at 86GHz using `resolve`. The contours representing the total intensity resolve posterior mean image increase by a factor of 2, starting from 10% of the peak resolve posterior mean total intensity.

Chapter 8

Bayesian calibration and imaging with VLA Hydra A

This chapter is based on previous work using the `resolve` software (Arras et al. 2019b; Roth et al. 2023) to calibrate and image VLA data. The content of the following section is unpublished.

8.1 Bayesian calibration and imaging model using correlated data

Radio interferometric data with more than 20 antennas are challenging to image using forward modeling algorithms since the amount of the visibility data scales quadratically with the number of antennas. The calibration is even more demanding numerically since we need to deal with larger volume of the data than imaging to correct data corruption over frequency and time.

The scalability of `resolve` due to variational inference methods enables to apply the Bayesian calibration and imaging method to large data sets (the number of visivilities $> 10^6$), such as observations with the Very Large Array (VLA), Atacama Large Millimeter Array (ALMA), and MeerKAT, without extreme data averaging (Arras et al. 2021; Tychoniec et al. 2022; Roth et al. 2023, 2024).

This chapter demonstrates that we are able to perform calibration and imaging using correlated raw Hydra A VLA data at 2563MHz. Hydra A is one of the brightest extragalactic radio sources (Taylor et al. 1990), and therefore is an excellent source for validating the performance of our Bayesian calibration and imaging method. The data were observed on 27. Feb. 2014 with VLA A configuration (the longest baseline $\sim$ 36km). The correlated data was channel averaged over 128 channels (bandwidth = 128MHz) and time bin was 2 seconds. More details regarding the data can be found in Baidoo et al. (2023).

8.2 Method

In this work, we solve the Bayes' theorem to estimate the posterior distribution of the image I and the gain G given the visibility data V:

$$P(I,G|V) = \frac{P(V|I,G)P(I,G)}{P(V)}, \tag{8.1}$$

where $P(V|I,G)$ is the likelihood distribution, $P(I,G)$ is the prior, and $P(V)$ is the evidence.

Prior to the calibration and imaging, radio frequency inference (RFI) flagging was performed using `CASA` software (CASA Team et al. 2022). Note that RFI flagging using Bayesian approach is a potential application since RFI has a different correlation structure compared to the source signal, and therefore can be identified and removed effectively in Bayesian framework. A detailed investigation of Bayesian RFI flagging is beyond the scope of this dissertation.

In `resolve`, we can perform calibration including flux density calibration, gain calibration, and self-calibration and imaging simultaneously in a probabilistic setup (Arras et al. 2019b). For calibration, 3C286 data were used for the flux density calibration with the reported spectral flux density in the polynomial expression (Perley & Butler 2017):

$$\log(S) = 1.2481 - 0.4507\log(f) - 0.1798\log^2(f) + 0.0357\log^3(f), \tag{8.2}$$

where S is the flux density in Jy and f is the frequency in GHz.

As a gain calibrator, J0902-1415 located nearby the target source (angular separation between the target and the calibrator $\sim 4°$) was utilized.

Our calibration and imaging model for the correlated visibility data is similar to the Bayesian self-calibration and imaging model in chapter 5 (Hamaker et al. 1996; Smirnov 2011):

$$\begin{pmatrix} R_i R_j^* & 0 \\ 0 & L_i Lj^* \end{pmatrix} = \begin{pmatrix} g_i^R(t) & 0 \\ 0 & g_i^L(t) \end{pmatrix} \mathbb{FT}\left[\begin{pmatrix} I(\vec{x}) & 0 \\ 0 & I(\vec{x}) \end{pmatrix}\right] \begin{pmatrix} g_j^R(t) & 0 \\ 0 & g_j^L(t) \end{pmatrix}^\dagger, \tag{8.3}$$

where $R_i R_j^*$ and $L_i Lj^*$ are the parallel correlation functions in the visibility data, $g_{(i,j)}^{(R,L)}(t)$ is the gain for right and left circular polarization (R,L) and antenna (i,j), $I(\vec{x})$ is the total intensity sky image, and $\dagger$ denotes complex conjugation.

In `resolve`, we can infer the gain solutions and science target image from calibrators and target data at once. The antenna gain amplitude are inferred by the flux density calibrator, gain calibrator, and the target data and the antenna gain phase are inferred by the gain calibrator and the target data without the flux density calibrator, since the angular separation between flux density calibrator and target source is large. In this work, we assume that the data corruptions can be approximately described as antenna-based direction-independent gain corruptions.

Additionally, we utilized a point source model at the center of the field of view for calibrators. In other words, the visibility V of the calibrator is $|A| + 0j$, where $|A|$ is the uniform amplitude. The amplitude of flux density calibrator 3C286 was calculated from Equation 8.2 and the amplitude of gain calibrator J0902-1415 was inferred from the data using a log-normal prior. The point source calibrator model is a reasonable approximation at 2563MHz since the calibrators do not have complex structure due to the limited angular resolution in S-band. We note that, at higher frequencies, the complex structure of calibrators needs to be taken into account properly in order to obtain high-fidelity images.

To solve the Bayes' theorem in Equation 8.1, we need a likelihood and prior model. First of all, the full likelihood distribution is the product of the individual likelihoods for calibrators and the science target:

$$P(V|I, G) = \prod_k P(V_k|I_k, G). \tag{8.4}$$

In `resolve`, the negative log likelihood, namely likelihood Hamiltonian for the data V_k is utilized to solve the inference problem numerically:

$$\mathcal{H}(V_k|I_k, G) \approx \frac{1}{2} \sum_n \frac{|V_k - g_i g_j^* \mathbb{FT}[I_k]|^2}{\sigma^2}, \tag{8.5}$$

where I_k is point source model for calibrators or Stokes I image for the science target, n is the total number of data points, $\mathbb{FT}$ is Fourier transform operator, and σ is the standard deviation of the visibility data.

Note that the likelihood is analogous to the data fidelity term in Regularized Maximum Likelihood (RML) methods

$$\mathcal{H}(V|I, G) = \mathcal{H}(V_{flux}|I_f, |g|, arg(g_f)) + \mathcal{H}(V_{gain}|I_g, G) + \mathcal{H}(V_{target}|I, G) \tag{8.6}$$

where I_{flux} is the point source model for the flux density calibrator, g_f is the gain phase model for the flux density calibrator, and I_g is the gain calibrator point source model.

For the prior model, a Gaussian process with a non-parametric correlation kernel in `NIFTy` (Arras et al. 2019a) is employed for the image and gain solutions. With the likelihood and prior, we estimated the posterior distribution of the gains and image using the Metric Gaussian Variational Inference (MGVI) method (Knollmüller & Enßlin 2019). More information regarding the posterior estimation in `resolve` can be found in Arras et al. (2019b); Roth et al. (2023).

In conventional `CASA` calibration (CASA Team et al. 2022), the flux density and gain calibration are performed separately in an iterative fashion. We then self-calibrate the data using the target source, if the data have sufficient S/N, and reconstruct a Stokes I image with calibrated (including self-calibration) data. User-dependent procedures, such as manual flagging in the self-calibration and imaging and `CLEAN` windows hinder reproducibility and may induce human biases. On the other hand, in Bayesian imaging, we can infer calibration solutions and images simultaneously from the correlated raw data including self-calibration without additional flagging after RFI flagging. Therefore, we can perform calibration and imaging in a less supervised fashion and utilize all the data (calibrators and target data) at the same time. Note that the bandpass calibration was not applied since the bandwidth in the data is small (128MHz) and all channels were frequency averaged.

8.3 Results and conclusions

Figure 8.1 shows the image of the posterior mean of total intensity for Hydra A using `resolve` with 512 × 512 pixels, which correspond to a field of view of 120 × 120 arcseconds. The image is consistent with the `CLEAN` image in Figure 6 of Baidoo et al. (2023). In the `CLEAN` reconstruction, data with multiple intermediate frequencies (IFs) and all four different VLA configurations were used. As shown in Figure 8.1, `resolve` allows us to create images with super-resolution without requiring full S-band data sets. This ability to only use a subset of the full data implies that a large fraction of information in the data is potentially redundant and there may be a method of selecting a subset of data for image reconstruction without degrading image fidelity. Further investigation is left to future work.

Figure 8.2 and Figure 8.3 depict the posterior mean (solid line) amplitude gains and phase gains with their posterior standard deviation (semi-transparent color) for the right circular polarization (RCP) and left circular polarization (LCP), respectively. From the posterior standard deviation, we are able to dis-

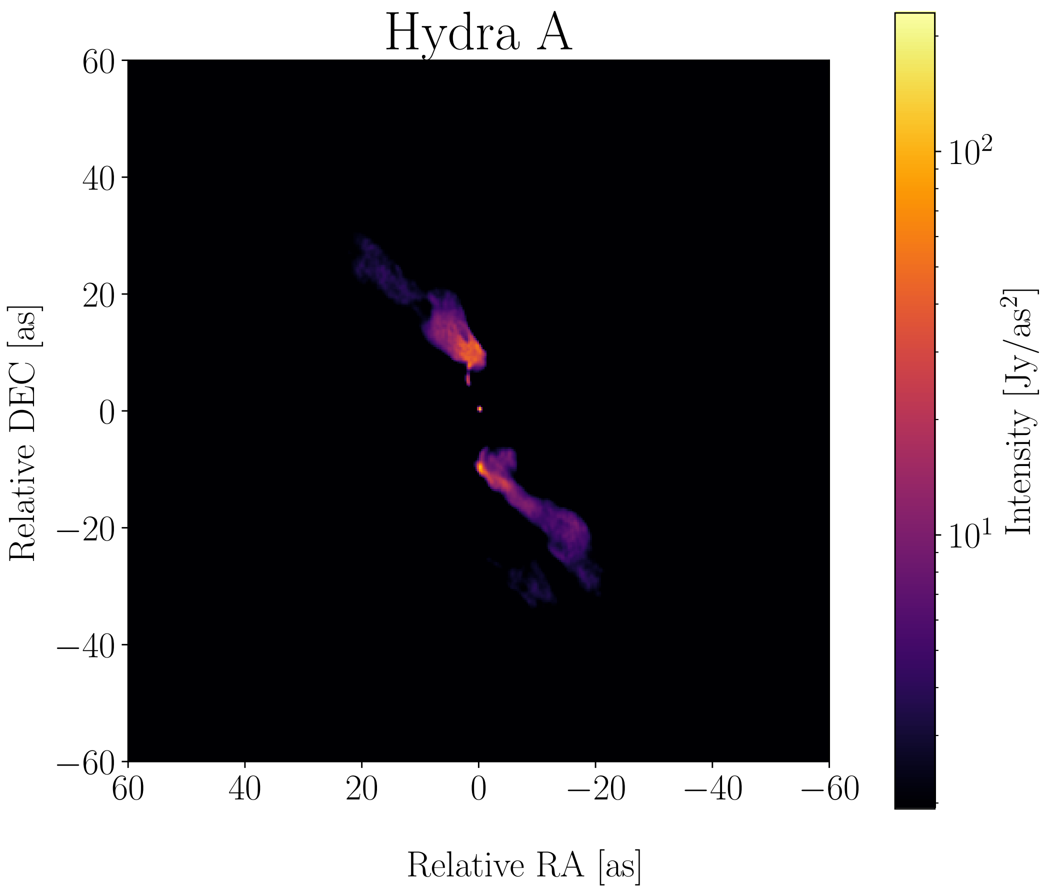

Figure 8.1: VLA Hydra A posterior mean image at 2563 MHz using Bayesian calibration and imaging method in `resolve` from correlated data.

tinguish problematic antennas, that are not well constrained by the data (e.g., E40 in RCP and W16 in LCP). As a result, we are able to quantify the reliability of our reconstructed calibration solutions from uncertainty estimation. This information may then be incorporated in an automatic flagging routine.

It has been demonstrated that `resolve` is able to solve degenerate inverse problems effectively, such as a joint inference of calibration solutions and imaging from radio interferometric data, with a Gaussian process prior model encoding prior knowledge about the instrument and penalizing unphysical solutions (Arras et al. 2019b, 2022; Roth et al. 2023; Kim et al. 2024, 2025a).

The reconstructed Hydra A total intensity image and gain calibration solutions show that Bayesian calibration and imaging method can be successfully applied to correlated raw data. At this stage of research, Bayesian calibration and imaging for larger data volume than VLA is still computationally demanding. Notably, Roth et al. (2024) introduce a new Bayeisan imaging approach inspired by major and minor cycles in `CLEAN` with GPUs for Bayesian imaging with MeerKAT data. With the help of algorithmic development, the automated Bayesian calibration and imaging pipeline will be able to process huge amount of

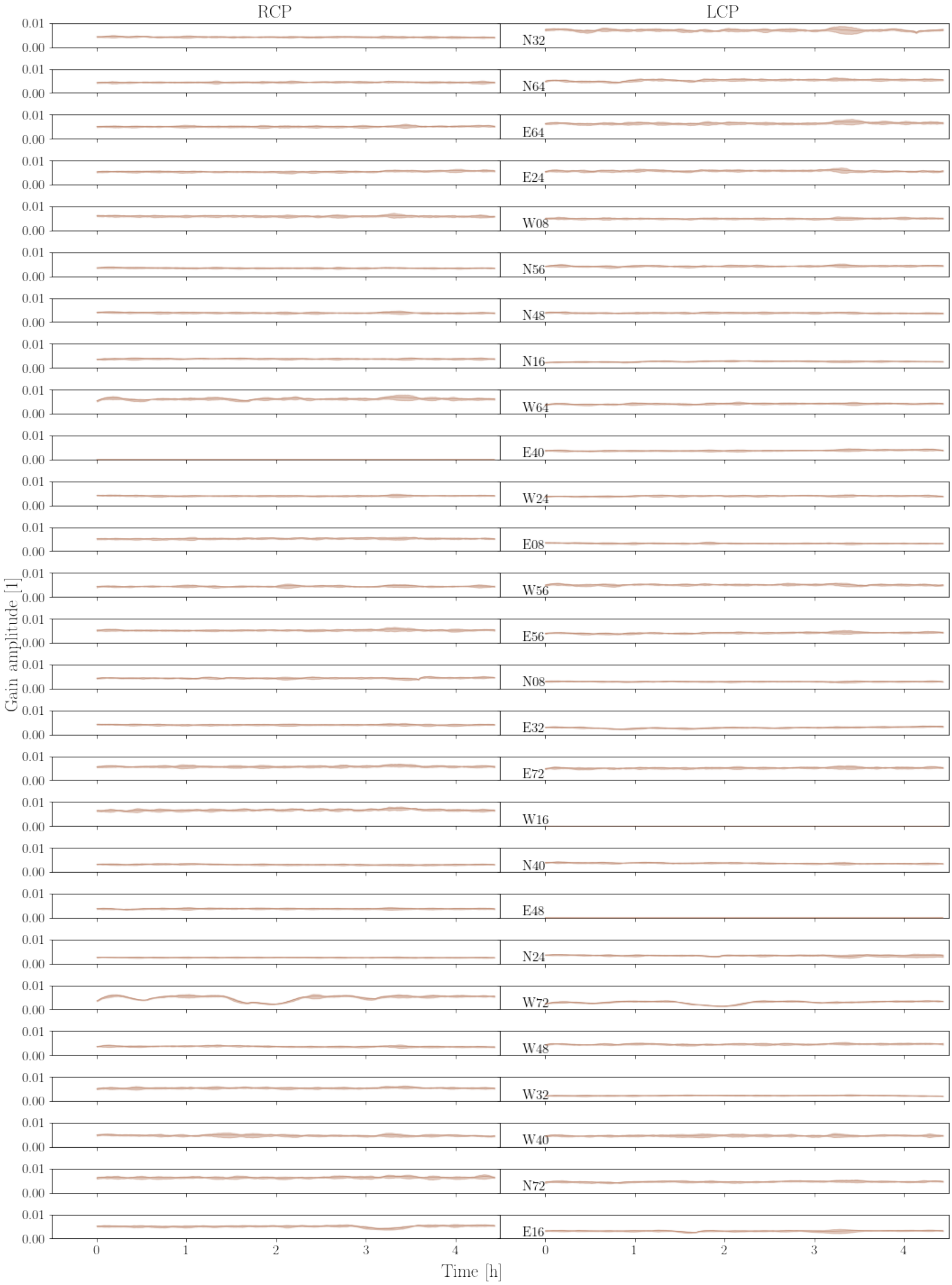

Figure 8.2: The `resolve` posterior amplitude gains. The left and right columns of the figure show amplitude gains from the right (RCP) and left (LCP) circular polarizations correspondingly. The amplitude gains as a function of time are illustrated as a thin line with a semi-transparent standard deviation. Each row represent an individual VLA antenna.

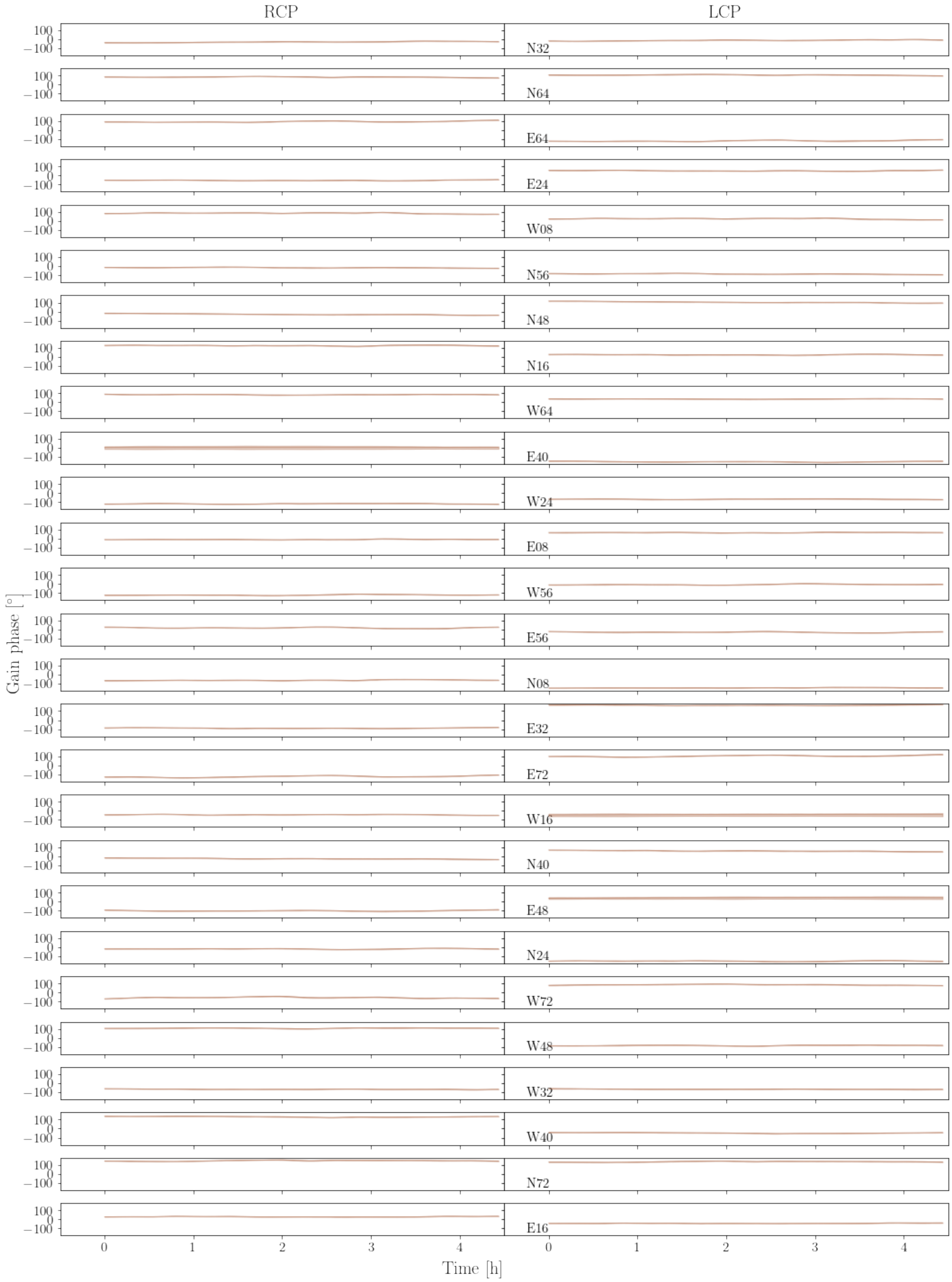

Figure 8.3: The `resolve` posterior phase gains. The left and right columns of the figure show phase gains from the right (RCP) and left (LCP) circular polarizations correspondingly. The phase gains as a function of time are illustrated as a thin line with a semi-transparent standard deviation. Each row represent an individual VLA antenna.

data from future telescopes, such as Square Killometer Array (SKA) and ngVLA, and therefore can obtain reliable calibration solutions and images.

Chapter 9

Conclusion

This thesis presents a comprehensive study of applications of Bayesian calibration and imaging methods for analysis of radio interferometric data using Bayesian imaging software `resolve`. Bayesian approach offers a robust framework to solve degenerate and ill-posed problems by encoding prior knowledge as a probability distribution. A probabilistic approach for imaging in radio interferometry is highly desirable, since no unique solution can be obtained in image reconstruction from interferometric data, owing to the sparsity and noise in the data. Particularly, in VLBI, robustness of image reconstruction depends strongly on simplifying assumptions about the source and instrument because both calibration and imaging of VLBI data are severely underdetermined problems.

In Bayesian framework, the degeneracy between calibration solutions and images can be explored, and multiple possible image reconstructions can be obtained instead of a single image typically provided by other imaging algorithms. Furthermore, incorporating calibration into imaging is a natural extension of Bayesian imaging because calibration uncertainties principally should be taken into account to obtain robust images. In imaging studies, the calibration uncertainties are often overlooked, in contrast to considerations given to the imaging uncertainties. On the other hand, `resolve` is able to disentangle the degeneracy between the calibration solutions and images and to provide a reliable reconstruction with uncertainty estimation.

A joint inference of calibration and imaging has another advantage: we can perform calibration and imaging in a less supervised way. Upcoming radio telescopes, such as SKA and ngVLA, will provide orders of magnitude larger data volumes, and the availability of an automated calibration and imaging pipeline therefore would be crucial for their success. The automated Bayesian calibration and imaging method based on the radio interferometer measurement equation (RIME) can offer a viable solution to resolve this issue.

In chapter 5 and chapter 6, we utilized a Bayesian self-calibration and imaging method for mm-VLBI data in order to obtain high-resolution total intensity images of galaxy M87 at 43 and 86 GHz. Our Bayesian calibration and imaging method performs self-calibration and imaging simultaneously and does not require extensive flagging since the uncertainty in the data are handled naturally in a probabilistic setup. Furthermore, amplitude and phase self-calibration are performed in a single step, without manual steering of the calibration solution interval, which can provide more robust results against non-Gaussian errors at low S/N.

In chapter 6, we revisited the GMVA+ALMA observation of M87 in 2018 (Lu et al. 2023) and confirmed the simultaneous observation of the black hole shadow and the relativistic jets of galaxy M87 using `resolve` and `DoG-HiT` software. This work has demonstrated the robustness and effectiveness of the Bayesian imaging approach in comparison to the original imaging discussed in Lu et al. (2023) where the `CLEAN` method was not able to reconstruct a robust ring-like structure due to its suboptimal resolution, and the RML-based imaging software `SMILI` was utilized to reconstruct the black hole shadow of M87 without the jet and with a smaller field of view.

Furthermore, in our analysis of the ring-like structure in M87 we explored the posterior distribution of ring feature parameters (diameter, width, and ellipticity) from posterior sample images. The ring diameter measured from the `resolve` reconstruction is $60.9 \pm 2.2\,\mu$as ($16.0 \pm 0.6\,r_g$) in agreement with the estimation in Lu et al. (2023) ($64^{+4}_{-8}\,\mu$as). Our results can provide more reliable error estimates than the previous report since the uncertainty is estimated from a reconstruction of posterior sample images, not from a selected top-set of images. The ring diameter is approximately 1.5 times larger than the EHT M87 observation at 1 mm in 2018. The spectral index of this compact region is slightly positive ($\alpha \approx 0.4$), based one the `resolve` image at 3 mm and EHT results at 1 mm. It indicates the black hole shadow of M87 at 3 mm has a significant contribution from accretion flows. Furthermore, our `resolve` and `DoG-HiT` reconstructions show a consistent limb-brightened jet structure, although the central spine is less prominent compared to the earlier `CLEAN` reconstruction of Lu et al. (2023). Our results provide stringent observational constraints on theoretical models and numerical simulations to study the connection between the supermassive black hole and the jet launching mechanism.

In chapter 7, we introduce a novel, RIME-based Bayesian polarization calibration and imaging method for VLBI. In conventional `CLEAN`-based methods, a simple image model, namely similarity approximation (Cotton 1993; Leppanen et al. 1995), is employed in order to estimate antenna leakages. However, this assumption has limitations in describing complex polarized source structures. On the other hand, our RIME-based Bayesian polarization calibration and imaging method is able to obtain robust calibration solutions (gains and leakages) and images simultaneously, which are consistent with the entire data set. Calibration uncertainties are systematically accounted for image reconstruction by exploring gain and leakage posterior distributions. Furthermore, polarization constraints ($I \geq \sqrt{Q^2 + U^2 + V^2}$) are encoded in the polarimetric image prior in order to obtain physically plausible images. In addition, polarization calibration with several sources and multi-intermediate frequencies (multi-IFs) are supported in order to maximize the parallactic angle coverage and identify instrumental corruptions per IF.

Our Bayesian polarization calibration and imaging method enables us to examine magnetic field structures in the vicinity of supermassive black holes and relativistic jets. For instance, the `resolve` image of the quasar 3C 273 made from the VLBA data at 15 GHz reveals a detailed core structure, with the fractional linear polarization in relativistic jets in accordance with theoretical predictions of polarized synchrotron radiation. In addition, we revisited the 86 GHz GMVA+ALMA observation of the blazar OJ287 made in 2017 and imaged previously in Zhao et al. (2022), using our Bayesian polarization calibration and imaging method. The resulting `resolve` reconstruction provided more detail in the wiggling toroidal magnetic field structure than the `CLEAN` or `ehtim` software and revealed a consistent diverging EVPA pattern in the jet, indicating the potential presence of oblique or recollimation shocks (Zhao et al. 2022).

In chapter 8, we discuss Bayesian calibration and imaging method with a Hydra A observation made with the VLA at 2.5 GHz to validate the Bayesian calibration and imaging method using raw correlated radio interferometric data. The results show that our Bayesian calibration and imaging method is able to perform full calibration and imaging including flux density calibration, gain calibration, and self-calibration.

Altogether, the work described in this dissertation demonstrates that employing the automated Bayesian calibration and imaging approach is beneficial for image reconstruction from interferometric data with full polarimetry and it has a great potential for application in future radio arrays, such as SKA and ngVLA.

Some of the perspective further developments of this approach include performing rotation measure analysis using the Bayesian polarization calibration and imaging method with uncertainty estimation. Furthermore, global fringe fitting and Stokes V calibration can be incorporated in `resolve`. In addition, Bayesian multi-frequency imaging using simultaneous multi-band observations in VLBI can provide more detailed and reliable spectral information. The development of more scalable Bayesian calibration and imaging algorithms is another important direction for processing data from next-generation radio telescopes. Roth et al. (2024) introduced `fast-resolve` motivated by the concept of minor and major cycles in the `CLEAN` algorithm. Gain calibration and leakage calibration can be incorporated in the `fast-resolve` and this work is left for the future.

Bibliography

Abbott, B. P., Abbott, R., Abbott, T. D., et al. 2016, Phys. Rev. Lett., 116, 061102

Abbott, R., Abbott, T. D., Abraham, S., et al. 2020, Phys. Rev. Lett., 125, 101102

Akiyama, K., Kuramochi, K., Ikeda, S., et al. 2017, ApJ, 838, 1

Arras, P., Baltac, M., Ensslin, T. A., et al. 2019a, ascl:1903.008

Arras, P., Bester, H. L., Perley, R. A., et al. 2021, A&A, 646, A84

Arras, P., Frank, P., Haim, P., et al. 2022, Nature Astronomy, 6, 259

Arras, P., Frank, P., Leike, R., Westermann, R., & Enßlin, T. A. 2019b, A&A, 627, A134

Arras, P., Roth, J., Reinecke, M., et al. 2025, arXiv e-prints, arXiv:2504.00227

Asada, K., Inoue, M., Uchida, Y., et al. 2002, PASJ, 54, L39

Baidoo, L., Perley, R. A., Eilek, J., et al. 2023, ApJ, 955, 16

Betancourt, M. 2017, arXiv e-prints, arXiv:1701.02434

Blackburn, L., Pesce, D. W., Johnson, M. D., et al. 2020, ApJ, 894, 31

Blandford, R. D. & Payne, D. G. 1982, MNRAS, 199, 883

Blandford, R. D. & Znajek, R. L. 1977, MNRAS, 179, 433

Blei, D. M., Kucukelbir, A., & McAuliffe, J. D. 2016, arXiv e-prints, arXiv:1601.00670

Bolton, C. T. 1972, Nature, 235, 271

Bower, G. C., Falcke, H., Sault, R. J., & Backer, D. C. 2002, ApJ, 571, 843

Broderick, A. E., Gold, R., Karami, M., et al. 2020a, ApJ, 897, 139

Broderick, A. E. & Pesce, D. W. 2020, ApJ, 904, 126

Broderick, A. E., Pesce, D. W., Tiede, P., Pu, H.-Y., & Gold, R. 2020b, ApJ, 898, 9

Carroll, S. M. 2004, Spacetime and geometry. An introduction to general relativity

CASA Team, Bean, B., Bhatnagar, S., et al. 2022, PASP, 134, 114501

Chael, A. A., Johnson, M. D., Bouman, K. L., et al. 2018, ApJ, 857, 23

Chael, A. A., Johnson, M. D., Narayan, R., et al. 2016, ApJ, 829, 11

Clark, B. G. 1980, A&A, 89, 377

Cornwell, T. J. 2008, IEEE Journal of Selected Topics in Signal Processing, 2, 793

Cotton, W. D. 1993, AJ, 106, 1241

Curtis, H. D. 1918, Publications of Lick Observatory, 13, 9

Doeleman, S. S., Weintroub, J., Rogers, A. E. E., et al. 2008, Nature, 455, 78

Dyson, F. W., Eddington, A. S., & Davidson, C. 1920, Philosophical Transactions of the Royal Society of London Series A, 220, 291

Edenhofer, G., Frank, P., Roth, J., et al. 2024, Journal of Open Source Software, 9, 6593

EHT MWL Science Working Group, Algaba, J. C., Anczarski, J., et al. 2021, ApJ, 911, L11

Einstein, A. 1915a, Sitzungsberichte der Königlich Preussischen Akademie der Wissenschaften, 844

Einstein, A. 1915b, Sitzungsberichte der Königlich Preussischen Akademie der Wissenschaften, 831

Einstein, A. 1916, Annalen der Physik, 354, 769

Einstein, A. 1917, Sitzungsberichte der Königlich Preussischen Akademie der Wissenschaften, 142

Enßlin, T. A. 2019, Annalen der Physik, 531, 1800127

Event Horizon Telescope Collaboration, Akiyama, K., Alberdi, A., et al. 2024, ApJ, 964, L25

Event Horizon Telescope Collaboration, Akiyama, K., Alberdi, A., et al. 2022, ApJ, 930, L12

Event Horizon Telescope Collaboration, Akiyama, K., Alberdi, A., et al. 2019a, ApJ, 875, L1

Event Horizon Telescope Collaboration, Akiyama, K., Alberdi, A., et al. 2019b, ApJ, 875, L5

Event Horizon Telescope Collaboration, Akiyama, K., Alberdi, A., et al. 2019c, ApJ, 875, L3

Event Horizon Telescope Collaboration, Akiyama, K., Algaba, J. C., et al. 2021, ApJ, 910, L12

Falcke, H., Melia, F., & Agol, E. 2000, ApJ, 528, L13

Fernini, I., Leahy, J. P., Burns, J. O., & Basart, J. P. 1991, ApJ, 381, 63

Fletcher, A., Beck, R., Shukurov, A., Berkhuijsen, E. M., & Horellou, C. 2011, MNRAS, 412, 2396

Frank, P., Leike, R., & Enßlin, T. A. 2021, Entropy, 23, 853

Gabuzda, D. C., Murray, É., & Cronin, P. 2004, MNRAS, 351, L89

Gaia Collaboration, Panuzzo, P., Mazeh, T., et al. 2024, A&A, 686, L2

Gebhardt, K., Adams, J., Richstone, D., et al. 2011, ApJ, 729, 119

Genzel, R., Eisenhauer, F., & Gillessen, S. 2010, Reviews of Modern Physics, 82, 3121

Genzel, R., Eisenhauer, F., & Gillessen, S. 2024, A&A Rev., 32, 3

Genzel, R., Schödel, R., Ott, T., et al. 2003, Nature, 425, 934

Ghez, A. M., Salim, S., Weinberg, N. N., et al. 2008, ApJ, 689, 1044

Ghisellini, G. 2013, Radiative Processes in High Energy Astrophysics, Vol. 873

Gillessen, S., Eisenhauer, F., Trippe, S., et al. 2009, ApJ, 692, 1075

Ginzburg, V. L. & Syrovatskii, S. I. 1965, ARA&A, 3, 297

Gralla, S. E., Holz, D. E., & Wald, R. M. 2019, Phys. Rev. D, 100, 024018

GRAVITY Collaboration, Abuter, R., Aimar, N., et al. 2022a, A&A, 657, A82

GRAVITY Collaboration, Abuter, R., Aimar, N., et al. 2022b, A&A, 657, L12

GRAVITY Collaboration, Abuter, R., Amorim, A., et al. 2018, A&A, 618, L10

GRAVITY Collaboration, Abuter, R., Amorim, A., et al. 2019, A&A, 625, L10

Hada, K., Asada, K., Nakamura, M., & Kino, M. 2024, A&A Rev., 32, 5

Hada, K., Doi, A., Kino, M., et al. 2011, Nature, 477, 185

Hada, K., Kino, M., Doi, A., et al. 2016, ApJ, 817, 131

Hamaker, J. P., Bregman, J. D., & Sault, R. J. 1996, A&AS, 117, 137

Hartle, J. B. 2003, Gravity : an introduction to Einstein's general relativity

Högbom, J. A. 1974, A&AS, 15, 417

Homan, D. C. & Wardle, J. F. C. 1999, AJ, 118, 1942

Honma, M., Akiyama, K., Uemura, M., & Ikeda, S. 2014, PASJ, 66, 95

Hovatta, T., Lister, M. L., Aller, M. F., et al. 2012, AJ, 144, 105

Issaoun, S., Johnson, M. D., Blackburn, L., et al. 2019, ApJ, 871, 30

Jansky, K. G. 1933, Nature, 132, 66

Janssen, M., Goddi, C., van Bemmel, I. M., et al. 2019, A&A, 626, A75

Jennison, R. C. 1958, MNRAS, 118, 276

Johnson, M. D., Lupsasca, A., Strominger, A., et al. 2020, Science Advances, 6, eaaz1310

Jones, R. C. 1941, Journal of the Optical Society of America (1917-1983), 31, 488

Jorstad, S. G., Marscher, A. P., Lister, M. L., et al. 2005, AJ, 130, 1418

Junklewitz, H., Bell, M. R., Selig, M., & Enßlin, T. A. 2016, A&A, 586, A76

Kellermann, K. I., Sramek, R., Schmidt, M., Shaffer, D. B., & Green, R. 1989, AJ, 98, 1195

Kerr, R. P. 1963, Phys. Rev. Lett., 11, 237

Kim, J.-S., Müller, H., Nikonov, A. S., et al. 2025a, A&A, 696, A169

Kim, J.-S., Nikonov, A. S., Roth, J., et al. 2024, A&A, 690, A129

Kim, J.-S., Roth, J., Park, J., Livingston, J. D., & Arras, P. 2025b, arXiv:2511.16556

KM3NeT Collaboration, S., A., Albert, A., Alhebsi, A. R., et al. 2025, Nature, 638, 376

Knollmüller, J., Arras, P., & Enßlin, T. 2023, arXiv e-prints, arXiv:2310.16889

Knollmüller, J. & Enßlin, T. A. 2019, arXiv e-prints, arXiv:1901.11033

Knollmüller, J. & Enßlin, T. A. 2018, Encoding prior knowledge in the structure of the likelihood

Krichbaum, T. P., Graham, D. A., Witzel, A., et al. 1998, A&A, 335, L106

Kullback, S. & Leibler, R. A. 1951, The Annals of Mathematical Statistics, 22, 79

Leike, R. H. & Enßlin, T. A. 2017, Entropy, 19, 402

Leike, R. H., Glatzle, M., & Enßlin, T. A. 2020, A&A, 639, A138

Leppanen, K. J., Zensus, J. A., & Diamond, P. J. 1995, AJ, 110, 2479

Lisakov, M. M., Kravchenko, E. V., Pushkarev, A. B., et al. 2021, ApJ, 910, 35

Lister, M. L. & Homan, D. C. 2005, AJ, 130, 1389

Lobanov, A. P. 1998a, A&AS, 132, 261

Lobanov, A. P. 1998b, A&A, 330, 79

Lu, R.-S., Asada, K., Krichbaum, T. P., et al. 2023, Nature, 616, 686

Mackay, D. J. C. 2003, Information Theory, Inference and Learning Algorithms

Marrone, D. P., Moran, J. M., Zhao, J.-H., & Rao, R. 2007, ApJ, 654, L57

Mei, S., Blakeslee, J. P., Côté, P., et al. 2007, ApJ, 655, 144

Müller, H. 2024, A&A, 689, A299

Müller, H. & Lobanov, A. P. 2022, A&A, 666, A137

Narayan, R. & Yi, I. 1994, ApJ, 428, L13

Natarajan, I., Deane, R., van Bemmel, I., et al. 2020, MNRAS, 496, 801

Oei, M. S. S. L., Hardcastle, M. J., Timmerman, R., et al. 2024, Nature, 633, 537

Penrose, R. 1969, Nuovo Cimento Rivista Serie, 1, 252

Perley, R. A. & Butler, B. J. 2017, ApJS, 230, 7

Perley, R. A., Dreher, J. W., & Cowan, J. J. 1984, ApJ, 285, L35

Pesce, D. W. 2021, AJ, 161, 178

Plavin, A., Kovalev, Y. Y., Kovalev, Y. A., & Troitsky, S. 2020, ApJ, 894, 101

Pound, R. V. & Rebka, G. A. 1960, Phys. Rev. Lett., 4, 337

Rayleigh. 1879, The London, Edinburgh, and Dublin Philosophical Magazine and Journal of Science, 8, 261–274

Roth, J., Arras, P., Reinecke, M., et al. 2023, A&A, 678, A177

Roth, J., Frank, P., Bester, H. L., et al. 2024, A&A, 690, A387

Rüstig, J., Guardiani, M., Roth, J., Frank, P., & Enßlin, T. 2024, A&A, 682, A146

Rybicki, G. B. & Lightman, A. P. 1979, Radiative processes in astrophysics

Ryle, M. 1962, Nature, 194, 517

Ryle, M. & Hewish, A. 1960, MNRAS, 120, 220

Schmidt, M. 1963, Nature, 197, 1040

Schwab, F. R. & Cotton, W. D. 1983, AJ, 88, 688

Schwarzschild, K. 1916, Sitzungsberichte der Königlich Preussischen Akademie der Wissenschaften, 189

Sebokolodi, M. L. L., Perley, R., Eilek, J., et al. 2020, ApJ, 903, 36

Selig, M., Bell, M. R., Junklewitz, H., et al. 2013, Astronomy Astrophysics, 554, A26

Shields, G. A. 1978, Nature, 272, 706

Smirnov, O. M. 2011, A&A, 527, A106

Steininger, T., Dixit, J., Frank, P., et al. 2019, Annalen der Physik, 531, 1800290

Taylor, G. B., Perley, R. A., Inoue, M., et al. 1990, ApJ, 360, 41

Tchekhovskoy, A. 2015, in Astrophysics and Space Science Library, Vol. 414, The Formation and Disruption of Black Hole Jets, ed. I. Contopoulos, D. Gabuzda, & N. Kylafis, 45

Thompson, A. R., Moran, J. M., & Swenson, Jr., G. W. 2017, Interferometry and Synthesis in Radio Astronomy, 3rd Edition

Tiede, P. 2022, The Journal of Open Source Software, 7, 4457

Truemper, J., Pietsch, W., Reppin, C., et al. 1978, ApJ, 219, L105

Twiss, R. Q., Carter, A. W. L., & Little, A. G. 1960, The Observatory, 80, 153

Tychoniec, L., Guglielmetti, F., Arras, P., Ensslin, T., & Villard, E. 2022, in Physical Sciences Forum, Vol. 5, Physical Sciences Forum, 52

Walker, R. C., Hardee, P. E., Davies, F. B., Ly, C., & Junor, W. 2018, ApJ, 855, 128

Walsh, D., Carswell, R. F., & Weymann, R. J. 1979, Nature, 279, 381

Webster, B. L. & Murdin, P. 1972, Nature, 235, 37

Westerkamp, M., Eberle, V., Guardiani, M., et al. 2024, A&A, 684, A155

Wiaux, Y., Jacques, L., Puy, G., Scaife, A. M. M., & Vandergheynst, P. 2009, MNRAS, 395, 1733

Wielgus, M., Issaoun, S., Martí-Vidal, I., et al. 2024, A&A, 682, A97

Wielgus, M., Moscibrodzka, M., Vos, J., et al. 2022, A&A, 665, L6

Zensus, J. A., Cohen, M. H., & Unwin, S. C. 1995, ApJ, 443, 35

Zhao, G.-Y., Gómez, J. L., Fuentes, A., et al. 2022, ApJ, 932, 72

Acknowledgements

To finish my PhD journey, I was fortunate to meet many wonderful people and grateful for the support I received from them. First and foremost, I am deeply grateful to my supervisor, Andrei Lobanov, for his patience, support, and wisdom. He always listened to me, offered his help, and guided me in refining my rough and abstract ideas. We also shared memorable moments outside of work, playing football together and enjoying time with friends over a beer. Without his guidance and encouragement, this dissertation would not have been possible. I would also like to express my sincere appreciation to Anton Zensus for his leadership and encouragement. He gave me the opportunity to pursue my PhD in a welcoming and friendly VLBI group in Bonn. I am also thankful to Torsten Ensslin for his mentorship and enthusiasm for science. I would like to thank my PhD dissertation committee members, Andreas Eckart, Dominik Riechers, Yaping Shao, and Yoko Okada.

I am deeply thankful to my PhD friends at MPIfR, Aleksei Nikonov, Hendrik Mueller, Petra Benke, Saurabh, Cecilia Agosti, Jan Roeder, Luca Ricci, Georgios Kalaitzidakis, and Lena Debbrecht for the wonderful memories, valuable discussions, generous help, and friendship. I enjoyed the trips we made and they helped me feel at home in Bonn. I would like to thank the members of our VLBI group in Bonn, Daewon Kim, Thomas Krichbaum, Eduardo Ros, Arman Tursunov, Jack Livingston, Yuri Kovalev, Vladislav Makeev, Vanessa Pinto, Michael Janssen, Alan Roy, Mikhail Lisakov, Yoonkyung Choi, Sebastiano von Fellenberg, Jan Wagner, Gunther Witzel, Guang-Yao Zhao, Asmita Gupta, and Galina Lipunova, for their kindness, support, lessons about the VLBI, and discussions. Everyone was willing to help me whenever I felt lost during my PhD journey. I have learned a great deal about VLBI technology as well as the mindset and attitude of a scientist. I will remember all the workshops, observations, conferences, gatherings, and especially the Christmas parties we shared. I really enjoyed working in this amazing group. I thank `resolve` team members, Jakob Roth, Philipp Arras, Jakob Knollmueller, Julian Ruestig, Richard Fuchs, and Vishal Johnson, for stimulating discussions, help, and support. I also greatly appreciated the workshops and meetings we organized together.

I thank the people who proofread this thesis, Jack Livingston, Saurabh, Arman Tursunov, Jakob Roth, Hendrik Mueller, Alan Roy, Petra Benke and Aleksei Nikonov. I would also like to thank Rick Perley for providing the VLA Hydra A data, Rusen Lu for GMVA+ALMA M87 data, Guang-Yao Zhao for GMVA+ALMA OJ287 data, and Yuri Kovalev for MOJAVE data. There are many others whom I may have missed mentioning here, and I sincerely thank you all.

Finally, I would like to express my deepest appreciation to my beloved parents and sister for their love and unconditional support. 마지막으로, 저의 사랑하는 부모님과 여동생에게 변함없는 사랑과 헌신적인 지원에 깊은 감사를 드립니다.